



HAL
open science

Bipolar cascade laser sources for directly modulated links

Frédéric Dross

► **To cite this version:**

Frédéric Dross. Bipolar cascade laser sources for directly modulated links. domain_other. Télécom ParisTech, 2004. English. NNT : 2004 E 017 . pastel-00001046

HAL Id: pastel-00001046

<https://pastel.hal.science/pastel-00001046>

Submitted on 18 Feb 2005

HAL is a multi-disciplinary open access archive for the deposit and dissemination of scientific research documents, whether they are published or not. The documents may come from teaching and research institutions in France or abroad, or from public or private research centers.

L'archive ouverte pluridisciplinaire **HAL**, est destinée au dépôt et à la diffusion de documents scientifiques de niveau recherche, publiés ou non, émanant des établissements d'enseignement et de recherche français ou étrangers, des laboratoires publics ou privés.

ECOLE DOCTORALE EDITE

Thèse

**Présentée pour obtenir le grade de docteur de l'Ecole Nationale
Supérieure des Télécommunications**

FREDERIC DROSS

**SOURCES LASER A CASCADE BIPOLAIRE POUR LA
MODULATION DIRECTE**

Soutenue le mardi 9 novembre 2004 devant le jury composé de :

Pr. Slimane Loualiche
Pr. Françoise Lozes-Dupuy
Dr. Joël Jacquet
Dr. Jean Chazelas
Pr. Afshin Daryoush
Pr. Borge Vinter
Pr. Philippe Gallion
Dr. Frédéric van Dijk

Président
Rapporteur
Rapporteur
Examineur
Examineur
Examineur
Directeur de thèse
Directeur de thèse

Direction :

Frédéric van Dijk Microwave Photonics Lab. Thales Research & Technology Domaine de Corbeville 91404 Orsay, cedex	Philippe Gallion Dept. COMELEC ENST 46, rue Barrault 75013 Paris
--	--

Remerciements

En ce début de vingt-et-unième siècle, les travaux de recherche effectués sont plus que jamais le résultat du fonctionnement d'une équipe. J'aimerais ainsi remercier tous les gens qui ont participé de près ou de loin à ce travail.

Je remercie Philippe Gallion, Professeur à l'ENST pour avoir assuré la direction universitaire de cette thèse. J'ai également utilisé son temps précieux pour développer avec sa collaboration le modèle d'estimation des caractéristiques dynamiques des BCL et je lui en suis reconnaissant.

Je remercie Julien Nagle, co-responsable du département composant de TRT, d'avoir posé régulièrement son regard critique et affuté sur mon travail. Il a tout à la fois apporté son point de vue éclairé sur la thèse et facilité à chaque instant son déroulement.

Je remercie l'ensemble des personnes avec qui j'ai partagé la vie du labo. Je pense en particulier à Mehdi Alouini, dont la clarté des idées sur nos sujets rayonne bien en dehors de son propre esprit ; Reynald Boula-Picard, dont l'assurance en manip est pour moi un mystère déroutant ; Jérôme Lopez, dont la polyvalence (théorie comme manips, composants comme systèmes...) est un atout sans prix pour son équipe ; Alain Enard, discret comme personne, efficace comme cinq ; Nicolas Michel, le roi du calcul analytique ; Chantal Moronvalle, les doigts de fée, l'assurance de la réussite d'une manip tordue ; Jacqueline Lehoux, pour son expérience et son professionnalisme ; Corinne Dernazaretian et ses câblages qui valent de l'or ! Je pense également à Alexandre Marceaux, dont la simplicité, l'écoute patiente et attentive, et les compétences scientifiques sont des qualités autant humaines que professionnelles qui en font un collègue hors-pair. Merci à tous, pour toutes ces discussions scientifiques et autres !

Je remercie les stagiaires du laboratoire : François-Xavier, Sébastien Berger, Damien Guiliéri (quand tu veux pour un tennis) et Cécilia Dupré. Merci à Clément Thibon qui malgré ses âneries (désolé Clément, il n'y a pas d'autres mots !), nous a fourni un travail expérimental conséquent, que j'ai d'ailleurs pu intégrer dans mon manuscrit. Merci également à Elroy Pluk pour la mise en place efficace du banc de test en courant pulsé (hartelijk dank!).

Merci aux gens du labo commun MPL, et en particulier Loïc Ménager, avec qui j'ai eu la chance d'échanger quelques vues sur la sommation. Je remercie également Jean Chazelas, responsable du MPL, qui en plus d'avoir suscité une bonne atmosphère dans la plupart des réunions, a accepté de faire partie de mon jury de thèse. Son tact et son humour en font un excellent manager.

Merci à Philippe Bois, Eric Costard et leur(s) équipe(s) pour m'avoir accepté quelques mois dans leur salle. Toute l'équipe peut être fière de la dernière réalisation (0.2 K, c'est bien ça ?), fruit d'une collaboration dynamique, d'un excellent niveau scientifique, et d'une atmosphère de travail stimulante, orchestrés

par les deux têtes (oserais-je dire “gueules” ?). Je remercie Mathieu Caras, Loïc Lanco et Alfredo de Rossi pour quelques discussions et coups de pouce qui m’ont été bien utiles.

Merci également à Michel Krakowski, Carlo Sirtori, Sukhdeep Dhillon, Martine Carbonelle, Michel Calligaro, pour leur aide technique et discussions survenues tout au long du projet. Merci à Christophe Kazmierski pour les manip de champ lointain en pulsé. Merci aussi à Shailendra Bansropun pour avoir apporté un peu de chaleur et beaucoup de bonne humeur à notre couloir excentré, et parfois même une chanson sifflotée qui reste dans la tête toute la journée !

Je remercie Chantal Lermenier et Mme Touati pour leur efficacité. Je remercie Claude Grattepain pour les mesures SIMS.

Merci à Françoise Lozes-Dupuy et Joël Jacquet pour avoir accepté d’être rapporteur de cette thèse. Merci à Afshin Daryoush d’avoir fait le déplacement pour assister à la soutenance, et pour les quelques discussions qui ont précédées et suivies cette soutenance (thank you very much!). Merci encore à Slimane Loualiche d’avoir accepté d’être Présid... enfin, je veux dire porte-parole du jury. Leur solide expérience est un gage de qualité pour ce travail.

Un remerciement particulier va à notre épitaxieur préféré, Olivier Parillaud, toujours prêt à relever les défis que nous livrent les sciences des matériaux, et à prendre un peu de son temps pour une discussion sur l’épitaxie, la vie, le monde...

Je voudrais remercier également particulièrement Nakita Vodjdani, responsable du laboratoire optique-hyperfréquence. J’ai pu apprécié sa rigueur scientifique, sa détermination, sa franchise, son honnêteté et son expérience scientifiques. Nos discussions animées sont toutes d’excellents souvenirs pour moi !

La potion magique de cette thèse est due à un seul homme, un druide au talent immense, Børge Vinter. Il m’a patiemment initié au culte du dieu HET-DIO, m’a expliqué le langage qu’il fallait employer, les règles à respecter, et un beau jour, comme par miracle, la divinité a bien voulu communiquer avec nous, pauvres mortels. Ce travail te doit beaucoup, Børge !

Mes remerciements s’adressent enfin tout particulièrement à Frédéric van Dijk, encadrant de cette thèse. Son écoute et sa disponibilité permanentes ont été un soutien extrêmement rassurant tout au long de la thèse. J’ai ainsi pu être le témoin impressionné de son optimisme à toute épreuve, de son immense curiosité scientifique, de son adaptabilité à toutes les situations et toutes les personnalités et de son sens aigu de l’humain qui lui ouvriront certainement de grandes portes. Ces qualités humaines et scientifiques en ont fait un encadrant de thèse que beaucoup d’étudiants thésards peuvent m’envier.

Je remercie également ma famille et mes amis pour leur soutien continu, pour avoir tenté de retenir le sujet de ma thèse et surtout pour leur affection sans borne.

J’aimerais finir par une pensée tendre et émue pour Ariane Labat, qui comprend tout, et tout le reste aussi !

Frédéric Dross

Résumé

1 Introduction générale

La technologie radar entame cette année son deuxième siècle. Le principe reste inchangé (émission puis réception de signaux électromagnétiques hyperfréquence pour détection d'objets distants), mais les technologies ont fortement évolué. En particulier, les systèmes actuels doivent présenter une bonne sensibilité sur une plage de fréquence s'étalant de quelques kHz à plusieurs dizaines de GHz. La transmission sur fibre optique monomode présente une bande passante supérieure de plusieurs ordres de grandeur à la transmission électronique hyperfréquence. De plus, les fibres optiques présentent des caractéristiques mécaniques (poids et volume) et d'insensibilité au rayonnement électromagnétique qui en font des composants de choix pour les systèmes embarqués. Néanmoins, pour être compétitif avec le câble coaxial, la liaison optique-hyperfréquence doit dépasser clairement les performances de son concurrent historique. Alors que les pertes dans la fibre sont extrêmement réduites, le rendement de conversion électro-optique à l'émission, comme à la réception dégrade le gain hyperfréquence de la liaison, et limite ainsi sa compétitivité. En particulier, le gain d'une liaison optique hyperfréquence à modulation directe est proportionnel au carré du rendement du laser, qui n'est à l'heure actuelle que d'environ 1 photon couplé dans la fibre pour 10 électrons injectés dans le laser.

Ce travail de thèse propose l'utilisation de sources laser à cascade bipolaire pour améliorer les caractéristiques des liaisons opto-hyperfréquence à modulation directe. Si N lasers sont connectés en série (mis en cascade), la modulation de courant se propage de laser en laser. Le signal hyperfréquence est donc converti N fois en modulation du signal optique. En combinant ensuite ces signaux on peut profiter de la conversion multiple. Le rendement électro-optique de la source et donc le gain hyperfréquence de la liaison sont améliorés.

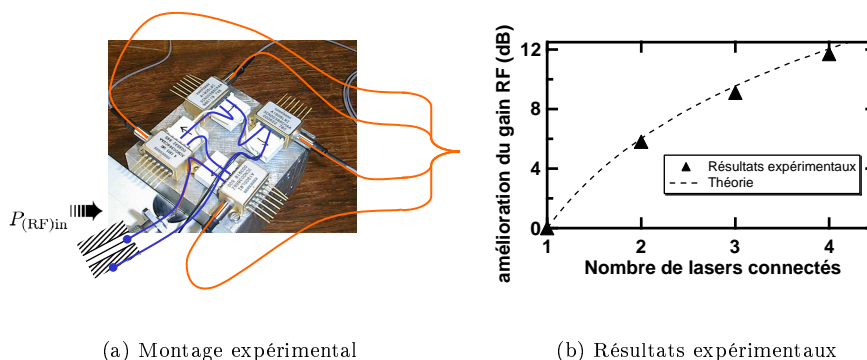
Dans l'Introduction Générale, nous présentons le principe des lasers à cascade bipolaire, ainsi qu'une bibliographie des recherches effectuées de par le monde sur le sujet. Les lasers à cascade bipolaire ont principalement été développés pour trois applications: augmenter la puissance optique émise, en retardant la destruction optique du composant ; augmenter le gain modal des lasers à cavités verticales, et améliorer ainsi leur performances ; augmenter le rendement différentiel pour des applications optique-hyperfréquence. Sur ce dernier sujet, il est nécessaire d'obtenir un fonctionnement monomode du composant, ce qui n'a pour l'instant pas encore été réalisé.

2 Emetteur à rapport signal-sur-bruit élevé : discussion sur les sources à cascade bipolaire d'un point de vue "système"

Nous comparons dans le chapitre 2 l'amélioration du gain hyperfréquence d'une liaison optique composée de plusieurs sources laser discrètes, suivant que les sources sont connectées en série ou en parallèle. Le schéma d'adaptation d'impédance joue également un rôle important pour définir l'amélioration que nous pouvons espérer de l'utilisation de telles sources. Le cas le plus répandu pour une transmission large bande est celui d'une adaptation d'impédance résistive : une résistance supplémentaire est mise en série avec le laser pour obtenir une résistance de source de 50 ohms. Dans ce cas précis, il n'y a pas d'amélioration du gain hyperfréquence à espérer pour une connection en parallèle, alors que le gain hyperfréquence d'une liaison utilisant une structure laser à cascade bipolaire augmente comme le carré du nombre de lasers mis en cascade.

Pour valider expérimentalement cet effet, nous avons utilisé quatre lasers de type "butterfly". Les lasers sont rapprochés au maximum les uns des autres pour éviter un déphasage entre les signaux optique-hyperfréquence émis qui serait synonyme de perte de puissance hyperfréquence. Puis, nous avons polarisé ces lasers et injecté 1 mW de signal hyperfréquence à 80 MHz dans la source composée des quatre lasers en série. En connectant successivement les fibres issues des lasers à quatre bras d'un coupleur 4×4, nous obtenons l'évolution expérimentale du gain hyperfréquence en fonction du nombre de lasers mis en série. La figure 1 montre une photo du montage expérimental et une comparaison des valeurs obtenues avec les valeurs prédites par la théorie.

Figure 1 Expérience pour valider les expressions théoriques de l'amélioration du gain RF



L'excellent accord entre la théorie et l'expérience valide le calcul du gain hyperfréquence effectué pour une source composée de lasers discrets avec une adaptation résistive. Nous obtenons théoriquement, comme expérimentalement une amélioration du gain hyperfréquence de presque 12 dB en utilisant 4 lasers discrets mis en cascade.

En outre, la sommation de plusieurs signaux optiques permet de moyennner le bruit d'intensité et donc de diminuer le bruit d'intensité relatif de la source

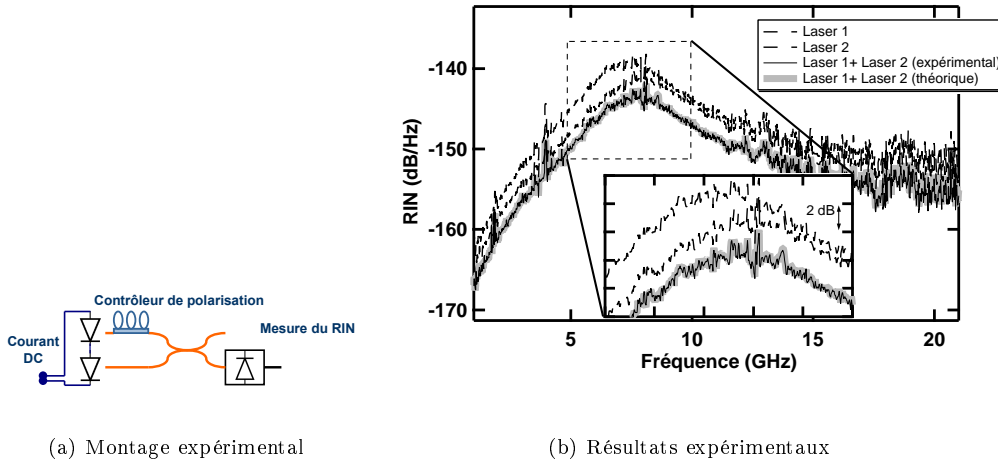
composite. Celui-ci s'écrit:

$$RIN_{\text{source}} = \frac{\sum_i RIN_{\text{lasi}} P_{(\text{opt})\text{lasi}}^2}{(\sum_i P_{(\text{opt})\text{lasi}})^2} + \sum_{i \neq j} \frac{\langle \delta P_{(\text{opt})\text{lasi}} \delta P_{(\text{opt})\text{lasi}j} \rangle P_{(\text{opt})\text{lasi}} P_{(\text{opt})\text{lasi}j}}{(\sum_i P_{(\text{opt})\text{lasi}})^2} \quad (1)$$

Le deuxième terme représente les corrélations possibles entre les sources de bruit. L'utilisation d'isolateurs optiques permet d'éviter toute réinjection de puissance optique dans les lasers. De plus, nous avons vérifié expérimentalement que le niveau de bruit est le même lorsque les lasers sont polarisés en série avec la même source de courant ou avec des sources de courant séparées. Cette dernière constatation prouve que nous n'observons pas de corrélation des signaux optiques transmise par les connexions électriques pour nos niveaux de bruit et pour une résistance série d'environ 50 Ω .

Nous supprimons donc le deuxième terme de l'équation 1 et tentons de valider l'expression résultante. Nous avons ainsi utilisé deux lasers en module et nous avons réunis les faisceaux à l'aide d'un coupleur optique. La figure 2-(a) présente le dispositif expérimental, et la figure 2-(b) présente les mesures effectuées sur cette source laser complexe, en comparaison aux résultats attendus issus de l'équation 1.

Figure 2 Expérience pour valider les expressions théoriques de l'amélioration du bruit d'une source de lasers cascades.



Un contrôleur de polarisation placé dans l'un des bras du coupleur permet d'injecter les faisceaux avec des états de polarisation orthogonaux et d'éviter ainsi un battement hétérodyne qui peut ajouter un bruit supplémentaire au signal optique de sortie. Le bruit mesuré du signal de sortie suit parfaitement les courbes théoriquement calculées à partir de l'équation 1. Si les deux bras d'entrée sont parfaitement équilibrés (même puissance optique, même bruit d'intensité relatif), on obtient une amélioration du bruit d'intensité relatif proportionnelle au nombre de lasers qui composent la source optique. A puissance hyperfréquence injectée constante, le rapport signal-sur-bruit de sortie ainsi que

le facteur de bruit de la liaison sont également améliorés proportionnellement au nombre de lasers qui composent la source.

Cependant, l'utilisation de composants discrets ne présente un réel intérêt que si les signaux sont combinés sans perte optique. De plus, le déphasage hyperfréquence consécutif à la propagation du signal hyperfréquence d'un laser au suivant, et une connectique non-appropriée limite très rapidement la bande passante de la source composée de lasers discrets. Ces limitations interviennent principalement du fait de la distance qui sépare les sources individuelles, qui doit donc être réduite au minimum. Il est ainsi possible d'intégrer ce principe par une mise en cascade monolithique de plusieurs zones actives, c'est le laser à cascade bipolaire. Les zones actives sont connectées grâce à des jonctions pn en inverse fortement dopées, le courant traverse la jonction par effet tunnel. Pour assurer une sommation sans pertes, mais également pour pouvoir utiliser le composant dans un système optique-hyperfréquence, il est nécessaire que l'émission optique soit monomode.

3 Discussion d'un point de vue composant : un modèle simple pour comprendre le fonctionnement d'une structure à cascade bipolaire monomode

Le troisième chapitre de cette thèse présente un modèle basé sur les équations d'évolution pour estimer l'amélioration que nous pouvons espérer d'un tel composant monolithique. Le but est de créer un modèle le plus simple possible pour qu'il reste compréhensible, mais suffisamment précis pour rendre compte des caractéristiques des lasers à cascade bipolaires décrites dans la littérature. De plus, pour discriminer l'influence de l'augmentation du nombre de zones actives de celles de l'augmentation du nombre de puits quantiques, nous comparons dans un même formalisme un laser avec un puits quantique unique, un laser avec une zone active unique et deux puits quantiques et un laser avec deux zones actives, un puits quantique par zones actives.

Un bilan des particules créées et recombinées par unité de temps conduit à l'écriture d'un système de trois équations aux dérivées partielles couplées, fortement non-linéaires. Pour la structure à deux zones actives, les trois inconnues sont les populations de paires électron-trou disponibles pour une recombinaison radiative dans la première zone active, celle dans la seconde zone active et la population de photons dans le mode unique de la cavité.

La résolution de ces équations en régime établi ($\frac{d}{dt} = 0$) prévoit une évolution des caractéristiques cohérentes avec l'ensemble des résultats expérimentaux présentés dans la littérature: augmentation du rendement différentiel externe proportionnellement au nombre de zones actives, diminution du courant de seuil presque inversement proportionnelle au nombre de zones actives si les pertes internes n'augmentent pas.

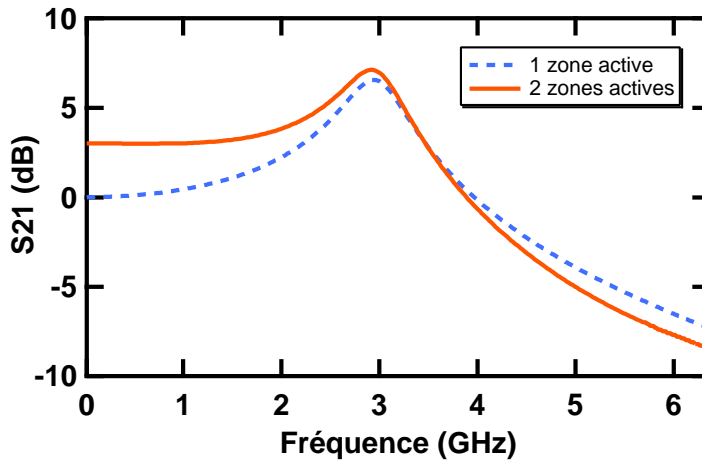
Nous considérons ensuite les variations instantanées $\delta X(t)$ des valeurs moyennes \overline{X} . En régime de modulation petit-signal, nous négligeons les termes non-linéaires et obtenons un système linéaire d'équations couplées. La transformée de Fourier de ces équations nous permet d'écrire la forme matricielle du système à résoudre. Pour les structures à deux puits quantiques ou à deux zones actives, nous nous intéressons uniquement à la variation temporelle de la somme des

populations de porteurs.

La modulation des populations des particules possède deux origines. Soit une modulation du courant de polarisation du laser, soit des sources de bruit, représentées dans ce modèle par des forces de Langevin.

La figure 3 présente la réponse du modèle à une modulation du courant de polarisation obtenue pour la structure à deux puits quantiques et pour la structure à deux zones actives. Les valeurs de réponse fréquentielle des systèmes sont normalisées à la réponse de la structure à deux puits quantiques en basse fréquence.

Figure 3 Réponse fréquentielle à une modulation de courant pour la structure à deux puits quantiques, et pour la structure à deux zones actives.



Les deux courbes présentent une allure similaire, avec une fréquence de résonance comparable. Nous pouvons observer qu'en basse fréquence, la réponse à une modulation du courant de la structure à deux zones actives est supérieure de 3 dB à la réponse de la structure à une zone active, deux puits quantiques. Cet effet est une conséquence directe de l'amélioration du rendement différentiel externe statique de la diode. Par contre, à plus haute fréquence, la réponse du laser à cascade bipolaire s'infléchit plus vite que celle du laser à zone active unique. Cette diminution de la bande passante du composant est la conséquence de l'évolution de l'impédance différentielle de la diode (notamment résistance série) ainsi que du temps non nul de transit des porteurs entre les zones actives. Même si les valeurs utilisées pour ces paramètres ne sont pour l'instant qu'estimées, et qu'elles demanderaient à être vérifiées expérimentalement, leur effet est effectivement pris en compte dans le modèle développé.

Le bruit d'intensité optique du laser apparaît du fait de la nature corpusculaire des porteurs électriques et de l'énergie lumineuse. Chaque échange corpusculaire entre les différents réservoirs suit une loi de probabilité poissonnienne. Le caractère aléatoire des instants d'arrivée des événements (émission d'un photon, recombinaison d'une paire électron-trou...) agit comme une source de fluctuation interne, à laquelle le système d'équations couplées va réagir. C'est la méthode de calcul de Langevin. Le bruit d'intensité relatif est alors calculé

3. DISCUSSION D'UN POINT DE VUE COMPOSANT

comme le rapport du carré moyen des fluctuations de puissance optique sur le carré de la puissance optique moyenne, et le résultat est le suivant :

$$RIN_{SQW}(\omega) = \frac{\eta_0^2}{S_{SQW}^2} \frac{|H(\omega)|^2}{\omega^4_{R(SQW)}} \{a_1 + a_2\omega^2\} \quad (2)$$

avec :

$$\begin{aligned} a_1 &= \tau_P^2 \omega_{R(SQW)}^4 D_{NN} + 4 \frac{\tau_P}{\tau_R} \omega_{R(SQW)}^2 D_{NP} + 4 \frac{1}{\tau_R^2} D_{PP} \\ &\quad + 2 \frac{1}{\eta_0} \tau_P \omega_{R(SQW)}^4 D_{NS} + \frac{1}{\eta_0} \frac{2}{\tau_R} \omega_{R(SQW)}^2 D_{PS} \\ a_2 &= D_{PP} + 2 \frac{1}{\eta_0} \tau_P \omega_R^2 D_{PS} \end{aligned}$$

Les notations sont explicites dans le manuscrit, D_{XX} sont les coefficients de diffusion de Langevin. La formule est la même pour le laser à cascade bipolaire et le laser à zone active simple, et à deux puits quantiques. Néanmoins, les coefficients de diffusion de Langevin sont différents car les échanges entre les réservoirs de particules sont différents. Le tableau 1 recense les expressions de ces coefficients de diffusion pour les deux structures.

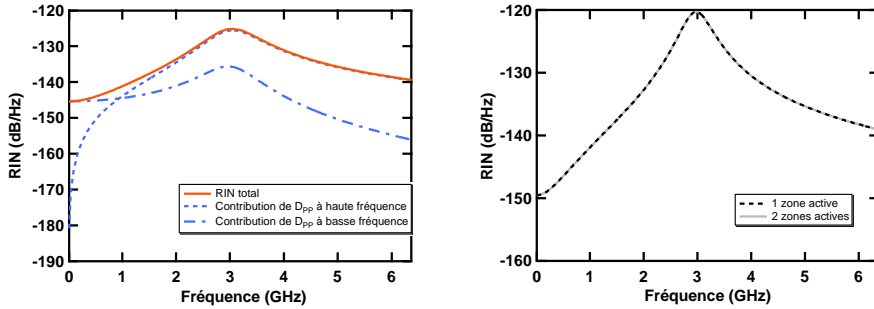
Forces de Langevin	Expressions
<i>Laser à 1 zone active</i>	
$D_{NN^{(+)}_{DQW}}$	$\frac{\bar{I}}{e} + \frac{\bar{N}_{DQW}^{(+)}}{\tau_E} + (2n_{sp(DQW)} - 1) \frac{\bar{P}_{DQW}}{\tau_P}$
$D_{N^{(+)}P_{DQW}}$	$-(2n_{sp(DQW)} - 1) \frac{\bar{P}_{DQW}}{\tau_P} - \beta \frac{\bar{N}_{DQW}^{(+)}}{\tau_E}$
$D_{PP_{DQW}}$	$2n_{sp(DQW)} \frac{\bar{P}_{DQW}}{\tau_P} + \beta \frac{\bar{N}_{DQW}^{(+)}}{\tau_E}$ (with $n_{sp(DQW)} = \frac{\bar{N}_{DQW}^{(+)}}{\bar{N}_{DQW}^{(+)} - 2N_0}$)
<i>Laser à cascade bipolaire</i>	
$D_{NN^{(+)}_{CQW}}$	$\frac{\bar{I}}{e} + \frac{\bar{N}_{CQW}^{(2)}}{\tau_E} + (2n_{sp(CQW)} - 1) \frac{\bar{P}_{CQW}}{2\tau_P}$
$D_{N^{(+)}P_{CQW}}$	$-(2n_{sp(CQW)} - 1) \frac{\bar{P}_{CQW}}{2\tau_P} - \beta \frac{\bar{N}_{CQW}^{(2)}}{\tau_E}$
$D_{PP_{CQW}}$	$2n_{sp(CQW)} \frac{\bar{P}_{CQW}}{\tau_P} + \beta \frac{\bar{N}_{CQW}^{(+)}}{\tau_E}$ (with $n_{sp(CQW)} = \frac{\bar{N}_{CQW}^{(+)}}{\bar{N}_{CQW}^{(+)} - 2N_0}$)

Table 1: Résumé des coefficients de diffusion estimés pour la méthode de calcul de bruit de Langevin. n_{sp} est le facteur d'inversion de population.

Malgré ces différences, le calcul du bruit d'intensité relatif des deux lasers produit, pour une population de photon égale dans les deux types de structures, des résultats très similaires comme nous pouvons le voir sur la figure 4-(b). La raison pour une différence si peu marquée dans l'estimation du bruit d'intensité relatif est présentée à la figure 4-(a), qui montre l'évolution de deux composantes du RIN qui dominent à haute et à basse fréquence. Ces composantes sont celles

issues du bruit des photons dans la cavité. Pour un laser monomode, le bruit est donc dominé par les fluctuations créées par les processus supposés poissonniens de création et de disparition des photons dans la cavité. Le niveau de ce bruit est donc fixé par la population de photons dans la cavité. Les caractéristiques en bruit des lasers à cascade bipolaire seront donc équivalentes à celles des lasers à simple zone active, à moins que le recyclage des porteurs ne permette d'augmenter la population de photons dans la cavité.

Figure 4 Résultats théoriques obtenus par résolution du modèle des équations d'évolution.



(a) Composantes principales du RIN

(b) Comparaison des RIN pour le laser à zone active unique et à deux zones actives

En particulier, la même comparaison pour un courant de polarisation constant donne une population de photons plus importante pour le laser à cascade bipolaire, et donc un RIN plus faible.

L'intégration de plusieurs zones actives dans un même mode optique permet théoriquement une amélioration du rendement différentiel externe du laser d'un facteur n , où n est le nombre de zones actives, et donc du gain hyperfréquence de la liaison à modulation directe d'un facteur n^2 . Cette propriété est conservée sur une bande passante plus importante que ne le permet l'architecture monolithique. Par contre, malgré les espoirs qui reposent sur ces structures pour obtenir des composants faible bruit [1,2], et contrairement à l'architecture utilisant des lasers discrets, notre modèle montre qu'il n'est possible de diminuer le RIN qu'en augmentant la densité de photons dans la cavité, et donc la puissance émise.

4 Modèle électronique du laser à cascade bipolaire monomode

La fabrication de lasers à cascade bipolaire monomodes transverse nécessite une très forte intégration des différentes couches de semiconducteurs. Plusieurs zones actives ainsi que des régions fortement dopées doivent être comprises dans une épaisseur d'environ un micron. Pour concevoir de telles structures complexes, nous avons utilisé et développé un logiciel de simulation auto-consistant qui modélise le fonctionnement des lasers à cascade bipolaire.

Le logiciel est basé sur un calcul 1D de la densité de porteurs, du potentiel électrostatique et des courants dans la direction perpendiculaire aux couches du semiconducteur. Les équations constitutives sont l'équation de Poisson, une équation de conservation pour chaque type de porteur, et une équation de courant "dérive-diffusion" pour chaque type de porteur. Ce système d'équation est de plus nourri par deux autres modules de calcul, l'un pour résoudre l'équation de Schrödinger dans le puits quantique et calculer ainsi le gain optique, et l'autre pour résoudre les équations de Maxwell dans la structure et obtenir la répartition de l'énergie optique dans les différentes couches de semiconducteur. C'est notamment grâce à ce dernier module que nous pouvons nous assurer que la structure aura bien un comportement monomode transverse.

Le logiciel initial n'était pas adapté à la simulation de structures laser à cascade bipolaire pour une émission à 1.5 μm , et une partie de ce travail de thèse a consisté à étendre les capacités du logiciel.

La première modification concerne le passage d'une modélisation sur matériaux pour une émission à 800-900 nm, à des matériaux à plus petit gap pour une émission à 1.5 μm . Outre l'extension de la base de données, les principales modifications sur le modèle ont concerné la prise en compte du courant de recombinaison Auger dans les puits quantiques (il y a plus d'un ordre de grandeur de différence dans le coefficient Auger pour les deux systèmes de matériaux), et l'utilisation de la statistique de Femi-Dirac sur l'ensemble de la structure.

Une deuxième modification importante concerne la prise en compte de plusieurs puits quantiques dans la structure. En effet, jusqu'à présent, le logiciel n'était compatible qu'avec des structures n'intégrant qu'un seul puits quantique. Les interactions entre les grandeurs à calculer (densités de porteurs, courants, potentiel électrostatique) étaient locale et la résolution par la méthode de Newton nécessitait l'inversion d'une matrice tri-diagonale par blocs, réalisée avec l'aide d'algorithmes utilisant cette propriété. Dans une structure qui intègre plusieurs puits quantiques, le courant de recombinaison par émission stimulée dans un puits quantique dépend du gain généré par l'ensemble des puits quantiques ainsi que de la densité de porteurs et du recouvrement avec l'onde optique de ce puits quantique. Le logiciel calcule donc un gain d'ensemble comme la somme du gain de chaque puits quantique avant de répartir ce coefficient sur chaque puits quantique pour calculer le courant de recombinaison local. Des termes non-diagonaux apparaissent caractéristiques de l'interaction entre les porteurs des différents puits quantiques via le champ électromagnétique. Ces termes non-diagonaux sont traités comme des termes perturbatifs.

Enfin, dernière modification nécessaire à la modélisation d'un laser à cascade bipolaire, la prise en compte du courant qui passe par effet tunnel dans une jonction fortement dopée $p^{++}-n^{++}$ polarisée en inverse. Nous développons dans le manuscrit l'intégralité du calcul basé sur la résolution de l'équation de Schrödinger jusqu'à obtenir la formule quasi-analytique proposée par E.O. Kane [3].

Le fort champ électrostatique présent au centre de la jonction tunnel courbe les bandes de conduction et de valence. La résolution de l'équation de Schrödinger perturbée par un terme de champ électrostatique ajouté à l'hamiltonien conduit à l'expression de fonctions d'onde des électrons proportionnelles à des fonctions de Airy. Ces fonctions ont la propriété d'avoir un recouvrement non nul (et donc les électrons ont une probabilité de présence non nulle également) à l'intérieur de la bande interdite. Le recouvrement des fonctions d'onde des électrons dans

la bande de valence et dans la bande de conduction conduit à la détermination d'une probabilité de transmission par effet tunnel d'un électron incident sur la barrière de potentiel de l'autre côté de celle-ci. Une intégration de cette probabilité de transmission sur l'ensemble des électrons incident conduit à l'expression suivante pour le courant tunnel [3]:

$$J_{\text{tunnel}} = \frac{em_r}{18\hbar^3} \exp\left(-\frac{\pi\sqrt{m_r E_g}}{2\sqrt{2}\hbar e F}\right) \left(\frac{\overline{E}_\perp}{2}\right) \times D \quad (3)$$

$$\text{avec } D = \int \left(f_1(E_1) - f_2(E_2)\right) \left(1 - \exp\left(-2\frac{E_s}{\overline{E}_\perp}\right)\right) dE$$

Le terme en exponentiel est le terme prépondérant, responsable du caractère très non-linéaire du courant tunnel. Le troisième terme tient compte de l'énergie transverse des électrons, et le dernier terme est homogène à une énergie et correspond à l'intégrale du courant tunnel sur l'ensemble des paires d'états à la même énergie, occupés dans la bande de valence et libres dans la bande de conduction.

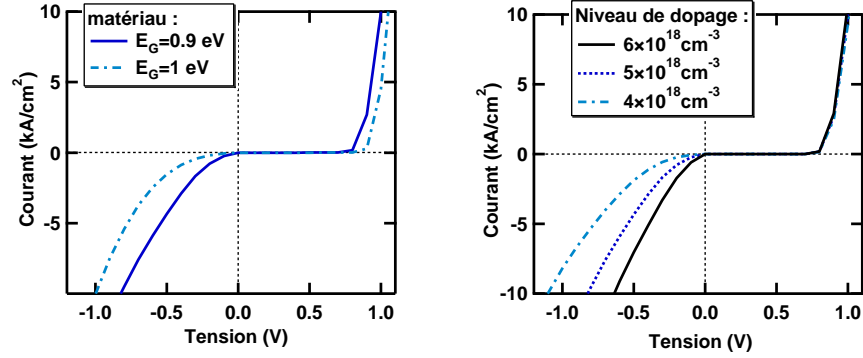
5 Conception d'un laser à cascade bipolaire monomode transverse

Dans le dernier chapitre qui compose cette thèse, nous utilisons tout d'abord le modèle présenté dans le chapitre précédent pour la conception de jonctions tunnel, et pour la conception de lasers à cascade bipolaire.

Il est souhaitable pour le bon fonctionnement du laser que la jonction tunnel implémentée soit le moins résistive possible. Pour cela, plusieurs paramètres peuvent être optimisés. Nous décrivons l'évolution du courant tunnel en fonction de deux paramètres critiques : les matériaux qui constituent la jonction, et le niveau de dopage de ces matériaux.

Aux vues de l'expression du courant tunnel donnée par l'équation 3, diminuer l'énergie de gap permet d'augmenter le courant qui traverse la jonction tunnel sous polarisation inverse. Ce phénomène est confirmé par la figure 5-(a) qui représente l'évolution de la caractéristique courant-tension calculée d'une diode tunnel en fonction du matériau qui la compose, pour un même niveau de dopage. Il est à noter que la diminution du gap du matériau s'accompagne d'une diminution de la masse effective de passage par effet tunnel qui augmente encore le courant tunnel. Néanmoins, un matériau avec une énergie de gap trop petite pourra être absorbant à la longueur d'onde d'émission. Nous optons pour un matériau ayant une longueur d'onde de photoluminescence de $1.35 \mu\text{m}$ qui présente un compromis entre l'énergie de gap et l'absorption fondamentale, et est par ailleurs un matériau dont nous connaissons les conditions de croissance, car il est utilisé pour d'autres types de structures.

Figure 5 Utilisation du logiciel précédemment décrit pour concevoir la jonction tunnel.



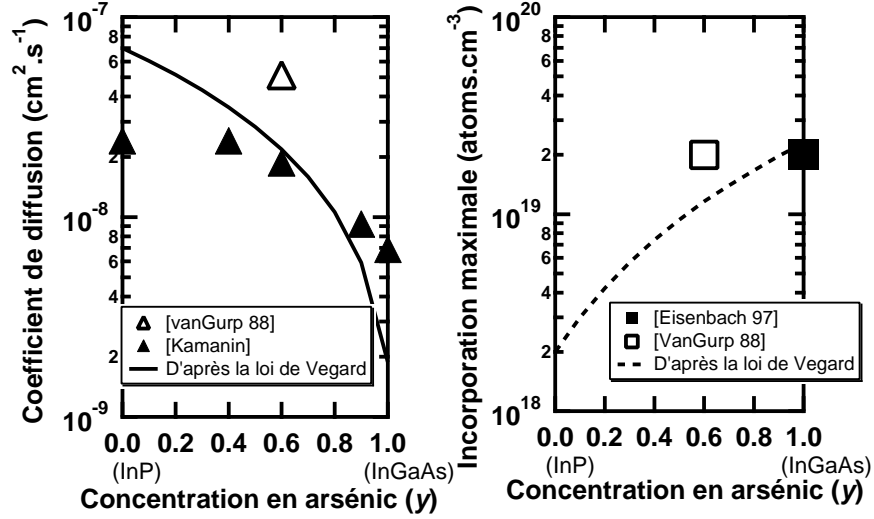
(a) Evolution du courant tunnel avec le matériau

(b) Evolution du courant tunnel avec le niveau de dopage

Le deuxième paramètre que nous pouvons optimiser est le niveau de dopage du matériau constituant la jonction tunnel. Augmenter le niveau de dopage permet d'augmenter le champ électrostatique dans la structure ainsi que le niveau de dégénérescence du matériau, qui contrôle le nombre d'états occupés de la bande de valence avec la même énergie qu'un état libre dans la bande de conduction. Une illustration est présentée sur la figure 5-(b) qui montre l'évolution de la caractéristique courant-tension calculée pour une jonction tunnel réalisée dans un matériau 1.35 μm pour un dopage variant de $4 \times 10^{18} \text{ cm}^{-3}$ à $6 \times 10^{18} \text{ cm}^{-3}$. Pour une tension en inverse donnée, le courant qui traverse la diode augmente fortement, même pour une variation minimale du dopage du matériau. A nouveau, il existe un compromis sur le niveau de dopage optimal, car une augmentation du niveau de dopage augmente les pertes par porteurs libres qui peuvent jouer un rôle important, en particulier pour les lasers à cascade bipolaire monomodes, pour lesquels la jonction tunnel se situe à l'intérieur du mode optique. Cette fois-ci, le niveau de dopage va en fait être choisi non pas comme compromis entre les pertes et la conductivité tunnel, mais plutôt comme limite intrinsèque d'incorporation du dopant Zn que nous utilisons pour le dopage p de la structure.

Le dopant Zn est le dopant généralement utilisé comme accepteur pour la structure InGaAsP/InP en MOCVD. Néanmoins, un des inconvénients de son utilisation est le fort coefficient de diffusion qu'il peut montrer pour des densités de dopage importantes [4]. Nous présentons dans ce manuscrit une revue bibliographique qui nous permet de nous familiariser avec les mécanismes d'incorporation et de diffusion de cet atome dans la maille cristalline. Nous étudions également l'influence des paramètres de croissance sur les profils et les coefficients de diffusion. Finalement, nous essayons d'estimer les coefficients de diffusion que nous risquons d'obtenir sur nos matériaux en appliquant une loi de Vegard sur les coefficients de diffusion publiés sur matériaux binaires. La figure 6 présente le coefficient de diffusion, et l'incorporation maximale d'atomes estimée en fonction de la concentration en arsenic.

Figure 6 Coefficient de diffusion et incorporation maximale du Zn dans InGaAsP/InP estimé à partir d'une loi de Vegard sur les binaires.

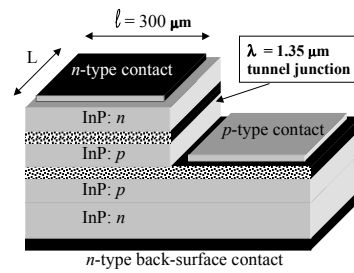


Afin d'estimer expérimentalement la résistivité que nous pouvons espérer obtenir dans nos jonctions tunnel, nous avons réalisé une structure de test dans des conditions aussi proches que possible des conditions réelles d'implémentation dans une structure laser à cascade bipolaire. La figure 7 décrit la structure réalisée.

Figure 7 Structure réalisée dans le but d'estimer la résistivité ajoutée par une jonction tunnel.

Couche	épaisseur	dopage (cm^{-3})
InP	$0.5 \mu\text{m}$	$n: 10^{18}$
$\lambda_{\text{PL}} = 1.35 \mu\text{m}$	25 nm	$n: 5 \times 10^{18}$
$\lambda_{\text{PL}} = 1.35 \mu\text{m}$	25 nm	$p: 5 \times 10^{18}$
InP	$0.1 \mu\text{m}$	$p: 10^{18}$
$\lambda_{\text{PL}} = 1.35 \mu\text{m}$	$0.5 \mu\text{m}$	$p: 5 \times 10^{18}$
InP	$0.1 \mu\text{m}$	$p: 10^{18}$
InP	$0.5 \mu\text{m}$	$n: 10^{18}$

(a) Liste des couches de semiconducteur



(b) Représentation schématique de la structure

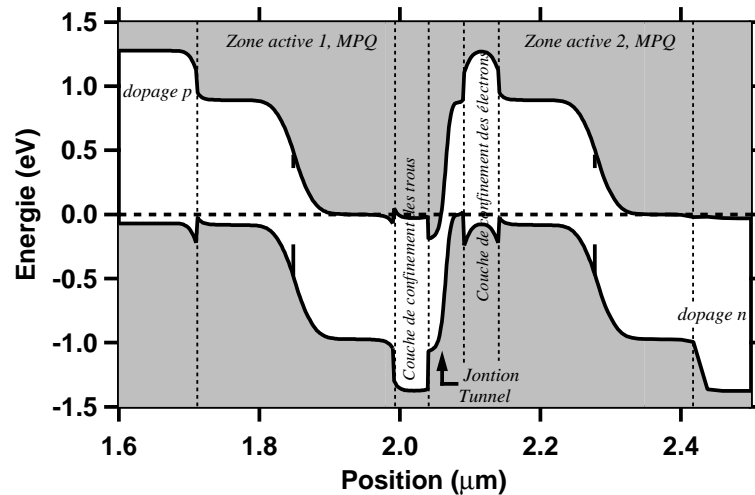
Trois électrodes sont fabriquées sur la structure : une électrode de type n pleine plaque, en face arrière, une électrode de type n sur le dessus d'un ruban gravé de $300 \mu\text{m}$, et une électrode de type p déposée à la suite de la gravure complète de la jonction tunnel sur le matériau $1.35 \mu\text{m}$ fortement dopé p , qui nous sert également de couche d'arrêt de gravure humide. La connaissance (suite

à des mesures TLM) des résistances de contact et la différence des mesures des caractéristiques courant-tension entre le sommet du ruban et la face arrière (jonction tunnel et jonction pn en directe) et entre l'électrode p et la face arrière (uniquement jonction pn en directe) nous permet d'accéder à la mesure du courant tunnel en fonction de la tension appliquée sur la jonction tunnel. Cette mesure nous donne une estimation de la résistivité de la jonction tunnel. Malheureusement, un courant surfacique important, estimé en mesurant les caractéristiques pour des puces de longueur différentes limite la précision de la mesure. De plus, la résistance chute très rapidement en dessous de quelques ohms, ce qui est très faible pour espérer une mesure fiable. Malgré ces limitations, nous obtenons une estimation de la résistance tunnel rapportée à une structure de dimension $3 \mu\text{m}$ par $300 \mu\text{m}$ de l'ordre de 42Ω .

Pour tenter de comprendre cette forte résistivité de la jonction tunnel, nous réalisons des mesures SIMS sur la structure de test ainsi que sur les structures laser qui intègrent une jonction tunnel. La diffusion des dopants et les niveaux de dopage sont dans les limites de résolution de la technique de caractérisation, rejetant l'hypothèse d'un problème survenu au niveau de la croissance du composant.

La conception du laser à cascade bipolaire ne s'arrête pas à celle de la jonction tunnel. En particulier, la forte intégration de couches de semiconducteur ayant chacune leur nécessité conduit à une conception spécifique de ces structures. Nous utilisons le logiciel décrit dans le chapitre précédent pour concevoir des structures à cascade bipolaire monomode transverse. La figure 8 présente le diagramme de bande d'un laser à cascade bipolaire à l'équilibre thermodynamique.

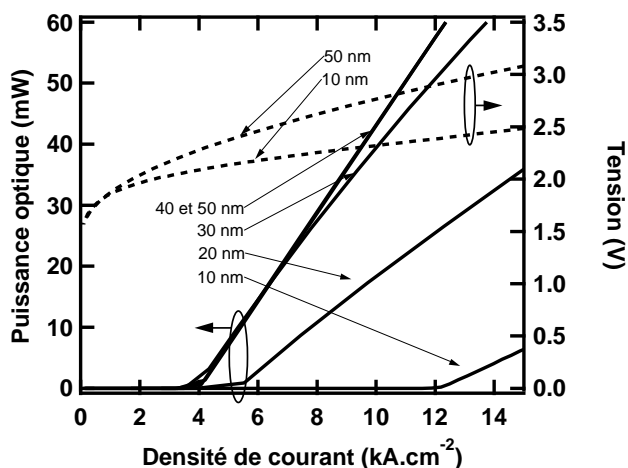
Figure 8 Diagramme de bande d'un laser à cascade bipolaire à l'équilibre thermodynamique.



Pour illustrer le besoin d'une conception spécifique, nous discutons l'influence de l'épaisseur des couches de confinement des porteurs de part et d'autre de la jonction tunnel. Ces couches sont dopées. Si ces couches sont trop épaisses, le recouvrement avec le mode optique augmente les pertes par porteurs libres.

Par contre, si ces couches sont trop fines, les porteurs (et en particulier les électrons) peuvent passer par effet thermoionique au-delà de ces barrières. Les électrons sont ensuite entraînés dans la deuxième zone active par le fort champ électrostatique de la jonction tunnel et ne participent pas au recyclage et donc à l'amélioration du rendement différentiel. Ce phénomène est modélisé par le logiciel spécialement développé, et les résultats sont présentés sur la figure 9, qui montre les caractéristiques puissance-courant et tension-courant des lasers à cascade bipolaire pour différentes épaisseurs de cette barrière de confinement. La courbe puissance-courant se redresse au fur et à mesure que l'on augmente l'épaisseur de la barrière de confinement.

Figure 9 Evolution des caractéristiques statiques calculées de lasers à cascade bipolaire, pour différentes épaisseurs de couches de confinement des porteurs.

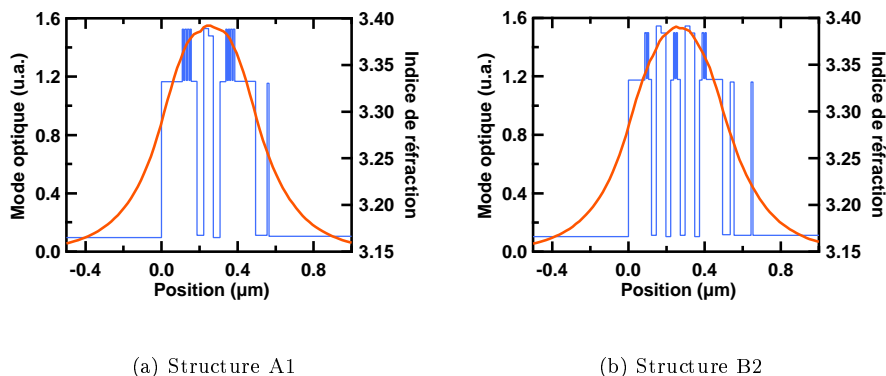


Nous avons réalisé quatre structures à cascade bipolaire, réparties en deux séries. La série A possède deux zones actives de quatre puits quantiques chacune, et a été réalisée en une seule épitaxie. La série B intègre trois zones actives chacune possédant deux puits quantiques et intègre un réseau de Bragg qui a nécessité une croissance en deux étapes. La figure 10 présente la répartition modale dans les structures A1 et B2, calculées pour n'accepter l'oscillation que d'un seul mode transverse. La structure A2 est similaire à la structure A1. Seule une couche de 30 nm de confinement des trous a été enlevée. La structure B1 est similaire à la structure B2, mais cette fois-ci toutes les couches de confinement électronique ont été enlevées.

Nous observons d'abord que les structures qui ne possèdent pas l'ensemble des couches de confinement électrique (A2 et B1) fonctionnent dans un régime différent des structures qui intègrent toutes les couches de confinement électrique (structure A1 et B2). Le saut de tension est beaucoup plus faible et proche du saut nécessaire à la polarisation d'une seule zone active. Les porteurs ne sont en fait pas recyclés, et ces structures se comportent comme des structures à simple zone active. Ce qui était plutôt un défaut de conception va finalement nous être très utile. Nous allons en effet pouvoir comparer des structures épitaxiales similaires dont la seule différence est le chemin énergétique emprunté par les électrons pour traverser la structure. Dans un cas, nous sommes assuré de

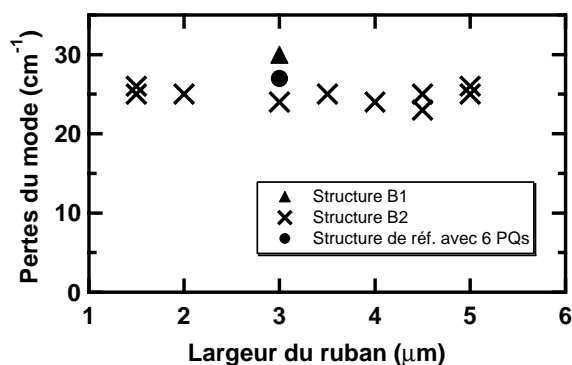
n'avoir pas de recyclage, dans l'autre cas, nous allons pouvoir observer l'influence d'un recyclage éventuel des porteurs. L'ensemble des résultats expérimentaux ont été obtenus en courant pulsé à la température ambiante, car les structures ne présentent pas d'effet laser en courant continu.

Figure 10 Distribution modale de l'énergie lumineuse dans la cavité.



Nous étudions d'abord les pertes par transmission dans les structures monomodes. Nous n'observons pas de différence notable entre les pertes mesurées pour les structures possédant une jonction tunnel fortement dopée au centre du mode optique (B1 et B2) et des structures de référence à six puits quantiques, comme le montre le résultat de cette mesure sur la figure 11. Cette mesure a été réalisée en comparant le spectre résultant de la transmission d'un faisceau large bande optique.

Figure 11 Pertes pour différentes structures mesurées à partir du spectre de transmission de la structure passive.



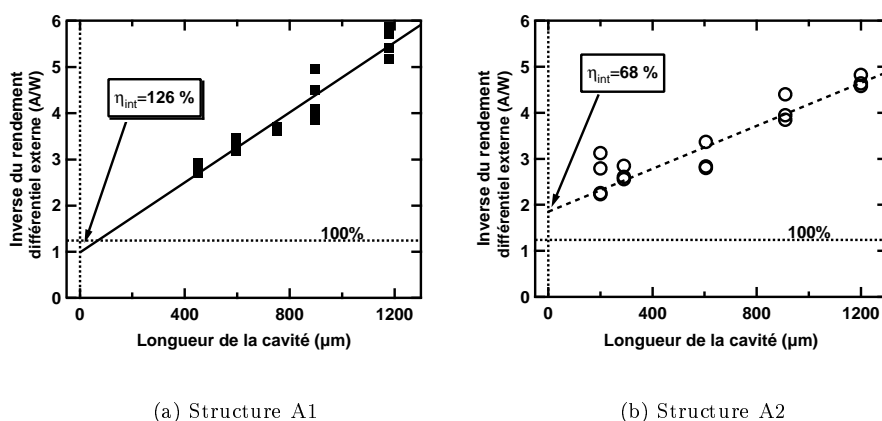
La mesure des caractéristiques tension-courant de la structure A1 sur des structures de différentes longueurs nous permet d'estimer le courant surfacique beaucoup plus limité que dans le cas de la structure test.

Afin d'estimer l'étalement des lignes de courant sur la jonction tunnel, nous

fabriquons deux types de rubans sur les structures de la série A. Un premier ruban étroit ($2.5 \mu\text{m}$) et peu profond est réalisé pour tenter d'obtenir un fonctionnement monomode. Ce ruban présente cependant l'inconvénient de ne pas empêcher l'étalement du courant. Une autre structure avec un ruban plus large ($18 \mu\text{m}$) et plus profond (l'ensemble des zones actives est gravé) nous permet de nous affranchir de l'étalement du courant. Une comparaison des courants de seuil de la même structure (A1) pour les deux technologies nous permet d'estimer, en supposant que les densités de porteurs au seuil sont les mêmes, la largeur effective d'étalement du courant sous le ruban de $2.5 \mu\text{m}$. Nous obtenons une valeur qui avoisine les $12 \mu\text{m}$.

Pour obtenir les caractéristiques intrinsèques, nous utilisons les structures à ruban profond qui empêchent complètement l'étalement du courant. Nous pouvons ainsi comparer le rendement quantique interne des structures A2 (structure qui ne recycle pas les porteurs) et A1 (structure à cascade bipolaire que nous caractérisons). La figure 12 présente le résultat des mesures du rendement différentiel externe en fonction de la longueur de la cavité. L'intersection de cette droite avec l'axe des ordonnées nous renseigne sur le rendement quantique interne.

Figure 12 Mesure des pertes internes et du rendement interne dans les structure A1 et A2 pour un ruban de $18 \mu\text{m}$.

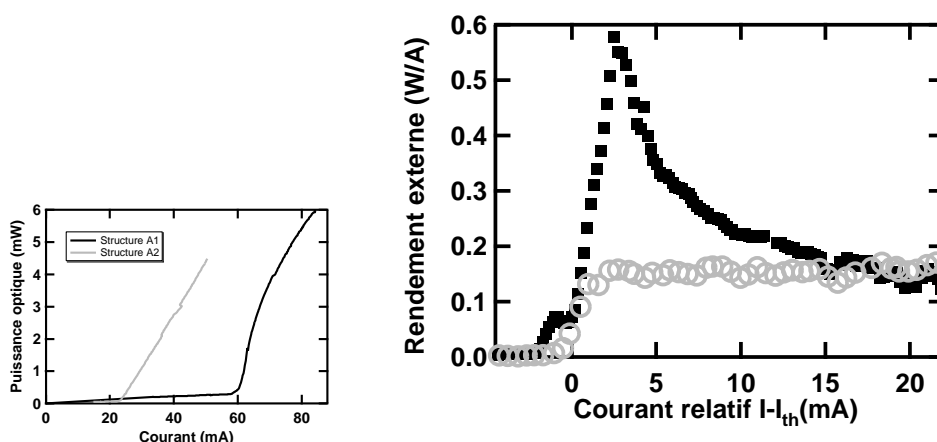


Nous obtenons un rendement de l'ordre de 68 % pour la structure A2, et un rendement de 126 % pour la structure A1. Le rendement est quasiment le double pour la structure A1, démontrant le recyclage des porteurs dans ces structures. Cette même régression linéaire nous renseigne sur les pertes de la structure que nous estimons à 16 cm^{-1} pour la structure A2, et à 43 cm^{-1} pour la structure qui recycle les porteurs. Cette très grande différence ne s'explique pas par un recouvrement plus important avec des couches de semiconducteur dopées car les structures sont de ce point de vue là quasiment identiques. Ce qui les différencie est uniquement le chemin de conduction énergétique des porteurs dans la structure. Dans la structure A2, ils passent au dessus des faibles barrières de confinement électronique, et dans la structure A1, ils passent par effet tunnel au travers d'une barrière de potentiel. Si cette barrière est plus large que ce

que prévoit notre modèle, il est possible que la jonction tunnel soit une zone où l'accumulation des porteurs augmente les pertes par porteurs libres.

Dans la dernière partie de ce chapitre, nous nous intéressons à la comparaison des structures A1 et A2 sur une structure à ruban étroit et peu profond. La figure 13 présente les caractéristiques puissance-courant pour les deux structures, ainsi que le rendement différentiel externe mesuré sur chaque structure.

Figure 13 Caractéristiques des structures avec un ruban étroit ($2.5 \mu\text{m}$).

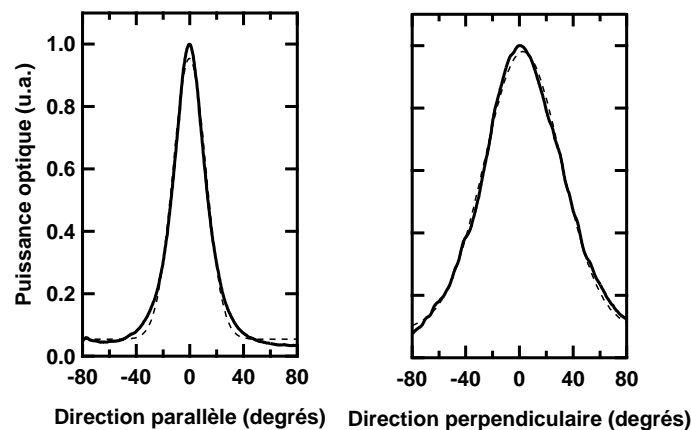


(a) Caractéristiques puissance-courant

(b) Comparaison des rendements différentiels externes

Contrairement à la caractéristique de la structure A2, celle de la structure A1 n'est pas très linéaire, ce qui pose un problème important pour l'utilisation de ces structures dans les systèmes optique-hyperfréquence. Nous pouvons également remarquer qu'au niveau du seuil, le rendement différentiel externe de la structure A1 atteint des valeurs très importantes que l'on peut expliquer par un phénomène d'absorption saturable, ou un resserrement des lignes de courant. Au-delà de cet accident, le rendement différentiel externe de la structure A1 surpasse largement celui de la structure A2 sur une plage de courant relativement importante, montrant ainsi l'amélioration du rendement différentiel externe par le recyclage des porteurs. Il reste ensuite à savoir si la structure est restée monomode transverse, ce que nous prouvons en mesurant le champ lointain qui décrit la distribution angulaire de l'énergie lumineuse à la sortie de la diode. Comme le montre la figure 14, le faisceau optique ne présente qu'un seul lobe dans la direction parallèle et dans la direction perpendiculaire aux couches. Ces diagrammes constituent la démonstration du fonctionnement d'un laser à cascade bipolaire monomode transverse.

Figure 14 Champ lointain des structures avec un ruban étroit ($2.5 \mu\text{m}$).



6 Conclusion

Après avoir démontré théoriquement et expérimentalement l'amélioration possible du gain hyperfréquence et du facteur de bruit d'une liaison optique-hyperfréquence sur une architecture de lasers discrets cascades, nous avons développé deux modèles de simulation des composants intégrés de manière monolithique. Le premier nous a permis de confirmer les attentes que l'on pouvait avoir pour améliorer le rendement différentiel externe des lasers, mais de rejeter l'espoir d'obtenir de meilleures caractéristiques en bruit que des lasers à simple zone active. Le deuxième est un logiciel de simulation pour assister la conception de laser à cascade bipolaire. Il repose sur la statistique de Fermi-Dirac, accepte plusieurs puits quantiques et calcule le courant qui traverse une jonction tunnel. A l'aide de ce logiciel, nous avons conçu puis réalisé des structures qui ont permis une amélioration d'un facteur 2 du rendement quantique interne, puis la démonstration d'un laser à cascade bipolaire monomode transverse.

Une voie d'exploration importante pour l'amélioration à court terme des structures (notamment pour éviter l'étalement du courant qui induit des non-linéarités, et pour obtenir un fonctionnement en courant continu) est l'amélioration de la jonction tunnel.

Références

- [1] J.K. Kim *et al.*, Epitaxially-stacked multiple-active-region $1.55 \mu\text{m}$ lasers for increased efficiency. In *IEEE Conference on Lasers and Electro-optics, CLEO'99*, page 139, Baltimore, MD, USA, May 1999
- [2] F. Rana *et al.*, Photon noise and correlations in semiconductor cascade lasers. *Applied Physics Letters*, 76(9):1083-10-85, Feb. 2000
- [3] E.O. Kane, Theory of Tunneling. *Journal of Applied Physics*, 32(1):83-91, Jan. 1961
- [4] Brian Tuck, Diffusion of acceptors in *n*-type and semi-insulating InP. *Journal of Crystal Growth*, 170:451-455, 1997

Contents

1	General Introduction	7
1.1	From the blurred origins of radar engineering to current research on opto-RF links	7
1.2	What industrial applications can gain from opto-RF links	9
1.2.1	Ground radars	9
1.2.2	Electronic warfare	10
1.2.3	Other advantages of opto-RF links	11
1.3	Current opto-RF links shortcomings	11
1.4	Principle of the bipolar cascade laser	12
1.5	History and state-of-the-art of bipolar cascade lasers	13
1.5.1	High-power applications	13
1.5.2	Bipolar Cascade Vertical Cavity Surface Emitting Lasers (BCVCSEL)	14
1.5.3	Microwave optic applications	16
1.6	Outline of the thesis	17
2	High signal-to-noise ratio emitter: discussion on a “system level” point of view	23
2.1	Introduction	23
2.2	What does combining mean?	24
2.2.1	Splitting...	25
2.2.2	... then combining the RF signal	25
2.2.2.1	Electronic combining after detection	25
2.2.2.2	Optical combining before detection	26
2.2.2.3	Electronic combining integrated to the photodetector	27
2.2.2.4	Advantages and drawbacks of the different architectures	29
2.2.3	Integrated splitting-to-parallel/combining architectures	30
2.2.3.1	Distributed photodiodes	30
2.2.3.2	Bipolar cascade lasers	31
2.3	Combining sources to improve the RF link gain	31
2.3.1	Definitions	31
2.3.2	RF output power	33
2.3.3	RF gain improvement	35
2.3.3.1	No impedance matching	35
2.3.3.2	Resistive impedance matching	37
2.3.3.3	Reactive impedance matching	38

2.3.4	Compression point	40
2.3.5	From the literature	41
2.3.5.1	Experimental results from the literature	43
2.3.5.2	Estimation of the RF gain improvement	44
2.3.6	Experimental achievements	46
2.4	Combining sources for improving the RF link noise figure	48
2.4.1	Introduction	48
2.4.2	Equivalent RIN source	49
2.4.2.1	Inter-correlation term	50
2.4.2.2	Scalability of the model	52
2.4.2.3	Results from the literature	53
2.4.3	Noise figure and signal-to-noise ratio improvement	53
2.4.3.1	Detailed comparison for series-connected laser sources with a resistive impedance matching	53
2.4.3.2	Literature available data	56
2.4.4	Experimental achievements	57
2.4.4.1	Experimental set-up	57
2.4.4.2	Experimental results	57
2.4.4.3	Effect of heterodyne beating	59
2.4.5	Limitations of the discrete element architecture	61
2.5	Conclusion	62
3	“Component level” point of view: a comprehensive model of the integrated device	67
3.1	Introduction to rate equation analysis	67
3.1.1	General description of the model	68
3.1.2	Carrier population rate equation	69
3.1.3	Photon population rate equation	72
3.1.4	Laser threshold	72
3.1.5	Expression of τ_P	72
3.1.6	Output power	73
3.1.7	Comparing different QW structures	74
3.1.8	Approximations	76
3.2	Steady-state solution	77
3.2.1	Single QW, single active junction (SQW)	77
3.2.2	Two QW, single active junction (DQW)	78
3.2.3	Two active junctions, each including a single QW (CQW)	80
3.3	Dynamic behavior	81
3.3.1	Single QW, single active junction (SQW)	83
3.3.2	Two QWs, single active junction (DQW)	84
3.3.3	Two active junctions, each including a single QW (CQW)	86
3.4	RIN calculation	88
3.4.1	Noise definitions	88
3.4.2	Spectral density of the output power noise	89
3.4.3	Deriving the Langevin noise diffusion coefficients	92
3.4.3.1	Output power noise	93
3.4.3.2	Comparison of the three cases	93
3.4.3.3	Conclusion on the possible RIN improvement	97
3.5	Conclusion	97

4	Bipolar cascade laser modeling at an “electronic level” point of view	103
4.1	Introduction	103
4.2	Transport model used in simulations	104
4.2.1	Formerly-existing transport model	104
4.2.2	Physical model	105
4.2.3	Numerical implementation	106
4.3	Modifications for the modeling of laser diodes composed of materials lattice-matched to InP	108
4.3.1	Modifications of the data base entries	108
4.3.1.1	Effective masses	108
4.3.1.2	Band-gap energy	109
4.3.1.3	Band offset	109
4.3.1.4	Electron mobility	109
4.3.1.5	Hole mobility	110
4.3.1.6	Refractive index	110
4.3.1.7	Dielectric constant	110
4.3.2	Influence of the Auger recombination increase	110
4.4	From the Boltzmann statistics to the Fermi-Dirac statistics	110
4.4.1	Physical model	110
4.4.2	Numerical implementation: modification of the Scharfetter & Gummel scheme	111
4.5	Modifications for the modeling of multi-quantum-well laser diodes	112
4.5.1	Numerical implementation	112
4.5.2	Example of simulation	115
4.6	Esaki tunnel junction modeling	116
4.6.1	Principle of a tunnel junction	116
4.6.2	Electronic model	117
4.6.2.1	Introduction	117
4.6.2.2	The matrix element	119
4.6.2.3	$\mathbf{k} \cdot \hat{\mathbf{p}}$ -description of the semiconductor bands	122
4.6.2.4	The transmission coefficient	126
4.6.2.5	The tunnel current	127
4.6.3	Discussion on the tunnel-current model and on its implementation	129
4.6.3.1	The physical model	129
4.6.3.2	Numerical implementation	131
4.6.3.3	Example of simulation	132
4.7	Conclusion	132
5	Design of a single-transverse-mode bipolar cascade laser	137
5.1	Tunnel junctions	137
5.1.1	Improving the tunnel probability by changing the constituting materials	138
5.1.1.1	Band-gap energy	138
5.1.1.2	Effective mass	138
5.1.1.3	Band diagram	139
5.1.1.4	Calculated characteristic	140
5.1.1.5	Conclusion	141
5.1.2	Doping level	141

5.1.2.1	Additional losses while increasing the doping concentration	142
5.1.2.2	The trade-off given by the technological limit	143
5.1.3	Zn diffusion	143
5.1.3.1	General description of the zinc diffusion in III-V semiconductors	144
5.1.3.2	Influence of the epitaxial growth parameters	148
5.1.3.3	Influence of the grown structure	150
5.1.3.4	Influence of the post-growth treatment	150
5.1.3.5	Estimation of the material diffusion characteristics	151
5.1.4	Experimental achievements	153
5.1.4.1	Description of the test-structure	153
5.1.4.2	Current-voltage characteristics	154
5.1.4.3	Estimation of the tunnel junction resistance while implemented in a real laser	157
5.1.4.4	SIMS measurements of the tunnel junction directly on the laser structures	158
5.2	Bipolar cascade lasers	160
5.2.1	Optimization of the electrical confinement barriers	160
5.2.1.1	Introduction	160
5.2.1.2	Presentation of the designed structures	160
5.2.1.3	Results of the simulation	161
5.2.1.4	Discussion on the results	164
5.2.2	Experimental achievements	165
5.2.2.1	Description of the grown structures	165
5.2.2.2	Influence of the current blocking layers on the V(I) characteristics	168
5.2.2.3	Influence of the highly-doped tunnel junctions on the intrinsic losses	171
5.2.2.4	Estimation of the facet surface current for BCL	172
5.2.2.5	Influence of the current spreading	173
5.2.2.6	Demonstration of the carrier recycling effect	175
5.2.2.7	Influence of the number of active regions	177
5.2.2.8	Explanation of the non-lasing behavior of structure B2	178
5.2.2.9	Demonstration of a single-transverse-mode bipolar cascade laser	179
5.3	Conclusion	182
6	General conclusion and perspectives	189
6.1	Conclusions	189
6.1.1	Thesis overlook	189
6.1.2	Work achievements	190
6.2	Perspectives	192
6.2.1	Improvement of the discrete architectures	192
6.2.2	Improvement of the integrated monolithic BCL	193
A	Notations and parameters used in chapter 3	197

CONTENTS

B	Calculation steps for obtaining the expression of the tunneling current	201
B.1	Calculation step A.	202
B.2	Calculation step B.	202
B.3	Calculation step C.	203
B.4	Calculation step D.	204
B.5	Calculation step E.	205
B.6	Calculation step F.	206
B.7	Calculation step G.	207
C	Methods of structure characterization used in chapter 5	213
C.1	Four-probe measurement technique	213
C.2	Transmission Line Method	214
C.3	Loss transmission measurement	215
C.4	Laser loss measurement	217

Chapter 1

General Introduction

“The creation of the radar, which was claimed by the English who managed to spread this idea in America, was facilitated to them by the circumstances of the war and the occupation of France by the Germans. However the truth is other...”

Emile Girardeau, Member of the “Académie des Sciences morales et politiques”

1.1 From the blurred origins of radar engineering to current research on opto-RF links

RADAR (Radio Detection and Ranging) systems have a very controversial history. For the scientific principle, science historians are unanimous to claim that it all began in 1888 when Heinrich Rudolf Hertz (see figure 1.1-(a)) first experimentally proved the existence of electro-magnetic waves that James Maxwell theoretically predicted in 1873. For the technological realization however, there are divergent points of view. The paternity of the concept is currently attributed to Robert Wattson-Watt, who had radar stations installed for detecting ships or planes along Great Britain east coast in 1935. History retains his name because of the eminent role the detection system has played during WWII airborne battles in south Great Britain, in 1940.

But the existence of a French patent dated July 1934 [1] raises doubts about the British origin of the device. It describes electro-magnetic studies conducted near Palaiseau (south of Paris, France) with wavelength ranging from 16 cm to 80 cm. The first ship equipped with a radar detection system was the French cargo “Oregon”, on which detection was realized in 1934 up to 12 marine miles (≈ 20 km) [2]. It was then installed on the French ship “Normandie” (see figure 1.1-(b)). Still this is not the first and foremost appearance of a radar device.

Figure 1.1 History of the radar system: some pictures from the past.



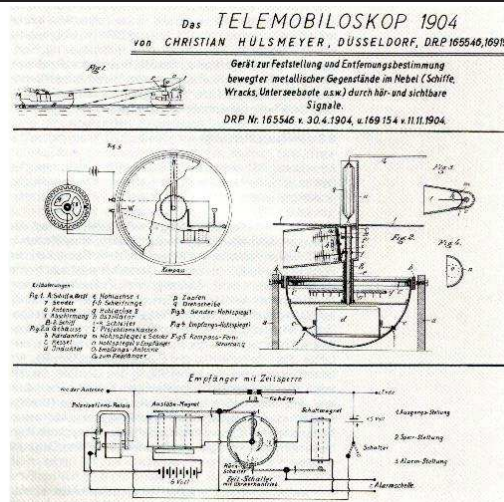
(a) Heinrich R. Hertz, 1890



(b) The radar system on the ship "Normandie", 1934

Because of the decisive use of radar systems by the Atlantic Coalition during the Second World War, it is actually surprising to find the father of the radar system on the other side of the French-German border. Christian Hülsmeyer invented in 1904 a device called "Telemobiloskop" [3, 4]. Designed to detect icebergs on transatlantic ships, this device is considered today as the true ancestor of modern radar (cf. figure 1.2). Thirty years later (early 1934), still in Germany, the first "modern" radar system for detecting ships is commercialized by the company GEMA founded by another radar pioneer: Dr. Hans E. Hollmann [4].

Figure 1.2 The German patent for "Telemobiloskop", the ancestor of modern radar.



Since the 30's, the radar emitter-detector device has not changed dramatically: in most types of antennas, a parabolic reflector concentrates the electro-

1.2 What industrial applications can gain from opto-RF links

magnetic signal to the active element. What has been drastically advanced however is the signal transmitted via the radar antenna and its corresponding receiver. There is now a need for carrier wavelength as short as possible to increase detection precision as well as high RF power to improve sensitivity. Furthermore, with the emergence of electronic warfare, we need to resolve the whole microwave spectrum, from a few kHz, to several tens of GHz! The requirements for radar systems and above all, the specifications required for radar-driving RF circuits have caught up with the electronic state of the art, for instance in terms of bandwidth transmission capacity.

Now, thanks to the very high bandwidth available in such systems, the recent development of optical transmission technologies appeared to be of major interest for use in radar systems. In this context, opto-RF link are currently developed to be implemented in radar systems. The research work presented in this thesis focuses on the improvement of opto-RF link characteristics by the use of a specific device: the bipolar cascade laser (BCL).

In the General Introduction I will list some applications for which the use of BCL can be a decisive asset, explain briefly the functions of the bipolar cascade laser, and describe the state-of-the-art of bipolar cascade laser. Eventually, I will give a brief outline of the following thesis report.

1.2 What industrial applications can gain from opto-RF links

The work presented in this thesis has been achieved within the Microwave Photonics Lab. (MPL) at Thales Research & Technology, Orsay, France. The MPL is a Thales Corporate research entity developing technologies intended to be incorporated in systems designed by Group Thales companies, namely Thales Airborne Systems, Thales Air defense, Thales Electron Devices, and Thales Communications. The MPL focuses on the development of components and systems aiming at transmitting the RF signal emitted/received by the radar antenna between the physical radiative element and the information processing module.

This section provides two typical examples of the use of opto-RF links, for which a bipolar cascade laser would be used, when its expected characteristics are to be attained.

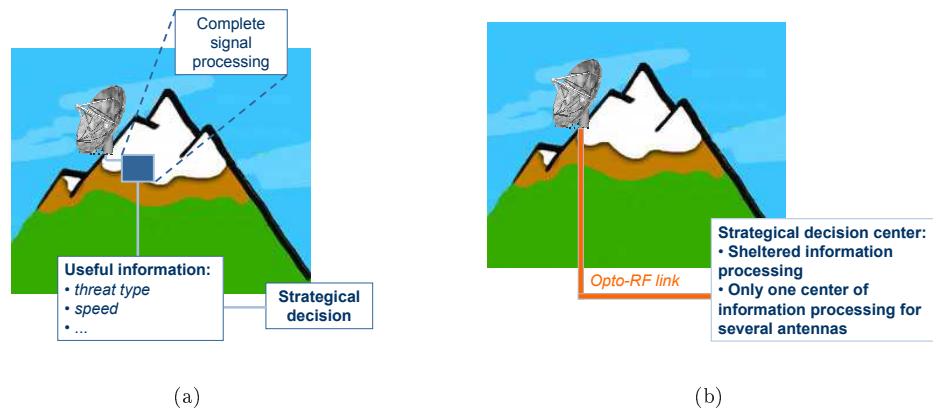
1.2.1 Ground radars

In the specific case of nowadays ground radars, the information processing module stands very close to the radiative element in order to reduce transmission losses. A schematic view of currently implemented architecture is depicted on figure 1.3-(a). The useful information is then transmitted to the decision module via standard base-band information transmission protocols. This architecture entails some important drawbacks:

- The expensive information processing module containing the main part of the link intelligence is vulnerable to weather conditions as well as enemy-caused interference.

- The information processing module is located as close as possible to the radiative elements. The transmitter unit generates heat that may alter the performances of the receiver module.
- The useful information may be intercepted along the transmission link.
- The information processing module containing the defense-protected algorithms need to be militarily secured.

Figure 1.3 Schematic comparison between currently used electrical (a), and proposed opto-RF (b) transmission architectures for ground radar.



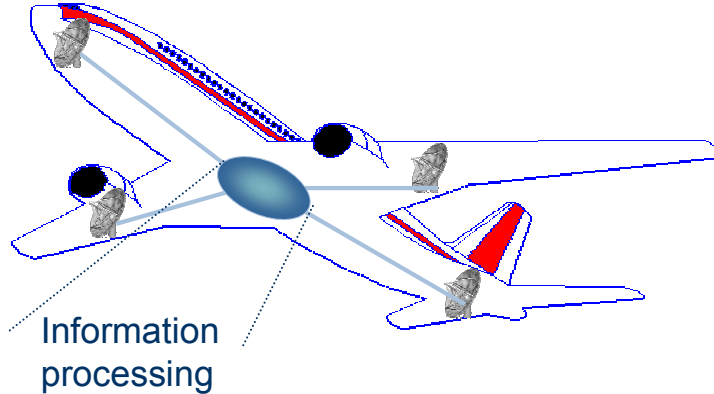
This architecture may be further enhanced using a fiber optical (FO) link, schematically represented on figure 1.3-(b). The FO link consists of a laser source, a photodiode, and the optical fiber. The RF signal is transmitted as-received directly to the central processing unit which centralizes also the waveform generation function. Even for several antennas, a unique secured shelter contains all the costly and defense-sensitive devices. Regarding the required bandwidth (up to 5-6 GHz), and the typical distance between the antenna and the shelter (a few hundred meters), this architecture cannot be realized with electronics transmission and requires opto-RF links.

1.2.2 Electronic warfare

Another domain of application concerns electronic warfare; the defense of the electro-magnetic spectrum. To prevent missile attacks or information spying, aircrafts need nowadays to get precise information on any electro-magnetic signal emitted in its vicinity over a very large bandwidth of interest (up to tens of GHz!)

1.3 Current opto-RF links shortcomings

Figure 1.4 Schematic of the electronic warfare equipment installed on an aircraft.



Receivers placed along the airplane transmit raw information to an information processing module. Figure 1.4 illustrates schematically this architecture. Phase triangulation enables for instance to identify the angle of arrival of a threat. The calculation of the angle is all the more accurate as the receiver elements are far from each other. For airborne applications, the fiber optic transmission of the raw data enjoys a lot of mechanical advantages: light weight, small bending radius which saves costly volume, immunity to electro-magnetic perturbation...

1.2.3 Other advantages of opto-RF links

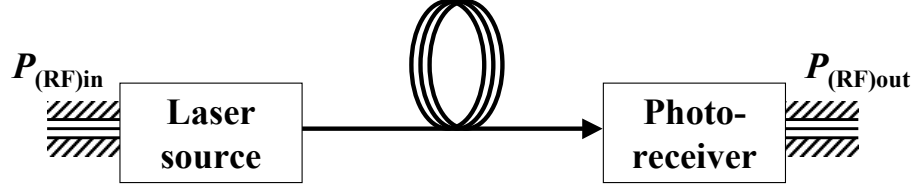
In addition, an optical information network enables the development of additional functions:

- Broad-band, flat amplification: optically amplifying a modulated light signal simultaneously amplifies the RF signal over the whole bandwidth.
- Use of wavelength multiplexing that enable parallel processing of different RF signals.
- Others specific properties such as bidirectional transmission of several RF carriers or local oscillators through an optical rotating joint.

1.3 Current opto-RF links shortcomings

Figure 1.5 displays the schematic of a simple opto-RF link. The directly modulated laser source converts the input RF signal into a modulated light signal. This light beam is transmitted via the optical fiber and converted again to an output RF signal in the photoreceiver.

Figure 1.5 Schematic of a simple opto-RF link.



The RF link gain, defined as $g_{\text{RF}} = \frac{P_{(\text{RF})\text{out}}}{P_{(\text{RF})\text{in}}}$ is very low for non-optimized opto-RF links (in the order of -30 dB). In order to be adopted in systems, despite all the remaining advantages of opto-RF links, the requirements are very ambitious: we need to achieve a loss-less link ($g_{\text{RF}} = 0$ dB!).

Besides, another key parameter is the noise figure (noise added by the opto-RF link), which is given by

$$NF = \frac{P_{(\text{RF})\text{in}}/P_{(\text{noise})\text{in}}}{P_{(\text{RF})\text{out}}/P_{(\text{noise})\text{out}}}$$

It currently lies in the order of 40 dB. This very high figure is mainly due to the poor link gain and some additional noise introduced by the laser. It should be reduced to 10 dB to spread its implementation in systems.

This thesis proposes a new laser device, the bipolar cascade laser (BCL), to increase the RF link gain in line with the objectives of the present research in the field of opto-RF transmission.

1.4 Principle of the bipolar cascade laser

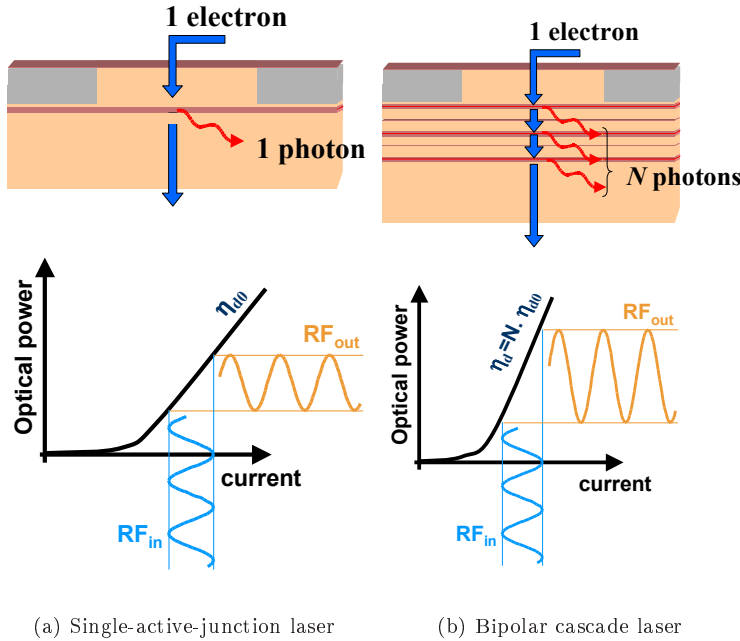
A semiconductor laser is usually composed of layers of semiconductor materials forming an active p - n junction. Above a current threshold, injected carriers (electrons in the n -side, and holes in the p -side) recombine in the active region and may give birth to one photon (see figure 1.6-(a)). In practice, the emission process encounters losses. The quantum external differential efficiency is defined as the number of photons emitted from one laser facet, for one electron-hole pair injected. This figure is proportional to the slope of the optical power-versus-current curve, which is called differential external efficiency (η_d) and is expressed in W/A. The quantum differential efficiency typically lies in the order of 25% (which corresponds to $\eta_d \simeq 0.2$ W/A for an emission at $1.55 \mu\text{m}$), and can be raised up to 50% ($\eta_d \simeq 0.4$ W/A) with proper high-reflectivity/anti-reflective coatings.

A bipolar cascade laser is composed of N p - n active junctions epitaxially stacked. The injected electrons go through the N junctions and potentially emit a photon in every junction (see figure 1.6-(b)). One electron may give birth to several photons! As a consequence, differential external efficiency η_d increases approximately by a factor of N , as shown in figure 1.6.

Besides, this differential efficiency is also the low frequency response to a current modulation. The same current modulation applied to the bipolar cascade laser will increase the amplitude of the light beam modulation thus leading

1.5 History and state-of-the-art of bipolar cascade lasers

Figure 1.6 Principle of the bipolar cascade laser, and schematic comparison between single-active-junction lasers and bipolar cascade laser. Schematic description of the role of the differential efficiency for increasing the RF link gain.



to an overall RF link gain improvement as compared to a single-active-region laser.

1.5 History and state-of-the-art of bipolar cascade lasers

There are three main applications for BCL: high power, VCSELs and microwave optics. Each of these applications uses very specific designs. Furthermore, even if no exhaustive bibliography review will be done, it should be noted that the principle of cascading active junctions carries some interest not only for lasers, but also for light-emitting-diodes (see for instance [5, 6]), and for tandem solar cells (see for instance [7]).

1.5.1 High-power applications

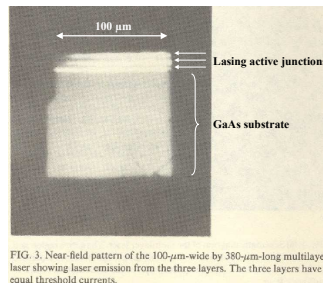
High power edge emitter BCLs usually consist in active regions separated by several microns: the light intensity can be spread among the different active regions, lowering, for a given output power, the maximum local electric field and pushing back the catastrophic optical damage threshold for GaAs-based devices. The device represents the integrated version of a vertical laser diode array, and is the building block for 2-D laser diodes arrays.

The first BCL was actually proposed in 1982 by van der Ziel *et al.* for high-power applications [8] (see figure 1.7-(a)). It was grown on a GaAs substrate. In 1997, Garcia *et al.* from Thales Research & Technology (Thomson-LCR at this time) demonstrated a two-active-junction, two-current-threshold, and even two-color multi-quantum-well BCL, still on GaAs substrate [9]. Soon afterwards, the same team (Laurent *et al.*, from Thales Research & Technology) transposed the concept to InP substrate, still for increasing the output power [10]. The tunnel junction was made of one *n*-doped ($\text{Si}:5 \times 10^{18} \text{ cm}^{-3}$) InGaAsP ($\lambda = 1.2 \mu\text{m}$) layer, and one *p*-doped ($\text{Zn}:5 \times 10^{18} \text{ cm}^{-3}$) InGaAsP ($\lambda = 1.2 \mu\text{m}$) layer.

The Massachusetts Institute of Technology (MIT) demonstrated in 1999, the first CW, room-temperature operation of a BCL, still on GaAs substrate, for a 980-nm-emission [11]. Meanwhile, an industrial team in Germany (Infineon Technologies Corporate Research and Osram Opto Semiconductors) studied the scalability of "microstack" lasers with two and three active junctions [12].

Since then, several investigations have been carried out mainly to improve the reliability of the devices: studies of the temperature properties (Patterson *et al.* at the MIT [13]), reliability tests using near-field optical microscopy (for Osram Semiconductors in Germany [14–16]) and optimization of the tunnel junction (by increasing the dopant concentration) for reducing the series resistivity and thus the power consumption [17]. Bipolar cascade lasers are even already commercially available for pulsed operation at 905 nm, up to 75 W [18] (see figure 1.7-(b))!

Figure 1.7 Twenty years of technological evolution!



(a) Near-field pattern of the first BCL (1982) [8]



(b) Commercially available BCL (2004) [18]

1.5.2 Bipolar Cascade Vertical Cavity Surface Emitting Lasers (BCVCSEL)

There are three main reasons why research on BCL was oriented towards vertical cavity surface emitting lasers (VCSELs). First, due to the very short cavity, the VCSEL round-trip gain is usually very low. Cascading several active junctions can provide a decisive asset to increase the laser gain (thus reducing the laser threshold and increasing the maximum output power). Secondly, the main difficulty in the fabrication of a bipolar cascade laser is the fabrication of a low-resistivity tunnel junction. The field of bipolar cascade lasers took advantage of

1.5 History and state-of-the-art of bipolar cascade lasers

all the research work already performed concerning the use of tunnel junctions for p -side mirror resistivity reduction. Thirdly, with the VCSEL concept, it is possible to design the BCL so that the knots of the standing waves coincide with the heavily-doped (and thus highly absorbing) tunnel junctions (see figure 1.8-(a)). The periodic structure (real and imaginary periodic refractive index) may also be used as a distributed-feedback mirror, as explained in the model proposed in [19].

The first BCVCSEL was grown on InP substrate by Kotaki in 1984 [20]. Afterwards, it lasted until 1998 to find a second example of implementation in the literature.

In the present (1998-present) state-of-the-art, two laboratories are leading the research on BCVCSELs worldwide: the University of Ulm (Germany) fabricated in 1998 the first MQW GaAs-based BCVCSEL [21] (see figure 1.8-(a)). The device already had (in pulsed operation) an external quantum efficiency exceeding unity! In 1999, they achieved CW, room-temperature operation [22]. Then after some technological improvement [23], they achieved in 2000 a RT-CW operation with quantum efficiency exceeding unity, and a maximum output power of 7.2 mW for an active diameter of 9 μm [24, 25]. In 2001, they studied the scaling behaviour of 1,2,3-active region VCSELs [26]. Their work thereafter focused on current spreading induced bistability either to benefit from the phenomenon (for optical memory for instance) [27], or to prevent the phenomenon and improve the device characteristics [28–30]. Eventually, they have recently proposed an overview of their research on BCVCSELs emitting at 980 nm [31].

This concept was also studied by the University of California, Santa Barbara (UCSB) for the development of monolithic 1.55 μm -emitting VCSELs, to counterbalance the lower reflectivities in the long-wavelength regime. They achieved in 1999 50% external efficiency at room temperature [32], which is good for a 1.55 μm VCSEL, as compared for instance to state-of-the-art single-active-region 1.55 μm VCSELs [32–34]. In 2000, they demonstrated the first 1.55 μm BCVCSEL with differential efficiency exceeding unity (at -10°C , pulsed operation) with $\text{Al}_{0.08}\text{Ga}_{0.22}\text{In}_{0.70}\text{As}$ active regions. The tunnel junctions consisted in $\text{Al}_{0.29}\text{Ga}_{0.19}\text{In}_{0.45}\text{As}$ layers which were doped (carbon on the p -side and silicon on the n -side) to concentration values exceeding 10^{19} cm^{-3} [35].

BCVCSELs are good candidates for microwave optics applications because they can be made single-longitudinal-mode. Unfortunately, the emitter aperture diameter controls the maximum output power (higher for larger diameters), together with the transverse-mode distribution. It is therefore rather difficult to obtain single-transverse-mode oscillation as well as high output power, even though both are needed for proper use in microwave optic links. For instance Kim *et al.* from UCSB found a multi-mode operation for their 50- μm -wide BCVCSEL (see figure 1.8-(b)).

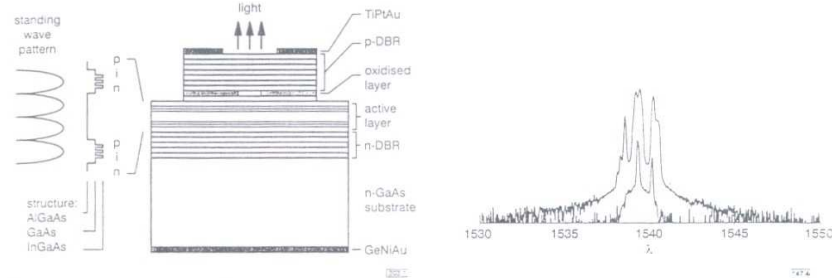
Figure 1.8 Examples of bipolar cascade VCSEL realizations.

Fig. 1 Structure of diode cascade VCSEL

Fig. 4 Spectra of 50 μm diameter VCSEL at 1.11 μm and 2I_n

(a) Structure and electric field distribution of the first MQW BCVCSEL (1998), from [21]

(b) Optical multi-mode spectrum of a 50 μm-diameter BCVCSEL on InP substrate (2000), from [35]

1.5.3 Microwave optic applications

In order to reach high external efficiency as well as single-mode emission at 1.55 μm, an edge-emitting design is more appropriate. Due to the real difficulty to achieve low resistivity tunnel diodes, there are only two examples of 1.55 μm edge-emitting BCL so far. The first one was realized in 1997 by N. Laurent *et al.* at Thales Research & Technology [10], the second one is due to J.K. Kim *et al.* [36, 37] from the University of California, Santa Barbara.

N. Laurent in fact focused on high-power applications. The results have already been exposed in section 1.5.1. In further investigations, we proved that this device was actually multi-mode in the direction perpendicular to the layers (for a 8 μm ridge), and oscillating on the second-order mode [38, 39] (see figure 1.9-(a)).

University of California's work was a fore-study to demonstrate the feasibility before implementing the design in a VCSEL (see paragraph 1.5.2). They nevertheless reached an external efficiency of 125% [37]. With a 50 μm Fabry-Perot ridge structure, the laser is highly multi-mode. They also implemented a transverse-third-order-mode structure with tunnel junctions placed at the nulls of the electric field [36].

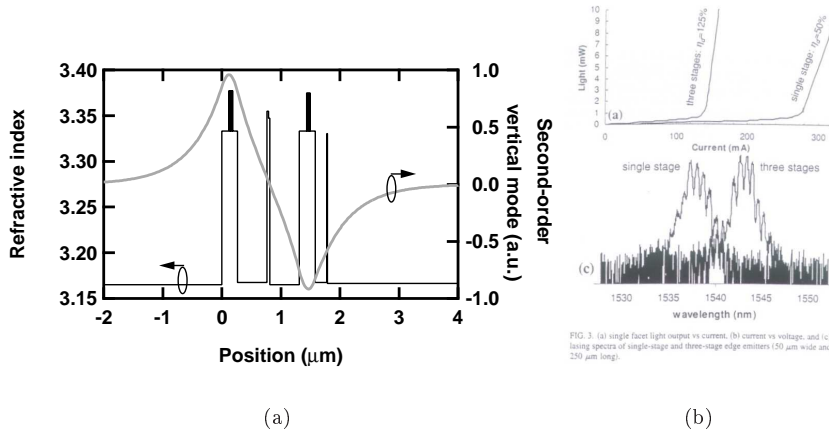
Another American laboratory plays an important role in microwave optic BCL: the Massachusetts Institute of Technology. Based on their experimental work on GaAs substrates exposed in section 1.5.1 [11, 13], they have theoretically studied the possible improvements on laser noise [40] and opto-RF noise figure [41, 42] by using a BCL. They also experimentally, as well as theoretically studied the electrically-induced photon noise correlation of lasers connected in parallel and series [40, 43]. According to a MIT internal technical report for the DARPA [44], they are now leading investigations towards the development of a multiple-active-region structure, combined with an anti-resonant waveguide to enforce single-mode emission (ARROW-BCL).

Up to now, no single-transverse-mode bipolar cascade laser have been demonstrated. The work presented in this thesis precisely aims at describing the specific advantages we would get from using such a device in opto-RF systems and

1.6 Outline of the thesis

at developing several tools for designing the device. The objective of this study is eventually to design and demonstrate the fabrication of single-transverse-mode bipolar cascade laser structures that can be further improved in a near future in order to reach systems specifications.

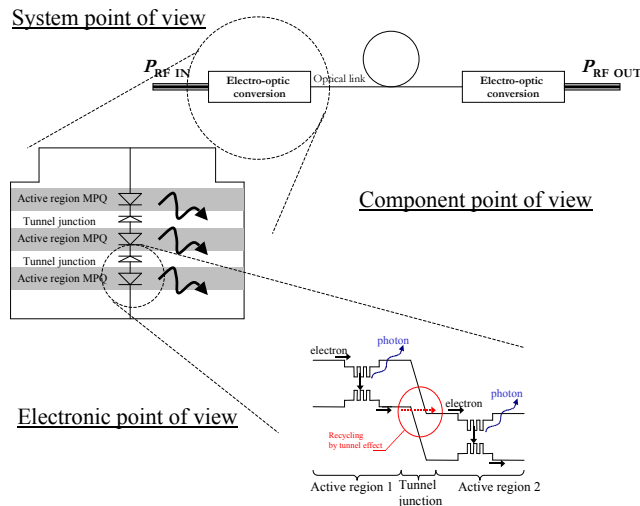
Figure 1.9 (a) Single-transverse-second-order mode emission (1997-2003), from [10, 38] (b) L-I and optical spectrum BCL characteristics (1999), from [37]



1.6 Outline of the thesis

The bipolar cascade laser has been studied according to three “levels of study”, each one corresponding to a macro-, meso-, and microscopic space scale. This concept is illustrated on figure 1.10.

Figure 1.10 Three points of view for a single object: the backbone of the thesis.



The first part of the thesis (Chapters 2, 3 and 4) focuses on the potential

advantages of cascading several active junctions, and describes the necessary trade-offs for designing a single-transverse-mode BCL.

Chapter 2 describes the system-level advantages of the device: using different electrical architectures, we will connect several discrete lasers and combine the light to track the possible improvements obtained by a light source composed of several lasers. This chapter contains a theoretical as well as an experimental study.

Chapter 3 goes downscale, to study the device from a component-level point of view. We will develop a theoretical model based on a rate equation formalism and check that the monolithic integration of the cascading of laser structures does not fundamentally ban the improvement we expect from the macroscopic study of combining discrete laser beams.

Chapter 4 goes even deeper into the component, to the electronic-level point of view, and studies microscopically the ingredients for the design of a single-transverse-mode BCL. A self-consistent transport model will be modified to account for several quantum wells, and several active regions into a single laser structure.

The second part of the thesis, chapter 5 focuses on the actual design of a bipolar cascade laser and the implementation of the designed structure into a real component. As it is the main difficulty to tackle in order to produce a single-transverse-mode bipolar cascade laser, we will discuss the optimization of the tunnel junction and the technological limitations of this process. Then we will describe the design of a bipolar cascade laser and present several bipolar cascade structures realized and characterized.

Eventually, the General Conclusion synthesizes the work and opens the discussion to future works for improving the characteristics of the bipolar cascade lasers.

Bibliography

- [1] Compagnie Générale de Télégraphie sans fil. French patent 788.795: Nouveau système de repérage d'obstacles et ses applications, Jul 1934.
- [2] <http://www.radar-france.fr>.
- [3] C. Hülsmeier. German patent 165,546: Means for reporting distant metallic bodies to an observer by use of electric waves, 1904.
- [4] <http://www.radarworld.org>.
- [5] X. Guo, L. Balk, K. Wang, et al. Thermal property of tunnel-regenerated multiactive-region light-emitting diodes. *Applied of Physics Letters*, 82(25):4417–4419, Jun. 2003.
- [6] C.H. Chen et al. Nitride-Based Cascade Near White Light-Emitting Diodes. *IEEE Photonics Technology Letters*, 14(7):908–910, Jul. 2002.
- [7] J. M. Olson, S. R. Kurtz, A. E. Kibbler, and P. Faine. A 27.3% efficient Ga_{0.5}In_{0.5}P/GaAs tandem solar cell. *Applied Physics Letters*, 56(7):623–625, Feb. 1990.
- [8] J.P. van der Ziel et al. Integrated multilayer GaAs lasers separated by tunnel junctions. *Applied Physics Letters*, 41(6):499–501, 1982.
- [9] J. Ch. Garcia et al. Epitaxially stacked lasers with Esaki junctions: a bipolar cascade laser. *Applied Physics Letters*, 26(71):3752–3754, 1997.
- [10] N. Laurent et al. Injection locking between laser layers in a InP/InGaAsP bipolar cascade laser. In *CLEO'98*, pages 468–469, San Francisco, USA, May 1998.
- [11] S. G. Patterson et al. Continuous-wave room temperature operation of bipolar cascade laser. *Electronics Letters*, 35(5):395–396, Mar. 1999.
- [12] C. Hanke et al. High-power AlInGaAs/GaAs double and triple microstack lasers at 808 nm. In *LEOS'99, IEEE Lasers and Electro-Optics Society*, volume 1, pages 80–81, San Francisco, USA, Nov. 1999.
- [13] S.G. Patterson et al. High temperature properties of bipolar cascade lasers. In *CLEO'00*, number CWF7, pages 268–269, 2000.
- [14] V. Malyarchuck, M. Behringer, et al. Uniformity tests of individual segments of interband cascade diode laser Nanostacks. *Journal of Applied Physics*, 92(5):2729–2733, Sept. 2002.

-
- [15] V. Malyarchuk et al. Optical spectroscopy of individual segments of inter-band cascade diode laser Nanostacks. In *CLEO '03*, number CC6-4-WED, Munich, Germany, Jun. 2003.
- [16] Martin Behringer, Franz Eberhard, Gerhard Herrmann, Johann Luft, J. Maric, Stefan Morgott, Marc Philippens, and W. Teich. High Power Diode Lasers Technology and Application in Europe. In *Proceedings of SPIE*, pages 4–13, Osaka, Japan, Mar. 2003.
- [17] W.J. Siskanietz et al. Reduced power consumption in GaAs-based bipolar cascade lasers. *Electronics Letters*, 38(21):1259–1261, Oct. 2002.
- [18] Osram. Opto semiconductors. <http://www.osram-os.com/>. product ref. SPL PL90 3.
- [19] A.N. Korshak et al. Tunnel-junction-connected distributed-feedback vertical-cavity surface-emitting laser. *Applied Physics Letters*, 73(11):1475–1477, Sept. 1998.
- [20] Y. Kotaki et al. GaInAsP/InP Surface Emitting Laser with Two Active Layers. In *Conf. Solid State Devices and Materials (SSDM'84)*, number C-2-3, pages 133–136, Kobe, Japan, Aug. 1984.
- [21] W. Schmid et al. CW operation of a diode cascade InGaAs quantum well VCSEL. *Electronics Letters*, 34(6):553–555, Mar. 1998.
- [22] T. Knödl et al. CW room temperature operation of a diode cascade InGaAs-AlGaAs quantum-well VCSEL. In *Proc. of IEEE LEOS Annual Meeting 1999*, volume 2, pages 143–144, San Francisco, CA, USA, Nov. 1999.
- [23] T. Knödl et al. Improvement of a Diode Cascade VCSEL Performance. In *CLEO Europe 2000*, number CThK7, Nice, France, Sept. 2000.
- [24] T. K Knödl et al. Multi-diode cascade VCSEL with 130 % differential quantum efficiency at CW room temperature operation. *Electronics Letters*, 37(1):31–33, Jan. 2001.
- [25] T. Knödl et al. Bipolar Cascade VCSEL with 130% Differential Quantum Efficiency. Annual Report, Optoelectronics Department, University of Ulm, Germany, 2000.
- [26] T. Knödl et al. Scaling behavior of bipolar cascade VCSELs. *IEEE Photonics Technology Letters*, 13(9):930–932, Sept. 2001.
- [27] T. Knödl et al. Current-spreading-induced bistability in bipolar cascade vertical-cavity surface-emitting lasers. *Applied Physics Letters*, 81(4):583–585, Jul. 2002.
- [28] T. Knödl et al. Bistability in bipolar cascade VCSELs. *Electronics Letters*, 38(8):370–371, Apr. 2002.
- [29] T. Knödl. Bistability in Bipolar Cascade VCSELs. Annual Report, Optoelectronics Department, University of Ulm, Germany, 2002.

BIBLIOGRAPHY

- [30] T. Knödl et al. Influence of design variations on bipolar cascade VCSEL performance. In *14th Annual Meeting of the IEEE LEOS*, volume 2, pages 463–464, Nov. 2001.
- [31] T. Knödl et al. Multistage bipolar cascade vertical-cavity surface-emitting lasers: Theory and experiment. *IEEE Journal of Selected Topics in Quantum Electronics*, 9(5):1406–1414, Sept.-Oct. 2003.
- [32] J. K. Kim et al. Room-temperature, electrically-pumped multiple-active-region VCSELs with high differential efficiency at 1.55 μm . *Electronics Letters*, 35(13):1084–1085, Jun. 1999.
- [33] S. Nakagawa et al. 1.55- μm InP-Lattice-Matched VCSELs With AlGaAsSb-AlAsSb DBRs. *IEEE Journal on selected topics in Quantum Electronics*, 7(2):224–230, Mar. 2001.
- [34] N. Nishiyama et al. High efficiency long-wavelength VCSEL on InP grown by MOCVD. *IEEE Electronics Letters*, 39(5):437–439, Mar. 2003.
- [35] J. K. Kim et al. Near-room-temperature continuous-wave operation of multi-active-region 1.55 μm vertical-cavity lasers with high differential efficiency. *Applied Physics Letters*, 77(20):3137–3139, Nov. 2000.
- [36] J.K. Kim et al. Epitaxially-stacked multiple-active-region 1.55 μm lasers for increased efficiency. In *IEEE Conference on Lasers and Electro-Optics, CLEO'99*, page 139, Baltimore, MD, USA, May 1999.
- [37] J. K. Kim et al. Epitaxially-stacked multiple-active-region 1.55 μm lasers for increased differential efficiency. *Applied Physics Letters*, 74(22):3251–3253, May 1999.
- [38] F. Dross et al. Transverse mode analysis of a bipolar cascade laser. In *Conference on Laser and Electro-Optics Europe (CLEO)*, number CC6-1-WED, Munchen, Germany, Jun. 2003.
- [39] F. Dross et al. Analyse modale d'un laser à cascade bipolaire. In *Journées Nationales d'Optique Guidée*, Valence, France, Jul. 2003.
- [40] F. Rana et al. Photon noise and correlations in semiconductor cascade lasers. *Applied Physics Letters*, 76(9):1083–1085, Feb 2000.
- [41] R. J. Ram et al. High Performance Microwave Optical Links. In *International Conference on Communications, Computing and Devices*, pages 290–294, Kharagpur, India, Dec. 2000.
- [42] R. J. Ram et al. Cascade Semiconductor Lasers for Telecommunications (Invited). In *IEEE Annual Meeting of the IEEE Laser and Electro-Optic Society, LEOS'02*, number WV3, Glasgow, Scotland, Nov. 2002.
- [43] F. Rana et al. Correlated Photon emissions in Electrically Coupled Semiconductor Lasers. In *SLC'02*, WA4, pages 115–116, Oct. 2002.
- [44] Microsystems Technology Laboratories Massachusetts Institute of Technology. http://www-mtl.mit.edu/mtlhome/6Res/AR2002/10_optoel/.

Chapter 2

High signal-to-noise ratio emitter: discussion on a “system level” point of view



Courtesy of S. Harris

2.1 Introduction

As it was briefly discussed in the introduction, recycling electrons and producing more photons than injected electrons is theoretically a very promising target. The first step towards achieving empirically this ambitious challenge is to look into the recycling process on a “system level” point of view.

In this chapter, we will therefore focus our study on a single device composed of several laser modules electrically connected. The electrical connections can be very diverse: in series, in parallel, and with different impedance matching schemes. Nevertheless, for any electrical architecture, the light produced by each individual laser will be optically combined into a common and single optical

receiver.

What are the characteristics of a laser source composed of several electrically connected laser modules? Is it possible to improve the RF link gain, or the RF noise figure by using macroscopical series or parallel connection? We will see in this chapter that combining several laser beams enables to push back the fundamental shortcomings of a single laser source. These problematics are sometimes referred to as “combining process”.

Even though some results may apply to external modulation, we will focus only on directly modulated lasers sources: the current modulation is applied directly to the light emitting device [1].

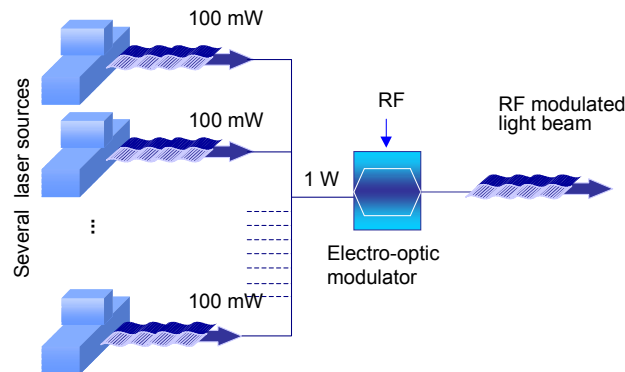
Section 2.2 sheds light on the ambiguous process of “combining” and intends to synthesize of the current research on combining processes worldwide. Section 2.3 is dedicated to the theoretical improvements on the RF link gain that can stem from different electrical configurations of a composed source. It ends with an experimental improvement of the link gain for lasers connected in series. Section 2.4 discusses the theoretical improvements on the RF link noise figure. An experimental study of the laser relative intensity noise improvement is also carried out.

2.2 What does combining mean?

Both optoelectronic receivers and emitters are limited to a maximum optical power. Either break-down of the device [2, 3] or non-linearities occur above this maximum power, which ban their use in systems above nominal conditions.

For RF optoelectronic applications, these shortcomings may be overcome by the use of several devices in parallel. For instance, in order to obtain a single-mode $1.55\ \mu\text{m}$ laser beam of 1 W (which is not achievable for the moment with a monolithic semiconductor device [4, 5]), we may use ten 100-mW single-mode lasers and collect the ten beams together in the same medium.

Figure 2.1 Example of the use of several lasers in parallel for relaxing the basic constraints on laser diodes in an externally modulated link [6]



Under this very simple formulation lies a huge difficulty: the power carried by the different light beams needs, at some point, to be concentrated. Studying

2.2 What does combining mean?

“combining” experiments entails collecting the energy of different sources into a single medium.

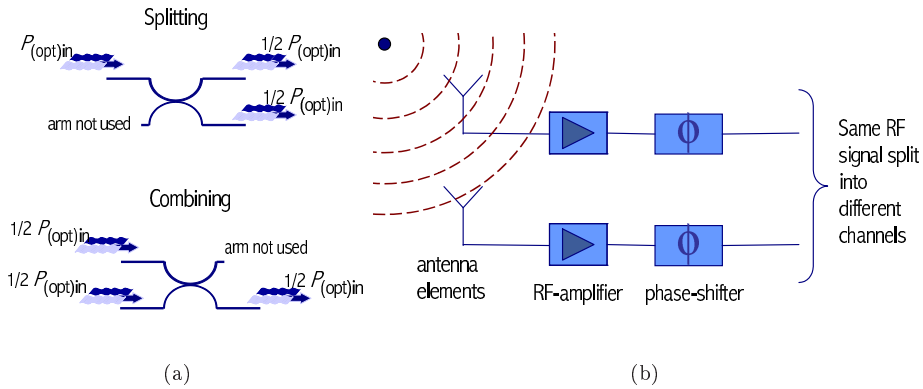
2.2.1 Splitting the RF signal

In directly modulated lasers architectures, the link carries a single input electrical RF signal and delivers a single output electrical RF signal. In order to benefit from combining architectures, the RF signal is first split into the different arms of the parallel architecture. Compared to combining, low-loss splitting of RF power is very easy to achieve: the RF signal split can be achieved with negligible loss using a regular RF coupler or a regular 50:50 optical coupler when the RF signal is carried by an optical signal.

For combining several RF signals however, the situation is not reciprocal. A regular coupler combines two signals (RF, or optical) with 3 dB intrinsic insertion loss, as shown on figure 2.2-(a).

The case of phased-array antennas deserve specific consideration, since by principle, the signal is transmitted to each antenna element in parallel (cf. figure 2.2-(b)). The system already provides numerous beams carrying the same RF signal. The signal is already split and we only need to combine it into a single medium.

Figure 2.2 (a) Non reciprocity of splitting and combining of light beams with optical couplers (b) Principle of parallel reception in phased-array antennas



2.2.2 Combining the RF signal

For combining however, the challenge is more difficult to achieve and many architectures are still being developed. We describe here the advantages and drawbacks of each architecture and then summarize them in table 2.1, on page 29.

2.2.2.1 Electronic combining after detection

It is the solution implemented in optoelectronic RF systems today. Several discrete photodiodes collect the incoming optical signals carrying the same RF signal. All the components combine then in an electrical RF coupler. This

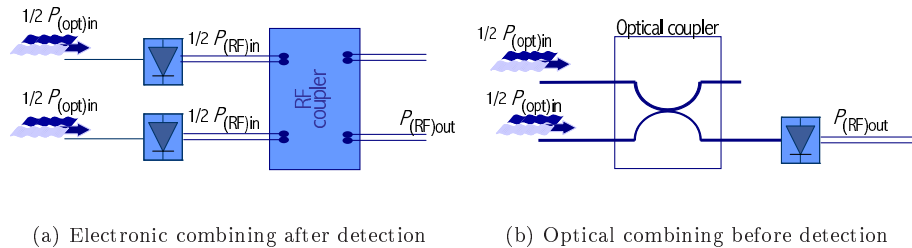
2. High signal-to-noise ratio emitter: discussion on a “system level” point of view

architecture has the advantages of being already available, and being implemented with any kind of laser or photodetector. Nevertheless, the insertion losses increase with the number of channels, and the volume and weight of such electronic components is always a drawback for implementation in systems such as airborne systems. In addition, the electronic combiners are limited to a narrow bandwidth operation.

2.2.2.2 Optical combining before detection

To circumvent the drawbacks (in terms of volume, weight and frequency bandwidth) of an electronic combining, optical architectures can be proposed, beginning with the most simple one using a standard coupler. This architecture works well if some care is taken on the polarization states of the input light beams to prevent heterodyne beating, as it is explained in great details in [7, 8]. It has the huge advantage of being available and very low cost. In the conditions of polarization states controlled, the device is limited to two channels. In addition, it suffers from 3-dB intrinsic insertion loss on the optical power.

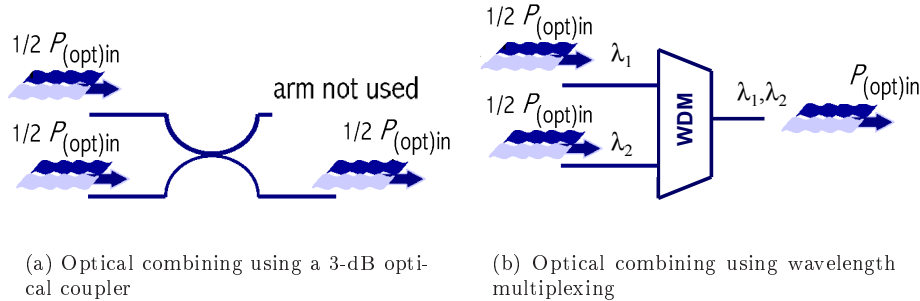
Figure 2.3 Schematic representation of optical and electronic combining architectures



To avoid intrinsic injection loss, and optical heterodyne beating between channels, a wavelength multiplexer is an interesting alternative. The transmission exhibits less optical power loss, and the beams are optically filtered. This solution is more costly than the standard coupler because lasers must be sorted to match the comb of wavelength filters [6]. In addition, the filtering may increase the amplitude noise of the lasers, either by a simple effect of filtering the Fabry-Perot longitudinal modes (the noise increases because of optical mode competition; this additional noise is negligible for DFB-lasers, where the longitudinal modes are already filtered), or by conversion of the phase noise to amplitude noise when the laser is on the steep edges of the filters [7, 9]. In some very specific cases, some other issues need to be tackled such as the operation point of the external modulator following the combining architecture, or problems related to the optical fiber wavelength dispersion [10] . . .

2.2 What does combining mean?

Figure 2.4 Comparison of two optical combining architectures



Eventually, for two-beam combining only, a polarization splitter/combiner can be used with no injection loss, no heterodyne beating, and no drawbacks related to filtering (laser sorting, laser noise increase...) [8]. Unfortunately, this ideal scheme is limited to two channels combining, and loses somewhat the low-cost characteristic of the standard-coupler architecture. In addition, it cannot be used in systems together with devices sensitive to polarization, such as some electro-optic modulator.

All these architectures are easy to implement and already available. In the architectures that do not exhibit intrinsic losses (wavelength multiplexer and polarization combiner) the optical power increases with the number of channel, for which in turn the use of a high-power photodiode is required [11–13].

2.2.2.3 Electronic combining integrated to the photodetector

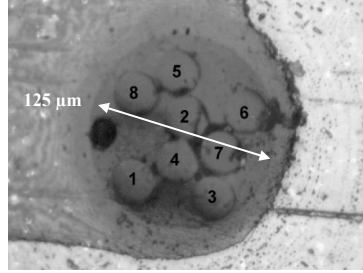
In order to avoid heterodyne optical beating, several architectures do not (optically) combine the light beams before detection.

It is indeed possible to spatially distribute the different light channels over the same absorbing *p-i-n* active area of a single photodiode. One way to proceed is to group several optical fiber cores into one single 125 μm optical fiber cladding [14]. See for instance figure 2.5-(a) where 8 fibers have been gathered into a single plastic cladding. This system has already been tested with good results [7]. Another way to proceed uses exactly the same principle as the multi-core fiber, and integrates optical passive waveguides or different types of optics to focus the light beams from each fiber into the single photodiode [14]. One last option is to design several independent photodiodes, to place them close to each other, and to deposit a single common electrode on top of the photodiode array [14]. The precisely same principle can be implemented by enlightening both sides of the same photodiode [14]. Figure 2.5 displays several examples of technological implementation of collecting several optical beams into a single *p-i-n* active area. In every case mentioned above, the combining process is an electronic process. This first group of technological solutions (that we will call “Electronic combining integrated to a single *p-i-n* active region”) is confronted with the problem of space management, limiting intrinsically the number of channels. In addition, this same problem of space obliges to use a large area photodiode which therefore exhibits early bandwidth shortcomings. For instance, in the case of the multi-core fiber with 8 fibers presented on figure

2. High signal-to-noise ratio emitter: discussion on a “system level” point of view

2.5-(a), the bandwidth is limited to 5 GHz [7].

Figure 2.5 Examples of proposed architectures for electronic combining integrated to a photodetector.



(a) Example of several fiber cores mechanically gathered into one 125 μm fiber cladding [14]

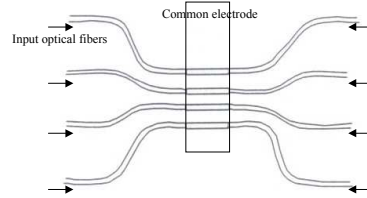
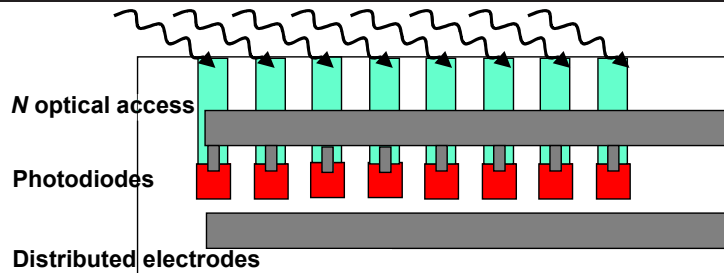


Figure 10: sommateur à 8 voies

(b) Example of architecture using one same electrode for several absorbing *p-i-n* junctions. In addition, both sides of the photodiodes are used [14]

The second group of electronic combining integrated to the photodetector is the following. For N channels, it is also possible to design N photodiodes collecting the light of the N beams. If these photodiodes are monolithically integrated, specifically designed electrodes collect the RF signals and combine them into a single RF integrated waveguide. The RF-frequency-independent combining (for high-bandwidth applications) is achieved with the help of traveling-wave electrodes [15]. Figure 2.6 shows a schematic representation of a traveling-wave array of photodiodes monolithically integrated. There are N optical inputs, and one RF output. This type of architecture is potentially suitable for high-bandwidth applications. It nevertheless requires a specific and more complex electrode design.

Figure 2.6 Schematic representation of a traveling-wave photodetector array [15]



2.2 What does combining mean?

2.2.2.4 Advantages and drawbacks of the different architectures

To put it in a nutshell, the following table lists the advantages and drawbacks of the different combining architectures.

Type of architecture	Advantages	Drawbacks
Electronic combining	<ul style="list-style-type: none"> ✓ available ✓ can be used with any kind of laser/detector 	<ul style="list-style-type: none"> ✓ increase of the insertion losses with the number of channels ✓ bandwidth limitation ✓ volume and weight
In-line optical combining	<p>coupler:</p> <ul style="list-style-type: none"> ✓ low-cost <p>multiplexer:</p> <ul style="list-style-type: none"> ✓ low insertion loss ✓ scalable <p>polarization combiner:</p> <ul style="list-style-type: none"> ✓ low insertion loss ✓ no filtering <p>all three:</p> <ul style="list-style-type: none"> ✓ available, simple 	<p>coupler:</p> <ul style="list-style-type: none"> ✓ requires a polarization control to avoid heterodyne beating noise ✓ limited to 2 channels (in the case of polarization control) ✓ intrinsic 3-dB insertion loss <p>multiplexer:</p> <ul style="list-style-type: none"> ✓ requires a precise and expensive laser wavelength sorting in particular to avoid frequency-to-amplitude noise conversion at the filter edges ✓ specific difficulties such as operation point of the external modulator and/or wavelength dispersion <p>polarization combiner:</p> <ul style="list-style-type: none"> ✓ requires a high-power detector ✓ limited to two channels at a time ✓ expensive architecture ✓ devices that follow should be insensitive to polarization ✓ requires a high-power detector
Electronic combining integrated to the photodetector	<p>single <i>p-i-n</i> active area:</p> <ul style="list-style-type: none"> ✓ optical gathering <p>traveling-wave photodetector:</p> <ul style="list-style-type: none"> ✓ integrated device ✓ can be used with any kind of detector, provided the design of electrode is made accordingly <p>both:</p> <ul style="list-style-type: none"> ✓ can be used with any kind of laser ✓ potentially low-loss ✓ potentially low-noise 	<p>single <i>p-i-n</i> active area:</p> <ul style="list-style-type: none"> ✓ trade-off between bandwidth shortcomings and mechanical limitations <p>traveling-wave photodetector:</p> <ul style="list-style-type: none"> ✓ development cost ✓ needs careful design of electrodes

Table 2.1: Advantages and drawbacks of the different combining architectures

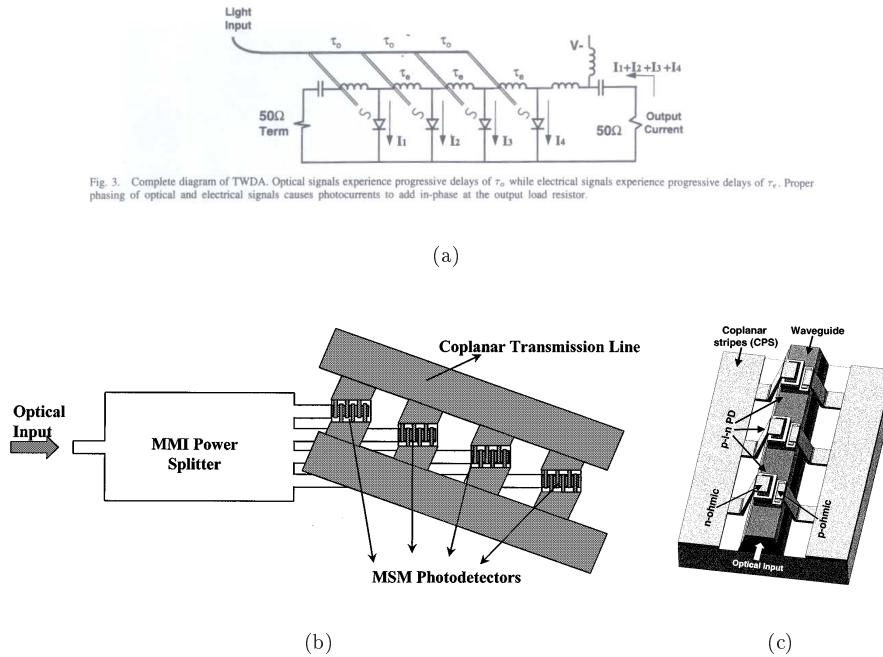
2.2.3 Integrated splitting-to-parallel/combining architectures

Besides this catalogue of combining architectures, we shall also mention opto-electronic devices which integrates both the parallel splitting and the combining process, in order to relax the device constrains.

2.2.3.1 Distributed photodiodes

In order to increase the input power allowable on a single receiver, photodiodes with a distributed absorption region have been proposed [11–13,16–18]. In order to ensure in-phase combining of the detected signals, a traveling-wave electrode needs to be designed. The devices are very similar to already discussed traveling-wave photodetectors, but allow only one input optical signal. This optical signal is first split into several beams that will be absorbed in different regions of the photodiode. The Rf signal signal is the electrically combined with the help of specifically designed electrodes. The splitting of the optical beam can either be achieved before reaching the photodiode (such as in [16] or [18] using a multimode interference (MMI) coupler, see figure 2.7-(a) and -(b)) or integrated to the photodiode by placing several discrete photodiodes along a passive waveguide [17] (see figure 2.7-(c)). This solution is the discrete version of a traveling-wave evanescently- coupled photodiode [11].

Figure 2.7 Example of (a) splitting the optical beam before a photodiode array [16] (b) integration of a MMI coupler with N photodiodes [18] (c) integration of several photodiodes on a single passive waveguide [17]

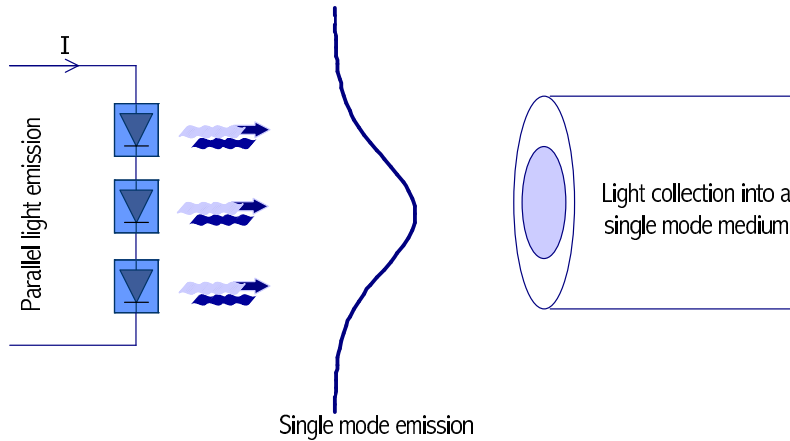


2.3 Combining sources to improve the RF link gain

2.2.3.2 Bipolar cascade lasers

Last, but obviously not least, the device described in details in this thesis (single-transverse-mode BCL) is an excellent example of the integration of a splitting-to-parallel/combining process. Each active region emits light in parallel. The combining of these photons into a single mode is inherent of the modal design of the structure.

Figure 2.8 Principle of optical combining within a single-transverse-mode BCL.



2.3 Combining sources to improve the RF link gain

The purpose of this chapter is to describe the interest of combining for increasing the RF link gain. Since the device we are proposing in this thesis (single-transverse-mode BCL) integrates the optical summation process, we will not discuss the achievability of a low-loss N -to-one optical Y-coupler necessary to benefit from the combining process.

The experiments were carried out with regular optical couplers and the comparison is done under conditions for which the coupler losses are always taken into account (even for a single device laser source).

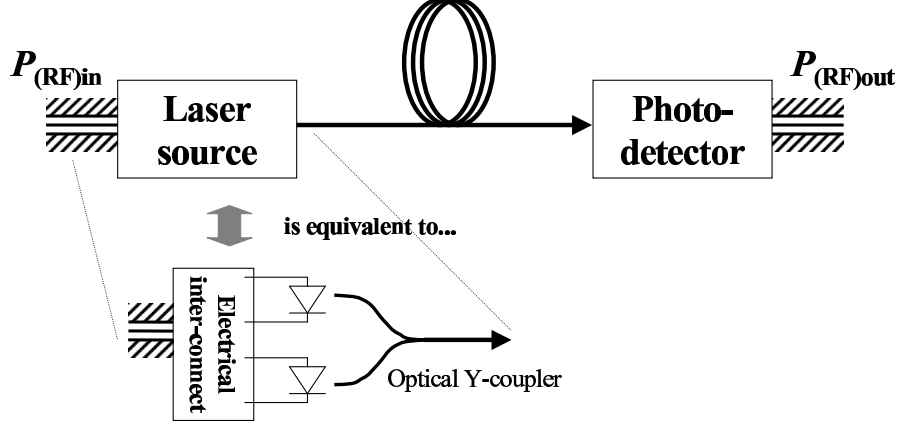
2.3.1 Definitions/Introduction regarding the RF link gain

First, we consider a very simple RF optical link composed of a directly modulated laser source, an optical link, and a photodiode (cf. figure 2.9).

The laser source is composed of N individual lasers coupled to one single optical fiber via a N -to-one Y-coupler. The characteristics of each components are summed up in table 2.2:

2. High signal-to-noise ratio emitter: discussion on a “system level” point of view

Figure 2.9 Schematic of a RF optical transmission link.



Component	Symbol	Characteristic	Dimension
Individual laser	$P_{\text{opt(las)}}$	average power at a given bias current I	W
	η_{las}	differential external efficiency	W/A
	R_{las}	differential series resistance	Ω
Y-coupler	η_{cpl}	losses introduced by the coupler	-
Optical medium	η_{med}	losses introduced by the medium (transmission and coupling losses)	-
Photodiode	η_{phD}	photodetection efficiency	A/W
	R_{phD}	load resistance	Ω

Table 2.2: Main components characteristics

The RF link gain is defined by:

$$g_{\text{RF}} \stackrel{\text{def}}{=} \frac{P_{(\text{RF})\text{out}}}{P_{(\text{RF})\text{in}}} \quad (2.1)$$

$\Leftrightarrow P_{(\text{RF})\text{out}}$ and $P_{(\text{RF})\text{in}}$ are respectively the RF link output RF power, and the input RF power injected.

A high RF link gain indicates that the signal is transmitted with few losses. One decisive advantage of opto-RF links is that this link gain is not significantly altered by an increased fiber length. One drawback however, is that usual non-amplified and non-impedance-matched opto-RF links have a very low RF gain (in the order of -30 dB).

In the following sections, we will discuss on the possible RF link gain improvement achievable with a source-combining architecture. In order to remain coherent when comparing several (sometimes very different) electrical architectures, we will first develop the calculation of the output RF power of the RF link $P_{(\text{RF})\text{out}}$. Afterwards, we will consider the input RF power injected $P_{(\text{RF})\text{in}}$ for different architectures and the RF link gain (and the RF link gain improve-

2.3 Combining sources to improve the RF link gain

ment) will follow. Eventually, we will draw our attention on the experimental validation of the discussion.

2.3.2 RF power at the end of the RF optical link

The electrical RF output power available at the end of the link is carried by the varying current across the photodiode. Due to possible impedance mismatch between the photodiode and the output coplanar RF waveguide, some power gets reflected. We can write:

$$P_{(\text{RF})\text{out}} = (1 - \rho_{\text{phD}}) R_{\text{phD}} \frac{\hat{I}_{\text{phD}}^2}{2}$$

- ☞ ρ_{phD} is the RF power reflection coefficient due to impedance mismatch
- ☞ \hat{I}_{phD} is the amplitude of the photo-current excursion on the photodiode. More generally, we will use the notation \hat{X} for the amplitude excursion of the varying signal X .

Assuming that the conversion from photons to electrons is linear in the photodiode, we write:

$$P_{(\text{RF})\text{out}} = (1 - \rho_{\text{phD}}) \frac{R_{\text{phD}}}{2} \left(\eta_{\text{phD}} \hat{P}_{\text{opt}(\text{phD})} \right)^2$$

The light is transmitted via the optical fiber before illuminating the photodiode. We write:

$$\begin{aligned} P_{(\text{RF})\text{out}} &= (1 - \rho_{\text{phD}}) \frac{R_{\text{phD}}}{2} \eta_{\text{phD}}^2 \eta_{\text{med}}^2 \hat{P}_{\text{opt}(\text{cpl})}^2 \\ &= (1 - \rho_{\text{phD}}) \frac{R_{\text{phD}}}{2} \eta_{\text{phD}}^2 \eta_{\text{med}}^2 \eta_{\text{cpl}}^2 N^2 \hat{P}_{\text{opt}(\text{las})}^2 \end{aligned}$$

Assuming that the optical power emitted is linear with the applied current, we eventually find:

$$P_{(\text{RF})\text{out}} = (1 - \rho_{\text{phD}}) \frac{R_{\text{phD}}}{2} \eta_{\text{phD}}^2 \eta_{\text{med}}^2 \eta_{\text{cpl}}^2 \eta_{\text{las}}^2 N^2 \hat{I}_{\text{las}}^2$$

- ☞ \hat{I}_{las} is the amplitude of the current signal directly applied to the laser.

The noticeable result is the proportionality of the output RF power with the square of the number of lasers and the square of the current signal modulating each individual laser:

$$P_{(\text{RF})\text{out}} \propto N^2 \hat{I}_{\text{las}}^2 \quad (2.2)$$

- ☞ It should be noted that equation 2.2 is valid whatever be the electrical connection scheme. No assumption are made on the laser bias scheme so far.

For RF applications, the same electrical signal must be transmitted to individual lasers of the laser source. Furthermore, to ensure electron-to-photon conversion, a bias current must be applied to each laser. The total current transmitted to the laser therefore consists in two components:

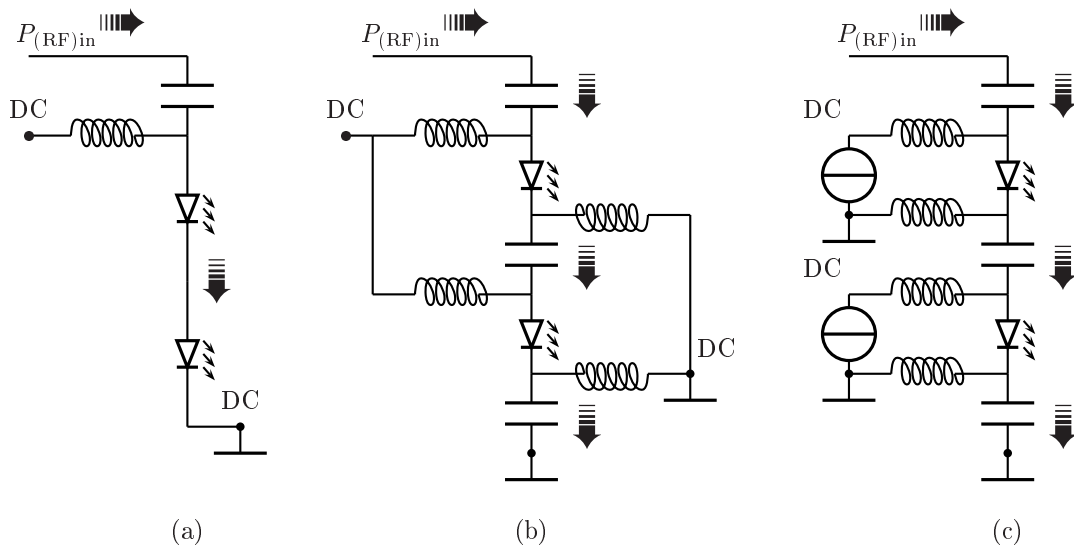
- a DC component that defines the bias point of the laser source,

2. High signal-to-noise ratio emitter: discussion on a “system level” point of view

- an RF component that carries the useful information.

The two components are usually gathered via a bias-T before being injected into the laser. In the case of several individual lasers composing a unique optical source, there are several configurations for injecting the bias components: the DC bias can either come from different DC current sources, or from the same current source. In the latter case, the individual lasers can be electrically connected in parallel or in series. The RF signal however needs to originate from the same source. It can nevertheless be injected in the individual lasers in parallel (via a RF coupler) or in series (in these conditions, the lasers are cascaded). Examples of possible connections are shown on figure 2.10. On figure 2.10-(a), the two components are injected in series in the different lasers, whereas on figure 2.10-(b) the DC component is injected in parallel, while the RF component is injected in series. On figure 2.10-(c) lasers are powered with different DC power sources and the RF component is injected in series.

Figure 2.10 Examples of possible electrical connections



All those cases need to be discussed in detail. Nevertheless, within a linear range, the RF link gain does not depend on the bias point (only on the RF signal amplitude), and therefore does not depend on the DC bias scheme. On the contrary, the equivalent Relative Intensity Noise (RIN) of the laser source strongly depends on the DC bias. As we will see in section 2.4.2, the DC bias scheme carries some interest for the estimation of the equivalent RIN of the combining source.

2.3 Combining sources to improve the RF link gain

2.3.3 Estimation of the RF gain improvement

The purpose is now to use equation 2.1 to estimate the gain improvement we can get from cascading lasers. In order to do so, we need the expression of the input RF power as a function of the current signal \hat{I}_{las} of each individual laser. This amplitude strongly depends on the electrical connection scheme and more precisely on the connection scheme of the RF signal (whether the DC bias is supplied by a single, or by a set of power sources is not a relevant question for the moment). It is also very dependent on the impedance matching scheme. It is interesting to compare series-connected lasers with parallel-connected lasers for three different impedance matching schemes: no impedance matching, a resistive impedance matching and a reactive impedance matching. To carry out the comparison, we will assume that lasers have only parasitic resistive differential impedance and no other parasitic impedance.

2.3.3.1 No impedance matching

Series-connected lasers: While injecting the RF input power $P_{(\text{RF})\text{in}}$, a part of the electrical RF power gets reflected due to impedance mismatch (namely $\rho_{\text{source}}P_{(\text{RF})\text{in}}$) and only $(1 - \rho_{\text{source}})P_{(\text{RF})\text{in}}$ is useful for information transmission. We then write:

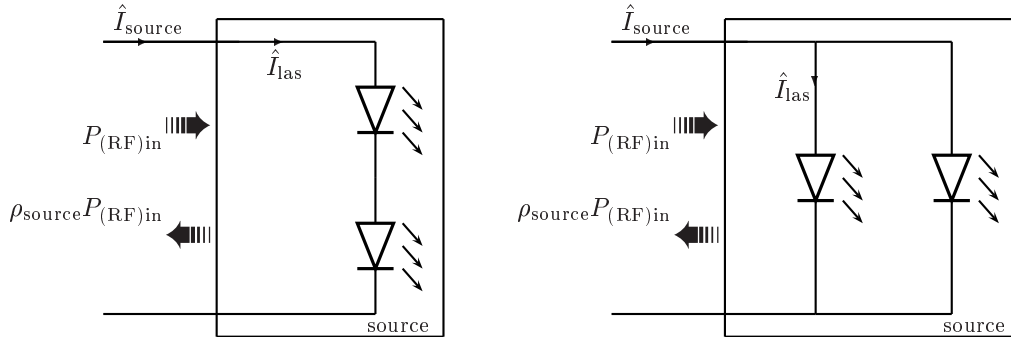
$$(1 - \rho_{\text{source}}) P_{(\text{RF})\text{in}} = \frac{R_{\text{source}}}{2} \hat{I}_{\text{source}}^2$$

☞ The variables ρ stand for the RF power reflection coefficient due to impedance mismatch.

Which gives, accordingly to figure 2.11:

$$P_{(\text{RF})\text{in}} = \frac{R_{\text{las}}}{2} \frac{N}{(1 - \rho_{\text{source}})} \hat{I}_{\text{las}}^2$$

Figure 2.11 Electronic scheme of a (a) series-connected and (b) parallel-connected laser source with no impedance matching



2. High signal-to-noise ratio emitter: discussion on a “system level” point of view

Following equation 2.1 and equation 2.2, the RF link gain becomes:

$$g_{\text{RF}} = \frac{P_{(\text{RF})\text{out}}}{P_{(\text{RF})\text{in}}} \propto (1 - \rho_{\text{source}}) N$$

☞ ρ_{source} is characteristic of the impedance mismatch between the laser and the coplanar RF waveguide.

☞ In these conditions, it can be written as: $\rho_{\text{source}} = \left| \frac{NR_{\text{las}} - Z_0}{NR_{\text{las}} + Z_0} \right|^2$ where $Z_0 = 50 \Omega$ is the characteristic impedance of the coplanar waveguide.

We can eventually write the RF gain improvement obtained by the use of a composed laser source:

$$\Delta g_{\text{RF}} = \frac{g_{\text{RF}(N \text{ las})}}{g_{\text{RF}(1 \text{ las})}} = \frac{1 - \rho_{\text{series}}}{1 - \rho_{\text{las}}} N \quad (2.3)$$

Parallel-connected lasers: In the case of parallel-connected lasers, an impedance mismatch also occurs and implies power losses by reflection. We write as well:

$$\begin{aligned} (1 - \rho_{\text{source}}) P_{(\text{RF})\text{in}} &= \frac{R_{\text{source}}}{2} \hat{I}_{\text{source}}^2 \\ P_{(\text{RF})\text{in}} &= \frac{R_{\text{las}}}{2N(1 - \rho_{\text{source}})} \left(N \hat{I}_{\text{las}} \right)^2 \\ P_{(\text{RF})\text{in}} &= \frac{R_{\text{las}}}{2} \frac{N}{1 - \rho_{\text{source}}} \hat{I}_{\text{las}}^2 \end{aligned}$$

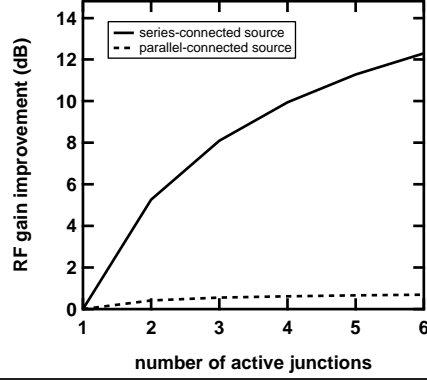
The expression of the input RF signal power is the same as in the case of series-connected lasers, but the reflection coefficient is higher. The parallel connection scheme will indeed decrease the already very low laser source impedance ($R_{\text{las}} \simeq 5 \Omega$). The improvement of the RF link gain is written:

$$\Delta g_{\text{RF}} = \frac{g_{\text{RF}(N \text{ las})}}{g_{\text{RF}(1 \text{ las})}} = \frac{1 - \rho_{\parallel}}{1 - \rho_{\text{las}}} N$$

Comparison: Figure 2.12 displays the comparison of the expected RF gain improvement for a parallel-connected source and for a series-connected source. The series-connection of lasers with a small impedance (in the order of 5Ω) improves the impedance matching. On the other hand, if no additional impedance matching is employed, the increasing mismatch with the parallel-connection configuration almost annihilate the improvement due to the summation process.

2.3 Combining sources to improve the RF link gain

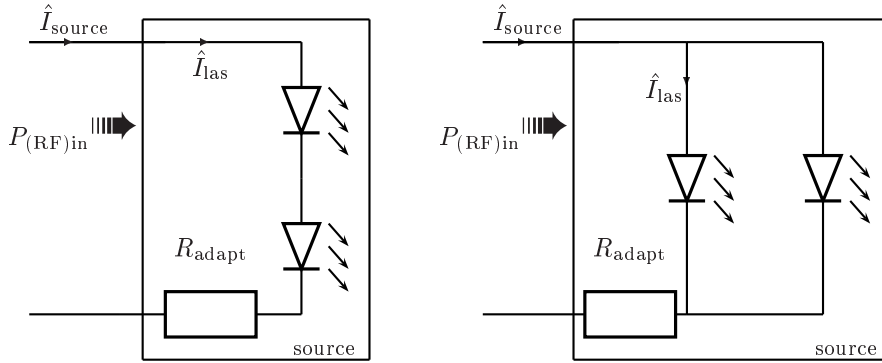
Figure 2.12 Comparison of expected RF gain improvement with N lasers connected in series, and in parallel, as compare to a single laser



2.3.3.2 Resistive impedance matching

For high-bandwidth applications, the impedance matching is usually obtained with a purely passive (resistive) scheme [19].

Figure 2.13 Electronic scheme of a (a) series-connected and (b) parallel-connected laser source with a resistive impedance matching



The laser is connected to a simple resistance which value is calculated to match 50Ω . In these conditions, we can assume that no RF power is reflected. The input RF power for the series-connected lasers is written:

$$\begin{aligned} P_{(RF)in} &= \frac{R_{source}}{2} \hat{I}_{source}^2 \\ &= \frac{Z_0}{2} \hat{I}_{las}^2 \end{aligned}$$

Which gives the RF link gain improvement:

$$\Delta g_{RF} = \frac{g_{RF(N \text{ las})}}{g_{RF(1 \text{ las})}} = N^2 \quad (2.4)$$

2. High signal-to-noise ratio emitter: discussion on a “system level” point of view

The RF link gain increase in the series-type source case is proportional to N^2 . The source behaves equivalently to a single laser with a differential efficiency increased by a factor of N .

For the parallel-connection scheme, we write as well:

$$\begin{aligned} P_{(\text{RF})\text{in}} &= \frac{R_{\text{source}}}{2} \hat{I}_{\text{source}}^2 \\ &= \frac{Z_0}{2} N^2 \hat{I}_{\text{las}}^2 \end{aligned}$$

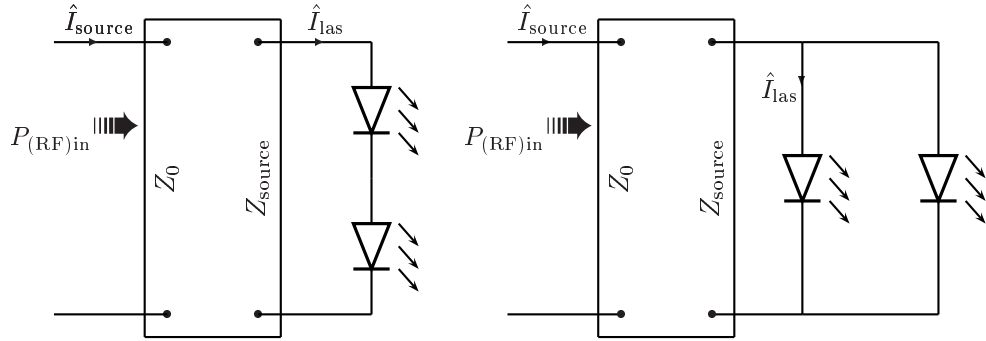
$P_{(\text{RF})\text{in}}$ as well as $P_{(\text{RF})\text{out}}$ is proportional to N^2 , proving that in these conditions the RF link gain is exactly the same whatever the number of series-connected lasers:

$$\Delta g_{\text{RF}} = 0 \text{ dB!}$$

The gain of the parallel-type source does not change with N . The RF power is spread among the different individual lasers, and recombined again, through the optical combining process.

2.3.3.3 Reactive impedance matching

Figure 2.14 Electronic scheme of a (a) series-connected and (b) parallel-connected laser source with a reactive impedance matching



For very specific narrow-band applications [20], it is sometimes required to match the components impedance using a reactive impedance matching scheme. In these conditions, the low laser impedance is a good advantage from which we must take benefit. In the series-case, the input RF power is written as:

$$\begin{aligned} P_{(\text{RF})\text{in}} &= \frac{NR_{\text{las}}}{2} \hat{I}_{\text{source}}^2 \\ &= \frac{R_{\text{las}}}{2} N \hat{I}_{\text{las}}^2 \end{aligned}$$

The improvement on the RF link gain derives:

$$\Delta g_{\text{RF}} = \frac{g_{\text{RF}(N \text{ las})}}{g_{\text{RF}(1 \text{ las})}} = N$$

2.3 Combining sources to improve the RF link gain

The parallel-connected laser source carries an input power of:

$$\begin{aligned} P_{(\text{RF})\text{in}} &= \frac{R_{\text{las}}}{2N} \hat{I}_{\text{source}}^2 \\ &= \frac{R_{\text{las}}}{2} N \hat{I}_{\text{las}}^2 \end{aligned}$$

This gives the same RF link gain improvement:

$$\Delta g_{\text{RF}} = \frac{g_{\text{RF}(N \text{ las})}}{g_{\text{RF}(1 \text{ las})}} = N$$

In the case of reactive impedance matching, the RF link gain improvement is the same for both types of electrical connection and scales linearly with N . However the reactive impedance matching will be all the more complicated and all the narrower (in terms of transmission bandwidth), as the series resistance of the laser source is low. Once again, the series-connected source is preferable to the parallel-type.

To put it in a nutshell, table 2.3 summarizes the RF link gain improvement Δg_{RF} for the different connection schemes and impedance matching architectures. For the three case-studies, a series-connection scheme is always preferable to a parallel-connection scheme. Furthermore, a RF link gain improvement proportional to N^2 is very attractive since it can theoretically achieve a 12 dB improvement with the use of 4 lasers, compared to a single-laser source.

	RF link gain improvement	
	series-connection scheme	parallel-connection scheme
no impedance matching	$\frac{1 - \rho_{\text{series}}}{1 - \rho_{\text{las}}} N$	$\frac{1 - \rho_{\parallel}}{1 - \rho_{\text{las}}} N$
resistive impedance matching	N^2	1
reactive impedance matching	N	N

Table 2.3: Summary of the predicted RF link gain improvement for different configurations

2.3.4 Compression point

Despite the arguments in favor of using the series-type connection, we may wonder at this point whether the parallel-type laser source does not have at least the advantage of presenting a higher compression point.

The input (resp. output) compression point is defined as the *maximum input (resp. output) RF power for which the response is linear*. Below the compression point, we can write:

$$P_{(\text{RF})\text{out}} = g_{\text{RF}} P_{(\text{RF})\text{in}}$$

⇨ Notice that g_{RF} is not dependent on $P_{(\text{RF})\text{in}}$.

For usual optical links, the laser response generally limits the linearity of the link response: up to a certain excursion $\hat{I}_{(\text{las})\text{max}}$, we have $\hat{P}_{(\text{las})\text{out}} < \eta_{\text{las}} \hat{I}_{\text{las}}$. If we are limited to a current amplitude $\hat{I}_{(\text{las})\text{max}}$ on each individual lasers, connecting N lasers in parallel permits to inject $\hat{I}_{(\text{source})\text{max}} = N \hat{I}_{(\text{las})\text{max}}$, as can be seen from figure 2.11, figure 2.13, and figure 2.14. The input compression point actually increases in this case by a factor of N^2 .

On the other hand, we have seen (c.f. equation 2.2) that the output power can be written in terms of \hat{I}_{las} independently of the electrical connection, or of the impedance matching scheme. As a consequence, since the limiting term is the laser current amplitude \hat{I}_{las} , the output compression point is the same for the series and the parallel-connection scheme. In other words, less RF power can be injected in the series-connected laser source, but in any case, the maximum output power will be the same.

Last but not least, even for parallel-like electrical connection, the last remark shows that the output compression point increases by a factor of N^2 . If only signal-to-noise ratio is considered, the parallel architecture is also interesting, as can be seen in reference [21].

2.3 Combining sources to improve the RF link gain

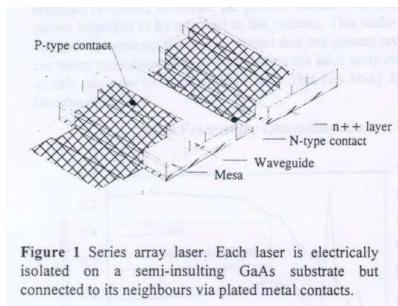
2.3.5 A range of technological options available from literature

The literature contains several technological solutions for cascading (series-connecting) laser sources in order to improve the RF link gain.

The proposed solutions can be categorized followingly:

1. Multiple Cavity Cascade Lasers (MCCL): separate laser cavities are electrically connected in series [1, 22, 23]. It can either be laser arrays [22, 23] electrically connected via a technological process on a single wafer, or separate laser modules [1] externally connected. As was already explained in section 2.2, the main problem to fix is coupling the light from different sources into one single medium. Specific optical coupling scheme need to be developed, such as specific optics, or devices to collect all the light into a single wide area photodiode [1, 14].

Figure 2.15 Examples of MCCLs.



(a) Proposed by Ayling *et al.* [22]

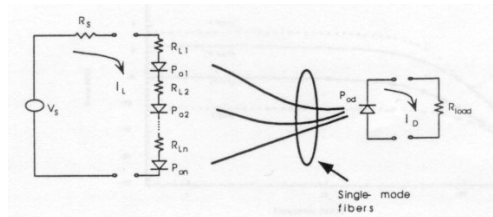


Fig. 1 Directly-modulated analog link with series-connected lasers

(b) Proposed by Cox *et al.* [1]

2. Split Waveguide Cascade Laser (SWCL): one single laser ridge is longitudinally segmented. Each segment is electrically isolated from the other ones. Metallic connections enable the cascading of each section [22, 24]. The main technological hurdle is the electrical isolation (passivation) of the different segments [22].

Figure 2.16 Architecture proposed by Ayling *et al.*, and Getty *et al.* [22, 24, 25]

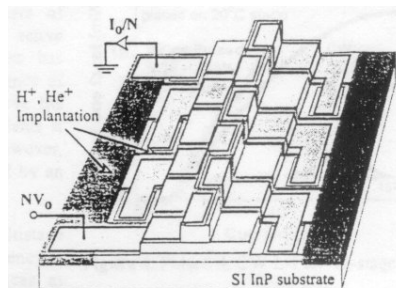


Figure 1. Series-connected, segmented laser

2. High signal-to-noise ratio emitter: discussion on a “system level” point of view

3. Bipolar Cascade Laser (BCL): the active junctions are epitaxially stacked. Highly-doped $p++/n++$ tunnel junctions ensure the series electrical cascading [26–29]. The device BCL is the general subject of this thesis. The main technological difficulties to overcome (such as the low loss, low resistivity tunnel junction design) are largely discussed in chapter 4. As already mentioned in the general introduction, there are two types of BCL. The first type caters to high power applications and usually consists in laser cavities separated by more than $1 \mu\text{m}$ and therefore optically uncoupled (cf. figure 2.17-(a,b)) [26–28, 30]. The second type focuses on RF applications. The active junctions are optically coupled into one single cavity (cf. figure 2.17-(c)) [29].

Figure 2.17 Example of bipolar cascade lasers.

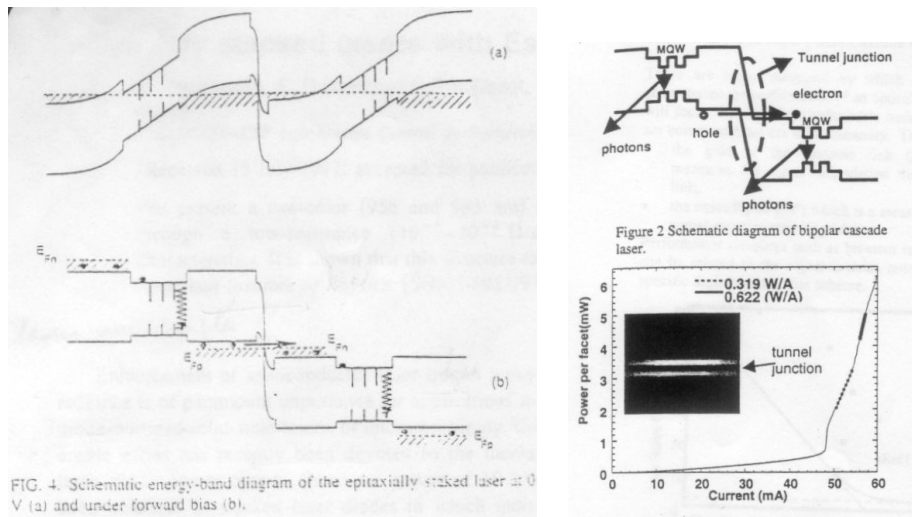


FIG. 4. Schematic energy-band diagram of the epitaxially stacked laser at 0 V (a) and under forward bias (b).

Figure 2 Schematic diagram of bipolar cascade laser.

(a) A BCL proposed by Garcia *et al.* [26]

(b) A BCL proposed by Patterson *et al.* [28]

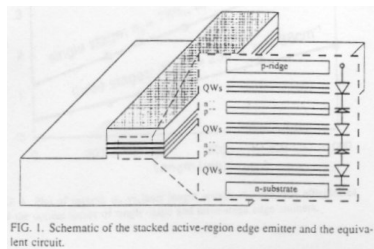


FIG. 1. Schematic of the stacked active-region edge emitter and the equivalent circuit.

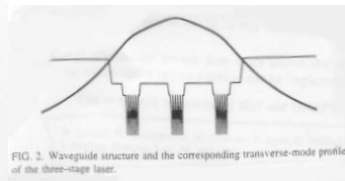


FIG. 2. Waveguide structure and the corresponding transverse-mode profile of the three-stage laser.

(c) A BCL proposed by Kim *et al.* [29]

2.3 Combining sources to improve the RF link gain

2.3.5.1 Experimental results from the literature

In this section, we have summed up the different results available from the literature. Some articles display the experimental equivalent external efficiency and series resistance of the laser source composed of individual lasers. Once we have gathered these features, we compile the values into the gain improvement calculation described in section 2.3.3 without impedance matching, and with a resistive impedance matching.

The equivalent external differential quantum efficiency (DQE) is plotted on figure 2.18. If N lasers are connected in series, the same current is N times recycled. The external differential efficiency is therefore expected to increase linearly with the number of cascaded individual lasers. This prediction is well confirmed experimentally, as shown on figure 2.18.

Figure 2.18 Equivalent external efficiency, and series resistance found in the literature for laser sources composed of cascaded individual lasers. The DQE is normalized compared to the value obtained with the same technology for a single laser source.

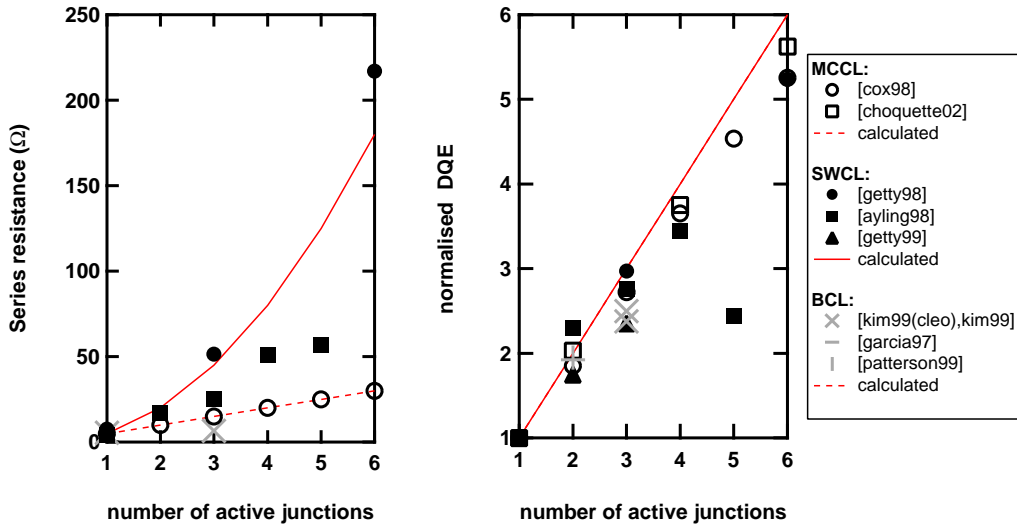


Figure 2.18 also displays the series differential resistance of the laser sources. For MCCL, the series resistance is expected to scale linearly with N . For BCL, the series resistance can be written as:

$$R_{BCL} = R_{\text{contacts}} + NR_{\text{semiconductor layers}} + (N - 1)R_{\text{tunnel}}$$

- ⊞ R_{contact} is the series resistance of the metal-semiconductor contacts.
- ⊞ $R_{\text{semiconductor layers}}$ include the series resistance of the heterojunctions' interfaces, and the resistivity of the semiconductor layers of a single-junction laser.
- ⊞ R_{tunnel} is the series resistance of the stacked highly-doped junction.

If we assume that the semiconductor resistance $R_{\text{semiconductor layers}}$ is negligible compared to the contact resistance R_{contact} , and that the series resistance

of the tunnel junction has the same magnitude as the series resistance of the laser device ($\approx 5 \Omega$), we may also expect the series resistance to increase linearly with N . The last assumption has to be justified experimentally. We describe in detail an accurate method for the estimation of the resistance of a tunnel junction in chapter 4.

For SWCL however, the length of the cavity remains constant while increasing the number of segments. The increase of the number of segments therefore divides the contact electrode area. For a given resistivity, the in-line resistance will therefore increase (geometrically) by a factor of N . Furthermore, the number of series resistance is N times increased as well. The series resistance of the device is then expected to scale with N^2 .

As can be seen from Figure 2.18, the experimental values fit well with the expected values. It should be noted that for literature available values for the BCL architecture, the series resistance increases slower than the number of cascaded regions.

2.3.5.2 Estimation of the RF gain improvement

We may now use these figures to estimate the RF link gain one should experimentally obtain by building an optical link with the cited laser source architectures.

No impedance matching We first estimate the RF gain improvement with no impedance matching. From equation 2.3, we write the link gain improvement:

$$\Delta g_{\text{RF}} = \frac{1 - \rho_{\text{source}}}{1 - \rho_{\text{las}}} \left(\frac{\eta_{\text{source}}}{\eta_{\text{las}}} \right)^2$$

Injecting the literature available series resistance and differential efficiency in the previous relation, we compare on figure 2.19 the gain improvement for the different architectures.

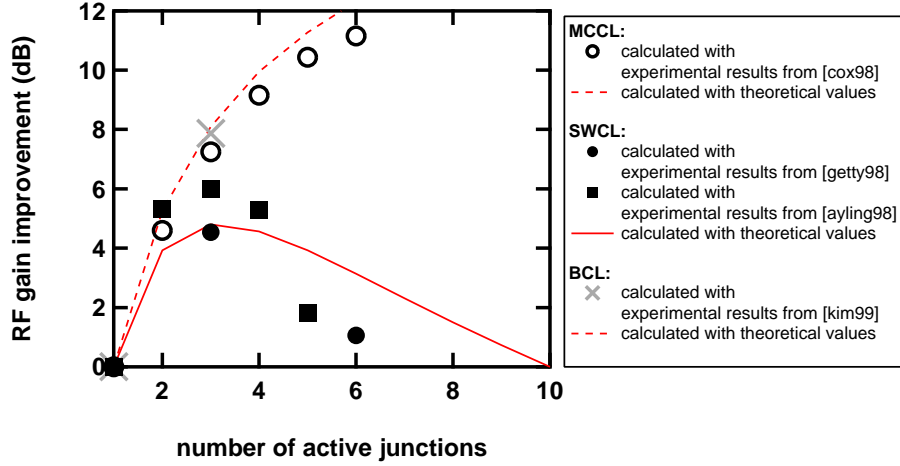
It should be noted (even if already mentioned) that these are not experimental measurements. Very few direct link gain measurements can be found in literature, but when available, direct measurements are similar to our calculations [1].

For SWCL devices, the increase in the series resistance dramatically predominates and annihilates the effect of current cascading for more than 3 segments. MCCL and BCL provide however a monotone improvement of the RF link gain up to 6 active junctions (even 10 in [1]). The higher gain increase with a monolithic device (+8 dB) is obtained by Kim *et al.* [29] with a BCL.

We should also carry out the same comparison for a resistive impedance matching scheme, since it is the usual scheme used in systems.

2.3 Combining sources to improve the RF link gain

Figure 2.19 Gain improvement for different technological architectures with no impedance matching, calculated from characteristics available in literature.



Resistive impedance matching While $Z_{\text{source}} < Z_0$, a resistive impedance matching is obtained by adding a series resistance $Z_0 - Z_{\text{source}}$. The gain improvement follows the rule given by equation 2.4. For SWCL devices of more than 3 segments, the impedance is higher than Z_0 . The resistive impedance matching is obtained with a resistance in parallel with the device such as

$$Z_{\text{adapt}} = \frac{Z_0 Z_{\text{source}}}{Z_0 + Z_{\text{source}}}$$

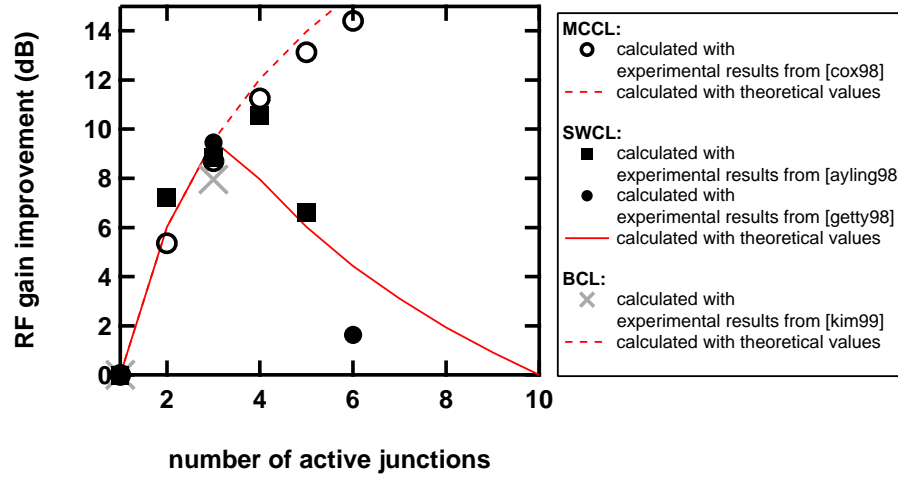
As a consequence, only a portion of \hat{I}_{source} will actually be available for information transmission. We therefore derive the available current and the gain improvement for each architecture:

$$\begin{aligned} \text{if } Z_{\text{source}} \leq Z_0, \quad \Delta g_{\text{RF}} &= \left(\frac{\eta_{\text{source}}}{\eta_{\text{las}}} \right)^2 \\ \text{if } Z_{\text{source}} > Z_0, \quad \Delta g_{\text{RF}} &= \frac{Z_0^2}{Z_{\text{source}}^2} \left(\frac{\eta_{\text{source}}}{\eta_{\text{las}}} \right)^2 \end{aligned}$$

Compiling this equation with literature available data, we compare on figure 2.20 the expected gain improvement for each architecture.

The use of literature available components in systems displays the same tendency for resistive as for no impedance matching. While the RF gain improvement increases in a monotone way with the number of active regions for MCCL and BCL structures, it reaches a maximum value for SWCL for about 3 active regions. Beyond, the increasing mismatch inhibits the RF gain improvement.

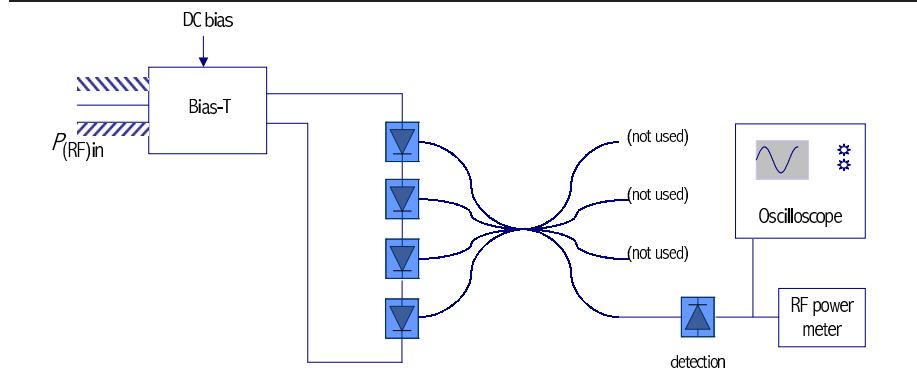
Figure 2.20 Gain improvement for different technological architectures with a resistive impedance matching, calculated from characteristics available in literature.



2.3.6 Experimental achievements

The previous results are obtained via literature available characteristics of the laser sources (η_{las} , R_{las}). In order to prove the possible RF link gain improvement reachable with a series-connection architecture, we have used four commercially available butterfly module DFB lasers and connected them in series. Figure 2.21 displays a schematic of the experimental set-up, while a picture of the laser series-connection can be seen on figure 2.22-(a).

Figure 2.21 Experimental set-up for measuring the RF link gain improvement with the use of a combining laser source

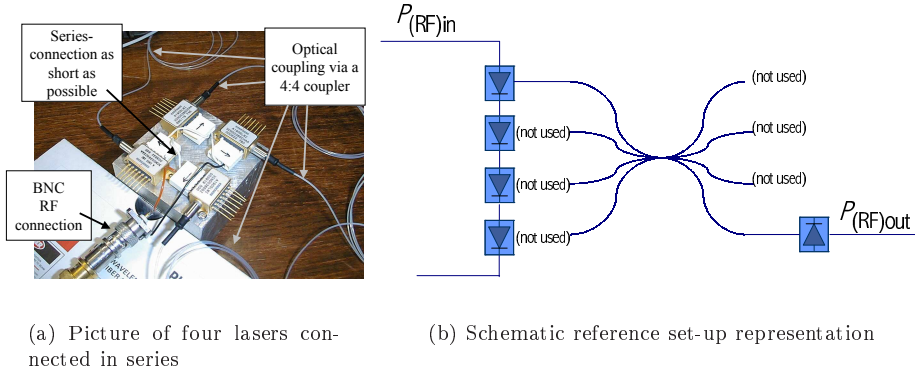


The modulated light beams are gathered via a 4:4 optical coupler. In order to estimate the benefit of the combining process, we took as a reference the opto-RF link described in figure 2.22-(b). Since the reflected input RF power (and thus the RF power transferred to an optical modulation) depends on the overall

2.3 Combining sources to improve the RF link gain

source impedance, we have chosen to keep the same electrical connection even for the single-laser source. Each laser module have a built-in 20Ω resistance connected in series with the laser. The overall impedance was therefore close to 100Ω . The laser outputs were plugged and unplugged to the optical coupler in order to simulate a 1,2,3,4-laser source with the same electrical impedance. Furthermore, the insertion loss of the optical coupler (energy lost in the arm not used) are regarded as transmission losses and kept the same for single-laser source and for several-laser sources.

Figure 2.22 Set-up for measuring the RF link gain improvement.



We injected $P_{(RF)in} = 0$ dBm at 80 MHz and measured $P_{(RF)out}$ with an electrical spectrum analyzer. The optical power transmitted by each laser was not exactly the same, probably due to different lasers characteristics, different effective impedance load, or different transmission loss in the coupler's arms. For each source type (1-laser, 2-laser, 3-laser and 4-laser), we measured the RF output power with several possible configurations (e.g. laser 1+laser 2, laser 1+laser 3, etc. for the 2-laser configuration). In table 2.4, we present the average output power obtained for each laser source type and the RF link improvement measured and calculated compared to the single-laser source.

	$P_{(RF)out}$ (dBm)	measured improvement (dB)	calculated improvement (dB)
1 laser (ref.)	-46.0	0	0
2 lasers	-40.2	5.8	6.0
3 lasers	-36.9	9.1	9.5
4 lasers	-34.3	11.7	12

Table 2.4: RF output power for different configurations in absolute value and relatively to the output power for the single-laser source

Although the absolute value of the link gain is quite low, the measured improvement matches perfectly the expected values. The link gain was improved by almost 12 dB with the combining of four lasers.

2.4 Combining sources for improving the RF link noise figure

2.4.1 About the noise factor of a complex laser source

Another important system-level RF link characteristic is the noise figure, defined by:

$$NF \stackrel{\text{def}}{=} \frac{P_{(\text{RF})\text{in}}/P_{(\text{noise})\text{in}}}{P_{(\text{RF})\text{out}}/P_{(\text{noise})\text{out}}} \quad (2.5)$$

⇨ $P_{(\text{noise})}$ are electrical noise power at the frequency nearby the signal frequency

The noise figure describes the degradation of the signal-to-noise ratio (SNR) during the signal transmission through the studied link. The noise usually originates from the laser source relative intensity noise which is defined in a Δf bandwidth by [31]:

$$RIN \stackrel{\text{def}}{=} \frac{\langle \delta P_{(\text{opt})\text{las}}^2 \rangle - 2h\nu\Delta f \langle P_{(\text{opt})\text{las}} \rangle}{\langle P_{(\text{opt})\text{las}} \rangle^2} \quad (2.6)$$

⇨ $\langle \rangle$ stands for time average, but is equivalent to statistical average in this context (phenomena are supposed ergodic).

Usual non-amplified and non-impedance-matched opto-RF links have typical noise figure in the order of 40 dB. This figure is actually one of the most limiting factor for spreading opto-RF technologies in radar systems. In order to be competitive with electrical RF technologies, the noise figure should approximately be reduced to 10 dB.

Below the compression point, we can write:

$$g_{\text{RF}} = \frac{P_{(\text{RF})\text{out}}}{P_{(\text{RF})\text{in}}} \quad (2.7)$$

$$P_{(\text{noise})\text{out}} = g_{\text{RF}} P_{(\text{noise})\text{in}} + P_{(\text{noise})\text{link}} \quad (2.8)$$

If we assume that the link noise originates mainly from the laser source, we can write:

$$\begin{aligned} P_{(\text{noise})\text{link}} &\propto \langle \delta P_{(\text{opt})\text{las}}^2 \rangle \\ &\propto RIN \langle P_{(\text{opt})\text{las}} \rangle^2 + 2h\nu\Delta f \langle P_{(\text{opt})\text{las}} \rangle \end{aligned} \quad (2.9)$$

⇨ The factor of proportionality arises from the conversion of the modulated optical beam to modulated electrical current in the photodiode. It is more precisely described in chapter 3.

At high optical output power (generally above a few mW), the shot noise contribution to $P_{(\text{noise})\text{link}}$ term of equation 2.9 is negligible compared to the RIN contribution.

Combining equations 2.5, 2.7, 2.8, 2.9, for high optical output power, we find that the noise figure can be written as:

$$NF = 1 + \frac{\alpha RIN \langle P_{(\text{opt})\text{source}} \rangle^2}{g_{\text{RF}} P_{(\text{noise})\text{in}}} \quad (2.10)$$

2.4 Combining sources for improving the RF link noise figure

☞ α is a factor of proportionality.

We see from equation 2.10, that an increase of the RF link gain or a decrease of the laser RIN (independently of the average optical power on the photodiode) improves the RF link noise figure.

It has been clearly shown in the previous section that using a multiple-laser source enables to improve the RF link gain. The RF noise figure will obviously benefit from the gain improvement providing that the equivalent RIN of the laser source does not increase dramatically. According to the literature [32], the RIN of multi-mode laser arrays is lower than the RIN of individual multi-mode sources. This section aims at demonstrating the possible RIN improvement that could benefit from the several-single-mode-laser source architectures that we have previously described. Therefore we will now estimate the equivalent RIN of a N -lasers source in comparison with individual lasers' RIN. In order to do so, we will focus on different electrical architectures. Eventually, we will confirm the model with experimental measurements.

2.4.2 Equivalent RIN source

Let us consider N lasers at a given bias current. According to equation 2.6, the relative intensity noise of each individual laser RIN_{las} is given as a function of their average optical output power $\langle P_{(\text{opt})\text{las}} \rangle$. The equivalent RIN of the source composed of N lasers (as shown for instance on figure 2.1, page 24) writes as well:

$$RIN_{\text{source}} = \frac{\langle \delta P_{(\text{opt})\text{source}}^2 \rangle - 2h\nu\Delta f \langle P_{(\text{opt})\text{source}} \rangle}{\langle P_{(\text{opt})\text{source}} \rangle^2} \quad (2.11)$$

Assuming all the photons are gathered with no loss before detection, we write:

$$\begin{aligned} \forall t, \quad \delta P_{(\text{opt})\text{source}}(t) &= \delta P_{(\text{opt})\text{las1}}(t) + \delta P_{(\text{opt})\text{las2}}(t) + \dots + \delta P_{(\text{opt})\text{lasN}}(t) \\ \forall t, \quad P_{(\text{opt})\text{source}}(t) &= P_{(\text{opt})\text{las1}}(t) + P_{(\text{opt})\text{las2}}(t) + \dots + P_{(\text{opt})\text{lasN}}(t) \end{aligned}$$

Inserting the sum into equation 2.11, the RIN source derives as follows:

$$RIN_{\text{source}} = \frac{\langle \left(\sum_{i=1}^N \delta P_{(\text{opt})\text{las}i} \right)^2 \rangle - 2h\nu\Delta f \langle \sum_{i=1}^N P_{(\text{opt})\text{las}i} \rangle}{\langle \sum_{i=1}^N P_{(\text{opt})\text{las}i} \rangle^2}$$

We now assume that all lasers have the same characteristics:

$$\begin{aligned} RIN_{\text{source}} &= \frac{N \langle \delta P_{(\text{opt})\text{las}}^2 \rangle + 2 \frac{N(N-1)}{2} \langle \delta P_{(\text{opt})\text{las}i} \delta P_{(\text{opt})\text{las}j} \rangle - 2N h\nu\Delta f \langle P_{(\text{opt})\text{las}} \rangle}{N^2 \langle P_{(\text{opt})\text{las}} \rangle^2} \\ &= \frac{1}{N} RIN_{\text{las}} + \frac{N-1}{N} \frac{\langle \delta P_{(\text{opt})\text{las}i} \delta P_{(\text{opt})\text{las}j} \rangle}{\langle P_{(\text{opt})\text{las}} \rangle^2} \end{aligned} \quad (2.12)$$

☞ The second term is representative of the inter-correlation of the noise signals of the different lasers.

If the inter-correlation term is weak, the equivalent RIN of the source scales almost linearly with $\frac{1}{N}$: the signal combines coherently (in power), whereas the noise combines not coherently.

2.4.2.1 Inter-correlation term

Assuming the laser noise is far above the shot noise, the inter-correlation term writes:

$$\begin{aligned}
 RIN_{\text{source}} &= \frac{1}{N}RIN_{\text{las}} + \frac{N-1}{N}C_{i,j}RIN_{\text{las}} & (2.13) \\
 C_{i,j} &= \frac{\langle \delta P_{(\text{opt})\text{las}i} \delta P_{(\text{opt})\text{las}j} \rangle}{\langle \delta P_{(\text{opt})\text{las}}^2 \rangle} \\
 &= \begin{cases} 1 & \text{if } \forall t, \delta P_{(\text{opt})\text{las}i}(t) = \delta P_{(\text{opt})\text{las}j}(t), \\ -1 & \text{if } \forall t, \delta P_{(\text{opt})\text{las}i}(t) = -\delta P_{(\text{opt})\text{las}j}(t), \\ 0 & \text{if } \delta P_{(\text{opt})\text{las}i} \text{ and } \delta P_{(\text{opt})\text{las}j} \text{ are not correlated} \end{cases}
 \end{aligned}$$

This inter-correlation term arises if the noise signals from the different optical sources are correlated. In the case of several laser cavities, the laser modes are not optically coupled, each laser being protected against feedback by an optical isolator. The inter-correlation term cannot have an optical origin. However, the lasers may be electrically linked to each others, and these connections can favor correlation (or anticorrelation): a photon burst in one laser will give rise to a carrier recombination burst and thus a current burst in all the electrical connections. If the lasers are connected in series, the burst will flow through each cascaded laser, giving rise to a strong correlation. On the other hand, if the lasers are connected in parallel, the burst in one arm will create an “antiburst” in the other arms, giving rise to anti-correlation.

In order to deepen the understanding of the correlation processes, we model the laser intensity noise as a noisy laser impedance:

$$r(t) = \langle r(t) \rangle + \delta r(t)$$

We assume in addition that the variations of the laser impedance (of characteristic time τ) are slow compared to the electronic relaxation times, so that:

$$\begin{aligned}
 \forall t, v(t) &= r(t) \times i(t) \\
 \tau &\gtrsim 50 \text{ ps}
 \end{aligned}$$

⇔ The value given for τ gives an order of magnitude, and corresponds approximately to intracavity carrier recombination times.

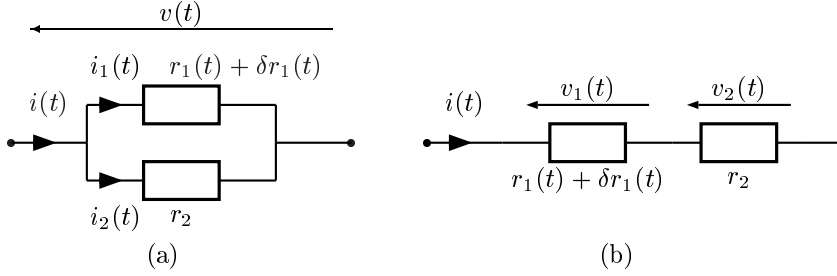
We consider two lasers connected in parallel and powered by a DC current bias:

$$i(t + \tau) = i(t)$$

Notations are described on figure 2.23.

2.4 Combining sources for improving the RF link noise figure

Figure 2.23 Noisy impedance model for the parallel- (a), and series-connection architecture (b)



If at some time t :

$$\begin{cases} r_1(t + \tau) > r_1(t) \\ r_2(t + \tau) = r_2(t) = r_2 \end{cases}$$

then:

$$\begin{cases} i_1(t + \tau) = \frac{r_2}{r_1(t + \tau) + r_2} i(t + \tau) < \frac{r_2}{r_1(t) + r_2} i(t) = i_1(t) \\ i_2(t + \tau) = i(t + \tau) - i_1(t + \tau) > i(t) - i_1(t) = i_2(t) \end{cases}$$

proving that an impedance variation of laser 1 gives rise to a current variation through laser 2. Furthermore, the current variation in laser 1 and laser 2 are anti-correlated ($C_{i,j} < 0$).

We now consider two lasers connected in parallel as well, but powered by a DC voltage bias:

$$v(t + \tau) = v(t)$$

If at some time t :

$$\begin{cases} r_1(t + \tau) > r_1(t) \\ r_2(t + \tau) = r_2(t) = r_2 \end{cases}$$

then:

$$\begin{cases} i_1(t + \tau) = \frac{v(t + \tau)}{r_1(t + \tau)} < \frac{v(t)}{r_1(t)} = i_1(t) \\ i_2(t + \tau) = \frac{v(t + \tau)}{r_2(t + \tau)} = \frac{v(t)}{r_2(t)} = i_2(t) \end{cases}$$

An impedance variation on laser 1 does not give rise to any current variation through laser 2. Few correlation will be detected.

Let us now consider two lasers connected in series, and powered by a DC current bias:

$$i(t + \tau) = i(t)$$

If at some time t :

$$\begin{cases} r_1(t + \tau) > r_1(t) \\ r_2(t + \tau) = r_2(t) = r_2 \end{cases}$$

then:

$$\begin{cases} i_1(t + \tau) = i(t + \tau) = i(t) = i_1(t) \\ i_2(t + \tau) = i(t + \tau) = i(t) = i_2(t) \end{cases}$$

2. High signal-to-noise ratio emitter: discussion on a “system level” point of view

An impedance variation modifies the voltage drop, but does not influence the current through the lasers. Few correlation is possible through electronic connections.

Eventually, we consider two lasers connected in series, and powered by a DC voltage bias:

$$v(t + \tau) = v(t)$$

If at some time t :

$$\begin{cases} r_1(t + \tau) > r_1(t) \\ r_2(t + \tau) = r_2(t) = r_2 \end{cases}$$

then:

$$\begin{cases} i_1(t + \tau) = \frac{v(t + \tau)}{r_1(t + \tau) + r_2} < \frac{v(t)}{r_1(t) + r_2} = i_1(t) \\ i_2(t + \tau) = i_1(t + \tau) < i_1(t) = i_2(t) \end{cases}$$

An impedance increase of laser 1 lowers both the current through laser 1 and laser 2. The noise correlation is positive ($C_{i,j} > 0$).

Table 2.5 summarizes the results obtained with the noisy impedance approach. The series connection gives a positive correlation, increasing therefore the equivalent RIN. The parallel connection however gives a negative correlation which will tend to decrease even more the equivalent RIN. The parallel connection therefore seems to be more attractive for RIN lowering. Unfortunately, if we want to benefit from the series-connection advantages described in section 2.3, we will not be able to benefit as well from the anti-correlated RIN of the parallel architecture.

	DC current bias	DC voltage bias
series connection	few correlation $C_{i,j} \approx 0$	positive correlation $C_{i,j} \approx 0.3$ [33]
parallel connection	negative correlation $C_{i,j} \approx -0.3$ [33]	few correlation $C_{i,j} \approx 0$

Table 2.5: Summary of results predicted by the varying impedance approach. For the cited estimation of $C_{i,j}$, see “Results from the literature”, on page 53.

2.4.2.2 Scalability of the model

We now consider N lasers connected instead of only two. Laser 1 is still the only impedance varying laser at time t .

For the parallel-connection, we can always write:

$$\forall j \in \llbracket 2, N \rrbracket, \quad i_j(t) = \frac{r_1(t) + r_2 + \dots + r_{j-1} + r_{j+1} + \dots + r_N}{r_1(t) + r_2 + \dots + r_N} \langle i \rangle$$

The differentiation gives:

$$\forall j \in \llbracket 2, N \rrbracket, \quad \frac{\partial i_j}{\partial r_1} = \frac{r_j}{(\langle r_1 \rangle + r_2 + \dots + r_N)^2} \langle i \rangle$$

The influence of the impedance variation δr_1 on the current $i_j(t)$ will be all the less important as more lasers are connected in parallel. The current fluctuation is “spread” among all the parallel arms.

2.4 Combining sources for improving the RF link noise figure

For the series-connection, we write as well:

$$\forall j \in \llbracket 2, N \rrbracket, \quad i_j(t) = \frac{\langle v \rangle}{r_1(t) + r_2 + \dots + r_N}$$

which gives:

$$\forall j \in \llbracket 2, N \rrbracket, \quad \frac{\partial i_j}{\partial r_1} = \frac{\langle v \rangle}{(\langle r_1 \rangle + r_2 + \dots + r_N)^2}$$

As opposed to the parallel-case, the partial derivate of the current in laser j is negative (giving rise to positive correlation). In addition, the correlation strength also decreases with the number of lasers cascaded. In this case, we consider that the voltage drop due to an increase of the laser 1 impedance is spread among the other lasers.

As a consequence, for each type of connection, the effect of the electrical noise correlation will be the most important for the 2-laser architecture.

2.4.2.3 Results from the literature

Rana *et al.* from the Massachusetts Institute of Technology also predicted a positive correlation for series-connection and a negative correlation for parallel-connection [34]. They also measured the correlation strength to be equal to $C_{i,j} \approx \pm 0.3$ whether the lasers are connected in series (DC voltage bias) or in parallel (DC current bias) [33]. We include these results in table 2.5.

2.4.3 Noise figure and signal-to-noise ratio improvement

In practical non-amplified and non-impedance-matched opto-RF links, the noise figure is close to 40 dB. In equation 2.10, the first term (which comes from the amplified noise power density) is negligible compared to the noise introduced by the link. The noise figure is in these conditions proportional to:

$$NF \propto \frac{RIN \langle P_{(\text{opt})\text{source}} \rangle^2}{g_{\text{RF}}}$$

According to equation 2.13, and assuming no or few electrical correlation for a DC current bias drive if lasers are connected in series or in parallel, the RIN is theoretically proportional to $\frac{1}{N}$.

The RF gain improvement is also completely independent of the bias point. It has also been described previously, with the results summarized in table 2.3 for the different electrical architectures.

On the contrary, the average optical power on the photodiode depends on the laser bias point and thus on the constrains of the system. The constrains vary from one electrical architecture to the other. We limit here the discussion to series-connected laser sources with a resistive impedance matching.

2.4.3.1 Detailed comparison for series-connected laser sources with a resistive impedance matching

In order to fully understand the complex comparison of a multiple-laser source and a single-laser source, we compare the system parameters of a composed laser source with two different single-laser references. Each reference corresponds to

2. High signal-to-noise ratio emitter: discussion on a “system level” point of view

a possibly implemented single-laser opto-RF link with a given set of constraints and limitations.

For reference (a), we have a given input RF power. We are then wondering what we can get in terms of noise factor and output signal-to-noise ratio improvements from combining laser sources. In the comparison of the combined source with reference (a), the same input RF power is injected:

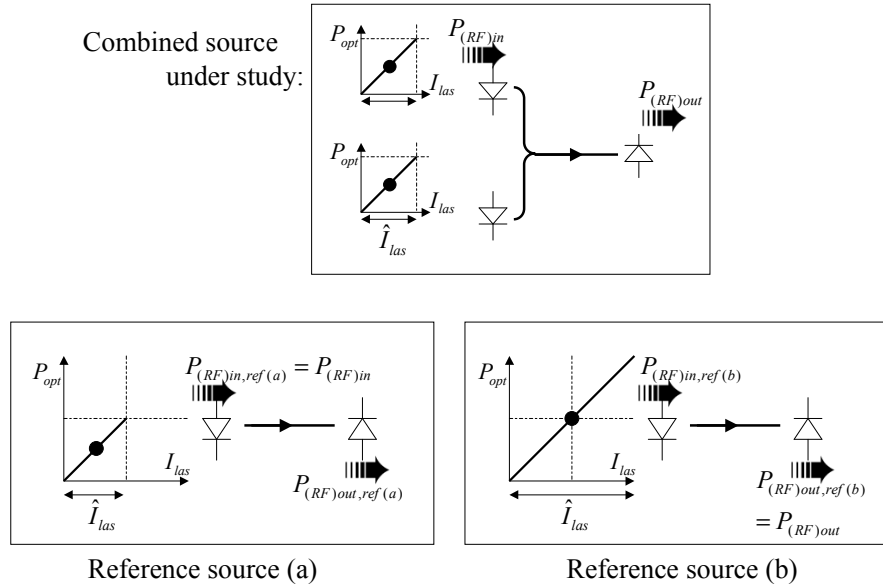
$$P_{(RF)in,ref(a)} = P_{(RF)in}$$

For reference (b), we need a given RF output power. We are then wondering how we can get this same RF power with a combined laser source, and whether it relaxes the constraints on the individual lasers. In the comparison of the combined source with reference (b), the same output RF power is obtained at the link output:

$$P_{(RF)out,ref(b)} = P_{(RF)out}$$

The two cases are schematically presented on figure 2.24.

Figure 2.24 Comparison of the combined architecture with (a) a single-laser source with equivalent input RF power, and (b) a single-laser source with equivalent output RF power.



The graphs shown on figure 2.24 display schematically a power-versus-current laser characteristic (supposedly perfectly linear for comprehension issues) for the composed laser source and for each reference. The dot symbolizes the bias point, and the diagonal line symbolizes the modulation amplitude in the P-versus-I curve.

For each of the two cases, we present in table 2.6 the factor of proportionality of the different system parameters of the composed laser source, as compared to the parameter of reference for the single-laser links references (a) and (b).

2.4 Combining sources for improving the RF link noise figure

The first column enumerates the lines and will be useful when discussing each result afterwards. The second column presents the system parameters and their calculation as a function of the other parameters. The third and fourth columns display the proportionality factor as compared to the single-laser links cases (a) and (b). For instance, the first line reads “the RF gain of a link using the multi-laser source is N^2 times higher than the RF gain of a link using the single-laser source of reference (a) and (b)”.

	Parameter	case (a): $P_{(\text{RF})\text{in,ref(a)}} = P_{(\text{RF})\text{in}}$	case (b): $P_{(\text{RF})\text{out,ref(b)}} = P_{(\text{RF})\text{out}}$
1	g_{RF} (previous sections)	N^2	N^2
2	RIN (previous sections)	$\frac{1}{N}$	$\frac{1}{N}$
3	$P_{(\text{RF})\text{in}}$ (by definition)	1	$\frac{1}{N^2}$
4	$P_{(\text{RF})\text{out}}$ (by definition)	N^2	1
5	$\text{SNR}_{\text{in}} = P_{(\text{RF})\text{in}}/P_{(\text{noise})\text{in}}$	1	$\frac{1}{N^2}$
6	$\langle P_{(\text{opt})\text{source}} \rangle \propto \sqrt{P_{(\text{RF})\text{out}}}$	N	1
7	$P_{(\text{noise})\text{out}} \propto RIN \times \langle P_{(\text{opt})\text{source}} \rangle^2$	N	$\frac{1}{N}$
8	$\text{SNR}_{\text{out}} = P_{(\text{RF})\text{out}}/P_{(\text{noise})\text{out}}$	N	N
9	$NF = \text{SNR}_{\text{in}}/\text{SNR}_{\text{out}}$	$\frac{1}{N}$	$\frac{1}{N^3}$

Table 2.6: Summary of the predicted system parameters for a series-connected resistive-impedance composed laser source, as compared to two different reference single-laser architectures.

Lines 1 and 2 The RF link gain and the relative intensity noise of the composed laser source have already been discussed earlier in this chapter for this configuration. For a series-connected laser source with a resistive impedance matching, the gain increases with N^2 , and the RIN decreases with $\frac{1}{N}$.

Lines 3 and 4 By definition of the case study, we compare the composed laser source with a reference single-laser source with equivalent input RF power (case (a)), and exhibiting equivalent output RF power (case (b)).

For reference (a), the output RF power is calculated as:

$$P_{(\text{RF})\text{out,ref(a)}} = g_{\text{RF}} P_{(\text{RF})\text{in}}$$

For reference (b), the input RF power is calculated as:

$$P_{(\text{RF})\text{in,ref(b)}} = \frac{P_{(\text{RF})\text{out}}}{g_{\text{RF}}}$$

In other words, as compared to reference (b), the requirements in terms of input RF power of the multi-laser source are N^2 times lower than in the single-laser source to achieve the same output RF power.

2. High signal-to-noise ratio emitter: discussion on a “system level” point of view

Line 5 The input RF noise power is assumed constant and equal for the two cases to $P_{(\text{noise})\text{in}}$. For case (b), as a direct consequence of the lower RF input power needed, the signal-to-noise ratio can be N^2 times lower than the single-laser case to obtain the same output power (reference (b)).

Line 6 Since we assume no loss introduced by the combining architecture, the optical power received by the photodiode increases for the multi-laser source by a factor of N , when compared to reference (a). For reference (b) however, an increase in the RF input power of the single-laser source by a factor of N^2 in order to deliver the same RF output power as the multi-laser source means an increase by a factor of N of the current modulation amplitude. This feature clearly appears in figure 2.24. Keeping the same rate of modulation, the bias point is also increased by a factor of N , and thus so is the average optical power received by the photodiode. The average optical power increases with the same rate (proportionally to N) for reference (b) and for the multi-laser architecture.

Line 7 The output RF noise power evolution is calculated directly as the product of the relative intensity noise by the square of the average optical power. This noise power decreases in case (b), whereas it increases in case (a), because the average optical power for the multi-laser source also increases as compared to reference (a).

Line 8 The two cases eventually provide the same output signal-to-noise ratio. While combining laser sources, we obtain an output RF signal-to-noise ratio that scales with N .

Line 9 The noise factor however is very different whether we compare the multi-laser source with a single-laser source for a given input RF power, or with a single-laser source that would exhibit the same output RF power. In the latter case, we need less input RF power (because of the high gain) and a lower input signal-to-noise ratio to eventually obtain the same output RF power and at least the same (in fact even a higher) output signal-to-noise ratio!

Notice that the architecture of reference (a) and reference (b) is exactly the same. The comparison held gives rise to a different noise factor because the noise factor of reference (a) is different from the noise factor of reference (b).

2.4.3.2 Literature available data

Unfortunately, there is only one noise figure experimental publication available from the literature, from C.H. Cox *et al.* [1]. We have seen previously that the measured RF gain data of this same publication are very much similar to predicted results ($\approx \pm 0.1$ dB). The comparison is held for a series-connected laser source with a resistive impedance matching, and for constant input RF power. These conditions are compatible with the comparison with reference (a) performed above. For six lasers, C.H. Cox *et al.* found a noise figure improvement of 6 dB, which should be compared to the $\frac{1}{6} = 7.8$ dB expected by the above calculation and discussion.

2.4 Combining sources for improving the RF link noise figure

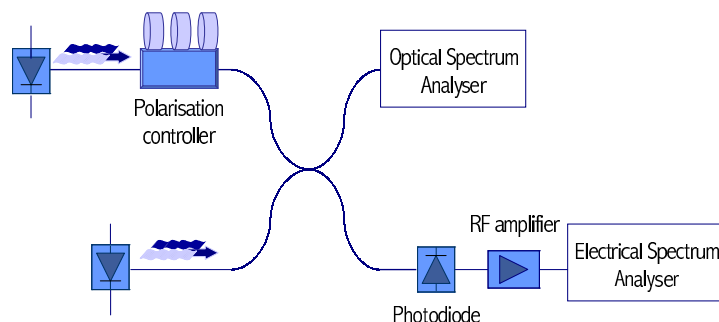
2.4.4 Experimental achievements

We have seen in the previous section that for series-connected lasers some correlation between the noise signals may alter the RIN improvement expected from independently-connected laser sources. The goal of this experimental section is to evaluate the amplitude of these electrical inter-correlation and to estimate whether or not they can be harmful to the RIN properties of a composed laser source.

2.4.4.1 Experimental set-up

We have used two commercially-available butterfly-module lasers and connected them in series. Figure 2.25 displays the experimental set-up.

Figure 2.25 Experimental set-up for measuring the RIN of a composed laser source.



The RIN measurement set-up consists in a high efficiency photodiode, a low-noise, large-bandwidth (0-21 GHz) RF amplifier, and a spectrum analyzer. The very sensible calibration protocol is described elsewhere [35]. On the other output arm of the coupler, an optical spectrum analyzer displays the combined signal optical spectrum.

A polarization controller is placed on one of the input arms of the coupler. The benefits from controlling the polarization difference between the two laser sources will be clarified afterwards (see section 2.4.4.3). A current power supply injects the current in series in the two lasers (70 mA), and we collect the light from both lasers with the coupler. For comparison, we have disconnected alternatively the input arms of the coupler in order to measure the individual laser RINs in the same electrical conditions.

2.4.4.2 Experimental results

Figure 2.26 presents the measured RIN of the combined signal (in thin black line) as compared to the RIN of each laser (in thin gray line). The inset shows a zoom in the resonance frequency region (from 5 to 10 GHz).

Since the lasers do not have the same characteristics (in terms of RIN, and of optical power), we need to generalize somewhat equation 2.12. The general

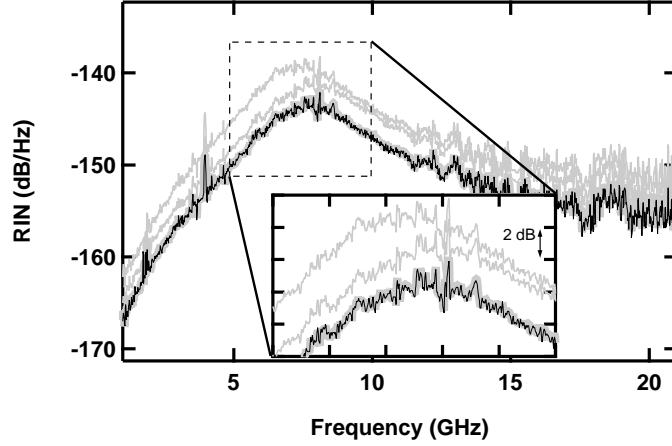
2. High signal-to-noise ratio emitter: discussion on a “system level” point of view

equation (including the inter-correlation term) writes:

$$RIN_{\text{source}} = \frac{\sum_i RIN_{\text{las}i} P_{(\text{opt})\text{las}i}^2}{(\sum_i P_{(\text{opt})\text{las}i})^2} + \sum_{i \neq j} \frac{\langle \delta P_{(\text{opt})\text{las}i} \delta P_{(\text{opt})\text{las}j} \rangle P_{(\text{opt})\text{las}i} P_{(\text{opt})\text{las}j}}{(\sum_i P_{(\text{opt})\text{las}i})^2}$$

⇨ The second term in the equation accounts for the correlation between the noise signals.

Figure 2.26 RIN measurements of the combined laser source (thin black line) as compared to individual laser RINs (thin gray lines). The bold gray line (perfectly matching the thin-black line) shows the calculated combined signal RIN spectrum.



We compare on figure 2.26 the measured RIN (thin black line) with the RIN calculated with the assumption that the noise signals are not correlated (bold gray line):

$$\forall i, \forall j \neq i, \langle \delta P_{(\text{opt})\text{las}i} \delta P_{(\text{opt})\text{las}j} \rangle = 0$$

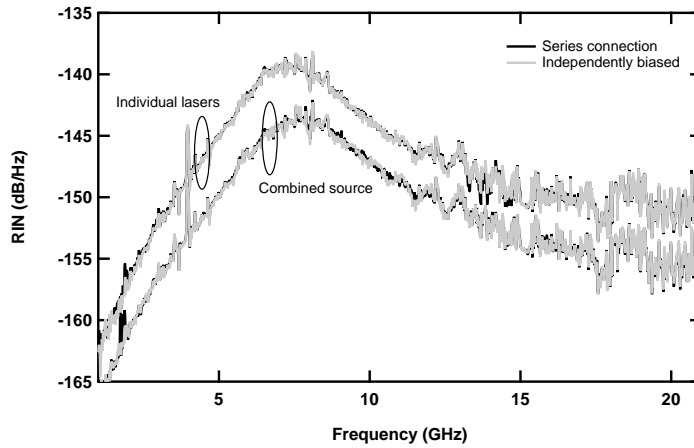
$$RIN_{\text{source}} = \frac{RIN_{\text{las}1} P_{(\text{opt})\text{las}1}^2 + RIN_{\text{las}2} P_{(\text{opt})\text{las}2}^2}{(P_{(\text{opt})\text{las}1} + P_{(\text{opt})\text{las}2})^2}$$

The calculated RIN (bold gray line) perfectly matches the measured data, proving that the correlation terms are negligible in this context.

In addition, we have compared the RIN of a combined laser source with series-connected lasers and the RIN of a combined laser source with separately biased lasers. Figure 2.27 displays the experimental data which results in very few discrepancy between the two noise measurements. No effect of electrical inter-correlation is visible neither on an individual laser RIN, nor on the combined source RIN.

2.4 Combining sources for improving the RF link noise figure

Figure 2.27 Comparison of individual-laser and combined-source RIN with different electrical connection schemes (series and separately biased).



2.4.4.3 Effect of heterodyne beating

In parallel of this study of series connected laser sources, we carried out an in-depth study to understand the heterodyne interaction between the laser signals injected in the coupler [8].

If we take no special care in the set-up protocol, the combining experiment via an optical coupler results in an important low-frequency (0-5 GHz) as well as high-frequency (≥ 15 GHz) noise increase (see figure 2.28).

Using an optical band-pass filter, we proved that this noise was actually almost blank over the whole electrical bandwidth, and due to optical heterodyne beating between the DFB peak of the first laser, and secondary optical modes of the second laser in the vicinity of the first laser peak [8]. It should be noted that this problem is therefore specific of externally combined laser sources. For several laser junctions in the same optical mode (such as in bipolar cascade lasers), this discussion is not relevant. The origin of this noise is exposed in figure 2.29.

One solution for avoiding heterodyne beating is to filter the secondary longitudinal modes with a band-pass filter. This principle has been proposed [36] and then successfully used in a MUX-combining experiment [6]. As already discussed in section 2.2, it nevertheless carries two drawbacks: the need for laser wavelength sorting, and the noise increase of each individual laser due to either the filtering of modes in competition with the DFB mode (modal partition noise), or the conversion of frequency noise into amplitude noise at the edge of the filters if the lasers are not well centered in the MUX-comb.

2. High signal-to-noise ratio emitter: discussion on a “system level” point of view

Figure 2.28 Comparison of RIN measurements with two different states of polarization difference between the two laser sources.

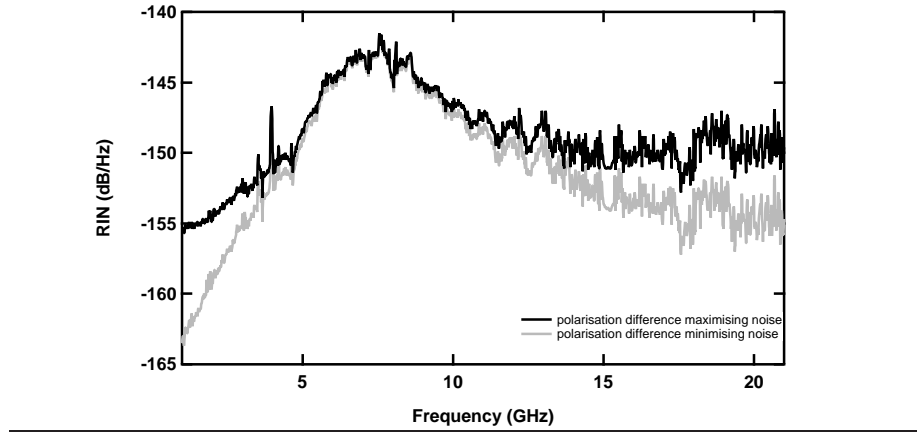
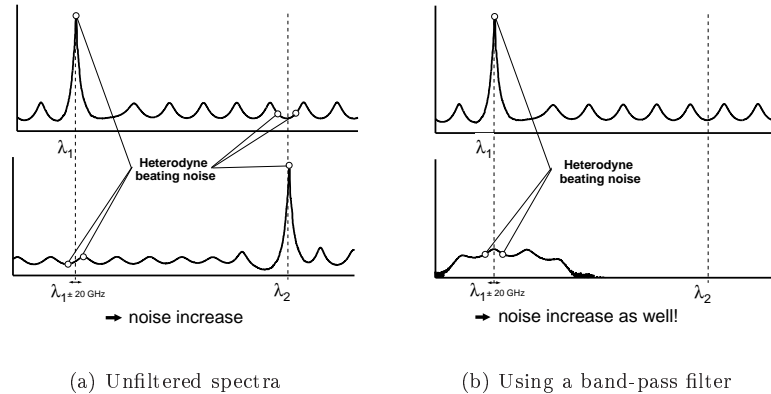


Figure 2.29 Principle schematic of heterodyne beating resulting in an important additional frequency noise.



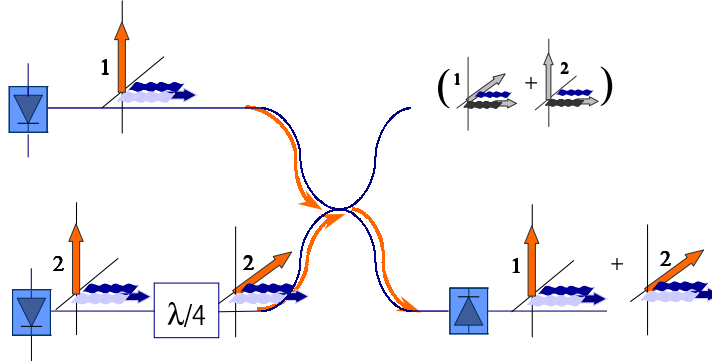
Another solution is to inject the light beams with crossed polarization. This observation explains why we have used a polarization controller on one input arm of the coupler on figure 2.25. Figure 2.28 shows the RIN spectra of the combined source with polarizations matched and polarizations in crossed-polarization.

This solution is very efficient (it can even be used for combining laser sources spectrally very close to each other), but requires a control of the polarization, and is limited intrinsically to two lasers!

Nevertheless, in order to make a more robust implementation in systems, it is possible to use polarization maintaining fibers and to inject the light beams in the coupler with crossed polarization. Besides, instead of using a simple coupler, it could be interesting to gather the light via a polarization combiner as proposed on figure 2.30.

2.4 Combining sources for improving the RF link noise figure

Figure 2.30 Proposed set-up for a more robust implementation in systems [8].



In addition to the 3-dB RIN improvement, we would also get a 3-dB optical power enhancement. The architecture would also be a lot more robust, which is an asset for implementation in systems such as airborne systems. To avoid any vibration sensitivity, it is also necessary to make all the optical connections using polarization-maintaining fibers. The whole set-up with polarization-maintaining fibers and the polarization combiner nevertheless annihilates the low-cost advantage of the simple coupler-based architecture.

2.4.5 Limitations of the discrete element architecture

According to the calculations performed and to the nice experimental demonstration of the theories exposed in this chapter, cascading N discrete lasers may increase the RF link gain by a factor of N^2 and reduce the output signal-to-noise ratio by a factor of $\frac{1}{N}$.

Unfortunately, the discrete configuration carries some intrinsic drawbacks that limit the maximum improvement we can get from cascading lasers.

The first limitation has already been focused in section 2.2 while discussing the crucial issue of combining optical light beams. It is indeed very difficult to combine with no loss and no additional noise several light beams carried by different media.

A second limitation has not yet been discussed in this chapter: the bandwidth limitation. Cascading lasers and driving them with the same RF signal implies that the RF signal reaches the different lasers with some delay. This delay triggers a RF phase shift that either needs to be optically compensated (as it is the case for the integrated traveling-wave photodetectors discussed in section 2.2), or will alter the RF gain. A very accurate, costly, and time-consuming packaging study is necessary to obtain a device transmission bandwidth suitable for use in systems.

If no optical compensation is used, then the bandwidth of the composed device is limited by the phase shift between the discrete lasers. We have intended to observe this bandwidth limitation, but using very simple electrical connections between the lasers (see for instance figure 2.22-(a) on page 47), it appeared that the major limitation came from the bandwidth of the electrical connections and not the intrinsic limitation due to propagation of the signal from discrete laser to discrete laser.

In order to circumvent these intrinsic limitations, it would be interesting to emit the different light beams directly into the same medium. In addition, the bandwidth shortcomings can be postponed if the laser structures are placed as close as possible to each other. The bipolar cascade laser structure, as it was already described in the general introduction therefore constitute the very natural improvement of this discrete architecture.

2.5 Conclusion

We have seen in section 2.3, that while considering the RF gain of the optical link composed of N individual lasers, it is theoretically always preferable to use a series connection scheme. In this context, a theoretical gain improvement proportional to N^2 can be achieved, and we experimentally reached an increase of almost 12 dB by the use of four commercially available butterfly packaged lasers.

Furthermore, we have shown in section 2.4, that except for heterodyne beating noise that is not to be considered in several active junctions integrated into a single laser mode, combining the light of N lasers tends to decrease the RIN by a factor of $\frac{1}{N}$. This feature was also proved experimentally when we observed a 3-dB RIN improvement while collecting the light from 2 lasers. The parallel configuration is theoretically preferable for noise reduction, but experimental data in our set-up conditions proved that the electrical inter-correlation term in the case of series-connected lasers is too weak to be observed.

It is therefore proven that cascading several individually packaged lasers enables to improve the optical link noise figure.

However, not-integrated combining source present the drawback of limiting the RF bandwidth. The following chapters will therefore consider several photon-emitting active regions into a single laser component. We will now investigate whether the results on the RF link gain and on the RIN remain promising even in a monolithic component, without degrading the device RF bandwidth.

Bibliography

- [1] C. H. Cox et al. Broadband, Directly Modulated Analog Fiber Link with Positive Intrinsic Gain and Reduced Noise Figure. In *Conference Microwave Photonics*, number TuC2, 1998.
- [2] Nicolas Michel. *Etude et Réalisation de Photodiodes-Guides Millimétriques de Puissance 1,5 micron*. PhD thesis, Université des Sciences et Technologies de Lille, March 2004. numéro d'ordre 3444.
- [3] J. Piprek et al. What Limits the Maximum Output Power of Long-Wavelength AlGaInAs/InP Laser Diodes? *IEEE Journal of Quantum Electronics*, 38(9):1253–1259, 2002.
- [4] Y. Inaba et al. High-Power 1.55- μm Mass-Transport-Grating DFB Lasers for Externally Modulated Systems. *IEEE Journal of Selected Topics in Quantum Electronics*, 7(2):152–158, Mar.-Apr. 2001.
- [5] Keishi Takaki et al. Reduced Linewidth Re-Broadening by Suppressing Longitudinal Spatial Hole Burning in High-Power 1.55- μm Continuous-Wave Distributed-Feedback (CW-DFB) Laser Diodes. *IEEE Journal of Quantum Electronics*, 39(9):1060–1065, Sept. 2003.
- [6] L. Ménager et al. Improved Microwave Figures of Externally Modulated Photonic Links with a Multi-Lasers Source. Private Communication, 2004.
- [7] Clément Thibon. Somme optique de signaux hyperfréquence. Master's thesis, Ecole Nationale Supérieure d'Ingénieur de Limoges, 2004.
- [8] C. Thibon, F. Dross, Marceaux A., and Vodjdani N. Discussion on RIN improvement using a standard 3-dB coupler. Submitted for Publication, 2004.
- [9] Philippe Agniel. Etude du bruit d'intensité relative d'un laser au sein d'une liaison optique multiplexée. Master's thesis, IUP Optoélectronique, Paris, 2001.
- [10] L. Ménager et al. Private Communication, 2004.
- [11] Nicolas Michel et al. High-power evanescently-coupled waveguide photodiode. Submitted for Publication, 2004.
- [12] S. Jasmin et al. Diluted- and distributed-absorption microwave waveguide photodiodes for high efficiency and high power. *IEEE Transactions on Microwave Theory and Techniques*, 45(8):1337–1341, Aug 1997.

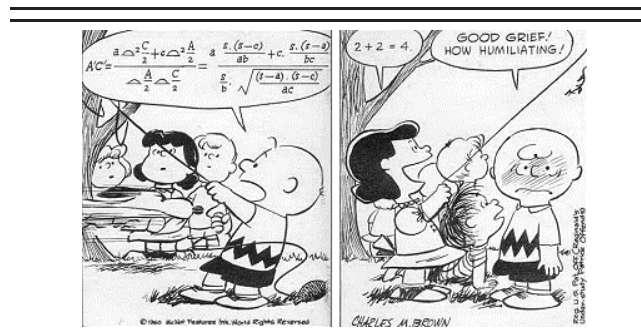
-
- [13] A. Achouche et al. New High Performance Evanescent Coupled Waveguide UTC Photodiodes for 40 GB/s Applications. In *European Conference on optical Communication ECOC'03*, pages 1048–1049, Rimini, Italy, 2003.
- [14] N. Breuil et al. Sommaton optique de signaux hyperfréquences. In *Journées Nationales Microondes JNM'03*, number 6c6, May. 2003.
- [15] A. Marceaux and N. Vodjdani. Traveling-wave electrodes for combining architectures. Private Communication, 2004.
- [16] C.L. Goldsmith et al. Principles and Performances of Traveling-Wave Photodetector Arrays. *IEEE Transactions on Microwave Theory and Techniques*, 45(8):1342–1349, Aug. 1997.
- [17] M.S. Islam et al. Velocity-Matched Distributed Photodetectors and Balanced Photodetectors with p-i-n Photodiodes. *IEEE Transactions on Microwave Theory and Techniques*, 49(10):1914–1920, Oct. 2001.
- [18] S. Murthy et al. A Novel Monolithic Distributed Traveling-Wave Photodetector with Parallel Optical Feed. *IEEE Photonics Technology Letters*, 12(6):681–683, Jun. 2000.
- [19] C. Kazmierski et al. 20 Ghz bandwidth 1.5 μm wavelength VUG DFB laser using a zero net strain $\text{In}_x\text{Ga}_{1-x}\text{As}_y\text{P}_{1-y}$ well active structure grown at constant y . *Electronic Letters*, 29(14):1290–1291, Jul. 1993.
- [20] F. Deborgies, E. Goutain, and J.C. Renaud. New Concepts for Millimeter Wave Optical Links. In *Proceeding EuMC, vol.2*, 1996.
- [21] R. Boula-Picard. Sommaton optique. Master's thesis, DEA Optique, Optoélectronique, Micro-ondes, Institut National Polytechnique de Grenoble (France), 1999.
- [22] S.G. Ayling et al. Novel Integrated Laser Devices with Greatly Enhanced Quantum Efficiency and Intrinsic RF Matching for Low Loss, Broad Band Opto-microwave Applications. In *Microwave Photonics*, pages TuC3: 161–164, Princeton, NJ , USA, Oct 1998.
- [23] K. D. Choquette, K. Geib, C. Cox, et al. Cascade Vertical Cavity Surface Emitting Laser Arrays. In *LEOS'02*, number TuAA1, Glasgow, Scotland, 2002.
- [24] J. T. Getty et al. Multistage Segmented 1.55 μm Lasers with Record Differential Efficiency, Low Thresholds, and 50- Ω Matching. In *LEOS'98*, number PD 1.2, Orlando, Florida, USA, Dec 1998.
- [25] J.T. Getty et al. CW Operation of 1.55- μm Bipolar Cascade Laser With Record Differential Efficiency, Low Threshold, and 50- Ω Matching. *IEEE Photonics Technology Letters*, 15(11):1513–1515, Nov 2003.
- [26] J. Ch. Garcia et al. Epitaxially stacked lasers with Esaki junctions: a bipolar cascade laser. *Applied Physics Letters*, 26(71):3752–3754, Dec. 1997.

BIBLIOGRAPHY

- [27] N. Laurent et al. Injection locking between laser layers in a InP/InGaAsP bipolar cascade laser. In *CLEO '98*, pages 468–469, San Francisco, USA, May 1998.
- [28] S. G. Patterson et al. Continuous-wave room temperature operation of bipolar cascade laser. *Electronic Letters*, 35(5):395–396, Mar. 1999.
- [29] J. K. Kim et al. Room-temperature, electrically-pumped multiple-active-region VCSELs with high differential efficiency at 1.55 μm . *Electronic Letters*, 35(13):1084–1085, Jun. 1999.
- [30] V. Malyarchuck et al. Uniformity tests of individual segments of interband cascade diode laser Nanostacks. *Journal of Applied Physics*, 92(5):2729–2733, Sept. 2002.
- [31] R. Schimpe. Intensity Noise Associated with the Lasing Mode of a (GaAl)As Diode Laser. *IEEE Journal of Quantum Electronics*, QE-19(6):895–897, Jun. 1983.
- [32] R. Pillai, E. Garmire, and P. Menedez-Valdes. Relative Intensity Noise of Laser-Diode Arrays. *IEEE Transactions Photonics Technology Letters*, 3(11):968–970, Nov. 1991.
- [33] F. Rana et al. Correlated Photon emissions in Electrically Coupled Semiconductor Lasers. In *Semiconductor Laser Conference SLC'02*, WA4, pages 115–116, Oct. 2002.
- [34] F. Rana et al. Photon noise and correlations in semiconductor cascade lasers. *Applied Physics Letters*, 76(9):1083–1085, Feb 2000.
- [35] M. B. Bibey. *Transmission optique d'un signal hyperfréquence à haute pureté spectrale*. PhD thesis, Université des Sciences et Technologies de Lille, Lille, France, Nov. 1998.
- [36] D.T.K. Tong et al. Multiwavelength microwave photonis systems - Beyond RIN-limited performance. In *Proceedings of the IEEE Conference on Laser and Electro-Optics CLEO '97*, volume 11 of *CWN4*, pages 295–296, May 1997.

Chapter 3

“Component level” point of view: a comprehensive model of the integrated device



3.1 Introduction to rate equation analysis

We have seen in chapter 2 that the external differential efficiency of a laser source composed of N lasers is higher than for one single laser. Such an architecture leads to an important link gain improvement. In addition, We have seen that it was possible to average and thus reduce the laser optical power fluctuations by combining the light from different discrete lasers. A RIN reduction was this time observed.

We are now interested in an integrated version of the cascaded laser source. As we already saw in the General Introduction, the literature claims that the external efficiency increases proportionally with N , and that the current threshold decreases with $\frac{1}{N}$ [1, 2]. It is also indicated that the relative intensity noise

of bipolar cascade laser decreases with $\frac{1}{N}$, in accordance with what was proved for discrete lasers in chapter 2 [2].

In this chapter we intend to check whether these features proved theoretically and experimentally for discrete lasers still remains for an integrated composed source. In order to do so, we use an equation rate laser model. We will first describe the general formalism; then calculate, for different type of structures (including bipolar cascade lasers) the steady-state and the dynamic behavior. Eventually, we will give an estimation of the noise properties of bipolar cascade lasers within the rate equation formalism.

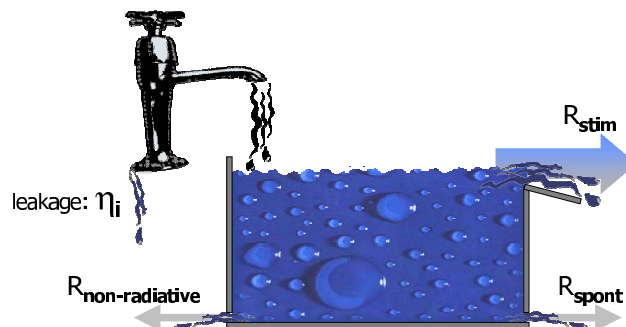
3.1.1 General description of the model

Each model needs to be specifically designed to account for the phenomena meant to be put forward. Here we intend to describe the single-mode BCL characteristics (at thermodynamic equilibrium but also dynamic characteristics) in comparison with more conventional laser structures. The comparison will be drawn with “high level” parameters, each one describing the overall characteristics of the structure. For instance, a single parameter will be used to describe the very complex photon-with-matter interaction that leads to optical amplification.

The “rate equation model” has the decisive advantage of presenting an empirical, comprehensive and accurate description of the complex semiconductor laser structure. This model is “classical”, in the sense that carriers (electron-hole pairs available for recombining) and photons are considered as particles with both known space coordinates, and known energy; but it accounts for quantum mechanical processes such as stimulated emission, for instance. It is even possible with the same description to account for non-classical light states (squeezing) [3, 4].

In order to introduce the rate equations, we will use a very strong metaphor borrowed from the hydrodynamic field. On figure 3.1, the laser is compared to a water reservoir [5, 6]. Carriers are continuously supplied to the structure as a flow of tap water. Continuous current leakage occurs (both radiative and non-radiative), and when the level reaches a threshold value, for every injected carrier, a photon is generated in the dominant mode.

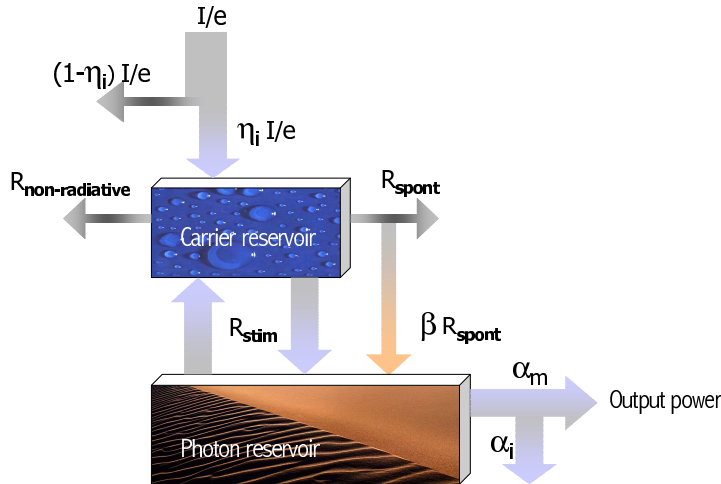
Figure 3.1 Hydrodynamic metaphor to embody a schematical laser mechanism [5, 6]



3.1 Introduction to rate equation analysis

In order to write the rate equations, we will rely on a reservoir model, schematized on figure 3.2.

Figure 3.2 The “reservoir” representation describes the rate equation approach [6]



3.1.2 Carrier population rate equation

When a current I goes through the device, $\eta_i \frac{I}{e}$ carriers are injected in the active region per unit time.

☞ η_i is the injection efficiency and accounts for electron leakage or more generally injected carriers that are never available for recombination.

These electron-hole pairs have, in semiconductors, a natural tendency to recombine spontaneously. The spontaneous recombination phenomenon in semiconductor is similar to the decay of radioactive particles discovered by Henri Becquerel in 1896. The rate equation model postulates that it is possible to describe the carrier population N evolution with the simple equation:

$$\frac{dN}{dt} = \frac{I}{e} - R$$

☞ R is a general recombination rate.

Furthermore, every recombination process dissipates some energy (the energy difference between the electron state and the hole state). This energy may either be transferred to the crystalline lattice by mechanical vibrations (phonons), or converted into an electro-magnetic oscillation (photons). In the latter case, the recombination is radiative. This recombination phenomenon is sometimes called “bimolecular recombination” since it requires an electron and a hole to interact simultaneously. Because two particles are involved in this process, it is consistent to find that its amplitude increases quadratically with

3. “Component level” point of view: a comprehensive model of the integrated device

the number of carriers (it can be considered similarly to the mass action law well known in chemistry [7, 8]):

$$R_{\text{spont}} = BN^2$$

☞ The recombination rates usually depend on the carrier density (and not on the carrier population). In InP, we find $B_{\text{density}} \simeq 10^{-10} \text{ cm}^3 \cdot \text{s}^{-1}$ [7, 9–11]. We use however the carrier population and multiply the coefficients with the volume of the active region when necessary to obtain the “population” coefficients. For instance: $B = \frac{B_{\text{density}}}{V_{\text{active}}}$

☞ Please note that the coefficients and notations used (and the reference sources) are summed up in appendix A.

There are several microscopic processes responsible for non-radiative recombinations. The most obvious is thermal recombination described by R. N. Hall in 1952 [12], and statistically calculated by Shockley and Read almost at the same time [13]. The process is often referred to as Shockley-Read-Hall (SRH) recombination. The crystalline lattice can not support a non-radiative recombination involving one single high-energy phonon that would stem from a non-radiative band-to-band recombination. Electron-holes actually recombine via intermediate states caused by the presence of defects or impurities. The annihilation comes in two steps: first, the defect traps a carrier of one type (electron or hole), then this carrier is recombined with the complementary carrier (hole or electron). Following the law of mass action, we would expect this process to be linear with the number of carriers (because it only involves one carrier at a given time), and actually we have:

$$R_{\text{SRH}} = AN$$

☞ In InP, $A_{\text{density}} \simeq 10^8 \text{ s}^{-1}$ [11, 14].

A more complex process involves three carriers and is known as Auger recombination. The recombination energy is transferred to another free carrier which makes an intra-band transition and further dissipates its energy by several, low energy, vibrational transitions. Although not dominant in GaAs-based devices, the process carries a major interest for narrow-band-gap ($\simeq 1.5 \mu\text{m}$) lasers [15–17]. Three carriers interact simultaneously, which is once again consistent with the N^3 evolution:

$$R_{\text{Auger}} = CN^3$$

☞ In GaAs-based lasers, $C_{\text{density}} \simeq 3.5 \times 10^{-30} \text{ cm}^6 \cdot \text{s}^{-1}$ [6], whereas for InP-based lasers, $C_{\text{density}} \simeq 5 \times 10^{-28} \text{ cm}^6 \cdot \text{s}^{-1}$ [11, 14, 15, 18–20].

Last, but not least, following Max Planck’s (1858-1947) brand new radiation law [21] (1900), Albert Einstein elaborated a theory of light composed of energy quanta (photons) and proposed, in 1905, a recombination process by stimulated emission. This process requires a first photon to trigger the recombination of an

3.1 Introduction to rate equation analysis

electron-hole pair simultaneously with a second-photon emission. This process is the building block of every laser (Light Amplification by Stimulated Emission Radiation) and gratified A. Einstein with the Nobel Price in 1921 [22]. To be efficient, this process requires several conditions:

- sufficient carrier (electron-hole pairs) density,
- sufficient photon density.

If too few photons interact with atoms, the stimulated process is negligible. If too few carriers are available for recombination, the reciprocal interaction takes place, namely: absorption.

We will therefore define a “transparency” number of carriers N_0 below (resp. above) which absorption (resp. stimulated emission) will be dominant. The stimulated emission rate writes:

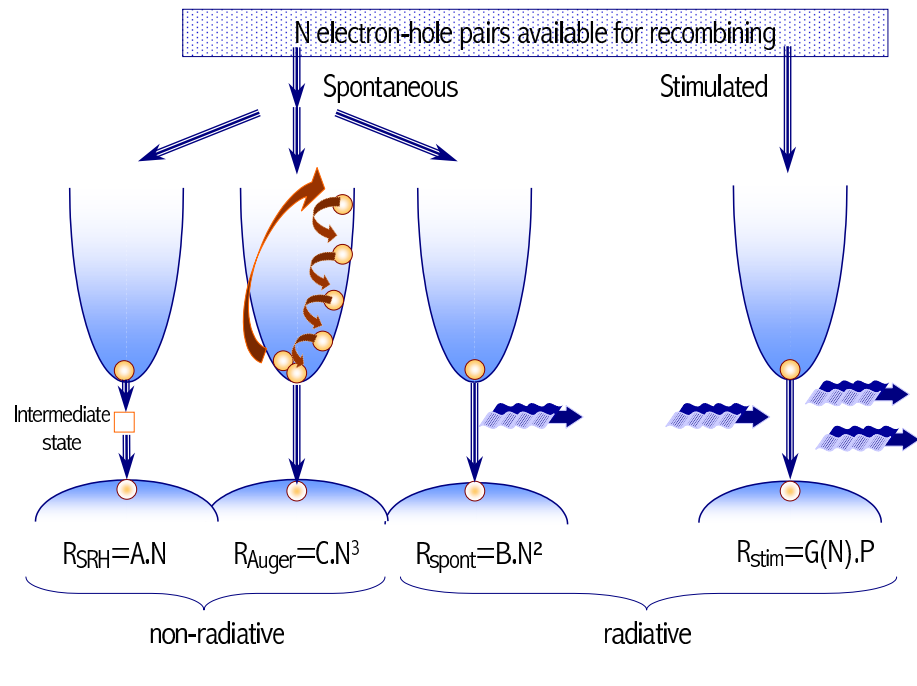
$$R_{\text{stim}} = G(N)P$$

$$\begin{cases} G(N) > 0, & \text{if } N > N_0 \\ G(N) < 0, & \text{if } N < N_0 \end{cases}$$

⇒ The net gain G is a function of N , and is characteristic of the QW geometry and materials.

Figure 3.3 displays a summary of each type of electron-hole pair recombinations that can occur in a semiconductor.

Figure 3.3 Summary of the different type of recombinations in a semi-conductor laser



The electron rate equation then writes:

$$\begin{aligned}\frac{dN}{dt} &= \eta_i \frac{I}{e} - (R_{\text{stim}} + R_{\text{spont}} + R_{\text{SRH}} + R_{\text{Auger}}) \\ &= \frac{I}{e} - G(N)P - (AN + BN^2 + CN^3)\end{aligned}\quad (3.1)$$

3.1.3 Photon population rate equation

The photon population of the dominant mode can also be described by a rate equation:

$$\frac{dP}{dt} = R_{\text{stim}} + \beta R_{\text{spont}} - \frac{P}{\tau_P} \quad (3.2)$$

- ☞ A stimulated emission recombination increases the number of photons in the dominant mode
- ☞ The individual spontaneous emission radiations have no phase relationship. Only a small portion β of the photons spontaneously emitted are collected into the dominant mode.
- ☞ τ_P stands for the photon lifetime due to losses of the cavity.
- ☞ No gain saturation is assumed.

3.1.4 Laser threshold

When no carrier is injected in the device, the (“cold”) cavity exhibits losses, characterized by the photon-population-decay time τ_P . We therefore have $R_{\text{stim}} \ll \frac{P}{\tau_P}$ and equation 3.2 tends to decrease the (already very low) photon population. Now if the injection is sufficient to create gain inside the cavity such as $R_{\text{stim}} > \frac{P}{\tau_P}$, we would then, according to equation 3.2 have a continuously-increasing photon population! This very naive interpretation is false and may be corrected by noticing that the stimulated emission process depletes the carrier population in equation 3.1.

Nevertheless, the simple interpretation shows that at some point, the gain will reach a threshold value above which the stimulated process will be dominant. Practically speaking, we observe that below a certain current density, almost no photons are emitted by the device. Above this current threshold, the stimulated (laser) effect starts, the slope of the power-versus-current characteristics abruptly changes and the output power increases by several orders of magnitude. This current threshold will be calculated in this chapter for the different device configurations.

3.1.5 Expression of τ_P

In order to describe a little more precisely what lies behind the “high-level” loss coefficient τ_P (and also to calculate the output power), we consider the light inside the cavity as consisting of particles (photons) traveling with a mode group velocity:

$$v_g = \frac{c}{n_{\text{eff}}}$$

- ☞ c is the speed of light.

3.1 Introduction to rate equation analysis

☞ n_{eff} is the effective index of the dominant lasing mode.

These dominant-mode photons therefore achieve a round trip inside the cavity in a time τ_{RT} :

$$\tau_{\text{RT}} = \frac{2L}{v_g}$$

☞ L is the cavity longitudinal dimension.

☞ We need to assume here that photons are not absorbed during this round-trip time. This approximation is not valid for the “cold” cavity: $\tau_{\text{RT}} < \tau_P$. Nevertheless, we will use this approximation for calculating the characteristic of the laser over threshold, where the gain almost equals the losses, and the photon lifetime tends to infinity.

If P photons reach the first mirror, an average of $R_1 P$ will be reflected. Taking into account the second mirror and the internal scattering losses (due to impurities or to the optical waveguide geometry), a small portion actually achieve the round-trip:

$$P_{\text{after RT}} = P_{\text{before RT}} \times R_1 R_2 e^{-2L\alpha_i}$$

τ_P is characteristic of the photon population time-decay in the cavity, we write:

$$P_{\text{after RT}} = P_{\text{before RT}} \times e^{-\frac{\tau_{\text{RT}}}{\tau_P}}$$

The average time-decay therefore comes:

$$\begin{aligned} \frac{1}{\tau_P} &= v_g(\alpha_i + \alpha_m) \\ \alpha_m &= \frac{1}{2L} \ln \frac{1}{R_1 R_2} \end{aligned} \quad (3.3)$$

☞ The photon decay due to losses through the mirrors is averaged spatially and characterized by a linear mirror loss coefficient α_m . We define only one average mirror loss coefficient, but we could have as well define one loss coefficient for each mirror.

☞ $R_{1,2}$ are the mirror power reflectivities of facet 1,2. if no special facet coating is deposited $R_1 = R_2 = \left| \frac{n_{\text{eff}} - 1}{n_{\text{eff}} + 1} \right|^2$. For instance, if $n_{\text{eff}} = 3.3$, then $R_1 = R_2 \approx 0.29$.

☞ n_{eff} is the effective refractive index of the lasing mode.

3.1.6 Output power

The photon losses through the mirrors are *not* properly speaking “losses” because they constitute the output laser beam. What is not reflected inside springs out of the cavity. The output optical power may then be written in terms of optical losses:

$$S = \frac{1}{2} \alpha_m v_g h\nu P \quad (3.4)$$

☞ $h\nu$ is the energy of the photon resulting from recombination processes.

☞ The output power is generally collected only from one laser facet, thus the $\frac{1}{2}$ term for identical mirrors.

3. “Component level” point of view: a comprehensive model of the integrated device

☞ Notice that S is an optical power measured in Watts, whereas P is a number of photons.

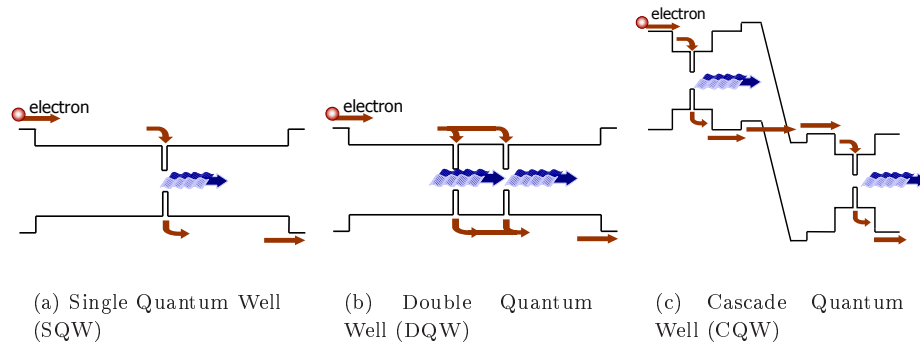
For simplified expression, we will sometime use $\eta_0 = \frac{1}{2}\alpha_m v_g h\nu$. The output power then yields :

$$S = \eta_0 P \quad (3.5)$$

3.1.7 Comparing different QW structures

The studied BCL structure exhibits several active regions and thus also several quantum wells (at least one per active region). The laser characteristics are modified with the BCL structure, but it is not obvious to estimate whether the change is due to the increased number of QWs or the increased number of active regions. To put it the other way, a two-active region BCL (each active region containing one QW) will have electrical properties comparable to a one-QW structure, but the optical properties will be more comparable to a two-QW structure. Figure 3.4 shows a schematic view of the three structures that will be compared within this model.

Figure 3.4 Schematic representation of the different QW structures studied in this chapter



For the first structure (SQW), the rate equations are the one described previously:

$$\frac{d}{dt}(N_{\text{SQW}}) = \eta_i \frac{I}{e} - G(N_{\text{SQW}})P_{\text{SQW}} - [AN_{\text{SQW}} + BN_{\text{SQW}}^2 + CN_{\text{SQW}}^3] \quad (3.6)$$

$$\frac{d}{dt}(P_{\text{SQW}}) = G(N_{\text{SQW}})P_{\text{SQW}} + \beta BN_{\text{SQW}}^2 - \frac{P_{\text{SQW}}}{\tau_P} \quad (3.7)$$

For the second structure (DQW), the current is spread among the two QWs. We can describe each QW separately and consider a reservoir for each carrier

3.1 Introduction to rate equation analysis

population.

$$\begin{aligned} \frac{d}{dt}(N_{\text{DQW}}^{(1)}) &= \eta_i^{(1)} \frac{I}{2e} - G(N_{\text{DQW}}^{(1)}) P_{\text{DQW}} \\ &\quad - [AN_{\text{DQW}}^{(1)} + BN_{\text{DQW}(1)}^2 + CN_{\text{DQW}(1)}^3] \end{aligned} \quad (3.8)$$

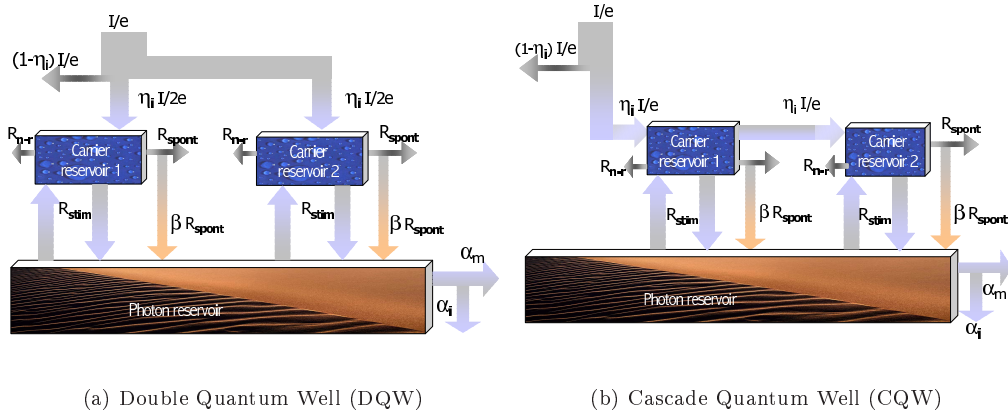
$$\begin{aligned} \frac{d}{dt}(N_{\text{DQW}}^{(2)}) &= \eta_i^{(2)} \frac{I}{2e} - G(N_{\text{DQW}}^{(2)}) P_{\text{DQW}} \\ &\quad - [AN_{\text{DQW}}^{(2)} + BN_{\text{DQW}(2)}^2 + CN_{\text{DQW}(2)}^3] \end{aligned} \quad (3.9)$$

$$\begin{aligned} \frac{d}{dt}(P_{\text{DQW}}) &= [G(N_{\text{DQW}}^{(1)}) + G(N_{\text{DQW}}^{(2)})] P_{\text{DQW}} \\ &\quad + \beta B [N_{\text{DQW}(1)}^2 + N_{\text{DQW}(2)}^2] - \frac{P_{\text{DQW}}}{\tau_P} \end{aligned} \quad (3.10)$$

☞ In the present chapter, we will use either $N_{\text{XQW}}^{(i)}$, or $N_{\text{XQW}(i)}$ to point out the same carrier population of reservoir i in the configuration XQW. The index appears sometimes in subscript to prevent confusion with an exponential term.

Figure 3.5 shows the “reservoir” representation used to derive the rate equations for DQW and CQW. The overall loss is supposed unchanged, and the characteristics of the QWs are supposed to be the same for every QW.

Figure 3.5 “Reservoir” diagram for structures DQW and CQW



For the third structure (CQW), the current is assumed to be entirely recycled from the first active region, into the second active region. The other overall

characteristics remain unchanged.

$$\begin{aligned} \frac{d}{dt}(N_{\text{CQW}}^{(1)}) &= \eta_i \frac{I}{e} - G(N_{\text{CQW}}^{(1)}) P_{\text{CQW}} \\ &\quad - [AN_{\text{CQW}}^{(1)} + BN_{\text{CQW}(1)}^2 + CN_{\text{CQW}(1)}^3] \end{aligned} \quad (3.11)$$

$$\begin{aligned} \frac{d}{dt}(N_{\text{CQW}}^{(2)}) &= \eta_i \frac{I}{e} - G(N_{\text{CQW}}^{(2)}) P_{\text{CQW}} \\ &\quad - [AN_{\text{CQW}}^{(2)} + BN_{\text{CQW}(2)}^2 + CN_{\text{CQW}(2)}^3] \end{aligned} \quad (3.12)$$

$$\begin{aligned} \frac{d}{dt}(P_{\text{CQW}}) &= [G(N_{\text{CQW}}^{(1)}) + G(N_{\text{CQW}}^{(2)})] P_{\text{CQW}} \\ &\quad + \beta B [N_{\text{CQW}(1)}^2 + N_{\text{CQW}(2)}^2] - \frac{P_{\text{CQW}}}{\tau_P} \end{aligned} \quad (3.13)$$

Eventually, since there is only one optical mode for the three types of cavity, the equation 3.4 coupling the output power to the inside number of photons is the same for the three structures:

$$S_{\text{XQW}} = \eta_0 P_{\text{XQW}} \quad (3.4)$$

⇨ η_0 does not depend on the considered structure.

3.1.8 Approximations

The rate equations as derived above are strongly non-linear. The purpose of this section is not to develop a complete solution that would take into account every non-linear small-effect phenomenon (such a discussion can for instance be found in [6] for a single-active region laser). It is here useful (and already challenging) to build a simple model that will lead us to understanding the basic but fundamental difference between the three proposed cases. As a consequence, we will assume approximations and try to identify the causes that induce major effects on the characteristics. The approximations used all over this chapter are the following:

- The evolution of the gain factor, while increasing the carrier density is usually considered as non-linear [6, 7]. Here, in a purpose to simplifying calculations, we consider the gain as linearly dependent of the carrier density:

$$G = G_0(N - N_0)$$

⇨ G_0 is the gain characteristic of the QW.

⇨ N_0 is the number of carriers in each QW required to reach transparency.

⇨ We also neglect the gain compression and the gain thermal roll-off.

- The internal differential quantum efficiency η_i as defined above is currently found with values around 70% for 1.55 μm ridge-waveguide InGaAsP/InP lasers [17]. Here, in order to simplify expressions, and to put the emphasis on the fundamental effects that lie behind the new cascade structure, we set η_i to 1 whatever be the considered structure.

3.2 Steady-state solution

- Last but not least, $G(N)$ usually refers to the modal gain, i.e. the optical gain relatively to the overlap factor between the optical mode and the active region [6]. This overlap differs if more QWs are inserted in the structure, or if the QWs are not in the center of the optical cavity. Here we consider that the overlap is the same whatever be the considered QW and whatever be the number of QWs.

3.2 Steady-state solution

Let us first consider those equations under steady-state conditions. In order to do so, we inject in the equations $\frac{d}{dt} = 0$ to account for a steady-state solution.

Additional approximations for steady-state

In order to simplify calculations and to make possible the comparison between structures, we only account for a spontaneous recombination rate linear with the carrier population. We suppose that spontaneous recombinations dominate non resonant recombinations, and that the number of recombinations per time unit is proportionnal to the carrier population:

$$\begin{aligned} AN &\simeq 0 \\ BN^2 &= \frac{N}{\tau_E} \\ CN^3 &\simeq 0 \end{aligned}$$

- ⇒ The approximation is not completely accurate for calculating the output power below threshold (spontaneous emission). Over threshold, the carrier population does not vary much, and the spontaneous recombination term can be linearised.

3.2.1 Single QW, single active junction (SQW)

The first case to analyze is the most simple case where the laser contains only one active junction, with one single QW. Considering the approximations mentioned above, as well as the characteristics inherent from steady-state solutions, we have:

$$\begin{aligned} 0 &= \frac{I}{e} - G_0(\overline{N}_{\text{SQW}} - N_{0(\text{SQW})})\overline{P}_{\text{SQW}} - \frac{\overline{N}_{\text{SQW}}}{\tau_E} \\ 0 &= G_0(\overline{N}_{\text{SQW}} - N_{0(\text{SQW})})\overline{P}_{\text{SQW}} + \beta \frac{\overline{N}_{\text{SQW}}}{\tau_E} - \frac{\overline{P}_{\text{SQW}}}{\tau_P} \end{aligned}$$

Below threshold, we neglect the stimulated emission term

$$G_0(\overline{N}_{\text{SQW}} - N_{0(\text{SQW})})\overline{P}_{\text{SQW}} \simeq 0$$

We get:

$$\begin{aligned} \overline{N}_{\text{SQW}} &= \tau_E \frac{I}{e} \\ \overline{P}_{\text{SQW}} &= \beta \frac{\tau_P}{\tau_E} \overline{N}_{\text{SQW}} \end{aligned}$$

3. “Component level” point of view: a comprehensive model of the integrated device

Above threshold, the spontaneous emission term is neglected $\beta \frac{\overline{N}_{\text{SQW}}}{\tau_E} \simeq 0$, and the gain is clamped to its threshold value:

$$\begin{aligned}\overline{P}_{\text{SQW}} &= \frac{\tau_P}{e} (\overline{I} - I_{\text{th(SQW)}}) \\ I_{\text{th(SQW)}} &= \frac{eN_{\text{th(SQW)}}}{\tau_E} \\ N_{\text{th(SQW)}} &= \frac{1}{G_0 \tau_P} + N_{0(\text{SQW})}\end{aligned}$$

↷ N_{th} is the carrier population at threshold.

↷ I_{th} is the current threshold.

According to equation 3.4 and equation 3.3, the output power writes:

$$\begin{cases} \text{If } I \leq I_{\text{th(SQW)}}, & \overline{S}_{\text{SQW}} = \frac{1}{2} \beta \frac{\alpha_m}{\alpha_i + \alpha_m} \frac{h\nu}{e} \overline{I} \\ \text{If } I > I_{\text{th(SQW)}}, & \overline{S}_{\text{SQW}} = \frac{1}{2} \frac{\alpha_m}{\alpha_i + \alpha_m} \frac{h\nu}{e} (\overline{I} - I_{\text{th(SQW)}}) \end{cases} \quad (3.14)$$

The term in factor of the current term is the slope of the light-versus-current $S(I)$ characteristic. It is referred to as the external differential efficiency $\eta_{d(\text{SQW})}$ and is expressed in A/W. The external differential quantum efficiency (DQE) $\eta_{\text{DQE}(\text{SQW})}$ is the same physical characteristic, but normalized to a number of output photons for one input electron:

$$\eta_{d(\text{SQW})} = \frac{1}{2} \frac{\alpha_m}{\alpha_i + \alpha_m} \frac{h\nu}{e} \quad (3.15)$$

$$\eta_{\text{DQE}(\text{SQW})} = \frac{1}{2} \frac{\alpha_m}{\alpha_i + \alpha_m} \quad (3.16)$$

3.2.2 Two QW, single active junction (DQW)

In the case of multiple QWs in the same active region, we can simply add the first two equations. We take the sum of the carrier population as the new variable:

$$\overline{N}_{\text{DQW}}^{(+)} = \overline{N}_{\text{DQW}}^{(1)} + \overline{N}_{\text{DQW}}^{(2)}$$

in this case, we get a more simple two-equation system:

$$\begin{aligned}0 &= \frac{I}{e} - G_0 (\overline{N}_{\text{DQW}}^{(+)} - 2N_{0(\text{SQW})}) \overline{P}_{\text{SQW}} - \frac{\overline{N}_{\text{DQW}}^{(+)}}{\tau_E} \\ 0 &= G_0 (\overline{N}_{\text{DQW}}^{(+)} - 2N_{0(\text{SQW})}) \overline{P}_{\text{SQW}} + \beta \frac{\overline{N}_{\text{DQW}}^{(+)}}{\tau_E} - \frac{\overline{P}_{\text{SQW}}}{\tau_P}\end{aligned}$$

Once again, we neglect stimulated emission below threshold:

$$\begin{aligned}\overline{N}_{\text{DQW}}^{(+)} &= \tau_E \frac{I}{e} \\ \overline{P}_{\text{DQW}} &= \beta \frac{\tau_P}{\tau_E} \overline{N}_{\text{DQW}}^{(+)}\end{aligned}$$

3.2 Steady-state solution

And above threshold, spontaneous emission is neglected:

$$\begin{aligned}\bar{P}_{\text{DQW}} &= \frac{\tau_P}{e} (\bar{I} - I_{\text{th(DQW)}}) \\ I_{\text{th(DQW)}} &= \frac{eN_{\text{th(DQW)}}^{(+)}}{\tau_E} \\ N_{\text{th(DQW)}}^{(+)} &= N_{\text{th(DQW)}}^{(1)} + N_{\text{th(DQW)}}^{(2)} = \frac{1}{G_0\tau_P} + 2N_0(\text{SQW})\end{aligned}$$

The output power writes:

$$\begin{cases} \text{If } I \leq I_{\text{th(DQW)}}, & \bar{S}_{\text{DQW}} = \frac{1}{2}\beta \frac{\alpha_m}{\alpha_i + \alpha_m} \frac{h\nu}{e} \bar{I} \\ \text{If } I > I_{\text{th(DQW)}}, & \bar{S}_{\text{DQW}} = \frac{1}{2} \frac{\alpha_m}{\alpha_i + \alpha_m} \frac{h\nu}{e} (\bar{I} - I_{\text{th(DQW)}}) \end{cases}$$

Comparison to previous results

If we consider that photon lifetime is similar for SQW and DQW, we can derive:

$$\begin{aligned}\frac{1}{\tau_P} = G_0(N_{\text{th(SQW)}} - N_0(\text{SQW})) &= G_0(N_{\text{th(DQW)}}^{(+)} - 2N_0(\text{SQW})) \\ N_{\text{th(SQW)}} - N_0(\text{SQW}) &= N_{\text{th(DQW)}}^{(+)} - 2N_0(\text{SQW}) \\ N_{\text{th(DQW)}}^{(1)} &= \frac{N_{\text{th(SQW)}} + N_0(\text{SQW})}{2}\end{aligned}$$

then as $N_0(\text{SQW}) < N_{\text{th(SQW)}}$,

$$\frac{N_{\text{th(SQW)}}}{2} \lesssim N_{\text{th(DQW)}}^{(1)} < N_{\text{th(SQW)}}$$

If we can neglect $N_0(\text{SQW})$, that is to say when $N_0(\text{SQW}) \ll N_{\text{th(SQW)}}$, the inequality becomes equality. We can then get with $N_{\text{th(DQW)}}^{(+)} = 2N_{\text{th(DQW)}}^{(1)}$, following equation 3.17:

$$\begin{aligned}I_{\text{th(DQW)}} &= \frac{eN_{\text{th(DQW)}}^{(+)}}{\tau_E} \\ &= \frac{2eN_{\text{th(DQW)}}^{(1)}}{\tau_E} \\ &\gtrsim \frac{eN_{\text{th(SQW)}}}{\tau_E} \\ &\gtrsim I_{\text{th(SQW)}}\end{aligned}$$

The threshold current increases with the number of quantum wells. More current is required to drive more QWs to transparency.

The external efficiency on the other hand is not modified with the approximation that the internal efficiency does not change with the number of QWs.

3.2.3 Two active junctions, each including a single QW (CQW)

We set as well $\overline{N}_{\text{CQW}}^{(+)} = \overline{N}_{\text{CQW}}^{(1)} + \overline{N}_{\text{CQW}}^{(2)}$; the system is then a two-equation non-linear system:

$$\begin{aligned} 0 &= \frac{2I}{e} - G_0(\overline{N}_{\text{CQW}}^{(+)} - 2N_{0(\text{SQW})})\overline{P}_{\text{CQW}} - \frac{\overline{N}_{\text{CQW}}^{(+)}}{\tau_E} \\ 0 &= G_0(\overline{N}_{\text{CQW}}^{(+)} - 2N_{0(\text{SQW})})\overline{P}_{\text{CQW}} - \frac{\overline{P}_{\text{CQW}}}{\tau_P} \end{aligned}$$

We neglect stimulated emission below threshold :

$$\begin{aligned} \overline{N}_{\text{CQW}}^{(+)} &= \tau_E \frac{2I}{e} \\ \overline{P}_{\text{CQW}} &= \beta \frac{\tau_P}{\tau_E} \overline{N}_{\text{CQW}}^{(+)} \end{aligned}$$

And above threshold, spontaneous emission is neglected:

$$\overline{P}_{\text{CQW}} = \frac{2\tau_P}{e} (\overline{I} - I_{\text{th}(\text{CQW})}) \quad (3.17)$$

$$I_{\text{th}(\text{CQW})} = \frac{eN_{\text{th}(\text{CQW})}^{(+)}}{2\tau_E} \quad (3.18)$$

$$N_{\text{th}(\text{CQW})}^{(+)} = N_{\text{th}(\text{CQW})}^{(1)} + N_{\text{th}(\text{CQW})}^{(2)} = \frac{1}{G_0\tau_P} + 2N_{0(\text{SQW})} \quad (3.19)$$

The output power writes:

$$\begin{cases} \text{If } I \leq I_{\text{th}(\text{CQW})}, & \overline{S}_{\text{CQW}} = \frac{1}{2} \beta \frac{\alpha_m}{\alpha_i + \alpha_m} \frac{h\nu}{e} \overline{I} \\ \text{If } I > I_{\text{th}(\text{CQW})}, & \overline{S}_{\text{CQW}} = \frac{1}{2} \frac{\alpha_m}{\alpha_i + \alpha_m} \frac{h\nu}{e} (\overline{I} - I_{\text{th}(\text{CQW})}) \end{cases}$$

Comparison to previous results

For the same reasons previously mentioned, we have:

$$\frac{N_{\text{th}(\text{SQW})}}{2} \lesssim N_{\text{th}(\text{CQW})}^{(1)} < N_{\text{th}(\text{SQW})}$$

We derive with $N_{\text{th}(\text{CQW})}^{(+)} = 2N_{\text{th}(\text{CQW})}^{(1)}$, following 3.19:

$$\begin{aligned} I_{\text{th}(\text{CQW})} &= \frac{eN_{\text{th}(\text{CQW})}^{(+)}}{2\tau_E} \\ &= \frac{eN_{\text{th}(\text{DQW})}^{(1)}}{\tau_E} \\ I_{\text{th}(\text{CQW})} &= \frac{I_{\text{th}(\text{DQW})}}{2} \end{aligned}$$

3.3 Dynamic behavior

Leading to:

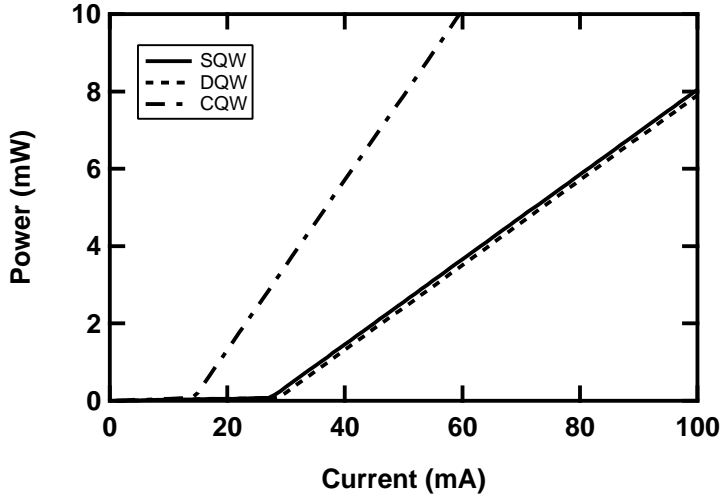
$$\frac{I_{\text{th(SQW)}}}{2} \approx I_{\text{th(CQW)}} < I_{\text{th(SQW)}}$$

Electrically connecting several active regions enables the current threshold to decrease linearly with the number of active regions in comparison with DQW. Comparing with SQW, we get a linear diminution of the threshold current only if transparency population can be neglected as compared to threshold population.

In addition, the external efficiency DQE is linearly increased with the number of cascade lasers. The electroluminescence below threshold also increases linearly with the number of active cascaded regions.

Figure 3.6 compares the calculated characteristics for SQW, DQW and CQW. As compared to SQW, the threshold current increases while more QWs are grown inside the same active region (DQW), and it is almost divided by a factor of N , if N active regions are cascaded in the same optical cavity. The external efficiency is approximately the same for SQW and DQW, whereas it increases by a factor of 2 for the cascaded structure.

Figure 3.6 Compared calculated power-vs-current characteristics for SQW, DQW and CQW.



☞ The parameters used for calculation are listed in appendix A.

3.3 Dynamic behavior

There is no known analytical solution to the non-linear coupled differential rate equations systems. Their resolution usually requires a numerical process. In order to obtain analytical expressions we need to linearise the problem.

In this section, and in the following, we will consider a laser structure current-biased with a time-average value \bar{I} . From the previous section, we can derive the average carrier and photon populations (\bar{N} and \bar{P}). We now consider the

3. “Component level” point of view: a comprehensive model of the integrated device

instantaneous departure from their average values:

$$X(t) = \bar{X} + \delta X(t)$$

where X stands for I , N , P or S . We inject the new variables δI , δN , δP and δS into the rate equations 3.6 to 3.13.

The average values exactly fulfill the steady-state rate equations and therefore vanish out. Furthermore, for small deviations we can neglect the second-order or third-order terms and we eventually get a differential-equation system linear for the new variables:

$$\begin{aligned} \frac{d}{dt}(\delta N_{\text{SQW}}(t)) &= \frac{\delta I(t)}{e} - \frac{\delta P_{\text{SQW}}(t)}{\tau_P} - \left(G\bar{P}_{\text{SQW}} + \frac{1}{\tau'_E}\right)\delta N_{\text{SQW}}(t) \\ \frac{d}{dt}(\delta P_{\text{SQW}}(t)) &= G\bar{P}_{\text{SQW}} \delta N_{\text{SQW}}(t) \end{aligned}$$

$$\Leftrightarrow \text{We set: } \frac{1}{\tau'_E} = A + 2B\bar{N}_{\text{SQW}} + 3C\bar{N}_{\text{SQW}}^2$$

and the output power fluctuations are given by:

$$\delta S_{\text{SQW}}(t) = \eta_0 \delta P_{\text{SQW}}(t)$$

The power fluctuations may also arise from noise. In order to account for noise generated fluctuations, we include an additional term in the rate equations. These terms are known as Langevin sources and will be described in more details in section 3.4.3 on page 92. The rate equations become:

$$\begin{aligned} \frac{d}{dt}(\delta N_{\text{SQW}}(t)) &= \frac{\delta I(t)}{e} - \frac{\delta P_{\text{SQW}}(t)}{\tau_P} \\ &\quad - \left(G\bar{P}_{\text{SQW}} + \frac{1}{\tau'_E}\right)\delta N_{\text{SQW}}(t) + F_{N_{\text{SQW}}}(t) \end{aligned} \quad (3.20)$$

$$\frac{d}{dt}(\delta P_{\text{SQW}}(t)) = G\bar{P}_{\text{SQW}} \delta N_{\text{SQW}}(t) + F_{P_{\text{SQW}}}(t) \quad (3.21)$$

$$\Leftrightarrow F_{Y_{\text{XQW}}}(t) \text{ are the Langevin noise sources.}$$

and the output power fluctuations:

$$\delta S_{(\text{SQW})_{\text{opt}}}(t) = \eta_0 \delta P_{\text{SQW}}(t) + F_{S_{\text{SQW}}}(t) \quad (3.22)$$

As we expect to obtain the frequency response of the structure, we consider harmonic deviations from the average values $\delta X(t, \omega) = \delta X(\omega) \cos(\omega t)$. If the real modulation is not purely harmonic, it could still be expressed as a sum of harmonic signals; and because the system is linear, the response would eventually be the sum of the responses to harmonic signals.

In order to deal with the temporal derivation, it is useful to express the variables within a complex representation: $\delta X(t, \omega) = \delta X(\omega) e^{i\omega t}$. $\delta X(\omega)$ is then the Fourier transform of $\delta X(t)$:

$$\begin{aligned} \delta X(t) &= \frac{1}{2\pi} \int \delta X(t, \omega) d\omega \\ &= \frac{1}{2\pi} \int \delta X(\omega) e^{i\omega t} d\omega \end{aligned}$$

3.3 Dynamic behavior

The system of equations becomes:

$$\begin{aligned}
 i\omega \delta N_{\text{SQW}}(\omega) &= \frac{\delta I(\omega)}{e} - \frac{\delta P_{\text{SQW}}(\omega)}{\tau_P} \\
 &\quad - \left(G_0 \bar{P}_{\text{SQW}} + \frac{1}{\tau'_E} \right) \delta N_{\text{SQW}}(\omega) + F_{N_{\text{SQW}}}(\omega) \\
 i\omega \delta P_{\text{SQW}}(\omega) &= G_0 \bar{P}_{\text{SQW}} \delta N_{\text{SQW}}(\omega) + F_{P_{\text{SQW}}}(\omega)
 \end{aligned}$$

Eventually, the linear system can be expressed in its matrix form:

$$\begin{pmatrix} G_0 \bar{P}_{\text{SQW}} + \frac{1}{\tau'_E} + i\omega & \frac{1}{\tau_P} \\ -G_0 \bar{P}_{\text{SQW}} & i\omega \end{pmatrix} \begin{pmatrix} \delta N_{\text{SQW}}(\omega) \\ \delta P_{\text{SQW}}(\omega) \end{pmatrix} = \begin{pmatrix} \frac{\delta I(\omega)}{e} + F_{N_{\text{SQW}}}(\omega) \\ F_{P_{\text{SQW}}}(\omega) \end{pmatrix} \quad (3.23)$$

with the solution:

$$\begin{pmatrix} \delta N_{\text{SQW}}(\omega) \\ \delta P_{\text{SQW}}(\omega) \end{pmatrix} = \frac{1}{\Delta} \begin{pmatrix} i\omega & -\frac{1}{\tau_P} \\ G_0 \bar{P}_{\text{SQW}} & G_0 \bar{P}_{\text{SQW}} + \frac{1}{\tau'_E} + i\omega \end{pmatrix} \begin{pmatrix} \frac{\delta I(\omega)}{e} + F_{N_{\text{SQW}}}(\omega) \\ F_{P_{\text{SQW}}}(\omega) \end{pmatrix}$$

⇨ Δ is the transfer function matrix determinant

The left-hand-side term is the variable to be calculated; the center matrix is the transfer function matrix of the modulated laser structure; the right-hand-side term is the source modulation term. It is clear from this equation that the modulation around an average value can either be expected and encouraged in the case of directly modulated lasers $\left(\frac{\delta I(\omega)}{e} \gg F_X(\omega) \right)$, or unwanted in the case of self-established noise modulation $\left(F_X(\omega) \gg \frac{\delta I(\omega)}{e} \right)$.

The response of the different laser structures to a controlled current modulation will be studied in this section, while we will focus on intensity noise calculations in the next section.

3.3.1 Single QW, single active junction (SQW)

Let us first neglect the noise source of modulation and only consider the response to a current modulation. Solving equation 3.23 the frequency response can be written as :

$$\begin{aligned}
 \frac{\delta P_{\text{SQW}}}{\delta I}(\omega) &= \frac{\tau_P}{e} \frac{\omega_{R(\text{SQW})}^2}{\omega_{R(\text{SQW})}^2 - \omega^2 + 2i \frac{\omega}{\tau_{R(\text{SQW})}}} \\
 \omega_{R(\text{SQW})}^2 &= \frac{G_0 \bar{P}_{\text{SQW}}}{\tau_P} \\
 \tau_{R(\text{SQW})} &= \frac{2\tau'_E}{G_0 \bar{P}_{\text{SQW}} \tau'_E + 1}
 \end{aligned}$$

According to equation 3.22, the output power modulation writes:

$$\frac{\delta S_{\text{SQW}}}{\delta I}(\omega) = \frac{1}{2} \frac{\alpha_m}{\alpha_i + \alpha_m} \frac{h\nu}{e} \frac{\omega_{R(\text{SQW})}^2}{\omega_{R(\text{SQW})}^2 - \omega^2 + 2i \frac{\omega}{\tau_{R(\text{SQW})}}}$$

When the carrier population is increased in equation 3.20 the photon population will increase because the two equations are coupled by the particle exchange stimulated emission term $G_0(N - N_0)P$. Meanwhile, an instantaneous

increase in the photon population leads to a decrease in the carrier population, as can be seen from equation 3.21. These two effects are compensative, their coupling implies a self-frequency resonance. Therefore, it is not surprising to find a second-order transfer function, with a resonance frequency that can be derived from the intrinsic laser parameters.

This response is composed of the low frequency response, the external conversion efficiency from electrons to photons η_d (which was of major interest in chapter 2 because it is directly proportional to the square root of the RF electric gain of the opto-RF link), and of a frequency dependent factor, the transfer function $H(\omega)$ of the laser:

$$\begin{aligned} \frac{\delta S_{\text{SQW}}}{\delta I}(\omega) &= \eta_{d(\text{SQW})} H(\omega) \\ \eta_{d(\text{SQW})} &= \frac{1}{2} \frac{\alpha_m}{\alpha_i + \alpha_m} \frac{h\nu}{e} \end{aligned} \quad (3.24)$$

Apart from the intrinsic modulation response, the inherent parasitic laser complex impedance needs to be taken into account to correctly determine the overall frequency response. This parasitic impedance includes the contact as well as the junction impedance and can be very complicated to determine and describe. Here we consider that the major effect is a low-pass filter behavior induced by the series resistance R_S and parallel capacitance C_{parasit} of the device. We then simply multiply (in the Fourier domain) the transfer function of the laser with the parasitic filter transfer function with a frequency cut $\tau_{\text{parasit}} = R_S C_{\text{parasit}}$:

$$\begin{aligned} \frac{\delta S_{\text{SQW}}}{\delta I}(\omega) &= \eta_{d(\text{SQW})} H(\omega) H_{\text{parasit}}(\omega) \\ &= \eta_{d(\text{SQW})} H(\omega) \frac{1}{1 + j\omega\tau_{\text{parasit}}} \end{aligned}$$

3.3.2 Two QWs, single active junction (DQW)

Following the derivation of the SQW case, a differential-equation system, linear for variables $\delta N_{\text{DQW}}^{(1)}(t)$, $\delta N_{\text{DQW}}^{(2)}(t)$ and $\delta P_{\text{DQW}}(t)$ can be derived. Following the derivation of the steady-state case, if we set $N_{\text{DQW}}^{(+)}(t) = N_{\text{DQW}}^{(1)}(t) + N_{\text{DQW}}^{(2)}(t)$, we obtain a two-variable differential equation system. Projecting the linear differential system in the Fourier domain, we have:

$$\begin{pmatrix} G_0 \bar{P}_{\text{DQW}} + \frac{1}{\tau_E} + i\omega & \frac{1}{\tau_P} \\ -G_0 \bar{P}_{\text{DQW}} & i\omega \end{pmatrix} \begin{pmatrix} \delta N_{\text{DQW}}^{(+)}(\omega) \\ \delta P_{\text{DQW}}(\omega) \end{pmatrix} = \begin{pmatrix} \frac{\delta I(\omega)}{e} \\ 0 \end{pmatrix}$$

The system is solved as previously:

$$\begin{aligned} \frac{\delta P_{\text{DQW}}}{\delta I}(\omega) &= \frac{\tau_P}{e} \frac{\omega_{R(\text{DQW})}^2}{\omega_{R(\text{DQW})}^2 - \omega^2 + 2i \frac{\omega}{\tau_{R(\text{DQW})}}} \\ \omega_{R(\text{DQW})}^2 &= \frac{G_0 \bar{P}_{\text{DQW}}}{\tau_P} \\ \tau_{R(\text{DQW})} &= \frac{2\tau_E'}{G_0 \bar{P}_{\text{DQW}} \tau_E' + 1} \end{aligned}$$

3.3 Dynamic behavior

And the output power modulation writes:

$$\frac{\delta P_{(\text{DQW})\text{opt}}}{\delta I}(\omega) = \frac{1}{2} \frac{\alpha_m}{\alpha_i + \alpha_m} \frac{h\nu}{e} \frac{\omega_{R(\text{DQW})}^2}{\omega_{R(\text{DQW})}^2 - \omega^2 + 2i \frac{\omega}{\tau_{R(\text{DQW})}}}$$

The parasitic RC transfer function is derived in the same manner as in the SQW case ($\tau_{\text{parasit}} = R_S C_{\text{parasit}}$); the complete frequency response to a current modulation is expressed as follows:

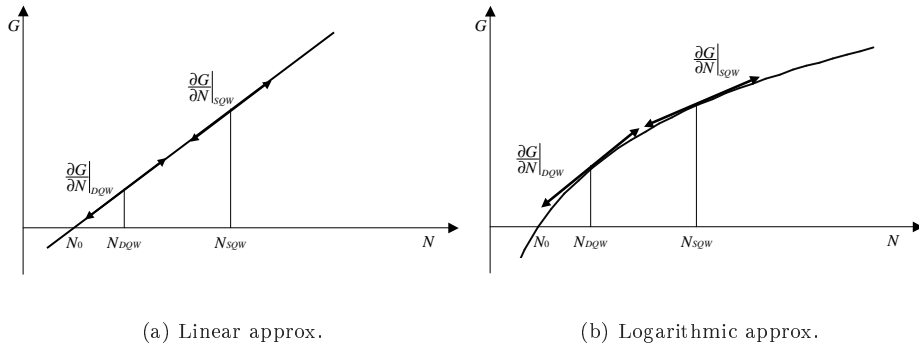
$$\begin{aligned} \frac{\delta S_{\text{DQW}}}{\delta I}(\omega) &= \eta_{d(\text{DQW})} H(\omega) H_{\text{parasit}}(\omega) \\ &= \eta_{d(\text{DQW})} H(\omega) \frac{1}{1 + j\omega\tau_{\text{parasit}}} \end{aligned}$$

Comparison to previous results:

Within our approximations, the transfer function obtained is exactly the same for SQW and DQW. Numerous publications [23–25], including experimental results [24, 25] report on an enhanced modulation bandwidth for multiple-QWs structures as opposed to SQW. This incoherence is explained by the linear gain model we have decided to use to describe the structure behavior. If we consider for instance a logarithmic gain variation $G = G_0 \ln(N/N_0)$ [6, 7], the differential gain $\frac{\partial G}{\partial N}$ decreases as the QWs are filled with carriers. We have seen in the previous section that the carrier population at threshold decreases with the overall number of QWs. As a consequence, an increase of the number of QWs implies an increase in the differential gain.

Figure 3.7 describes the inaccuracy triggered by the approximation of the linear gain.

Figure 3.7 Comparison of the differential gain model whether the gain is assumed to follow a linear or logarithmic variation with the number of carrier



The carrier population at threshold for SQW is twice the carrier population at threshold for DQW. Within a linear gain description, the differential gain $\frac{\partial G}{\partial N}$ is not affected. For a logarithmic gain description however:

$$\frac{\partial G}{\partial N}|_{\text{SQW}} < \frac{\partial G}{\partial N}|_{\text{DQW}}$$

3.3.3 Two active junctions, each including a single QW (CQW)

The active junctions are electrically connected in series. The recycled carriers go through several layers of semiconductor before reaching the second active layer. The carriers therefore undergo some delay τ_{tunnel} while passing through the Esaki tunnel junction. At high frequency, this time delay might be sufficient to imply a shift in the phase of the optical signal modulation of the second active junction as compared to the first active junction. The linearized coupled differential equations system can be expressed as follows:

$$\begin{aligned}\frac{d}{dt}(\delta N_{\text{CQW}}^{(1)}(t)) &= \frac{\delta I(t)}{e} - G_0(\overline{N}_{\text{CQW}}^{(1)} - N_{0(\text{SQW})})\delta P_{\text{CQW}}(t) \\ &\quad - \left[G_0\overline{P}_{\text{CQW}} + \frac{1}{\tau'_E} \right] \delta N_{\text{CQW}}^{(1)}(t) \\ \frac{d}{dt}(\delta N_{\text{CQW}}^{(2)}(t)) &= \frac{\delta I(t + \tau_{\text{tunnel}})}{e} - G_0(\overline{N}_{\text{CQW}}^{(2)} - N_{0(\text{SQW})})\delta P_{\text{CQW}}(t) \\ &\quad - \left[G_0\overline{P}_{\text{CQW}} + \frac{1}{\tau'_E} \right] \delta N_{\text{CQW}}^{(2)}(t) \\ \frac{d}{dt}(\delta P_{\text{CQW}}(t)) &= G_0\overline{P}_{\text{CQW}} \left[\delta N_{\text{CQW}}^{(1)}(t) + \delta N_{\text{CQW}}^{(2)}(t) \right]\end{aligned}$$

Setting as well $N_{\text{CQW}}^{(+)} = N_{\text{CQW}}^{(1)} + N_{\text{CQW}}^{(2)}$, we obtain the two-variable linear equation system in the Fourier domain:

$$\begin{pmatrix} G_0\overline{P}_{\text{CQW}} + \frac{1}{\tau'_E} + i\omega & \frac{1}{\tau_P} \\ -G_0\overline{P}_{\text{CQW}} & i\omega \end{pmatrix} \begin{pmatrix} \delta N_{\text{CQW}}^{(+)}(\omega) \\ \delta P_{\text{CQW}}(\omega) \end{pmatrix} = \begin{pmatrix} \frac{\delta I(\omega)}{e} (1 + e^{i\omega\tau_{\text{tunnel}}}) \\ 0 \end{pmatrix}$$

The system is solved as previously:

$$\begin{aligned}\frac{\delta P_{\text{CQW}}}{\delta I} &= \frac{\tau_P}{e} \frac{\omega_{R(\text{CQW})}^2}{\omega_{R(\text{CQW})}^2 - \omega^2 + 2i\frac{\omega}{\tau_{R(\text{CQW})}}} (1 + e^{i\omega\tau_{\text{tunnel}}}) \\ \omega_{R(\text{CQW})}^2 &= \frac{G_0\overline{P}_{\text{CQW}}}{\tau_P} \\ \tau_{R(\text{CQW})} &= \frac{2\tau'_E}{G_0\overline{P}_{\text{CQW}}\tau'_E + 1}\end{aligned}$$

And the output power modulation writes:

$$\frac{\delta S_{\text{CQW}}}{\delta I}(\omega) = \frac{1}{2} \frac{\alpha_m}{\alpha_i + \alpha_m} \frac{h\nu}{e} \frac{\omega_{R(\text{CQW})}^2}{\omega_{R(\text{CQW})}^2 - \omega^2 + 2i\frac{\omega}{\tau_{R(\text{CQW})}}} (1 + e^{i\omega\tau_{\text{tunnel}}})$$

To this intrinsic frequency response, we convolute the parasitic frequency response. Here the effect can be more important since the overall impedance is greatly changed as compared to the SQW case (as can be seen in chapter 2). For the resistive part, we need to add an additional tunnel resistance ($R_{S(\text{CQW})} = R_{S(\text{SQW})} + R_{\text{tunnel}}$); for the capacitive part, the quantitative effect on $C_{\text{parasit}(\text{CQW})}$ of cascading junctions cannot be easily foreseen, but it deserves

3.3 Dynamic behavior

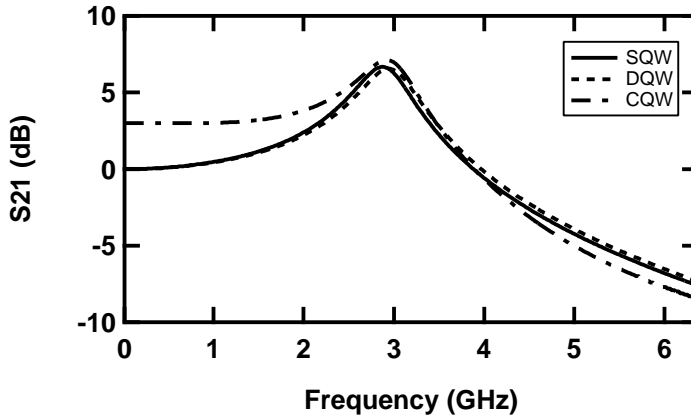
taking into account. We have :

$$\begin{aligned}\frac{\delta S_{\text{CQW}}}{\delta I}(\omega) &= \eta_{d(\text{CQW})} H(\omega) (1 + e^{i\omega\tau_{\text{tunnel}}}) H_{\text{parasit}}(\omega) \\ &= \eta_{d(\text{CQW})} H(\omega) (1 + e^{j\omega\tau_{\text{tunnel}}}) \frac{1}{1 + i\omega\tau_{\text{parasit}}}\end{aligned}$$

$$\Rightarrow \tau_{\text{parasit}} = R_{\text{S}(\text{CQW})} C_{\text{parasit}(\text{CQW})}.$$

Figure 3.8 compares the frequency response for SQW, DQW, and CQW at equal bias rate. The output power is almost the same in the different cases. The results are normalized to the response of the SQW structure at frequency null. The parameter values used for the numerical application are listed in appendix A, on page 197.

Figure 3.8 Compared frequency response characteristics for SQW, DQW, and CQW at equal bias rate.



Comparison to previous results

The devices are compared for equal bias rate ($I = 2I_{\text{th}}$). The slight bandwidth improvement observed for DQW is explained by the slightly higher bias point.

No RF bandwidth improvement can be expected from cascaded active junctions. The delay introduced for carriers to go through the tunnel junction, and the increased series resistance limit the modulation bandwidth, as compared to the modulation bandwidth obtained for SQW and DQW by introducing a low-pass filter additional factor to the frequency response. At best, τ_{tunnel} is sufficiently small so that its influence does not affect too much the frequency response.

In addition, the low frequency response to modulation is increased by a factor $(1 + e^{i\omega\tau_{\text{tunnel}}})$, which is close to 2 when ω is small ($\omega \rightarrow 0$), resulting in a 3 dB-improvement for the CQW structure at low frequency. The effect of external differential efficiency enhancement was already described in chapter 2, and mentioned in section 3.2. The delay introduced by the tunnel process limits this phenomenon for high-frequencies (namely, if $\omega \gtrsim \frac{1}{\tau_{\text{tunnel}}}$).

3.4 RIN calculation

Unfortunately, there is no need to modulate the laser to obtain a high-frequency modulation. Even with no intended modulation, the fluctuations of fundamental parameters occurring in the laser structure induces an intensity (and also a phase) modulation of the optical signal. In this section, we intend to calculate this self-established noise modulation for bipolar cascade laser and compare it to the noise of standard lasers.

3.4.1 Noise definitions

Let us consider a laser structure current-biased above threshold. The light power S (in Watts) of the laser beam fluctuates around its time-averaged value:

$$S(t) = \bar{S} + \delta S(t)$$

The parameter used to characterize the intensity noise behavior of a laser device is the relative intensity noise (RIN), usually expressed in dB, and defined as [26]:

$$RIN_{\text{tot}} \stackrel{\text{def}}{=} \frac{\overline{\delta S(t)^2} - \overline{\delta S_{\text{shot}}(t)^2}}{\bar{S}(t)^2} \quad (3.25)$$

☞ $\overline{\delta S_{\text{shot}}(t)^2}$ is the mean square shot noise fluctuations [26]. This term is added to ensure that the RIN definition is white and not dependent of the attenuation of the optical signal. The signal might actually be attenuated before detection for noise measurements in order not to saturate the photodetector.

☞ The Agrawal definition $RIN_{\text{tot}} = \frac{\overline{\delta S(t)^2}}{\bar{S}(t)^2}$ is dependent on the attenuation [18, 27].

Following Parseval’s theorem, the time averaged square value of the fluctuations can be expressed in terms of the single-sided noise spectral density:

$$\overline{\delta S(t)^2} = \int_0^{2\pi\Delta f} W_S(\omega) d\omega$$

☞ Δf is the overall bandwidth of interest

According to the Wiener-Khinchin relations for stationary noise signals, the noise spectral density is the Fourier transform of the self-correlation function:

$$W_S(\omega) = \int \overline{\delta S(t)\delta S^*(t-\tau)} e^{-i\omega\tau} d\tau$$

Injecting this relation into equation 3.25 carries a severe drawback: the noise is integrated over the whole bandwidth of interest Δf and is not dependent of the pulsation ω . For narrow-band analog optical transmission, the noise spectral distribution is a major consideration since all the data is carried at the vicinity of a given RF frequency.

As a consequence, we prefer expressing the spectrally dependent RIN (in dB/Hz) and we define it as:

$$RIN(\omega) = \frac{\int_{\omega}^{\omega+2\pi\delta f} W_S(\omega) d\omega}{2\pi\delta f \bar{S}(t)^2} - \frac{W_{\text{shot}}}{\bar{S}(t)^2}$$

3.4 RIN calculation

- ☞ δf is the spectral resolution of the detection system. It should be as small as possible (ideally $\delta f \rightarrow 0$).
- ☞ W_{shot} is the shot noise spectral density, assumed to be white by definition.

When δf is sufficiently small, $W_P(\omega)$ is constant over δf and the definition simplifies to:

$$RIN(\omega) \stackrel{\text{def}}{=} \frac{W_S(\omega)}{S(t)^2} - \frac{W_{\text{shot}}}{S(t)^2} \quad (3.26)$$

- ☞ Since $W_S(\omega)$ has the unit of $(\text{power})^2 \cdot (\text{Hz})^{-1}$, this definition of RIN is in $(\text{Hz})^{-1}$, and is usually expressed in $(\text{dB}) \cdot (\text{Hz})^{-1}$.

To go further towards the RIN calculation, we need the spectral density of the output power noise $W_S(\omega)$.

Using the Wiener-Khinchin relations, and for stationary, ergodic processes, it can be proven (see for instance [6], Appendix XIII) that the spectral density is related to the frequency domain correlation function by the expression:

$$W_S(\omega) = \frac{1}{2\pi} \int \langle \delta S_{\text{SQW}}(\omega) \delta S_{\text{SQW}}^*(\omega') \rangle d\omega' \quad (3.27)$$

- ☞ since $\delta X(\omega)$ is the Fourier transform of $\delta X(t)$, it has the unit of $(\delta X(t)) \cdot (\text{seconds})$.
- ☞ Here $\langle \rangle$ denotes the statistics ensemble average, but is equivalent to time average for ergodic processes.

As a consequence, all we need to calculate is the frequency domain correlation function: $\langle \delta S_{\text{SQW}}(\omega) \delta S_{\text{SQW}}^*(\omega') \rangle$.

3.4.2 Spectral density of the output power noise

We take the SQW case to derive completely the equations, but the spectral density of the output power noise can be obtained from any of the three matrix expressions of the linear-coupled-equation system we found in the previous section. Only the Langevin noise sources F_X will differ while considering different configurations. In equation 3.20, the current modulation is set to zero:

$$\begin{pmatrix} \delta N_{\text{SQW}} \\ \delta P_{\text{SQW}} \end{pmatrix} = \begin{pmatrix} G_0 \bar{P}_{\text{SQW}} + \frac{1}{\tau_E} + i\omega & \frac{1}{\tau_P} \\ -G_0 \bar{P}_{\text{SQW}} & i\omega \end{pmatrix}^{-1} \begin{pmatrix} F_{N_{\text{SQW}}} \\ F_{P_{\text{SQW}}} \end{pmatrix}$$

The matrix calculation gives the following result, with notations from equation 3.24 on page 84:

$$\delta P_{\text{SQW}}(\omega) = \frac{H(\omega)}{\omega_R^2} \left[\omega_R^2 \tau_P F_{N_{\text{SQW}}}(\omega) + \left(\frac{2}{\tau_R} + i\omega \right) F_{P_{\text{SQW}}}(\omega) \right]$$

The output power fluctuations are given by equation 3.22 and reads:

$$\delta S_{\text{SQW}}(\omega) = \eta_0 \delta P_{\text{SQW}}(\omega) + F_{S_{\text{SQW}}}(\omega)$$

- ☞ Notice that $F_X(\omega)$ has no dimension, whereas $F_S(\omega)$ has the dimension of (energy).

3. “Component level” point of view: a comprehensive model of the integrated device

We multiply both hand-sides by $\delta S_{\text{SQW}}^*(\omega')$ and take the time-average. The self-correlation function for the output power writes:

$$\begin{aligned} \langle \delta S_{\text{SQW}}(\omega) \delta S_{\text{SQW}}^*(\omega') \rangle &= \eta_0^2 \langle \delta P_{\text{SQW}}(\omega) \delta P_{\text{SQW}}^*(\omega') \rangle \\ &+ 2\Re\{\eta_0 \langle \delta P_{\text{SQW}}(\omega) F_{\text{SSQW}}^*(\omega') \rangle\} \quad (3.28) \\ &+ \langle F_{\text{SSQW}} \rangle \quad (3.29) \end{aligned}$$

⇨ $\Re\{X\}$ denotes the real part of the expression X .

⇨ The Langevin noise forces are: $\langle F_{XY_{\text{SQW}}} \rangle = \langle F_{X_{\text{SQW}}}(\omega) F_{Y_{\text{SQW}}}^*(\omega') \rangle$.

We now calculate the different terms of equation 3.29. The first term is the self-correlation function of the photon population fluctuation. It writes:

$$\begin{aligned} \eta_0^2 \langle \delta P_{\text{SQW}}(\omega) \delta P_{\text{SQW}}^*(\omega') \rangle &= \eta_0^2 \frac{|H(\omega)|^2}{\omega_{R(\text{SQW})}^4} \left[\tau_P^2 \omega_{R(\text{SQW})}^4 \langle F_{\text{NNSQW}} \rangle \right. \\ &\left. + 4 \frac{\tau_P}{\tau_R} \omega_{R(\text{SQW})}^2 \langle F_{\text{NPSQW}} \rangle + \left(\frac{4}{\tau_R^2} + \omega^2 \right) \langle F_{\text{PPSQW}} \rangle \right] \end{aligned}$$

The second term describes the cross-correlation between the output fluctuations and the photon population. We find:

$$\begin{aligned} &2\Re\{\eta_0 \langle \delta P_{\text{SQW}}(\omega) F_{\text{SSQW}}^*(\omega') \rangle\} \\ &= 2\Re\left\{ \eta_0 \frac{H(\omega)}{\omega_{R(\text{SQW})}^2} \left(\omega_{R(\text{SQW})}^2 \tau_P \langle F_{\text{NNSQW}} \rangle + \left(\frac{2}{\tau_R} + i\omega \right) \langle F_{\text{PPSQW}} \rangle \right) \right\} \\ &= 2\eta_0 \frac{|H(\omega)|^2}{\omega_{R(\text{SQW})}^4} \Re\left\{ \left((\omega_{R(\text{SQW})}^2 - \omega^2) - 2i \frac{\omega}{\tau_R} \right) \right. \\ &\quad \left. \times \left[\omega_{R(\text{SQW})}^2 \tau_P \langle F_{\text{NNSQW}} \rangle + \left(\frac{2}{\tau_R} + i\omega \right) \langle F_{\text{PPSQW}} \rangle \right] \right\} \\ &= 2\eta_0 \frac{|H(\omega)|^2}{\omega_{R(\text{SQW})}^2} \left\{ \omega_{R(\text{SQW})}^2 \tau_P \langle F_{\text{NNSQW}} \rangle + \frac{2}{\tau_R} \langle F_{\text{PPSQW}} \rangle - \omega^2 \tau_P \langle F_{\text{PPSQW}} \rangle \right\} \end{aligned}$$

The last term in equation 3.29 is characteristic of the partition noise at the output mirror.

We combine these expressions into a single one and write the correlation function of the output power fluctuations as:

$$\langle \delta S_{\text{SQW}}(\omega) \delta S_{\text{SQW}}^*(\omega') \rangle = \eta_0^2 \frac{|H(\omega)|^2}{\omega_{R(\text{SQW})}^4} \{a'_1 + a'_2 \omega^2\} + \langle F_{\text{SSQW}} \rangle$$

with:

$$\begin{aligned} a'_1 &= \tau_P^2 \omega_{R(\text{SQW})}^4 \langle F_{\text{NNSQW}} \rangle + 4 \frac{\tau_P}{\tau_R} \omega_{R(\text{SQW})}^2 \langle F_{\text{NPSQW}} \rangle + 4 \frac{1}{\tau_R} \langle F_{\text{PPSQW}} \rangle \\ &\quad + 2 \frac{1}{\eta_0} \tau_P \omega_{R(\text{SQW})}^4 \langle F_{\text{NNSQW}} \rangle + \frac{1}{\eta_0} \frac{2}{\tau_R} \omega_{R(\text{SQW})}^2 \langle F_{\text{PPSQW}} \rangle \\ a'_2 &= \langle F_{\text{PPSQW}} \rangle + 2 \frac{1}{\eta_0} \tau_P \omega_{R(\text{SQW})}^2 \langle F_{\text{PPSQW}} \rangle \end{aligned}$$

3.4 RIN calculation

The next step is to integrate over the variable ω' and to divide by 2π , in order to obtain, accordingly to equation 3.27, the expression of the output power noise spectral density :

$$W_{S_{SQW}} = \eta_0^2 \frac{|H(\omega)|^2}{\omega_{R(SQW)}^4} \{a_1 + a_2\omega^2\} + D_{SS} \quad (3.30)$$

with:

$$\begin{aligned} a_1 &= \tau_P^2 \omega_{R(SQW)}^4 D_{NN} + 4 \frac{\tau_P}{\tau_R} \omega_{R(SQW)}^2 D_{NP} + 4 \frac{1}{\tau_R^2} D_{PP} \\ &\quad + 2 \frac{1}{\eta_0} \tau_P \omega_{R(SQW)}^4 D_{NS} + \frac{1}{\eta_0} \frac{2}{\tau_R} \omega_{R(SQW)}^2 D_{PS} \\ a_2 &= D_{PP} + 2 \frac{1}{\eta_0} \tau_P \omega_{R(SQW)}^2 D_{PS} \end{aligned}$$

⇨ $D_{XY} = \frac{1}{2\pi} \int \langle F_X(\omega) F_Y^*(\omega') \rangle d\omega'$ are the Langevin diffusion coefficients .

⇨ D_{XY} has the dimension of (power)².(Hz)⁻¹; D_{XS} has the dimension of (power); and D_{SS} has the dimension of (Hz).

Injecting this expression into equation 3.26, we eventually get the laser RIN expression:

$$\begin{aligned} RIN_{SQW}(\omega) &= \frac{W_{S_{SQW}}(\omega)}{\overline{S}_{SQW}^2} - \frac{W_{shot_{SQW}}}{\overline{S}_{SQW}^2} \\ &= \frac{\eta_0^2}{\overline{S}_{SQW}^2} \frac{|H(\omega)|^2}{\omega_{R(SQW)}^4} \{a_1 + a_2\omega^2\} + \frac{D_{SS} - W_{shot_{SQW}}}{\overline{S}_{SQW}^2} \end{aligned}$$

We will see, in the following paragraph, that D_{SS} and $W_{shot_{SQW}}$ exactly compensate. We can therefore write the expression of the relative intensity output power noise:

$$RIN_{SQW}(\omega) = \frac{\eta_0^2}{\overline{S}_{SQW}^2} \frac{|H(\omega)|^2}{\omega_{R(SQW)}^4} \{a_1 + a_2\omega^2\} \quad (3.31)$$

Similarly to the frequency response (c.f. equation 3.24), the RIN follows a $(a_1 + a_2\omega^2)|H(\omega)|^2$ dependence. It is not surprising to find that the natural resonance of the carrier-photon system amplifies any existing noise near that resonance frequency. Away from this resonance however, the laser “quiets”. For opto-RF application requiring low-noise laser source (such as for instance external modulation links), it might be interesting to design the laser so that the resonance is far from the application bandwidth. Studies still under development propose lasers with either resonance frequency pushed forward to high frequencies for low-frequency applications, or resonance frequency maintained at a very low frequency for high-frequency RF applications [28]. It is not as odd as it may seem to design a 20 GHz directly-modulated laser for opto-RF applications around 2 GHz!

In order to estimate the magnitude of the intensity noise, we need to calculate the Langevin diffusion coefficients D_{XY} .

3.4.3 Deriving the Langevin noise diffusion coefficients

The Langevin noise sources $F_X(t)$ do not have a physical reality. They are just a mathematical artifact to calculate the noise via the Langevin method. The only parameters that have a physical reality are precisely the Langevin diffusion coefficients defined by:

$$D_{XY} \stackrel{\text{def}}{=} \frac{1}{2\pi} \int \langle F_X(\omega) F_Y^*(\omega') \rangle d\omega'$$

The Langevin approach describes the intensity noise exclusively as a result of the inherent shot noise of every particle energy transfer event between particle reservoirs [6, 29, 30]: leakage, recombinations, absorption, and photon flow out of the laser cavity. For each event we can define and estimate the magnitude of the diffusion coefficient associated. Since each event is considered as having a shot noise character, the diffusion coefficient is equal to the average number of event occurring per time unit. If the injection rate for SQW is $\frac{\bar{I}}{e}$ carrier per second, the diffusion coefficient associated to this event can be written as: $D_I = \frac{\bar{I}}{e}$. The diffusion coefficient for the other events affecting the carrier population reservoir are calculated the same way (cf. equations 3.1 and 3.2):

- Non resonant recombination (non-radiative or spontaneous), $D_{NR} = \frac{\bar{N}_{SQW}}{\tau_E}$

⇒ We take here the linear approximation to recombination, as for the calculation of steady-state parameters.

- Resonant recombination, $D_R = G_0 \bar{N}_{SQW}$
- Resonant absorption, $D_A = G_0 N_0$

These elementary noises are not correlated. The Langevin noise diffusion coefficients associated to the considered reservoir is then the sum of the diffusion factors of the event affecting the reservoir:

$$D_{NN_{SQW}} = \sum_{\substack{X \\ \text{affect.} \\ \text{reservoir}}} D_X = \frac{\bar{I}}{e} + \frac{\bar{N}_{SQW}}{\tau_E} + G_0(\bar{N}_{SQW} + N_0)$$

The diffusion coefficient for the photon population is calculated as well:

$$D_{PP_{SQW}} = G_0(\bar{N}_{SQW} + N_0) + \beta \frac{\bar{N}_{SQW}}{\tau_E} + \frac{\bar{P}_{SQW}}{\tau_P}$$

There is nevertheless some correlation between the elementary noise of different reservoirs. For instance, a photon created by stimulated emission removes a carrier pair from the carrier reservoir. These negative-correlations between reservoirs are taken into account with the cross-reservoir Langevin noise diffusion coefficients which are equal to the rate of the correlated events between the considered reservoirs with a minus sign:

$$D_{NP_{SQW}} = D_{PN_{SQW}} = - \sum_{\substack{X \\ \text{betw.} \\ \text{reservoirs}}} D_X = -G_0(\bar{N}_{SQW} + N_0)$$

This negative-correlation strength between the carrier and the photon reservoirs is an intrinsic stabilization response of the laser. It is therefore relevant to notice that it reduces the overall RIN.

3.4 RIN calculation

3.4.3.1 Output power noise

The diffusion coefficient involving particles are different for the different study-cases. However, we have postulated that the optical modal distribution inside the laser cavity is the same for all three cases. Therefore the diffusion coefficient involving the output power will be the same and can be calculated here.

We consider that the noise created at the output facet is random-killing partition noise. We first convert the output power noise source $F_S(\omega)$ to number per time unit, and apply the same method of calculation previously used for the reservoirs' diffusion coefficients [6]:

$$\begin{aligned}\frac{1}{(h\nu)^2}D_{SS} &= \frac{\overline{S}}{h\nu} \\ D_{SS} &= h\nu\overline{S}\end{aligned}$$

- ☞ We find the expression of the shot noise. It proves that even if the photon population was perfectly constant in the laser cavity, the output light beam would always carry some noise. In typical use of lasers, the output power noise floor cannot go below the fundamental limit of shot noise.
- ☞ Even if shot noise is the floor limit for the Agrawal definition of RIN [18], the Schimpe definition [26] subtracts this term to evaluate the laser RIN. As we already foresaw in the previous section, D_{SS} exactly cancels out W_{shotsQW} , leading to the RIN expression of equation 3.31.

We also derive the diffusion coefficients accounting for the cross-correlation between the output power and the particles population. No direct correlation exists in our model between the carrier population and the output power:

$$D_{NS} = 0$$

For the photon population however, we write:

$$\begin{aligned}\frac{1}{h\nu}D_{PS} &= -\frac{\overline{S}}{h\nu} \\ D_{SS} &= -\overline{S}\end{aligned}$$

- ☞ This negative-correlation term reduces the laser noise. By a careful setup, it is possible to make use of this anti-correlation term to reduce the laser noise even below shot noise (squeezing) [4].

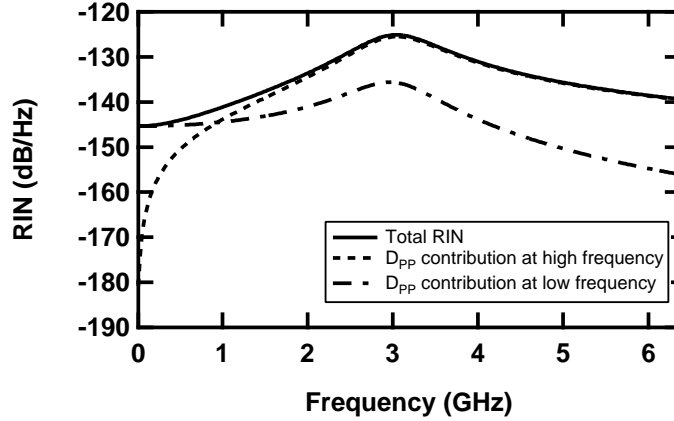
3.4.3.2 Comparison of the three cases

Table 3.1 summarizes the Langevin diffusion coefficients calculated with the previously described method.

Figure 3.9 plots the evolution with the RF frequency of the laser RIN as calculated with equation 3.31. It also displays the major contributions of the RIN which comes from the term $4\frac{\tau_P}{\tau_R}\omega_{R(\text{SQW})}^2 D_{NP} + 4\frac{1}{\tau_R}D_{PP}$ in a_1 of equation 3.30 at low frequency, and D_{PP} in a_2 at high frequency. The output power noise mainly arises from photon noise in our structure. The coefficients used for calculation are listed in annex A.

3. “Component level” point of view: a comprehensive model of the integrated device

Figure 3.9 Evolution with ω of the laser RIN and its main components.



For the DQW case, we set (as in the previous sections):

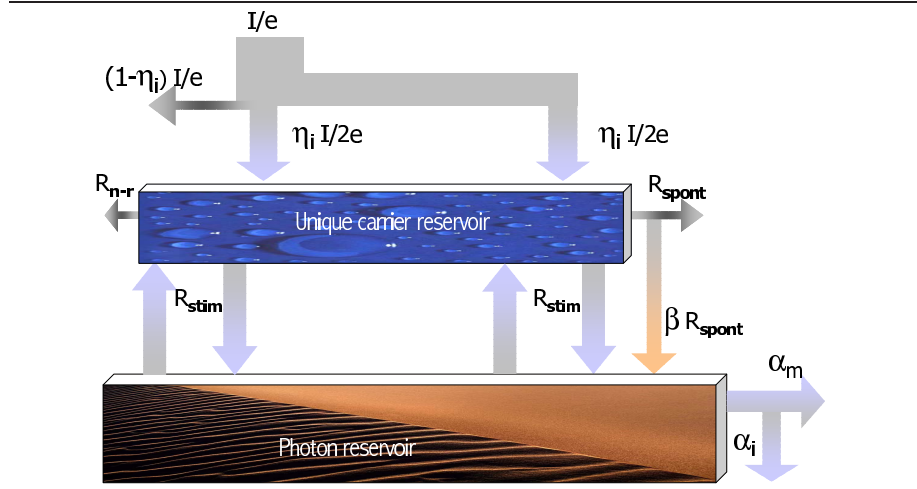
$$N_{\text{DQW}}^{(+)}(t) = N_{\text{DQW}}^{(1)}(t) + N_{\text{DQW}}^{(2)}(t)$$

We sum the two differential equations describing the carrier populations evolution, and therefore we write the Langevin composed noise source:

$$F_{N_{\text{DQW}}^{(+)}}(t) = F_{N_{\text{DQW}}^{(1)}}(t) + F_{N_{\text{DQW}}^{(2)}}(t)$$

For a given current source, when a carrier recombines in the first QW, it is not available for a recombination in the second QW. It therefore exists a correlation between recombinations in the first and in the second QW of the DQW structure. To account for this correlation, the simplest way to derive the Langevin diffusion coefficients is to consider the two carrier reservoirs as a single reservoir. Figure 3.10 shows the schematic reservoir model used to derive the noise equations for DQW.

Figure 3.10 “Reservoir” model used to derive the noise diffusion coefficients for DQW.



3.4 RIN calculation

The recombination noise diffusion coefficients are calculated the same way:

$$\begin{aligned}
D_{\text{NN}_{\text{DQW}}^{(+)}} &= \sum_{\substack{X \\ \text{affect.} \\ \text{reservoir}}} D_X \\
&= \frac{\bar{I}}{2e} + \frac{\bar{I}}{2e} + \frac{\bar{N}_{\text{DQW}}^{(1)} + \bar{N}_{\text{DQW}}^{(2)}}{\tau_E} + G_0(\bar{N}_{\text{DQW}}^{(1)} + N_0) \\
&\quad + G_0(\bar{N}_{\text{DQW}}^{(2)} + N_0) \\
D_{\text{PN}_{\text{DQW}}^{(+)}} &= -G_0(\bar{N}_{\text{DQW}}^{(1)} + N_0) - G_0(\bar{N}_{\text{DQW}}^{(2)} + N_0) \\
D_{\text{PP}_{\text{DQW}}} &= G_0(\bar{N}_{\text{DQW}}^{(1)} + N_0) + G_0(\bar{N}_{\text{DQW}}^{(2)} + N_0) + \beta \frac{\bar{N}_{\text{DQW}}^{(1)} + \bar{N}_{\text{DQW}}^{(2)}}{\tau_E} \\
&\quad + \frac{\bar{P}_{\text{DQW}}}{\tau_P}
\end{aligned}$$

The results of calculation are given in table 3.1.

For the CQW-case, a carrier recombining in the first active region will almost directly be available for recombination in the second active region. If we consider that the carrier reservoirs constitute a single reservoir, we can write that photons are created in the first active junction without loss of carriers available in the reservoir. The noise diffusion coefficients yields to:

$$\begin{aligned}
D_{\text{NN}_{\text{CQW}}^{(+)}} &= \frac{\bar{I}}{e} + \frac{\bar{N}_{\text{CQW}}^{(2)}}{\tau_E} + G_0(\bar{N}_{\text{CQW}}^{(2)} + N_0) \\
D_{\text{PN}_{\text{CQW}}^{(+)}} &= -G_0(\bar{N}_{\text{CQW}}^{(2)} + N_0) \\
D_{\text{PP}_{\text{CQW}}} &= G_0(\bar{N}_{\text{CQW}}^{(1)} + N_0) + G_0(\bar{N}_{\text{CQW}}^{(2)} + N_0) \\
&\quad + \beta \frac{\bar{N}_{\text{CQW}}^{(1)} + \bar{N}_{\text{CQW}}^{(2)}}{\tau_E} + \frac{\bar{P}_{\text{CQW}}}{\tau_P}
\end{aligned}$$

☞ The recombinations in the first active region and the current injection from the first to the second active region are not taken into account for calculating

$$D_{\text{NN}_{\text{CQW}}^{(+)}}$$

☞ The radiative recombinations in the first active region do not deplete the carrier reservoir $\bar{N}_{\text{CQW}}^{(1)} + \bar{N}_{\text{CQW}}^{(2)}$. Therefore they are not taken into account for calculating $D_{\text{PN}_{\text{CQW}}^{(+)}}$

Cascading several active regions limits the noise originating from carrier shot noise. The noise compensation due to the emission-depletion coupled mechanisms is also decreased. The noise originating from photon shot noise however remains unchanged.

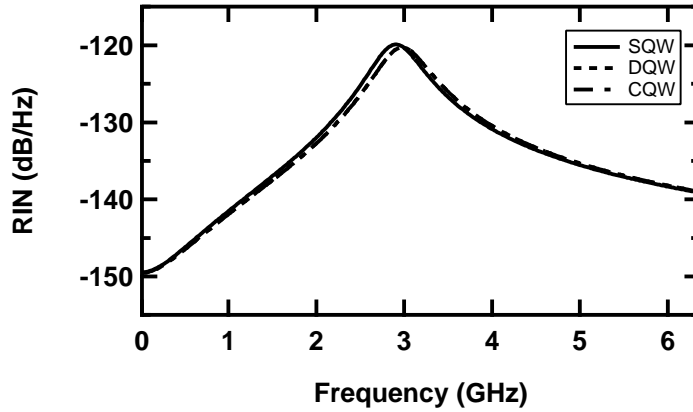
The Langevin diffusion coefficients for CQW are summed up in table 3.1. Figure 3.11 compares the RIN estimation for the three configurations at equal bias rate ($I = 2I_{\text{th}}$).

3. “Component level” point of view: a comprehensive model of the integrated device

Langevin noise forces	Expressions
<i>one QW, one active junction (SQW)</i> $D_{NN_{SQW}}$ $D_{NP_{SQW}}$ $D_{PP_{SQW}}$	$\frac{\bar{I}}{e} + \frac{\bar{N}_{SQW}}{\tau_E} + (2n_{sp} - 1) \frac{\bar{P}_{SQW}}{\tau_P}$ $-(2n_{sp} - 1) \frac{\bar{P}_{SQW}}{\tau_P} - \beta \frac{\bar{N}_{SQW}}{\tau_E}$ $2n_{sp} \frac{\bar{P}_{SQW}}{\tau_P} + \beta \frac{\bar{N}_{SQW}}{\tau_E}$ <p>(with $n_{sp} = \frac{\bar{N}_{SQW}}{\bar{N}_{SQW} - N_0}$)</p>
<i>two QWs, one active junction (DQW)</i> $D_{NN^{(+)}_{DQW}}$ $D_{N^{(+)}P_{DQW}}$ $D_{PP_{DQW}}$	$\frac{\bar{I}}{e} + \frac{\bar{N}_{DQW}^{(+)}}{\tau_E} + (2n_{sp(DQW)} - 1) \frac{\bar{P}_{DQW}}{\tau_P}$ $-(2n_{sp(DQW)} - 1) \frac{\bar{P}_{DQW}}{\tau_P} - \beta \frac{\bar{N}_{DQW}^{(+)}}{\tau_E}$ $2n_{sp(DQW)} \frac{\bar{P}_{DQW}}{\tau_P} + \beta \frac{\bar{N}_{DQW}^{(+)}}{\tau_E}$ <p>(with $n_{sp(DQW)} = \frac{\bar{N}_{DQW}^{(+)}}{\bar{N}_{DQW}^{(+)} - 2N_0}$)</p>
<i>two active junctions one QW per active junction (CQW)</i> $D_{NN^{(+)}_{CQW}}$ $D_{N^{(+)}P_{CQW}}$ $D_{PP_{CQW}}$	$\frac{\bar{I}}{e} + \frac{\bar{N}_{CQW}^{(2)}}{\tau_E} + (2n_{sp(CQW)} - 1) \frac{\bar{P}_{CQW}}{2\tau_P}$ $-(2n_{sp(CQW)} - 1) \frac{\bar{P}_{CQW}}{2\tau_P} - \beta \frac{\bar{N}_{CQW}^{(2)}}{\tau_E}$ $2n_{sp(CQW)} \frac{\bar{P}_{CQW}}{\tau_P} + \beta \frac{\bar{N}_{CQW}^{(+)}}{\tau_E}$ <p>(with $n_{sp(CQW)} = \frac{\bar{N}_{CQW}^{(+)}}{\bar{N}_{CQW}^{(+)} - 2N_0}$)</p>

Table 3.1: Summary of the diffusion coefficient estimated with the shot noise Langevin method. n_{sp} is the population inversion factor.

Figure 3.11 Compared RIN characteristics for SQW, DQW, and CQW for equal bias rate.



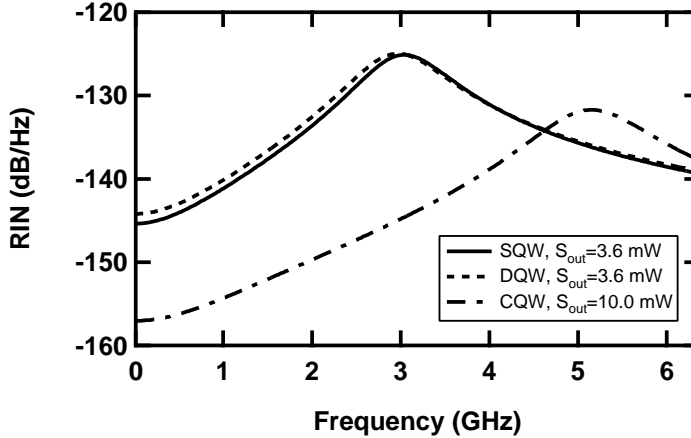
3.5 Conclusion

3.4.3.3 Conclusion on the possible RIN improvement

The RIN characteristics are displayed for the same bias rate and thus at almost equal photon population in the cavity. As seen from figure 3.11, the major contribution of the RIN comes from the photon noise. This feature is also true for cascaded devices. In opposition to what was predicted and experimentally verified in chapter 2 with discrete lasers, the RIN is not expected to be drastically ameliorated by cascading monolithically laser junctions. Integrating active regions in the same optical mode therefore annihilate the expected advantages of reducing the RIN.

Comparing now on figure 3.12 the RIN characteristics at a given current ($I = 60$ mA), since the photon population is higher for the CQW case (cf. figure 3.6), the RIN decreases accordingly.

Figure 3.12 Compared RIN characteristics for SQW, DQW, and CQW for equal bias current.



In order to play its role of RIN reducer, according to the results of chapter 2, the cascaded device needs to primarily deliver a higher output optical power.

This result appears in contradiction with other (theoretical) results from the literature [2]. In fact the bipolar cascade lasers studied in this article from the MIT have separate optical cavities, one cavity per active region. The comparison is besides carried out with a constant photon density in the laser cavity(ies). This comparison results obviously in an increased optical output power (in comparison with single-active-region lasers), and thus a decreased amplitude noise, in agreement with our model.

3.5 Conclusion

In this chapter we have used the rate equations formalism to build a comprehensive, but still accurate model for the simulation of the steady-state, as well as the dynamic expected behavior of single-transverse mode bipolar cascade lasers. In order to discriminate the improvement due to the use of several QWs and the improvement due to the cascading of active junctions, we have compared in a single formalism three structures: one single-QW structure (SQW),

3. “Component level” point of view: a comprehensive model of the integrated device

one double-QW structure (DQW), and one double-active-junction single-QW structure (CQW).

In continuity with chapter 2, we find that the steady-state differential efficiency is higher in the case of cascaded active regions (CQW), as compared to both other cases (SQW and DQW). In the specific case of single-transverse-mode structures, the current threshold is expected to decrease almost linearly with the number of cascaded junctions.

The integrated device pushes back the bandwidth limitations discussed in the case of discrete components described in chapter 2. The overall bandwidth is expected to remain close to the bandwidth of a single-active-region laser with comparable design.

We eventually investigated over the RIN characteristics expected from single-transverse-mode bipolar cascade. Considering that the major RIN contribution comes from the photon noise, the RIN is not expected to decrease as in the case of discrete-laser beam combining, unless the overall output power is increased.

These expectations have to be validated by experimentation. In order to pave the way for a device realization, we describe in the following chapter, a self-consistent, “electronic level” model for the design of bipolar cascade lasers.

Bibliography

- [1] J. K. Kim et al. Epitaxially-stacked multiple-active-region 1.55 μm lasers for increased differential efficiency. *Applied Physics Letters*, 74(22):3251–3253, May 1999.
- [2] F. Rana et al. Photon noise and correlations in semiconductor cascade lasers. *Applied Physics Letters*, 76(9):1083–1085, Feb 2000.
- [3] F. Jeremie, J.L. Vey, and P. Gallion. Optical corpuscular theory of semiconductor laser intensity noise and intensity squeezed-light generation. *Journal of Optical Society of America B*, 14-2(3):250–257, Feb. 1997.
- [4] F. Jeremie, C. Chabran, and P. Gallion. Room temperature generation of amplitude squeezed light from 1550 nm distributed feedback semiconductor laser. *Journal of Optical Society of America B*, 16-3(3):460–464, Mar. 1999.
- [5] P. Gallion. Bruit dans les lasers à semiconducteur. ENST Paris Classes document, 2000.
- [6] Larry A. Coldren and Scott W. Corzine. *Diode Lasers and Photonic Integrated Circuits*. Wiley, New York, NY, USA, 1995.
- [7] E. Rosencher and B. Vinter. *Optoelectronics*. Cambridge University Press, Cambridge, 2002.
- [8] E. Rosencher and B. Vinter. *Optoelectronique*. Dunod, Paris, 2nd edition, 2002.
- [9] D. McDonald and R.F. O’Dowd. Comparison of Two- and Three-Level Rate Equations in the Modeling of Quantum-Well Lasers. *IEEE Journal of Quantum Electronics*, 31(11):1927–1934, Nov. 1995.
- [10] E. Zielinsky et al. Excitonic transitions and exciton damping processes in InGaAs/InP. *Journal of Applied Physics*, 59(6):2196–2203, Mar. 1986.
- [11] CrossLight Software Inc. *PICS3D User’s manual*, 2000.
- [12] R. N. Hall. Electron-hole recombination in germanium. *Physical Review*, 87:387, 1952.
- [13] W. Shockley and W.T. Read. Statistics of the recombinations of holes and electrons. *Physical Review*, 87(5):835–842, Sept. 1952.
- [14] Ioffe Physico-Technical Institute. Physical Properties of Semiconductors. <http://www.ioffe.rssi.ru/SVA/NSM/Semicond/index.html>.

-
- [15] Olivier Gilard. *Contribution à la modélisation de diodes laser à puits quantiques contraints pour Télécommunications optiques*. PhD thesis, Université Paul Sabatier, Toulouse, France, Jan. 1999.
- [16] E.P. O'Reilly et al. Band-structure engineering in strained semiconductor lasers. *IEEE Journal of Quantum Electronics*, 30(2):366, Feb. 1994.
- [17] J. Piprek et al. What Limits the Maximum Output Power of Long-Wavelength AlGaInAs/InP Laser Diodes? *IEEE Journal of Quantum Electronics*, 38(9):1253–1259, Sept. 2002.
- [18] G.P. Agrawal and N.K. Dutta. *Long-Wavelength Semiconductor Lasers*. Van Nostrand Reinhold, 1986.
- [19] G. Rossi et al. SPICE Simulation for Analysis and Design of Fast 1.55 μm MQW Laser Diodes. *Journal of Lightwave Technology*, 16(109):1509–1516, Aug. 1998.
- [20] J. Piprek, P. Abraham, and J.E. Bowers. Efficient Analysis of Quantum Well Lasers using PICS3D. In *Integrated Photonics Research Conference*, Santa Barbara, Jul. 1999.
- [21] Max Planck. On the law of distribution of energy in the normal spectrum, more info on <http://www.nobel.se/physics/laureates/1918/index.html>. *Annalen der Physik*, 4:553, 1901.
- [22] For A. Einstein. <http://www.nobel.se/physics/laureates/1921/index.html>. For his services to Theoretical Physics, and especially for his discovery of the law of the photoelectric effect, links to some of Einstein publications in *Annalen der Physik* can be found at http://www.wordiq.com/definition/Albert_Einstein.
- [23] Y. Matsui et al. Novel Design Scheme for High-Speed MQW Lasers with Enhanced Differential Gain and Reduced Carrier Transport Effect. *IEEE Journal of Quantum Electronics*, 34(12):2340–2349, Dec. 1998.
- [24] Y. Matsui et al. Enhanced Modulation Bandwidth for Strain-Compensated InGaAlAs-InGaAsP MQW Lasers. *IEEE Journal of Quantum Electronics*, 34(10):1970–1978, Oct. 1998.
- [25] K. Uomi et al. Dependence of High-Speed Properties on the Number of Quantum Wells in 1.55 μm InGaAs-InGaAsP MQW $\lambda/4$ -shifted DFB Lasers. *IEEE Journal of Quantum Electronics*, 29(2):355–360, Feb. 1993.
- [26] R. Schimpe. Intensity Noise Associated with the Lasing Mode of a (GaAl)As Diode Laser. *IEEE Journal of Quantum Electronics*, 19(6):895–897, Jun. 1983.
- [27] P. Gallion. On the RIN. Private Communication, 2004.
- [28] Ghaya Baili. Réduction du RIN dans un laser à semiconducteur pour applications hyperfréquence. Master's thesis, Ecole Supérieure d'Optique, Paris, France, 2004.

BIBLIOGRAPHY

- [29] D.E. McCumber. Intensity Fluctuations in the Output of cw Laser Oscillators (I to III). *Physical Review*, 141(1):306–322, Jan. 1966.
- [30] Melvin Lax. Quantum Noise. IV. Quantum Theory of Noise Sources. *Physical Review*, 145(1):110–129, May 1966.

Chapter 4

Bipolar cascade laser modeling at an “electronic level” point of view



4.1 Introduction

In chapter 2, we have shown the possible system characteristic improvements that we aim to obtain by cascading several lasers. In chapter 3, we confirmed the possible link gain improvement, but realized that the equivalent RIN is likely to remain unchanged compared to a standard single-active-junction laser, unless we manage to increase the device output power. In this chapter, we go down

one step further into the device and present the model that we have developed for designing BCL.

The model is derived from a previously-existing transport model that is first described briefly. Then we present the modifications undertaken to account for the device specificity: materials lattice-matched to InP, the use of the Fermi-Dirac statistics, and the implementation of several quantum wells. Finally, we derive the calculation of the tunnel-current model that we have implemented to complete the self-consistent transport model.

4.2 Transport model used in simulations

4.2.1 Formerly-existing transport model

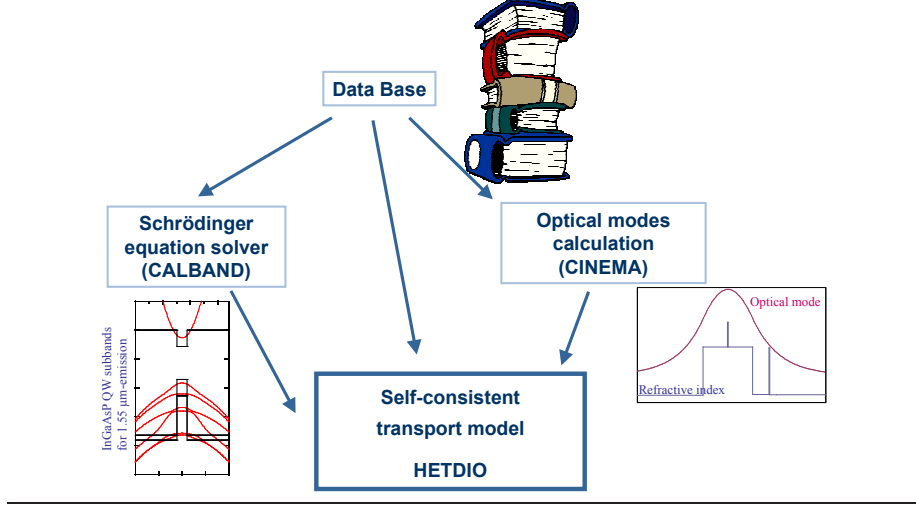
For the electronic simulation of the bipolar cascade structure, we have used a formerly existing transport model described with more details in [1] and [2]. The model was developed at Thales Research & Technology to simulate the behaviour of high power laser diodes. More precisely, its use was limited to the modeling of single-quantum-well diodes, grown on GaAs materials and for an emission wavelength around 980 nm. We therefore performed the necessary modifications in order to account for the behaviour of bipolar cascade lasers (which implies several quantum wells: at least one per active region), emitting around 1.55 μm (materials lattice-matched to InP).

The formerly-existing model is fed by several self-consistent calculation modules:

- A data base gives the material characteristics as a function of their chemical composition.
- A Schrödinger equation solver (CALBAND) predicts the quantum-well characteristics: anisotropic calculation of the dispersion diagram of every QW subband, and the associated density of states. This module, described in detail in [2], also takes into account the heavy-hole and light-hole mixing that occurs for \mathbf{k} parallel to the interfaces.
- A Maxwell equation solver (CINEMA) calculates the modal optical distribution (and the effective refractive index of each mode) in the structure as a function of the refractive index of every semiconductor layer. Information on this module can be found in [3].
- The main transport software (HETDIO) uses the output of the different calculation modules to estimate electronic transport and electro-optic gain in the QWs and displays as an output the band diagram of the structure and the static characteristics of the laser (optical power, voltage, current, carrier densities, etc.).

4.2 Transport model used in simulations

Figure 4.1 Description of the different elements constituting the transport program modified and used for BCL modeling.



4.2.2 Physical model

The carrier transport is based upon a drift-diffusion model described in detail (including the numerical implementation) in [1]. The five constitutive equations are the following:

$$-\vec{\nabla} \cdot (\epsilon \vec{\nabla} \Psi) = q(p - n + D) \quad (4.1)$$

$$\vec{J}_n = e\mu_e (U_T \vec{\nabla} n - n \vec{\nabla} [\Psi + \frac{\chi_n}{e} - \frac{3}{2} U_T \ln(m_e)]) \quad (4.2)$$

$$\vec{J}_p = -e\mu_h (U_T \vec{\nabla} p + p \vec{\nabla} [\Psi + \frac{\chi_p}{e} - \frac{3}{2} U_T \ln(m_h)]) \quad (4.3)$$

$$\vec{\nabla} \cdot \vec{J}_n = eR(n, p) \quad (4.4)$$

$$\vec{\nabla} \cdot \vec{J}_p = -eR(n, p) \quad (4.5)$$

- ☞ ϵ is the local dielectric constant,
- ☞ e is the electronic charge,
- ☞ D is the local net doping,
- ☞ $\mu_{e,h}$ is the electronic, hole mobility,
- ☞ $U_T = \frac{k_B T}{e}$ is the thermal voltage, with k_B the Boltzmann constant and T the temperature,
- ☞ $m_{e,h}$ is the effective electron, hole density of states mass,
- ☞ $R(n, p)$ stands for a general recombination coefficient, similar to the one defined in chapter 3.

The first equation 4.1 is known as the Poisson equation because it is derived from the work of Siméon Denis Poisson (cf. figure 4.2-(a)). It is an electromagnetic equation which asserts that the electrostatic potential is determined by the electronic charge distribution. Equations 4.2 and 4.3 are the expression of the current in the drift-diffusion model and come from Ludwig Boltzmann's

4. Bipolar cascade laser modeling at an “electronic level” point of view

transport equation (cf. figure 4.2-(b)). The third group of equations (4.4 and 4.5) are the equations of conservation and ensure conservation of the number of particles, taking into account generation and recombination.

Figure 4.2 Portraits of important scientists of the past.



(a) Siméon Denis Poisson (1781-1840)

(b) The statue on Boltzmann's tomb in Vienna (1844-1906)

4.2.3 Numerical implementation

The unknown components to be calculated by the model are the electrostatic potential Ψ , the carrier densities n and p , and the current carried by each carrier type \vec{J}_n and \vec{J}_p , for each node of the numerical mesh.

These equations need to be fulfilled for each of the nodes of the numerical mesh. The resulting system of equations is written as:

$$f(X_t) = (f_i(X_t)) = 0$$

⇔ X_t is the $(5.N)$ -column vector of unknown variables to be determined.

At each iteration t of the calculation, we check whether the system of equations is close to its solution:

$$f(X_t) \stackrel{?}{=} 0$$

If the set of variables is not the solution, we modify the set of variables by an amount δX_t calculated by a Newton method scheme:

$$\begin{aligned} J_f \cdot \delta X_t &= f(X_t) \\ \delta X_t &= X_{t+1} - X_t = J_f^{-1} \cdot f(X_t) \end{aligned} \tag{4.6}$$

4.2 Transport model used in simulations

We then check the convergence with $f(X_{t+1}) \stackrel{?}{=} 0$. J_f is the Jacobian matrix of the function f . It is composed of the partial derivatives of each function $f_i(X_t)$ over each individual variable:

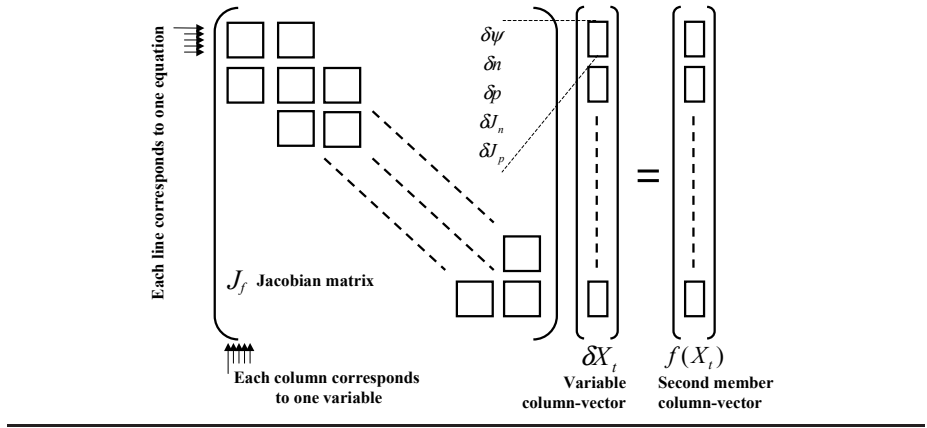
$$J_f = (J_f^{i,j})$$

$$\forall i, j \in [1; 5N], J_f^{i,j} = \left. \frac{\partial f_i}{\partial X_t^j} \right|_{X_t}$$

- ⇒ X_t^j is one of the variables ψ , n , p , \vec{J}_n , or \vec{J}_p , for one of the nodes of the numerical mesh.
- ⇒ The partial derivatives are usually calculated analytically, except for the nodes corresponding to the QWs or to the tunnel junctions, where a numerical calculation was necessary for the partial derivatives over the variables n , p , \vec{J}_n , and \vec{J}_p .

Equation 4.6 is schematically represented in figure 4.3. Each line of the matrix equation stands for one of the equations of the system (e.g. the first line corresponds to the Poisson law for the first node), whereas each column is related to one variable (e.g. the first column corresponds to $\psi(x_1)$).

Figure 4.3 Schematical description of the Newton method used for fast convergence.



For all the classical nodes (excluding the QW-nodes, and the tunnel-junction-nodes which will be treated afterwards), the system of equation has a local behavior: the partial derivatives of the node i equal to zero for variables belonging to the nodes before $i - 1$, and after $i + 1$. The resulting Jacobian matrix is a tri-diagonal block matrix.

Convergence is obtained by solving the linear system of equations, at each calculation step.

4.3 Modifications for the modeling of laser diodes composed of materials lattice-matched to InP

4.3.1 Modifications of the data base entries

In order to simulate the transport behavior of InP-based laser structures, we have completed the database for materials ($\text{In}_{1-x}\text{Ga}_x\text{As}_y\text{P}_{1-y}$, and $\text{In}_{1-x}\text{Ga}_x\text{As}$) lattice-matched to InP. The alloy is lattice-matched to InP if the following relationship is observed:

$$x = \frac{0.189y}{0.4184 - 0.013y}$$

☞ This relation gives $x = 0.53$ for the ternary alloy lattice-matched to InP.

In this section we sum up the parameters found in the literature and implemented in the database. The expressions for calculating the parameters are described in the following paragraphs whereas table 4.1 contains the parameters found in the literature.

4.3.1.1 Effective masses

The effective masses (both for conduction band and valence band) are calculated by a Vegard law on the binary data provided in table 4.1. The Luttinger coefficients for the valence band transport behavior are then given by:

$$\begin{aligned}\gamma_1 &= \frac{1}{2} \left(\frac{1}{m_{lh}^*} + \frac{1}{m_{hh\langle 100 \rangle}^*} \right) \\ \gamma_2 &= \frac{1}{4} \left(\frac{1}{m_{lh}^*} - \frac{1}{m_{hh\langle 100 \rangle}^*} \right) \\ \gamma_3 &= \frac{1}{4} \left(\frac{1}{m_{lh}^*} + \frac{1}{m_{hh\langle 100 \rangle}^*} - \frac{2}{m_{hh\langle 111 \rangle}^*} \right)\end{aligned}$$

Parameter	InP	InAs	GaP	GaAs	$\text{In}_{0.53}\text{Ga}_{0.47}\text{As}$
m_e^*	0.077 [4, 5]	0.02[4]	0.15 [6]	0.067[1]	0.037
m_{lh}^*	0.12 [4, 5]	0.026[4]	0.16 [4, 6]	0.09 [1]	
$m_{hh\langle 100 \rangle}^*$	0.56 [4]	0.16 [4]	0.41[6]	0.377[1]	
$m_{hh\langle 111 \rangle}^*$	0.6[4]	0.12[4]	0.67[4]	0.952[1]	
E_g (eV)	1.34	0.34	2.76 (in the Γ -valley)	1.42	0.75 [4]
ΔE_c (eV)	-0.37	0.16	-0.75	0	-0.60
μ_n ($\text{m}^2/\text{V/s}$)	0.5	1.1	n.d.	0.82	1.1
μ_p ($\text{m}^2/\text{V/s}$)	0.015	n.d.	n.d.	0.038	0.015
n_{eff}	3.1694	3.638	3.057	3.3769	3.5235
ϵ	12.6[4]	15.2[4]	11.1 [4]	13.18[4]	14.22

Table 4.1: Binary parameters found in the literature or parameters given by the database (when no citation is indicated) used for calculating the parameters of $\text{In}_{1-x}\text{Ga}_x\text{As}_y\text{P}_{1-y}$ lattice-matched to InP

4.3 Modifications for the modeling of laser diodes composed of materials lattice-matched to InP

4.3.1.2 Band-gap energy

The InP band-gap energy is first calculated as a function of the temperature, with the expression [4]:

$$E_g(\text{InP}) = 1.4236 - \frac{4.5 \times 10^{-4} T^2}{207 + T}$$

We then use the Vegard law, improved by the use of bowing parameters in order to fit in addition to the ternary alloys, the following band-gap energies [1]:

1. $E_g(\text{GaAs}_{0.5}\text{P}_{0.5}) = 2.02 \text{ eV}$ (in the Γ -valley)
2. $E_g(\text{Ga}_{0.5}\text{In}_{0.5}\text{As}) = 0.78 \text{ eV}$
3. $E_g(\text{Ga}_{0.52}\text{In}_{0.48}\text{As}) = 0.80 \text{ eV}$
4. $E_g(\text{In}_{0.5}\text{Ga}_{0.5}\text{P}) = 1.77 \text{ eV}$

In order to prevent discontinuities in the gap energy of InGaAs materials, we redefine the gap energy calculation using a bowing parameter to fit the gap of $\text{In}_{0.53}\text{Ga}_{0.47}\text{As}$:

$$E_g(\text{In}_{1-x}\text{Ga}_x\text{As}) = E_g(\text{InAs}) \times (1 - x) + E_g(\text{GaAs}) \times x + bx(1 - x)$$

☞ The bowing parameter b equals -0.4 in order to fit $E_g(\text{In}_{0.53}\text{Ga}_{0.47}\text{As}) = 0.75 \text{ eV}$.

4.3.1.3 Band offset

For calculating the conduction band offsets ΔE_c , the associative rule for heterojunctions is assumed and the reference material of the program is GaAs. In addition, the band-gap energy difference between InP and lattice-matched InGaAs is such that $\Delta E_c = 0.38 \Delta E_g$ [5]. The band offset for InGaAsP lattice-matched to InP is then given by:

$$\Delta E_c(\text{In}_{1-x}\text{Ga}_x\text{As}_y\text{P}_{1-y}) = \Delta E_c(\text{InP}) + 0.38 \times \{E_g(\text{InP}) - E_g(\text{In}_{1-x}\text{Ga}_x\text{As}_y\text{P}_{1-y})\}$$

☞ $\Delta E_c(\text{InP})$ is listed in table 4.1.

4.3.1.4 Electron mobility

The electron mobility is calculated for InP, as a function of the dopant concentration following a relation extrapolated from data found in [7]:

$$\text{For InP, } \mu_n(N_a, N_d) = 0.5 - 4 \times 10^{-24} (N_a + N_d)$$

☞ μ_n is expressed in $\text{m}^2/(\text{V}\cdot\text{s})$

☞ $N_{a,d}$ are in $\text{atoms}\cdot\text{m}^{-3}$

The electron mobility of InGaAsP(x,y) is then calculated with a linear interpolation between InP and the lattice-matched ternary alloy:

$$\mu_n(\text{In}_{1-x}\text{Ga}_x\text{As}_y\text{P}_{1-y}) = (1 - y)\mu_n(\text{InP}) + y\mu_n(\text{In}_{0.53}\text{Ga}_{0.47}\text{As})$$

The electron mobility supposedly does not vary with the electric field.

4.3.1.5 Hole mobility

The hole mobility supposed constant and equal to the hole mobility in InP for every lattice-matched alloy. As for the electron mobility, the hole mobility is supposedly not dependent on the electric field.

4.3.1.6 Refractive index

The refractive index is obtained in our simulation by a method described by Afromowitz in 1974 [8]:

$$n_{\text{Afromowitz}} = \sqrt{1 + \frac{E_d}{E_0} + \frac{E_d E_\lambda^2}{E_0^3} + \frac{E_d E_\lambda^4}{2E_0^3(E_0^2 - E_g^2)} + \ln \left| \frac{2E_0^2 - E_g^2 - E_\lambda^2}{E_g^2 - E_\lambda^2} \right|}$$

☞ E_g is the band-gap energy already discussed

☞ $E_\lambda = h\nu$ is the energy of one photon of the lasing mode, with h the Planck constant and ν the frequency of the electric field oscillation.

The empirical calculation uses several parameters that have been discussed by Broberg [9] for InGaAsP lattice-matched to InP:

$$\begin{aligned} E_0 &= 0.595x^2(1 - y) + 1.626xy - 1.891y + 0.524x + 3.391 \\ E_d &= (12.36x - 12.71)y + 7.54x + 28.91 \end{aligned}$$

4.3.1.7 Dielectric constant

We use the Vegard law on the binary alloy parameters presented in table 4.1.

4.3.2 Influence of the Auger recombination increase

As already explained in chapter 3, the Auger recombination process acquires an increasing importance as the materials' band-gaps are decreased. For GaAs-based QW lasers, the local Auger coefficient lies typically around $C_{\text{Auger (GaAs)}} \approx 3.5 \times 10^{-30} \text{ cm}^6 \cdot \text{s}^{-1}$ [10]. For InP-based components, Auger recombinations demonstrate a coefficient of the order of $C_{\text{Auger (InP)}} \approx 5 \times 10^{-28} \text{ cm}^6 \cdot \text{s}^{-1}$ [11–14]. This kind of recombination is not negligible anymore in the QWs and we therefore performed the necessary numerical implementation modifications by adding one parallel recombination current source at the QW-nodes.

4.4 From the Boltzmann statistics to the Fermi-Dirac statistics

4.4.1 Physical model

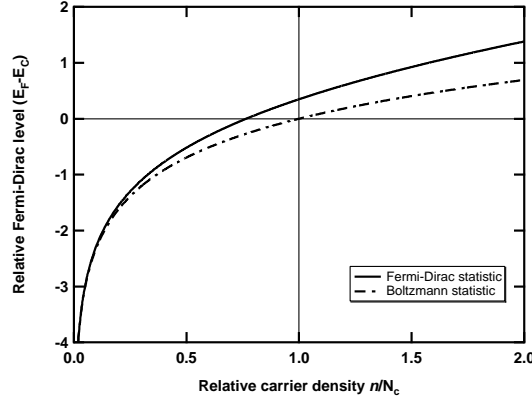
The structures studied in this thesis may include highly doped layers. For instance the tunnel junctions consist of a highly-doped n^{++} - p^{++} interface. Some materials might even be degenerate. The Boltzmann statistics is not sufficiently accurate in this case and strongly overestimates the carrier population for the same quasi-Fermi-level. For a reliable prediction of the carrier population distribution, we use the Fermi-Dirac statistics instead:

$$n = \mathcal{N}_c \mathcal{F}_{\frac{1}{2}} \left(-\frac{E_c - E_F}{kT} \right) \quad (4.7)$$

4.4 From the Boltzmann statistics to the Fermi-Dirac statistics

Figure 4.4 presents the comparison between the Fermi-Dirac and the Boltzmann statistics for highly-doped materials. The difference between the Fermi-level E_F and the conduction band energy E_c is plotted as a function of the electron density n divided by the effective density of states \mathcal{N}_c .

Figure 4.4 Comparison between the Fermi-Dirac and the Boltzmann statistics for highly-doped materials.



4.4.2 Numerical implementation: modification of the Scharfetter & Gummel scheme

The formerly-existing transport model uses a double mesh: the first mesh (defined by one set of nodes x_i , $i \in \llbracket 1, N \rrbracket$) is used for the electrostatic potential Ψ , and the carrier densities n and p . The second mesh is dedicated to the current values (\vec{J}_n and \vec{J}_p), and each node $x_{i+\frac{1}{2}}$ is situated in between two nodes of the first mesh, at $\frac{x_i + x_{i+1}}{2}$.

On the one hand the electrostatic potential Ψ , and the current terms (\vec{J}_n and \vec{J}_p) vary “slowly”, i.e. within a few μm . On the other hand, the carrier density may drastically vary in a few tenth of Ångström, because of the abrupt profile of doping concentrations. The current equations (equations 4.2 and 4.3) subtract two quickly varying expressions for calculating a slowly varying parameter. This may cause numerical convergence problems if the equations are implemented with no special care. Scharfetter & Gummel introduced in 1969 a more convenient and more robust scheme of implementation [15]. In this scheme, we multiply the quickly varying variables

$$\begin{cases} n(u) = \mathcal{N}_c \mathcal{F}_{1/2}(u) \\ p(u) = \mathcal{N}_v \mathcal{F}_{1/2}(u) \end{cases}$$

by the more slowly varying variable $z(u) = \mathcal{F}_{1/2}(u)e^{-u}$.

If the material is not degenerate, the Boltzmann statistics applies and the slowly varying variable is almost unity:

$$z(u) \approx 1$$

In the case of Fermi-Dirac statistics, we modify the Scharfetter & Gummel scheme which becomes:

$$\begin{aligned}\Delta z_i J_n &= e \tilde{\mu}_n z(\langle u \rangle) \left\{ \mathcal{N}_c(x_{i+1}) e^{u_{i+1}} B \left(\frac{E_n(x_{i+1}) \Delta x_i}{U_T} \right) - \mathcal{N}_c(x_i) e^{u_i} B \left(-\frac{E_n(x_{i+1}) \Delta x_i}{U_T} \right) \right\} \\ \Delta z_i J_p &= -e \tilde{\mu}_p z(\langle u \rangle) \left\{ \mathcal{N}_v(x_{i+1}) e^{u_{i+1}} B \left(-\frac{E_p(x_{i+1}) \Delta x_i}{U_T} \right) - \mathcal{N}_v(x_i) e^{u_i} B \left(\frac{E_p(x_{i+1}) \Delta x_i}{U_T} \right) \right\}\end{aligned}$$

The notations are very close to those used in [1]:

$$\begin{aligned}\Delta z_i &= z(u(x_{i+1})) - z(u(x_i)) \\ E_n(x_{i+1}) \Delta x_i &= \psi(x_{i+1}) - \psi(x_i) + \frac{\chi_n(x_{i+1})}{e} - \frac{\chi_n(x_i)}{e} \\ &\quad - \frac{3}{2} U_T [\ln m_e(x_{i+1}) - \ln m_e(x_i)] \\ E_p(x_{i+1}) \Delta x_i &= \psi(x_{i+1}) - \psi(x_i) + \frac{\chi_p(x_{i+1})}{e} - \frac{\chi_p(x_i)}{e} \\ &\quad - \frac{3}{2} U_T [\ln m_h(x_{i+1}) - \ln m_h(x_i)] \\ B(y) &= \frac{y}{e^y - 1} \\ \langle u \rangle &= \frac{u(x_i) + u(x_{i+1})}{2} \\ \tilde{\mu}_{n,p} &= \frac{2\mu_{n,p}(x_{i+1})\mu_{n,p}(x_i)}{\mu_{n,p}(x_i) + \mu_{n,p}(x_{i+1})}\end{aligned}$$

4.5 Modifications for the modeling of multi-quantum-well laser diodes

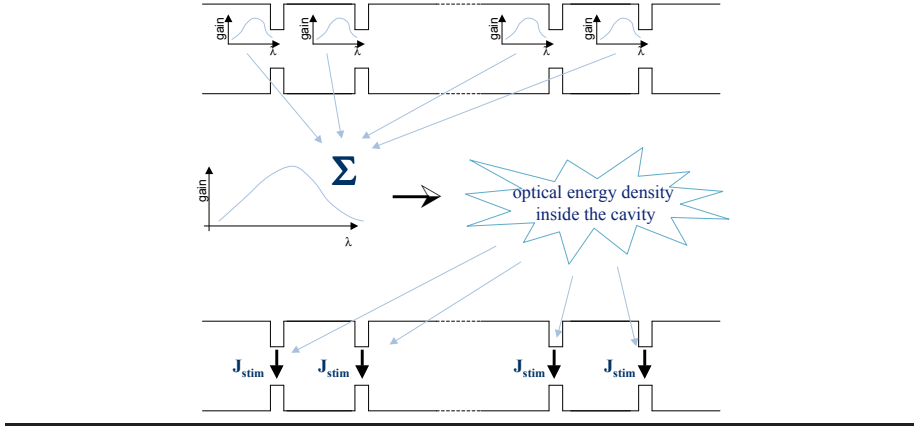
4.5.1 Numerical implementation

For one-QW structures, the calculation of the unknown components of one node ($i \in \llbracket 1, N \rrbracket$) involves only the components of two adjacent nodes ($i+1$ and $i-1$). The interaction between the different nodes is “local”. The matrix reduces to a tri-diagonal block matrix. We then use well-known and optimized methods for solving a scalar tri-diagonal matrix; the scalar inversion is replaced by (5×5)-block-matrix inversions.

For MQW structures however, an optical coupling between the different QW-nodes appears. For each QW, the transport model (HETDIO) uses the local carrier density, fills the subbands given by the Schrödinger equation solver, predicts the set of possible radiative recombinations, and thereafter calculates for each QW i the spectral distribution of the local optical gain $g_\lambda^L(\text{QW}_i)$ (we use the notations of [1], L stands for “linear”, and λ describes the spectral dependence of the local gain). Its calculation is described with great details in [1]. We want just to point out here that it relies on the whole set of parameters calculated by the Schrödinger equation solver (dispersion coefficients for every subband, matrix element for each transition), and not only on a user-adjustable parameter as it is often the case in other device modeling programs [16].

4.5 Modifications for the modeling of multi-quantum-well laser diodes

Figure 4.5 Schematical description of the numerical treatment of multiple-quantum-well structures.



All the QWs contribute to the common modal gain. The total global modal gain g_{tot}^λ is then calculated as the sum of the individual gains, weighted by the QWs overlap with the lasing mode Γ_{QW_i} :

$$g_{\text{tot}}^\lambda = \sum_{\text{QW}_i} \Gamma_{\text{QW}_i} g_\lambda^L(\text{QW}_i)$$

Following [1] (and using again its notations), the thermodynamic equilibrium solution to a rate equation similar to equations 3.1 and 3.2, then gives the optical energy density S_λ contained in the lasing mode of the cavity:

$$S_\lambda = \frac{(g_{\text{tot}}^\lambda - \alpha^T) + \sqrt{(g_{\text{tot}}^\lambda - \alpha^T)^2 + 4 \frac{n}{c} \epsilon g_{\text{tot}}^\lambda B_\lambda R_{\text{spont}}}}{2 \epsilon g_{\text{tot}}^\lambda}$$

- ☞ α^T is the total modal optical loss
- ☞ B_λ is the proportion of spontaneous emission coupled to the lasing mode
- ☞ R_{spont} spontaneous emission rate
- ☞ All of them are precisely defined in [1].

Once we have calculated this “global” parameter, we calculate the recombination current due to stimulated emission for each QW. The total recombination current in one QW is the sum of the “locally”-calculated spontaneous emission and non-radiative emission recombination current, and the stimulated emission current:

$$J_{\text{QW}_i} = e \sum_\lambda \frac{C}{n} g_\lambda(\text{PQ}_i) \Gamma_{\text{QW}_i} S_\lambda + e R_{\text{spont}}(\text{PQ}_i) + J_{\text{nr}}(\text{PQ}_i)$$

- ☞ $J_{\text{nr}}(\text{PQ}_i)$ is the non-radiative recombination current.
- ☞ The first term is associated to the stimulated emission and needs a “global” calculation.
- ☞ The last two terms are “locally” calculated.

4. Bipolar cascade laser modeling at an “electronic level” point of view

We see from this mechanism that an increase of the carrier density in one QW will influence not only its own recombination current, but also the recombination currents of the other QWs. This non-negligible, non-local influence needs to be taken into account and triggers non-tri-diagonal terms in the Jacobian matrix. The non-diagonal terms only appear in the conservation equations at the QW-nodes which become:

$$\begin{aligned} J_n(x_{N_{\text{QW}_i+\frac{1}{2}}}) - J_n(x_{N_{\text{QW}_i-\frac{1}{2}}}) &= e \frac{\Delta x_{N_{\text{QW}_i}} + \Delta x_{N_{\text{QW}_i+1}}}{2} \{R(n(x_{N_{\text{QW}_i}}), p(x_{N_{\text{QW}_i}})) + R_{\text{QW}_i}\} \\ J_p(x_{N_{\text{QW}_i+\frac{1}{2}}}) - J_p(x_{N_{\text{QW}_i-\frac{1}{2}}}) &= -e \frac{\Delta x_{N_{\text{QW}_i}} + \Delta x_{N_{\text{QW}_i+1}}}{2} \{R(n(x_{N_{\text{QW}_i}}), p(x_{N_{\text{QW}_i}})) + R_{\text{QW}_i}\} \end{aligned}$$

The recombination current R_{QW_i} writes:

$$R_{\text{QW}_i} = - \sum \frac{\partial J_{\text{QW}_i}}{\partial n_{\text{QW}_j}} \Delta n_{\text{QW}_j} - \sum \frac{\partial J_{\text{QW}_i}}{\partial p_{\text{QW}_j}} \Delta p_{\text{QW}_j} \quad (4.8)$$

All the terms with $i \neq j$ are non-tri-diagonal.

The method of resolution previously used did not allow for non-tri-diagonal terms. Since the non-tri-diagonal terms are few compared to the number of nodes, we have used a perturbative method using the Woodbury formula [17], considering the non-tri-diagonal terms as the perturbation. The problem can be written as:

$$J_f \cdot \delta x_t = (A + \Pi) \cdot \delta x_t = b \quad (4.9)$$

- ☞ A is the $(N \times N)$ -tri-diagonal- (5×5) -block Jacobian matrix of the problem without the non-diagonal terms,
- ☞ δx_t is the $(5N)$ -column-vector of unknown components that needs to be calculated,
- ☞ $b = f(x_t)$ is the second member of the linear equation,
- ☞ Π is the $(5N \times 5N)$ -non-diagonal matrix containing the perturbation. $\Pi = 0$ except for a limited number P of terms which constitute the perturbation.

If there are P non-diagonal perturbative elements, Π can be written as:

$$\Pi = \sum_{m=1}^P u_m \cdot v_m^t$$

- ☞ u_m and v_m are $(5N)$ -column vectors. $u_m, v_m = 0$ except for one element, which position in u_m and v_m determines the position of the non-diagonal element in the perturbation matrix Π .

The perturbation matrix can also be expressed as:

$$\Pi = U \cdot V^t$$

- ☞ U and V are the $(5N \times P)$ -matrices composed of the P column vectors u_m and v_m .

The Woodbury formula then asserts that:

$$(A + U \cdot V^t)^{-1} = A^{-1} - [A^{-1} \cdot U \cdot (1 + V^t \cdot A^{-1} \cdot U)^{-1} \cdot V^t \cdot A^{-1}]$$

This method replaces the very heavy inversion of a $(5N \times 5N)$ -matrix, by an inversion of the tri-diagonal-block matrix and the inversion of a very small $(P \times P)$ -matrix $(1 + V^t \cdot A^{-1} \cdot U)$.

Because A^{-1} is not available for storage, we first solve the P auxiliary problems:

$$\begin{aligned} A \cdot z_1 &= u_1 \\ A \cdot z_2 &= u_2 \\ &\dots \\ A \cdot z_P &= u_P \end{aligned}$$

☞ z_m are $(5N)$ -column vectors.

We define the matrix H by:

$$H = 1 + V^t \cdot Z$$

☞ H is therefore a $(P \times P)$ -matrix.

☞ The $(5N \times P)$ -matrix Z is constituted by the column vectors z_m .

We then solve the unperturbed problem:

$$A \cdot y = b$$

And the solution is given by:

$$\delta x_t = y - Z \cdot (H^{-1} \cdot (V^t \cdot y))$$

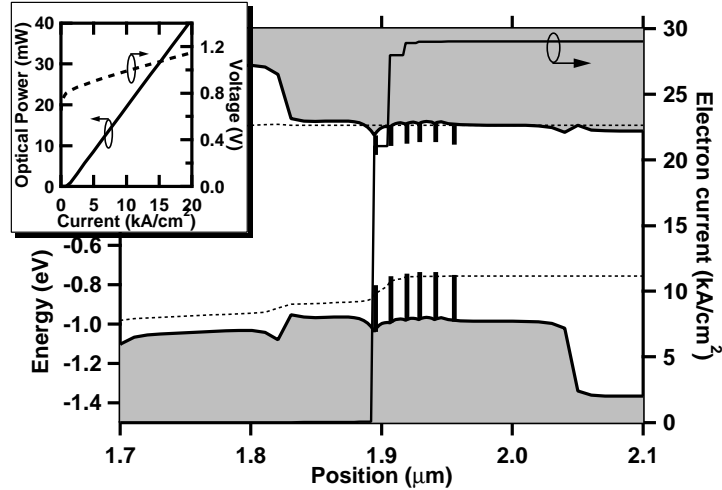
For our non-diagonal perturbation, P equals the sum of the number of QWs and the number of tunnel junctions.

4.5.2 Example of simulation

Figure 4.6 displays the results found for the simulation of a MQW-laser by the complete self-consistent laser simulation program. The structure is a vertical-single-mode device. The active region is composed of 4 InGaAsP ($\lambda_{PL} = 1.7 \mu\text{m}$)/InGaAsP ($\lambda_{PL} = 1.2 \mu\text{m}$) strained-QWs.

The figure focuses on the active region. On the right axis is depicted the current carried by the electrons. A drop in the electron current indicates an electron-hole recombination. We can see on figure 4.6, that the recombinations mainly occur in the QWs. We also see that all the QWs do not carry the same amount of current. The QW closest to the p -side is the place for more recombinations than the QW closest to the n -side. This non-uniform QW injection is attributed to the difference of mobility for holes and for electrons. Even if not of major interest for the purpose of this thesis, it is an important issue for designing high-frequency lasers.

Figure 4.6 Example of simulation of a multi-quantum-well (InGaAsP $\lambda_{PL} = 1.7 \mu\text{m}$ /InGaAsP $\lambda_{PL} = 1.2 \mu\text{m}$) laser: V-I characteristic and band diagram.



4.6 Esaki tunnel junction modeling

4.6.1 Principle of a tunnel junction

Leo Esaki, a Japanese physicist born in 1925 explains for the first time in 1958 [18] the very particular behaviour of electronic components known today as “tunnel diodes” or “Esaki diodes”. The history of science reveals that many scientists had been observing the phenomenon before, but the samples were systematically rejected because the current-voltage characteristic was not following the expected behaviour. In fact, tunneling of electrons through the forbidden gap of an insulator was at this time a known phenomenon (proposed by Zener in 1934 [19]), and had been successfully applied to account for current characteristic under reverse bias [20,21]. But Esaki was the first scientist to propose Zener tunneling to account for the forward-bias characteristics. For this reason, he was awarded the Nobel price in 1973.

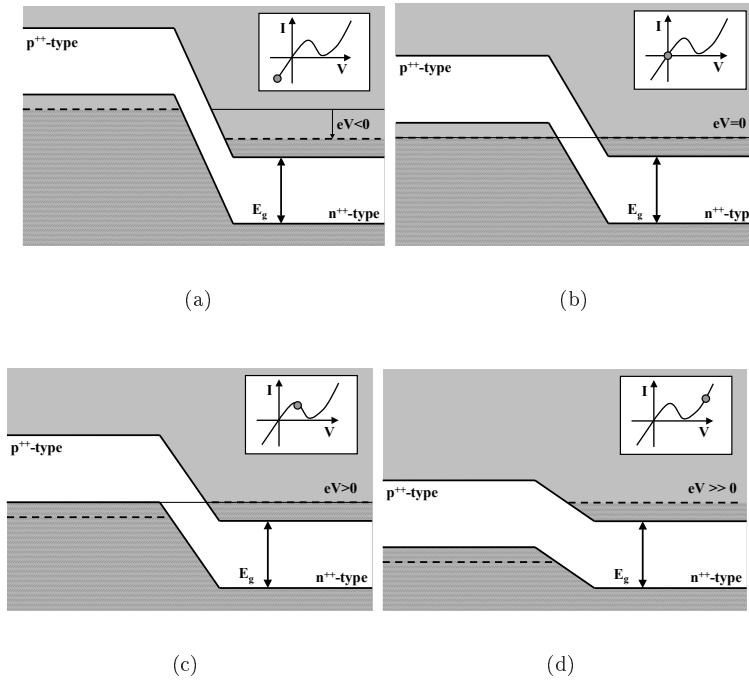
The tunnel process is hard to describe quantitatively because it has a very non-linear behavior, which therefore strongly depends on not perfectly known physical parameters of the materials (e.g. forbidden band gap energy E_G , dopant densities...), and case-study-dependent parameters (internal electric field) [22–24]. Nonetheless, the principle is easy to understand qualitatively and is shown in figure 4.7.

At 0 bias (figure 4.7-(b)), even though both bands are degenerate, the thermodynamic equilibrium imposes that recombinations exactly compensate for carrier creation, and the overall current is null. For backward bias (figure 4.7-(a)), the quasi-Fermi-level (QFL) of holes (p -side) is higher than the QFL of electrons (on the n -side) resulting in empty states on the n -side facing occupied states on the p -side. An electron current can spring off from p - to n -side, which is equivalent to a majority carrier creation on either side of the junction. For small forward bias (figure 4.7-(c)), the same phenomenon occurs, resulting here

4.6 Esaki tunnel junction modeling

in a net electron current from n - to p -side, equivalent to excess majority carrier recombination. For a certain regime, an increase in the forward bias gives rise to less electronic occupied states facing the valence band empty states. The current decreases while the polarisation increases, we locally have a negative differential resistance. For high-enough forward bias (figure 4.7-(d)), the current-voltage characteristic is similar to other types of semiconductor diodes over threshold: the current is thermo-activated.

Figure 4.7 A tunnel junction for different regimes of functioning: (a) for backward bias, (b) at 0 bias, (c) for small forward bias, (d) for high forward bias.



4.6.2 Electronic model

4.6.2.1 Introduction

Shortly after Esaki's publication, numerous physicists proposed various methods to predict the tunnel current. Some are mostly phenomenologic [18, 22, 24–30], others are more complex and almost self-consistent [31, 32], with acceptable agreement with experimental results.

The purpose of this section is to obtain a quantitative estimation of the Zener tunneling current through the highly-doped junction. We wish to insert the tunnel current calculation into the previously described transport model. The model must therefore take into account every microscopically varying relevant parameter. The model we have implemented (and we are rederiving in detail in this section) is due to E. O. Kane [21, 31].

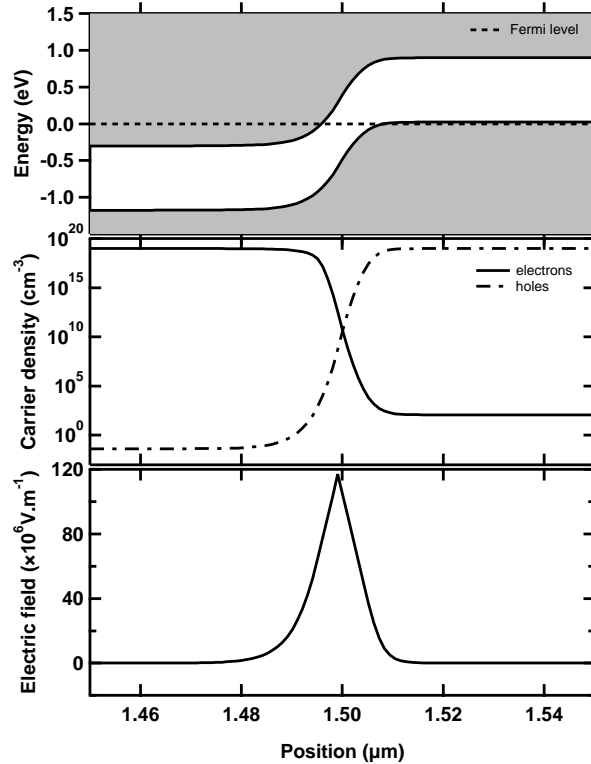
A little more precisely than we did while exposing its principle, we can describe a tunnel junction as an interface between two semiconductor layers,

4. Bipolar cascade laser modeling at an “electronic level” point of view

one is highly doped with donors, the other one is highly doped with acceptors. Under these conditions, the structure behaves very similarly to a p - n junction well-described in the literature [24, 30, 33, 34]: n -side excess electrons tend to diffuse to the p -side, but the ionized donors create an electrostatic attraction force that counteracts diffusion. The solution under zero bias is a three-region structure as can be seen in figure 4.8:

- a high-density n -type carrier area (that may be degenerate)
- a high-density p -type carrier area
- an internal area, depleted of carriers, hosting a very intense built-in field, which can reach 10^8 V.m⁻¹.

Figure 4.8 Band diagram, carrier populations and “build-in” electric field for a tunnel junction made of InGaAsP ($\lambda_{PL} = 1.35$ μm) doped to 10^{19} .



It is obvious from figure 4.8 that what makes the Zener process possible is the very high electric field, which bends the bands of the semiconductor and may offer (under polarization) a coupling between filled and empty states with the same energy separated by the bent gap. A classical approach to this problem would obviously forbid any particle transfer between bands. Quantum mechanics is therefore necessary to account for the effect.

Qualitatively speaking, the following discussion process is clear: we first calculate the wave functions of an electron in a given electronic band (the valence

4.6 Esaki tunnel junction modeling

band, and the conduction band). This will give us the probability of presence of the electron at the position \mathbf{r} in space. We will then notice that the wave functions of the two states separated by the band gap (but having the same energy) overlap. By calculating this overlap, we find the tunneling probability. We eventually multiply this tunneling probability by the incident current to find the tunneling current.

Now for a quantitative description, we need to take great care at each step of the formalism to ensure normalization coherence, proper boundary conditions, and rigorous calculation steps. The main equations are presented linearly in the following section, but in order to facilitate a comprehensive reading, the calculation steps (that we wanted as rigorous as possible) are detailed and grouped in Appendix B.

4.6.2.2 The matrix element

The electric field arises in the x -direction. The time-independent Hamiltonian that we will use in the Schrödinger equation to describe the electron behavior includes the electric field interaction:

$$\left[\frac{\hat{\mathbf{p}}^2}{2m_0} + V_c(\mathbf{r}) - eFx \right] \psi(\mathbf{r}) = E\psi(\mathbf{r}) \quad (4.10)$$

- ☞ m_0 is the electron mass,
- ☞ $\hat{\mathbf{p}} = \frac{\hbar}{i}\nabla$ is the momentum operator,
- ☞ \hbar is the reduced Planck constant,
- ☞ $V_c(\mathbf{r})$ is the crystal electronic potential (dependent on the position vector \mathbf{r}),
- ☞ F is the electrostatic field applied, giving rise to a varying potential along the x -direction,
- ☞ $\psi(\mathbf{r}) = \langle \hat{\mathbf{r}} | \psi \rangle$ is the wave function of the electron in the structure, to be determined, together with its energy E .

To calculate the wave functions solutions of equation 4.10, we will use a perturbation method, and first consider the undisturbed Schrödinger equation:

$$\left[\frac{\hat{\mathbf{p}}^2}{2m_0} + V_c(\mathbf{r}) \right] \varphi(\mathbf{r}) = E\varphi(\mathbf{r}) \quad (4.11)$$

According to the Bloch theorem [33–35], the rigorous solutions of equation 4.11 are a complete set of eigenvalues $E_n(\mathbf{k})$ and eigenfunctions $\varphi_{n,\mathbf{k}}(\mathbf{r})$, the Bloch-Floquet functions, which form a complete basis:

$$\varphi_{n,\mathbf{k}}(\mathbf{r}) = \langle \hat{\mathbf{r}} | n, \mathbf{k} \rangle = \frac{e^{i\mathbf{k}\cdot\mathbf{r}}}{\sqrt{V}} u_{n,\mathbf{k}}(\mathbf{r}) \quad (4.12)$$

- ☞ V is the volume of the crystal ensuring the normalization of the basis vectors,
- ☞ $u_{n,\mathbf{k}}(\mathbf{r})$ is the periodic part of the Bloch functions,
- ☞ $e^{i\mathbf{k}\cdot\mathbf{r}}$ is a plane wave.

4. Bipolar cascade laser modeling at an “electronic level” point of view

The wavefunctions $\psi(\mathbf{r})$, solutions of equation 4.10, can be decomposed on the $|n, \mathbf{k}\rangle$ -basis:

$$\psi(\mathbf{r}) = \sum_n \sqrt{\frac{V_{\text{cell}}}{(2\pi)^3}} \int a_n(\mathbf{k}) \varphi_{n,\mathbf{k}}(\mathbf{r}) d\mathbf{k} \quad (4.13)$$

⇨ V_{cell} is the volume of the unit cell of the lattice

Equation 4.10 can in these conditions be written (cf. Calculation step A., on page 202):

$$\left\{ E_n(\mathbf{k}) - ieF \frac{\partial}{\partial k_x} - E \right\} a_n(\mathbf{k}) - \sum_{n'} eF X_{nn'}(\mathbf{k}) a_{n'}(\mathbf{k}) = 0 \quad (4.14)$$

⇨ $X_{nn'}(\mathbf{k})$ is defined as $X_{nn'}(\mathbf{k}) = \langle n, \mathbf{k} | x | n', \mathbf{k} \rangle = \frac{i}{V_{\text{cell}}} \int_{\text{cell}} u_{n\mathbf{k}}^*(\mathbf{r}) \frac{\partial}{\partial k_x} u_{n'\mathbf{k}}(\mathbf{r}) d\mathbf{r}$

⇨ The first term describes the perturbation in the considered band, whereas the second term accounts for the coupling between bands.

We will now neglect the interband interaction to compute the wavefunctions solutions of equation 4.10. Within these approximations, for a given band n the solution $\psi_n(\mathbf{r})$ of equation 4.10 only depends on the solutions $\varphi_{n,\mathbf{k}}(\mathbf{r})$ of the unperturbed Schrödinger equation 4.11:

$$\psi_n(\mathbf{r}) = \sqrt{\frac{V_{\text{cell}}}{(2\pi)^3}} \int a_n(\mathbf{k}) \varphi_{n,\mathbf{k}}(\mathbf{r}) d\mathbf{k}$$

Still neglected the interband interaction, the second term of equation 4.14 drops and the solution to this equation can be found easily, with the result:

$$a_n(\mathbf{k}) = a_n(\mathbf{k}_\perp) a_n(0) \exp \left\{ \frac{i}{eF} \int_0^{k_x} (E - E_n(k'_x)) dk'_x \right\} \quad (4.15)$$

We need now to ensure the normalization of $\psi_n(\mathbf{r})$ over the whole crystal and to install proper boundary conditions which will, as a consequence, quantify the eigenvalues E of the Schrödinger equation 4.14. The normalization is given by (cf. Calculation step E., on page 205):

$$|a_n(\mathbf{k}_\perp)|^2 = |a(\mathbf{k}_\perp)|^2 = \delta(\mathbf{k}_\perp - \mathbf{k}_{\perp 0})$$

and

$$a_n(0) = a(0) = \frac{1}{\kappa_x}$$

⇨ κ_x is the length of the Brillouin zone in the x -direction

⇨ Equation 4.14 can be solved for any value $\mathbf{k}_{\perp 0}$ of \mathbf{k}_\perp , which is conserved when applying an electric field along x .

Now that the functions are normalized, we can set the boundary conditions: we impose for the eigenfunctions to be periodic in the reciprocal lattice. Each

4.6 Esaki tunnel junction modeling

component must therefore be periodic with the same periodicity. The argument of the expression 4.15 should be the same for k_x and $k_x + \kappa_x$:

$$\exp \left\{ \frac{i}{F} \int_0^{k_x} (E - E_n(k'_x)) dk'_x \right\} = \exp \left\{ \frac{i}{F} \int_0^{k_x + \kappa_x} (E - E_n(k'_x)) dk'_x \right\}$$

which implies:

$$\int_{k_x}^{k_x + \kappa_x} (E - E_n(k'_x)) dk'_x = F[2\pi]$$

The spacing between eigenvalues is then given by :

$$\Delta E = \frac{2\pi F}{\kappa_x} \quad (4.16)$$

Therefore, the density of allowed states will, within these boundary conditions be given by $\rho(E) = 1/\Delta E = \kappa_x/2\pi F$.

Combining equation 4.13 and equation 4.15, we now have an expression of the wave function of an electron in a band n (i.e. we know the probability of presence of this electron in the structure). Within the effective mass approximation, it is possible to prove that the envelope function of these wave functions are Airy functions, which have the following properties [33, 34, 36]:

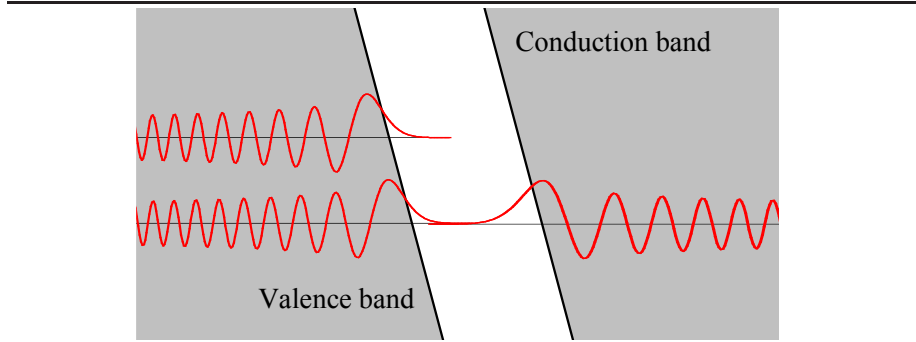
- The Airy function is a solution of the differential equation

$$\frac{d^2}{dx^2} Ai - x Ai(x) = 0$$

where we recognize the “general” shape of the Schrödinger equation 4.10.

- $Ai(x)$ tends to 0 for $x \rightarrow \infty$
- for $x < 0$, $Ai(x)$ oscillates with a frequency increasing with $|x|$.

Figure 4.9 Wave functions of the electrons (Airy functions) represented in the valence and conduction bands of a semiconductor which undergoes a high electric field



In other words, the probability for an electron to be inside the band gap is not completely null, but decays at an exponential rate. The overlap of the exponential arms of wave functions on each side of the band gap will give us an

4. Bipolar cascade laser modeling at an “electronic level” point of view

idea of the coupling between the two states, and therefore the probability for an electron in the first state to “appear” in the second state.

The “coupling strength” between states of equal energy but on different bands is given by the matrix element, which is, by definition:

$$M_{nn'} = \langle \psi_n | -eFx | \psi_{n'} \rangle = - \int \psi_n^* eFx \psi_{n'} d\mathbf{r} \quad (4.17)$$

The matrix element is derived in Calculation step F., on page 206, the result is :

$$M_{nn'} = -\frac{eF}{\kappa_x} \int X_{nn'}(\mathbf{k}) \exp\left(\frac{i}{eF} \int_0^{k_x} (E_{n'}(\mathbf{k}') - E_n(\mathbf{k}')) dk'_x\right) dk_x \quad (4.18)$$

4.6.2.3 $\mathbf{k} \cdot \hat{\mathbf{p}}$ -description of the semiconductor bands

This expression of the matrix element is very general. Here we only consider the top valence band and the lowest conduction band of a semiconductor.

The matrix element we need to compile then writes:

$$M_{cv} = -\frac{eF}{\kappa_x} \int X_{cv}(\mathbf{k}) \exp\left(\frac{i}{eF} \int_0^{k_x} (E_c(\mathbf{k}') - E_v(\mathbf{k}')) dk'_x\right) dk_x \quad (4.19)$$

In order to go further into the calculation of the matrix element, we need to express the Bloch functions $\varphi_{n,\mathbf{k}}(\mathbf{r})$ of the undisturbed crystal. The first option we have is to assume that $u_{n,\mathbf{k}}(\mathbf{r})$ is, for every \mathbf{k} , equal to its value at the center of the Brillouin zone:

$$\forall \mathbf{k}, u_{n,\mathbf{k}}(\mathbf{r}) \cong u_{n,0}(\mathbf{r})$$

This approximation is known as the envelope function approximation [33, 34], and is used by many authors to compute the band-to-band tunnel current [22, 29, 32, 37].

Kane shows that it is possible to obtain an analytical expression of the matrix element with a (somewhat) better description of the band structure [21]. Instead of considering the Bloch functions $u_{n,\mathbf{k}}(\mathbf{r})$ independent of \mathbf{k} we use the supposedly known $u_{n,0}(\mathbf{r})$ functions as a complete basis:

$$u_{n,\mathbf{k}}(\mathbf{r}) = \sum_m c_{n,m}(\mathbf{k}) u_{m,0}(\mathbf{r}) \quad (4.20)$$

This decomposition is known as the $\mathbf{k} \cdot \hat{\mathbf{p}}$ -method (or sometimes called effective masses method) and leads to an eigenproblem, where the eigenvalues are the total energies of the electronic states (as a function of \mathbf{k}), and the eigenfunction of the band n is the $c_{n,m}$ decomposition into the supposedly known complete basis $u_{m,0}$. The band-to-band influence on dispersion relations ($E_n(\mathbf{k})$) are all expressed in terms of $u_{m,0}$. The major interest of this method is then to transform the expression of $u_{m,0}$ into an expression function of parameters determined experimentally (for instance effective masses!). The general formalism is very powerful since the accuracy of the result depends on the number of considered bands, and therefore the problem can be derived with any desired complexity. We will fully take benefit of the great flexibility of the formalism and derive it for only two bands: the lowest conduction band, and the highest valence band.

4.6 Esaki tunnel junction modeling

This approximation is of course not rigorous, although it is valid for some direct-band gap semiconductors such as InSb for the light holes band [21].

The time-independent Schrödinger equations for each band of the periodic crystal are given by:

$$\left(\frac{\hat{\mathbf{p}}^2}{2m_0} + V(\mathbf{r}) \right) \varphi_{c,\mathbf{k}}(\mathbf{r}) = E_c(\mathbf{k})\varphi_{c,\mathbf{k}}(\mathbf{r}) \quad (4.21)$$

$$\left(\frac{\hat{\mathbf{p}}^2}{2m_0} + V(\mathbf{r}) \right) \varphi_{v,\mathbf{k}}(\mathbf{r}) = E_v(\mathbf{k})\varphi_{v,\mathbf{k}}(\mathbf{r}) \quad (4.22)$$

☞ $\varphi_{n,\mathbf{k}}(\mathbf{r}) = \frac{1}{\sqrt{V}}u_{n,\mathbf{k}}(\mathbf{r})e^{i\mathbf{k}\cdot\mathbf{r}}$ are the Bloch-Floquet functions of the undisturbed periodic crystal (the ones we are now looking for!)

☞ n either stands for c , for the conduction band, or for v for the valence band. We will use this notation when the expression is valid for each band

Using the definition of $\hat{\mathbf{p}} = \frac{\hbar}{i}\nabla$, we can rewrite for each band equations 4.21 and 4.22 as:

$$\left(\frac{\hat{\mathbf{p}}^2}{2m_0} + \frac{\hbar^2\mathbf{k}^2}{2m_0} + \frac{\hbar}{m_0}\mathbf{k}\cdot\hat{\mathbf{p}} + V(\mathbf{r}) \right) u_{n,\mathbf{k}}(\mathbf{r}) = E_n(\mathbf{k})u_{n,\mathbf{k}}(\mathbf{r})$$

Injecting the expression 4.20 into the previous equation, we find:

$$\left(\frac{\hat{\mathbf{p}}^2}{2m_0} + \frac{\hbar^2\mathbf{k}^2}{2m_0} + \frac{\hbar}{m_0}\mathbf{k}\cdot\hat{\mathbf{p}} + V(\mathbf{r}) - E_n(\mathbf{k}) \right) (c_{n,v}u_{n,0}(\mathbf{r}) + c_{n,c}u_{n,0}(\mathbf{r})) = 0$$

We then project these equations alternatively on each base vector $u_{c,0}$ and $u_{v,0}$, which follow by definition a supposedly solved Schrödinger equation:

$$\left(\frac{\hat{\mathbf{p}}^2}{2m_0} + V(\mathbf{r}) \right) u_{n,0}(\mathbf{r}) = E_n(0)u_{n,0}(\mathbf{r}) \quad (4.23)$$

We obtain the following $\mathbf{k}\cdot\hat{\mathbf{p}}$ -hamiltonian matrix:

$$\begin{aligned} H_{\mathbf{k}\cdot\hat{\mathbf{p}}} \begin{pmatrix} c_{n,c} \\ c_{n,v} \end{pmatrix} &= \begin{pmatrix} E_c(0) + \frac{\hbar^2\mathbf{k}^2}{2m_0} + \frac{\hbar}{m_0}\mathbf{k}P_c & \frac{\hbar}{m_0}\mathbf{k}P \\ \frac{\hbar}{m_0}\mathbf{k}P & E_v(0) + \frac{\hbar^2\mathbf{k}^2}{2m_0} + \frac{\hbar}{m_0}\mathbf{k}P_v \end{pmatrix} \begin{pmatrix} c_{n,c} \\ c_{n,v} \end{pmatrix} \\ H_{\mathbf{k}\cdot\hat{\mathbf{p}}} \begin{pmatrix} c_{n,c} \\ c_{n,v} \end{pmatrix} &= E_n(\mathbf{k}) \begin{pmatrix} c_{n,c} \\ c_{n,v} \end{pmatrix} \end{aligned} \quad (4.24)$$

☞ $P_n = \langle u_{n,0}^* | \hat{\mathbf{p}} | u_{n,0} \rangle \simeq 0$ if the Bloch functions are assumed to be symmetric in the Brillouin zone (which is not exactly the case for InGaAsP [4]),

☞ $P = \langle u_{c,0}^* | \hat{\mathbf{p}} | u_{v,0} \rangle$ is the $\mathbf{k}\cdot\hat{\mathbf{p}}$ -momentum matrix element.

In a more complex use of the formalism, equation 4.24 would give a whole matrix $P_{n,n'}$. The efficiency of the Kane's formalism relies upon the fact that those momentum matrix elements are thereafter expressed in terms of effective

4. Bipolar cascade laser modeling at an “electronic level” point of view

masses, that are experimentally available. If we take the top of the valence band as the energy reference, the $\mathbf{k} \cdot \hat{\mathbf{p}}$ -hamiltonian matrix becomes:

$$H_{\mathbf{k}, \hat{\mathbf{p}}} = \begin{pmatrix} E_g + \frac{\hbar^2 \mathbf{k}^2}{2m_0} & \frac{\hbar}{m_0} \mathbf{k} P \\ \frac{\hbar}{m_0} \mathbf{k} P & \frac{\hbar^2 \mathbf{k}^2}{2m_0} \end{pmatrix}$$

The eigenvalues are found easily:

$$E_{\pm} = \frac{E_g}{2} + \frac{\hbar^2 \mathbf{k}^2}{2m_0} \pm \frac{\eta}{2} \quad (4.25)$$

$$\eta^2 = E_g^2 + \frac{4\hbar^2 \mathbf{k}^2 P^2}{m_0^2} \quad (4.26)$$

☞ + refers to the conduction band, whereas – refers to the valence band.

☞ η is a function of \mathbf{k} and equals $\eta(\mathbf{k}) = E_c(\mathbf{k}) - E_v(\mathbf{k})$.

The calculation of the eigenfunctions gives the following result:

$$\begin{aligned} u_{c, \mathbf{k}}(\mathbf{r}) &= \frac{1}{\sqrt{2\eta}} \left\{ (\eta + E_g)^{\frac{1}{2}} u_{c,0}(\mathbf{r}) + (\eta - E_g)^{\frac{1}{2}} u_{v,0}(\mathbf{r}) \right\} \\ u_{v, \mathbf{k}}(\mathbf{r}) &= \frac{1}{\sqrt{2\eta}} \left\{ (\eta - E_g)^{\frac{1}{2}} u_{c,0}(\mathbf{r}) + (\eta + E_g)^{\frac{1}{2}} u_{v,0}(\mathbf{r}) \right\} \end{aligned}$$

☞ We have always: $\varphi_{n, \mathbf{k}}(\mathbf{r}) = \frac{e^{i\mathbf{k} \cdot \mathbf{r}}}{\sqrt{V}} u_{n, \mathbf{k}}(\mathbf{r})$

We can now compute $X_{cv}(\mathbf{k})$ with $|k_x| \gg |k_{\perp}|$:

$$X_{cv}(\mathbf{k}) = i \frac{E_g/2\eta}{(\eta^2 - E_g^2)^{\frac{1}{2}}} \frac{\partial \eta}{\partial k_x}$$

If we consider the \mathbf{k} values next to the center of the Brillouin zone, we have:

$$E_g > \frac{2\hbar \mathbf{k} P}{m_0}$$

We can rewrite equation 4.25 as:

$$E_{\pm} = \frac{E_g}{2} \pm \frac{\hbar^2 \mathbf{k}^2}{2m_{\pm}}$$

We introduce the effective masses m_{\pm} at the band edges, and a tunnel reduced effective mass, so that the momentum matrix element P , and therefore η can be expressed in terms of experimentally available effective masses:

$$\begin{aligned} \frac{1}{m_{\pm}} &= \frac{2P^2}{m_0^2 E_g} \pm \frac{1}{m_0} \\ \frac{1}{m_r} &= \frac{1}{m_+} + \frac{1}{m_-} \\ P &= \frac{m_0}{2} \sqrt{\frac{E_g}{m_r}} \end{aligned} \quad (4.27)$$

4.6 Esaki tunnel junction modeling

Rewriting equation 4.26, the momentum matrix element is replaced by an expression function of the reduced mass and we have:

$$\eta^2 = E_g^2 + \frac{E_g \hbar^2 \mathbf{k}^2}{m_r} \quad (4.28)$$

Noticing that $\eta(\mathbf{k}) = E_c(\mathbf{k}) - E_v(\mathbf{k})$, we can now give an expression of the terms in the tunneling matrix element (equation 4.19), as a function of \mathbf{k} and m_r :

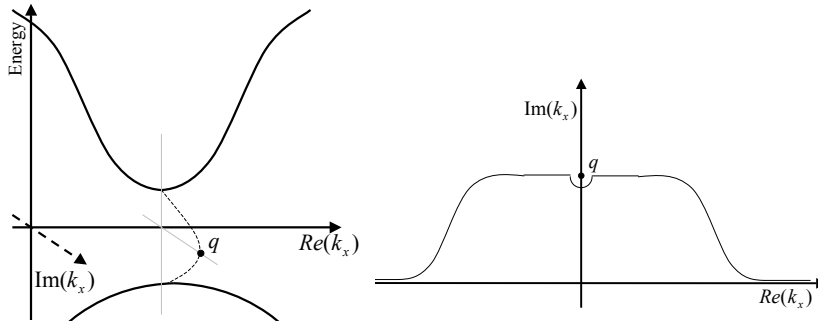
$$\begin{aligned} X_{cv}(\mathbf{k}) &= \frac{i\hbar E_g^{\frac{3}{2}}}{2m_r^{\frac{1}{2}} \eta^2} \quad (4.29) \\ \int_0^{k_x} \eta dk_x &= \frac{k_x \eta}{2} + \frac{\sqrt{m_r E_g}}{\hbar} \left\{ E_g + \frac{\hbar^2}{m_r} k_{\perp}^2 \right\} \\ &\quad \times \ln \left[\frac{\eta + \hbar k_x \sqrt{\frac{E_g}{m_r}}}{\left(E_g^2 + \hbar^2 k_{\perp}^2 \frac{E_g}{m_r} \right)^{\frac{1}{2}}} \right] \quad (4.30) \end{aligned}$$

During the tunneling process, the wave vector \mathbf{k} will be imaginary (because the wave function is evanescent inside the band gap). We see from equations 4.28 and 4.25 that for $k_x = q$, we have $\eta = 0$, and the two bands have the same energy. The tunneling current will therefore be maximum at this point q , which is schematically represented on figure 4.10-(a):

$$q = i \sqrt{\frac{m_r E_g}{\hbar^2} + k_{\perp}^2}$$

Instead of following the real axis for integration of equation 4.19, we will integrate over the Cauchy contour depicted on figure 4.10-(b), that passes by the ‘‘pole’’ q .

Figure 4.10 The maximum tunneling probability occurs near the ‘‘pole’’ q .



(a) Schematic representation of dispersion diagram with complex \mathbf{k} . The dashed lines represent imaginary wave vectors \mathbf{k} .

(b) Cauchy contour of integration 4.19

4. Bipolar cascade laser modeling at an “electronic level” point of view

The calculation is performed in Calculation step G., on page 207 , and the result is:

$$M_{cv} = \frac{\pi E_g^{1/2} m_r^{1/2}}{3\kappa_x \hbar q} eF \exp \left\{ \frac{i}{eF} \int_0^q \eta dk'_x \right\} \quad (4.31)$$

Combining this expression with the expression of the integral (equation 4.30), we find:

$$M_{cv} = \frac{\pi E_g^{1/2} m_r^{1/2}}{3\kappa_x \hbar q} eF \exp \left\{ \frac{-\pi \hbar |q|^2 E_g^{1/2}}{2eF m_r^{1/2}} \right\} \quad (4.32)$$

4.6.2.4 The transmission coefficient

The Fermi Golden Rule gives a quantitative description of the probability per time unit to make a transition from the first state into the second state. For an excitation at frequency null (electrostatic field), the Fermi golden rule claims that:

$$w = \frac{2\pi}{\hbar} |M_{cv}|^2 \rho_{jt}(E) \quad (4.33)$$

↪ $M_{cv} = \langle \psi_n | -eFx | \psi_{n'} \rangle$ is the matrix element that we have obtained in equation 4.32.

$\rho_{jt}(E)$ generally refers to the joint states density: the spectral density of states for states-pairs which follow the selection rules. Here, to allow the transition, we need $\mathbf{k} = \mathbf{k}'$ and $E = E'$. The eigenvalues, solutions of equation 4.14 are part of a quasi-continuum. For every wave function in the valence band, it is possible to find a state in the conduction band with the same energy (cf. figure 4.9). The density of joint states will therefore be equal to the density of states in one band, which is exactly the density of eigenvalues, quantified by the boundary conditions. We can then write:

$$\rho_{jt}(E) = \frac{1}{\Delta E} = \frac{\kappa_x}{2\pi eF}$$

The probability per unit time is then:

$$w = \frac{\kappa_x}{eF\hbar} |M_{cv}|^2$$

To calculate the tunneling current it is however more convenient to use the dimension-less transmission coefficient T defined by the following proposition: *If N_{in} electrons strike the barrier, then an average $N_{out} = TN_{in}$ electrons will be transmitted through the gap.* For the constant field case, it can be proven (see for instance [31, 38]) that the electron crosses repeatedly and periodically the Brillouin zone with the period

$$t_{BO} = \frac{\hbar \kappa_x}{eF}$$

This phenomenon is known as the Bloch oscillations .

Let us now consider one electronic state available for tunneling with wave vector k_x . During time t , the electron wave vector in the x -direction is N times ($N = \frac{t}{t_{BO}}$) equal to k_x . The probability of this electron to go through the band gap can be calculated by two different ways:

4.6 Esaki tunnel junction modeling

1. integrating over t the probability per time unit:

$$P_{\text{tunnel}}(t) = \int_0^t w dt' = wt = wt_{BO}N$$

2. using the definition of the transmission factor:

$$P_{\text{tunnel}}(N) = TN$$

Identifying the two expressions, we can then write the transmission coefficient as:

$$T = wt_{BO}$$

which gives:

$$T = \frac{\kappa_x^2}{(eF)^2} |M_{cv}|^2 \quad (4.34)$$

Using the matrix element expression available from equation 4.32, we compute the transmission coefficient through a band gap barrier:

$$\begin{aligned} T &= \frac{\pi^2}{9} \exp\left(\frac{-\pi m_r^{1/2} E_g^{3/2}}{2\sqrt{2}\hbar eF}\right) \exp\left(-2\frac{E_{\perp}}{\overline{E}_{\perp}}\right) \\ E_{\perp} &= \hbar^2(\mathbf{k}_{\perp}^2)/2m_r \\ \overline{E}_{\perp} &= \sqrt{2}\hbar eF/\pi\sqrt{m_r E_g} \end{aligned}$$

4.6.2.5 The tunnel current

The total tunnel current density J_t (in A.m⁻²) is obtained by multiplying the incident current density by the tunneling transmission coefficient derived in the previous section. In order to do so, we assume that far from the chemical junction, the built-in electric field is screened by the high dopant density and the bands are flat. The current density must be integrated over all the possible \mathbf{k} vectors. The elementary k -volume is the cylinder portion $2\pi\mathbf{k}_{\perp} d\mathbf{k}_{\perp} dk_x$. The elementary incident current per unit area is then given by:

$$dj_{\text{incident}} = ev_{gx}\rho_{\text{RL}}(k)2\pi\mathbf{k}_{\perp} d\mathbf{k}_{\perp} dk_x$$

☞ $\rho_{\text{RL}}(k) = \frac{1}{(2\pi)^3}$ is the density of states in the \mathbf{k} -space, RL stands for “reciprocal lattice”.

☞ $v_{gx} = \frac{1}{\hbar}\nabla_{k_x} E \simeq \frac{\hbar k_x}{m_x}$ is the classical group velocity of the electrons with wave vector k_x in the x -direction.

Including a factor 2 for spin, and using the effective mass approximations in x - and perpendicular-direction ($E_x = \frac{\hbar^2 k_x^2}{2m_x}$ and $E_{\perp} = \frac{\hbar^2 \mathbf{k}_{\perp}^2}{2m_{\perp}}$), the elementary current density becomes:

$$dj_{\text{incident}} = e\frac{m_{\perp}}{2\pi\hbar^3} dE_x dE_{\perp}$$

To simplify calculation, we take here the effective masses as isotropic and equal for n - and p -side to the reduced mass m_r . Multiplying by the transmission

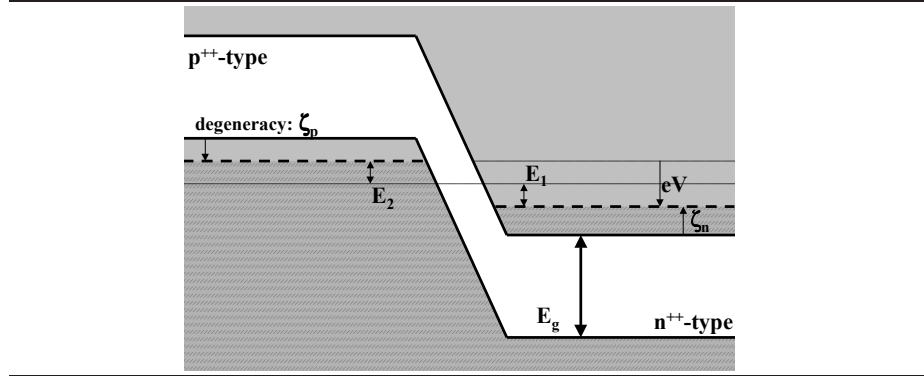
4. Bipolar cascade laser modeling at an “electronic level” point of view

coefficient and integrating over E_x and E_\perp gives the tunnel current density [31]:

$$\begin{aligned} J_{\text{tunnel}} &= \int T dj_{\text{incident}} \\ &= \frac{em_r}{18\hbar^3} \exp\left(\frac{-\pi\sqrt{m_r E_g}}{2\sqrt{2}\hbar e F}\right) \iint (f_1(E_1) - f_2(E_2)) \exp\left(-2\frac{E_\perp}{E_\perp}\right) dE dE_\perp \end{aligned}$$

☞ f_1 and f_2 are the occupancy factors, the energies are defined according to figure 4.11

Figure 4.11 Definitions of the variables used in [31] to derive the tunnel current



It should be noted that since $E = E_x + E_\perp$, the limits of integration are

$$\begin{aligned} 0 &\leq E_\perp \leq E_s \\ 0 &\leq E \leq \zeta_n + \zeta_p - eV \end{aligned}$$

☞ E_s is the smaller of E_1 and E_2 , the degeneracy factors ζ_n and ζ_p are defined by figure 4.11

The integral over E_\perp gives the result:

$$J_{\text{tunnel}} = \frac{em_r}{18\hbar^3} \exp\left(\frac{-\pi\sqrt{m_r E_g}}{2\sqrt{2}\hbar e F}\right) \left(\frac{\overline{E_\perp}}{2}\right) \times D \quad (4.35)$$

$$\text{with } D = \int (f_1(E_1) - f_2(E_2)) \left(1 - \exp\left(-2\frac{E_s}{E_\perp}\right)\right) dE$$

☞ D has the dimension of energy, depends on the temperature (via the occupancy factors) and of the degeneracy ζ_n and ζ_p (depth of penetration of the Fermi levels into the energy bands)

☞ an increase of $\overline{E_\perp}$ implies a decrease in J_{tunnel} which is consistent with the classical representation of tunneling: if the electron has a higher transverse \mathbf{k} -vector, it has to go through a wider potential barrier.

A complete set of formulas are given in [31] at $T = 0$ K (f_1 and f_2 are step functions), and for $\zeta_n > 0$ and $\zeta_p > 0$ (n - and p -side degenerate). The

4.6 Esaki tunnel junction modeling

expression of D differs slightly if one side is not degenerate (as it is the case for our study case). In particular, no negative resistance is observed, and the tunnel current appears only after a negative polarization threshold. For $\zeta_n > 0$ but $\zeta_p < 0$, and still at $T = 0$ K, we have:

$$\begin{aligned} \text{if } eV > \zeta_p, & \quad D = 0 \\ \text{if } \zeta_p > eV > \zeta_p - \zeta_n, & \quad D = eV - \zeta_p + \frac{E_\perp}{2} \left(1 - \exp \left\{ -\frac{2}{E_\perp} (\zeta_p - eV) \right\} \right) \\ \text{if } eV < \zeta_p - \zeta_n, & \quad D = eV - \zeta_p + \frac{E_\perp}{2} \left(1 + \exp \left\{ -\frac{2\zeta_n}{E_\perp} \right\} - 2 \exp \left\{ \frac{eV - \zeta_n - \zeta_p}{E_\perp} \right\} \right) \end{aligned}$$

As shown in [31], D describes the general shape of the I(V) characteristic. The magnitude of the transmitted current is mainly controlled by the exponential term:

$$J_{\text{tunnel}} \propto \exp \left(-\frac{\pi \sqrt{m_r E_g}}{2\sqrt{2} \hbar e F} \right)$$

Consistently with what can be intuitively deduced, the tunnel current is all the higher as:

1. The band-gap energy E_g of the material is low
2. The effective mass m_r is low
3. The doping concentration (and thus the degeneracy) is high
4. The internal electric field is high

We will see in chapter 5 the quantitative effect of the material and of the dopant concentration on the tunnel current.

4.6.3 Discussion on the tunnel-current model and on its implementation

4.6.3.1 The physical model

The Kane model we have chosen to implement is the most rigorous band-to-band tunneling model we have found in the literature:

1. The calculation only relies on intrinsic material parameters (no phenomenological fit parameters such as in [18, 26, 28]).
2. The band model assumed to calculate the matrix element is a 2-band description, instead of a parabolic approximation [32, 37] or a constant matrix element model [39].
3. The conservation of momentum is taken into account (the theory mainly relies on this selection rule), and the transverse momentum is included [24, 39].

Despite all the advantages, the model still suffers from some drawbacks or at least strong approximations are used to derive analytical expressions:

4. Bipolar cascade laser modeling at an “electronic level” point of view

1. The main approximation probably consists in the semiconductor bands description. The 2-band model, although fairly accurate for InSb, is not rigorous for InP-based semiconductors [4, 5, 31]. A rigorous account for the spin-orbit split-off band can be found from the derivation of a higher-order use of the $\mathbf{k} \cdot \hat{\mathbf{p}}$ -method, and would require a numerical integration of equation 4.19. Kane proposes an alternative solution supposing that the transmission coefficient T does not strongly differ from the 2-band calculation. The correction comes from a more accurate expression of $E(\mathbf{k})$ found in [40]. This leads to the reformulation of the effective masses, but also of D and E [31]. It should be noted here that although the effective masses are taken as equal for light holes and electrons for calculating the tunneling probability, the quasi-Fermi-levels (QFL) are determined by a transport model that describes well the discrepancy between electron and hole mobility.
2. Another serious approximation is the assumption of a constant field. If we want to account for field variations, then equation 4.35 must be numerically integrated over the junction [22, 31]. Kane proposes to take an average field to determine D [31]. We follow Adar [22] who has shown that, for backward bias, the result is close to the one obtained numerically by taking the field equal to its value at midgap.
3. The third important effect neglected is the perturbation of the high impurities concentration on the band gap. The effect is known as band tailing [39, 41, 42] and is characterized by a band gap shrinkage [39].
4. The other neglected effects are of smaller importance for our study case: several authors have studied in a more detailed way the forward bias tunneling process which gives rise to negative differential resistance. The previously described model must be completed with phonon interactions [31, 32] and with an “excess current” model involving tunneling between the bands and intermediate impurity levels inside the band gap [43, 44]. For our purpose, we are only interested in the backward Zener-like tunneling process. In addition, according to some authors, the Coulomb interaction across the band gap should also be taken into account [21, 31, 37, 39]. It results in an additional factor dependent of the band gap and on the dielectric constant of the material.
5. There are several other limitations: the model only calculates the direct tunneling (indirect-phonon-assisted tunneling is not taken into account); the model is valid only for homojunctions (same material on n - and p -side); the description of the parameter D is done at $T = 0$ K (which is not a real problem for backward tunneling, but might overestimate the forward tunneling current), etc.

Eventually, we would like to point out the fact that reverse tunnel diodes present *a priori* good characteristics for implementation in microwave optical systems:

- The electron tunneling transit time is lower than the one for conventional conduction processes [24, 45].
- Backward diodes have low $1/f$ noise [24, 27, 46].

4.6 Esaki tunnel junction modeling

- The 0-bias reverse resistivity is not very much sensitive to temperature variations [18, 24]. The variation with temperature only comes from the variation of the material properties.

4.6.3.2 Numerical implementation

The implementation of equation 4.35 was carried out in the transport model described in section 4.2 on page 104. The electrons tunneling at a rate given by equation 4.35 are considered in the model as a source of electron-hole pairs generation localized at the chemical junction: majority carriers are created in the case of backward tunneling and are recombined in the case of forward bias tunneling.

As for the calculation of the process, the electric field is assumed to be constant and equal to the electric field at the chemical junction where it reaches its maximum value. The degeneracy factors ζ_n (resp. ζ_p) are calculated in the middle of the n - (resp. p -) side region, in the “neutral” region (with no electric field), using the Fermi-Dirac statistics for carrier concentration. The other parameters (e.g. E_G , m_r) are supposed equal for both sides.

This implementation also requires a non-local treatment of the generation-recombination rate calculation injected in equation 4.4 of the drift-diffusion model. The problem is numerically solved by using the Woodbury formula, already described in section 4.5, on page 112.

Figure 4.12 Highly-doped homojunction InGaAsP ($\lambda = 1.35\mu\text{m}$ doped to 5×10^{18}) under reverse bias with (a) a model which does not allow for tunneling generation, and (b) a model that permits electron band-to-band tunneling.

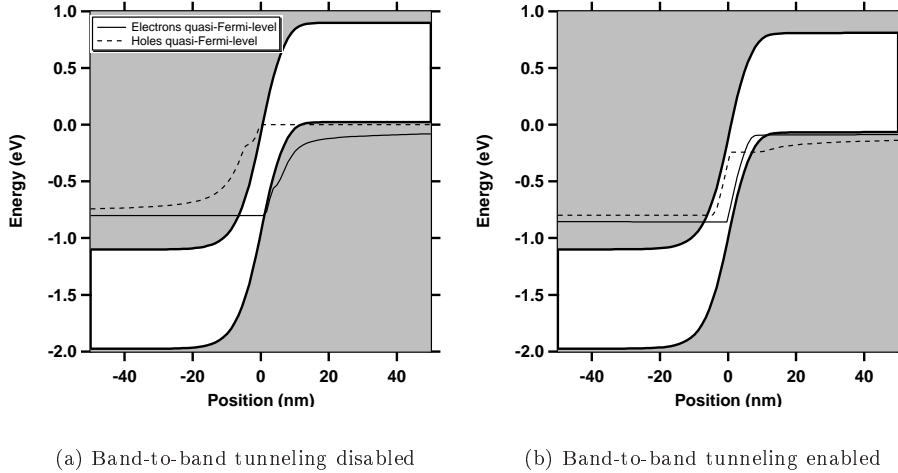


Figure 4.12 presents a highly-doped p - n junction while tunneling is and is not permitted by the modeling program. The effect of allowing for tunnel processes is to increase the number of electrons (resp. holes) in the n - (resp. p -) type region. We see from figure 4.12-(b) that the quasi-Fermi-level (QFL) for electrons (resp. holes) increases (resp. decreases) strongly at the chemical junction, resulting

4. Bipolar cascade laser modeling at an “electronic level” point of view

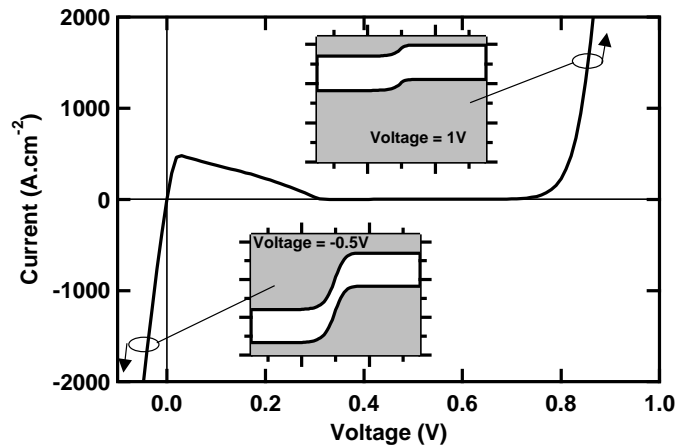
in a net p to n -side electron current. For the same voltage drop (1 V over the whole structure), the total current increases dramatically (from 10^{-11} $\text{kA}\cdot\text{cm}^{-2}$ in figure 4.12-(a) to 200 $\text{kA}\cdot\text{cm}^{-2}$ in figure 4.12-(b)) while the tunneling current is enabled. For the same voltage drop over the whole structure, the voltage drop over the tunnel junction is reduced while the band-to-band tunneling is enabled.

4.6.3.3 Example of simulation

Eventually, we present in figure 4.13 a simulation of a highly-doped (10^{19} cm^{-3}) Esaki junction on InGaAsP ($\lambda_{\text{PL}} = 1.35$ μm).

Very consistently with what was intuitively and qualitatively described in section 4.6.1, for backward bias, a high amount of tunnel current goes through the pn -junction. The local negative resistance is also observed in our simulation and its shape is characteristic of a tunnel junction with the n -side more degenerate than the p -side ($\zeta_n > \zeta_p$) [31]. For voltage exceeding the band-gap energy ($eV \geq E_G \approx 0.8\text{eV}$), thermoionic carrier emission takes place and the current easily flows through the forward-bias diode.

Figure 4.13 Example of simulation of a highly-doped InGaAsP ($\lambda = 1.35\mu\text{m}$ doped to 10^{19}): V-I characteristic and band diagram.



4.7 Conclusion

Whereas chapter 2 and chapter 3 intended to demonstrate the possible improvements obtained for cascading several active junctions, we have described in this chapter a very complete self-consistent transport model with every element for the simulation of bipolar cascade laser.

We have elaborated a parameter database for the simulation of devices grown on InP substrate. We have implemented the Fermi-Dirac statistics in order to account for very high dopant concentrations and carrier population, and allowed for multi-quantum-well device simulation. Eventually, we have derived

4.7 Conclusion

a self-consistent calculation for modeling the tunnel current through the tunnel junctions.

The next and last chapter of this thesis is mainly experimental. We use the transport model described in this chapter to design and produce tunnel junctions and single-transverse-mode bipolar cascade lasers. We will then present the characteristics of the produced devices.

Bibliography

- [1] Arnaud Fily. *Modèle pour diodes laser de puissance*. PhD thesis, Université Paris X, Paris, France, Dec. 1998.
- [2] Eddy Chirlias. *Contribution à l'ingénierie et à la modélisation d'hétérostructures (Ga,In)(As,P)/GaAs pour diodes lasers*. PhD thesis, Université Paris VI, Paris, France, Jul. 2001.
- [3] Eric Ducloux. Méthodes numériques de calcul de modes optiques 1D pour des guides à profil d'indice complexe. Technical Report MAN-94-3, Thomson-CSF Laboratoire Central de Recherche (now Thales Research & Technology), Orsay, France, Sept. 1994.
- [4] Otfried Madelung. *Semiconductors - Basic Data*. Springer-Verlag, Berlin Heidelberg New York, 2nd revised edition, 1996.
- [5] S. Adachi. Band structure of InGaAsP, Optical Properties of InGaAsP: Discussion, Optical Functions of InGaAsP: Tables. *INSPEC, Properties of InP and related compounds*, pages 387–428, 1991.
- [6] M. P. C. M. Krijn. Heterojunction Band Offsets and Effective Masses in III-V Quaternary Alloys. *Semiconductors Science and Technology*, 6:27–31, 1991.
- [7] D. Lancefield. Electron Mobility in InP: Overview, Electron Mobility in VPE and MOVPE InP. *INSPEC, Properties of InP and related compounds*, pages 63–69, 1991.
- [8] M. A. Afromowitz. Refractive index of $\text{Ga}_{1-x}\text{Al}_x\text{As}$. *Solid State Communications*, 15(1):59–63, 1974.
- [9] B. Broberg and S. Lindgren. Refractive index of $\text{In}_{1-x}\text{Ga}_x\text{As}_y\text{P}_{1-y}$ layers and InP in the transparent wavelength region. *Journal of Applied Physics*, 55(9):3376, May 1984.
- [10] Larry A. Coldren and Scott W. Corzine. *Diode Lasers and Photonic Integrated Circuits*. Wiley, New York, NY, USA, 1995.
- [11] Olivier Gilard. *Contribution à la modélisation de diodes lasers à puits quantiques contraints pour télécommunications optiques*. PhD thesis, Université Paul Sabatier, Toulouse, France, Jan. 1999.

BIBLIOGRAPHY

- [12] G. Rossi et al. SPICE Simulation for Analysis and Design of Fast 1.55 μm MQW Laser Diodes. *Journal of Lightwave Technology*, 16(109):1509–1516, Aug. 1998.
- [13] J. Piprek, P. Abraham, and J.E. Bowers. Efficient Analysis of Quantum Well Lasers using PICS3D. In *Integrated Photonics Research Conference*, Santa Barbara, Jul. 1999.
- [14] Ioffe Physico-Technical Institute. Physical Properties of Semiconductors. <http://www.ioffe.rssi.ru/SVA/NSM/Semicond/index.html>.
- [15] D. L. Scharfetter and H. K. Gummel. Large-signal analysis of a silicon read diode oscillator. *IEEE Transactions on Electronic Devices*, ED-16(1):64–77, Jan. 1969.
- [16] Universidad Politécnica de Madrid. *Harold version 3.0*, 1998.
- [17] W.H. Press, W.T. Vetterling, S.A. Teukolsky, and B.P. Flannery. *Numerical Recipes in Fortran*. Cambridge University Press, United Kingdom, 2nd Ed. edition, 1992.
- [18] Leo Esaki. New Phenomenon in Narrow Germanium p - n Junctions. *Physical Review*, 109:603–604, 1958.
- [19] Clarence Zener. A Theory of Electrical Breakdown of Solid Dielectrics. *Proceeding of the Royal Society*, A 145(523):523–529, 1934.
- [20] A. G. Chynoweth and K. G. McKay. Internal Field Emission in Silicon p - n Junctions. *Physical Review*, 106:418–426, May 1957.
- [21] E. O. Kane. Zener Tunneling in Semiconductors. *J. Phys. Chem. Solids*, 12:181–188, 1959.
- [22] R. Adar. Spatial integration of direct band-to-band tunneling currents in general device structures. *IEEE Transactions on Electronic Devices*, 39(4):976–981, Apr. 1992.
- [23] W. A. Beck and N. E. Byer. Calculation of Tunneling Currents in (Hg,Cd)Te Photodiodes Using a Two-Sided Potential. *IEEE Transactions on Electron Devices*, ED-31(3):292–297, Mar. 1984.
- [24] S.M. Sze. *Physics of Semiconductor Devices*. Wiley, Murray Hill, NJ, 1969.
- [25] Joachim Piprek. *Semiconductor Optoelectronic Devices, Introduction to Physics and Simulation*. Academic Press, San Diego, Ca, USA, 2003.
- [26] C. W. Bates. Tunneling Current in Esaki Diodes. *Physical Review*, 121(4):1070–1071, Feb. 1961.
- [27] Sverre T. Eng. Low-Noise Properties of Microwave Backward Diodes. *IRE Transactions on Microwave Theory and Techniques*, pages 419–425, Sept. 1961.
- [28] J. Karlovsky. Simple Method for Calculating the Tunneling Current of an Esaki Diode. *Physical Review*, 127(2):419, Jul. 1962.

-
- [29] G.A.M. Hurkx et al. A new recombination model for device simulation including tunneling. *IEEE Transactions on Electron Devices*, 39(2):331–338, Feb. 1992.
- [30] H. Mathieu. *Physique des semiconducteurs et des composants électroniques*. Masson, Paris, France, 3ème edition, 1996.
- [31] E. O. Kane. Theory of Tunneling. *Journal of Applied Physics*, 32(1):83–91, Jan 1961.
- [32] L. V. Keldysh. Behavior of non-metallic crystals in strong electric fields. *Soviet Physics JETP*, 6 (33)(4):763–770, Apr. 1958.
- [33] E. Rosencher and B. Vinter. *Optoelectronics*. Cambridge University Press, Cambridge, 2002.
- [34] E. Rosencher and B. Vinter. *Optoelectronique*. Dunod, Paris, 2nd edition, 2002.
- [35] C. Kittel. *Quantum Theory of Solids*. Wiley, New York, USA, 1963.
- [36] M. Abramowitz and I.A. Stegun. *Handbook of Mathematical Functions, 9th printing*. Dover Publications, INC, New York, USA, 1972.
- [37] Walter Franz. Zener-Effekt und Stossionisation (in German). In *International Conference on Semiconductor*, pages 317–328, Garmisch-Partenkirchen, Germany, 1956.
- [38] C. Kittel. *Physique de l'état solide, (Traduction) 5ème Ed*. Dunod Université, Paris, France, 1983.
- [39] H. C. Jr Casey et al. Concentration-dependent absorption and spontaneous emission of heavily-doped GaAs. *Journal of Applied Physics*, 47(2):631–643, Feb. 1976.
- [40] E. O. Kane. Band Structure of Indium Antimonide. *Journal of Phys. Chem. Solids*, 1:249–261, 1957.
- [41] T.P. Brody. Nature of the Valley Current in Tunnel Diodes. *Journal of Applied Physics*, 33(1):100–111, Jan. 1962.
- [42] H. C. Jr Casey et al. Concentration-dependence of the absorption coefficient for *n*-type and *p*-type GaAs between 1.3 and 1.6 eV. *Journal of Applied Physics*, 46(1):250–257, Jan. 1975.
- [43] Dietrich Meyerhofer et al. Degenerate Germanium. I. Tunnel, Excess, and Thermal Current in Tunnel Diodes. *Physical Review*, 126(4):1329–1341, May 1962.
- [44] A.G. Chynoweth et al. Excess Tunnel Current in Silicon Esaki Junctions. *Physical Review*, 121(3):684–694, Feb. 1961.
- [45] K. K. et al. Thornber. The Tunneling Time of an Electron (Communications). *Journal of Applied Physics*, 38(5):2384–2385, Apr. 1967.
- [46] H. V. Shurmer. Backward diodes as microwave detectors. In *Proceedings IEE*, volume 111, Sept. 1964.

Chapter 5

Design of a single-transverse-mode bipolar cascade laser

“Si tu vois la lumière au bout du tunnel, prie pour que ce
ne soit pas le train . . .”
French popular saying

The previous chapter described on an “electronic level” point of view a self-consistent model for modeling Esaki tunnel junctions and bipolar cascade lasers. This model relies on Fermi-Dirac statistics, is compatible with multi-quantum-well structures, and accounts for band-to-band tunneling.

This chapter deals with the design of a single-transverse-mode bipolar cascade laser. The major obstacle to overcome is the crucial design of the tunnel junction. Therefore we first use the electronic transport model to optimize the tunnel junction that will be implemented in the bipolar cascade laser. In particular, using zinc atoms as p -type dopants entails some drawbacks that deserve detailed investigation. Some experimental measurements of the characteristics of the optimized tunnel junctions will also be presented.

Once the parameters of the tunnel junction are optimized, the electronic transport model is used to design a single-transverse-mode bipolar cascade laser. The structure is rather complicated but should nevertheless remain single-transverse-mode. This very specific constraint leads to corresponding optimizations such as, for instance, the width of the electron confinement barrier layer between the MQW layers and the tunnel junctions. We also provide some interesting experimental measurements on fabricated devices.

☞ Please note that all simulations are done at room temperature (293 K).

5.1 Tunnel junctions

The amplitude of the backward-tunnel current through a tunnel junction was accurately calculated in chapter 4. We eventually derived an analytical solution (except for an energy parameter D describing the overall shape of the

current-versus-voltage curve) depicted by equation 4.35, while considering a set of approximations displayed in section 4.6.3.3. This analytical expression of the tunnel current is proportional to:

$$J_{\text{tunnel}} \propto \frac{em_r}{18\hbar^3} \exp\left(-\frac{\pi\sqrt{m_r E_g}}{2\sqrt{2}\hbar e F}\right) \left(\frac{\bar{E}_\perp}{2}\right) \quad (5.1)$$

with $\bar{E}_\perp = \frac{\sqrt{2}\hbar e F}{\pi\sqrt{m_r E_g}}$

As we already explained previously (cf. section 4.6.2.5 on page 129), the main parameters that influence the amplitude of the tunnel current are the following:

- The tunnel effective mass m_r ,
- The band-gap energy E_G ,
- The level of degeneracy in each side of the junction ζ_n and ζ_p ,
- The electric field at the junction chemical interface (where the tunneling process occurs) F .

The tunnel effective mass and the band-gap energy can not be changed separately. Changing the constitutive material changes both of them. Similarly, a change in the level of degeneracy (i.e. a change in the doping levels) also causes a change in the resulting internal electric field for a given voltage bias.

5.1.1 Improving the tunnel probability by changing the constituting materials

5.1.1.1 Band-gap energy

According to the relation 5.1, one way to reduce the voltage bias necessary to achieve a given current density is to decrease the energy gap of the material constituting the junction.

Intuitively speaking, reducing the material band-gap is equivalent (for a given electric field) to reducing the triangular-like tunnel barrier width, and thus the tunnel probability.

Figure 5.1 presents the evolution of the band-gap energy of $\text{In}_{1-x}\text{Ga}_x\text{As}_y\text{P}_{1-y}$ lattice-matched on InP as a function of the arsenic proportion (y).

As the material gets closer to $\text{In}_{0.53}\text{Ga}_{0.47}\text{As}$, the band-gap energy decreases. A tunnel junction made in a material with a higher proportion of arsenic will then enable a higher tunnel current for a given voltage bias.

5.1.1.2 Effective mass

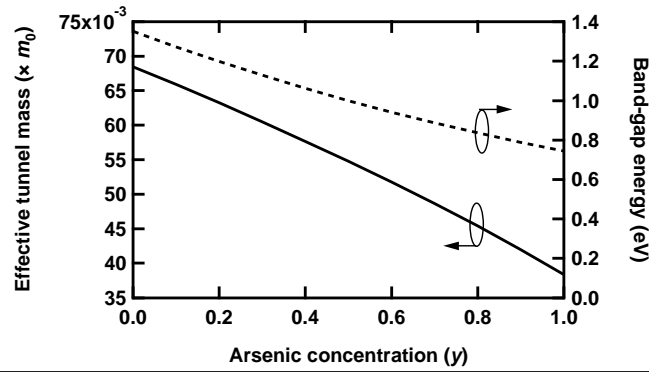
In addition, while we design the material band-gap, we modify the effective mass involved in the tunneling probability. Figure 5.1 displays the evolution of the tunnel effective mass, as calculated by equation 4.27, that we rewrite here:

$$\frac{1}{m_r} = \frac{1}{m_c} + \frac{1}{m_v} \quad (5.2)$$

5.1 Tunnel junctions

- ☞ m_c is the electron effective mass in the conduction band
- ☞ $m_v = (m_{ih}^3 + m_{hh}^3)^{\frac{1}{3}}$ is the density of state hole effective mass in the valence band

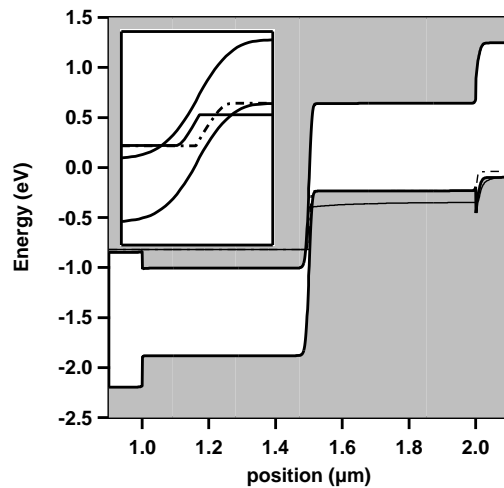
Figure 5.1 Evolution of the band-gap energy, and of the effective mass of $\text{In}_{1-x}\text{Ga}_x\text{As}_y\text{P}_{1-y}$ lattice-matched on InP as a function of the arsenic proportion (y).



5.1.1.3 Band diagram

Figure 5.2 shows the calculated band diagram for a $\lambda_{\text{PL}} = 1.35 \mu\text{m}$ -based TJ for a current density of $10 \text{ kA}\cdot\text{cm}^{-2}$.

Figure 5.2 Calculated band diagram for a tunnel junction under reverse bias. The calculated current flow is $10 \text{ kA}\cdot\text{cm}^{-2}$. Also shown are the quasi-Fermi levels of holes (dot-dashed thin line), and electrons (full thin line). Insert shows a zoom of the depletion zone.



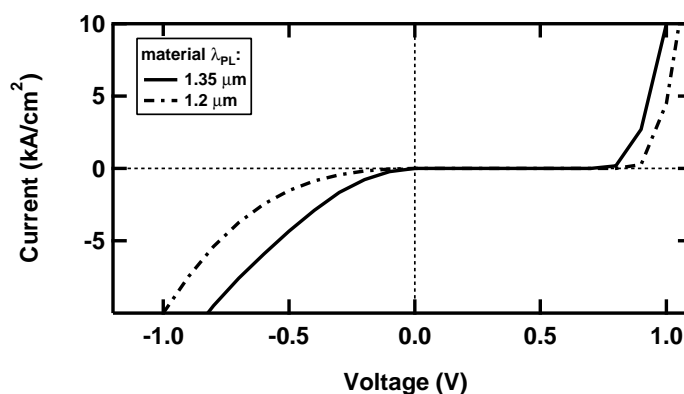
Due to very high doping values, no gradient of electrical potential can settle in the materials composing the tunnel junction. The bands are very flat except

for the pn -junction at the interface between the highly-doped materials. This interface exhibits a very high electric field built up in the region depleted of carriers.

5.1.1.4 Calculated characteristic

Figure 5.3 presents the calculated $J(V)$ characteristic of a InGaAsP $\lambda_{\text{PL}} = 1.2\text{-}\mu\text{m}$ ($E_g = 1.03\text{ eV}$) TJ, compared to a InGaAsP $\lambda_{\text{PL}} = 1.35\text{-}\mu\text{m}$ ($E_g = 0.91\text{ eV}$) TJ. "PL" stands for "photoluminescence". The calculated $J(V)$ characteristic is displayed with the conventions used for pn junctions: a positive voltage is a forward bias on the pn -diode (the electrical potential on the p -side exceeds the electrical potential on the n -side). We are here interested in the reverse bias regime (negative voltage). All the materials are doped to 5×10^{18} atoms/cm³.

Figure 5.3 Comparison of the calculated $J(V)$ characteristics for InGaAsP $\lambda_{\text{PL}} = 1.2\text{-}\mu\text{m}$, and InGaAsP $\lambda_{\text{PL}} = 1.35\text{-}\mu\text{m}$ -based tunnel junctions. All materials are doped $5 \times 10^{18}\text{ cm}^{-3}$.



The $J(V)$ characteristics are not linear with the current. Therefore we need to compare the voltage drop obtained for a given current density. A conventional single-mode, single-active-region laser usually exhibits a current density threshold of approximately 1 to 3 kA.cm⁻². We choose then to compare the characteristics at a significantly higher reference current density of $J_{\text{ref}} = 10\text{ kA.cm}^{-2}$.

According to the calculation plotted on figure 5.3, J_{ref} can be obtained for a voltage bias of 1.0 V for $\lambda_{\text{PL}} = 1.2\text{-}\mu\text{m}$ materials whereas $V = 0.82\text{ V}$ is enough for reaching J_{ref} with a $\lambda_{\text{PL}} = 1.35\text{-}\mu\text{m}$ -based TJ. The resistivity of the tunnel junction is also a parameter of importance. The calculated resistivity is close to $7 \times 10^{-5}\text{ }\Omega\text{.cm}^2$ (which corresponds to a resistance of approximately 5 Ω for a $3\text{ }\mu\text{m} \times 500\text{ }\mu\text{m}$ -device) at 3 kA.cm⁻² and goes down to $4 \times 10^{-5}\text{ }\Omega\text{.cm}^2$ (which corresponds to a resistance of approximately 3 Ω for a $3\text{ }\mu\text{m} \times 500\text{ }\mu\text{m}$ -device). The resistivity were found to be almost the same for the two types of materials for the current density we have chosen as a reference.

Note on figure 5.2 that the n -type InGaAsP ($\lambda_{\text{PL}} = 1.35\text{ }\mu\text{m}$) is degenerate, whereas the p -type is not completely, but is on the verge of degeneracy. According to the expressions of the energy coefficient D derived in section 4.6.2.5, if one of the constitutive junction material is not degenerate, the tunnel process

5.1 Tunnel junctions

undergoes a reverse bias voltage threshold. The reverse tunneling effect appears on figure 5.3 above a very small voltage threshold of 1.5 mV.

5.1.1.5 Conclusion

As the proportion of arsenic (y) increases, both the band-gap energy, and the tunnel effective mass decrease. We need to use materials with an arsenic proportion as high as possible for increasing our tunnel conductivity.

However, for a 1.55 μm emission, we need to stay away from the fundamental absorption of the semiconductor, especially since the high-doping concentration may reduce the effective band-gap due to band-tailing [1–3].

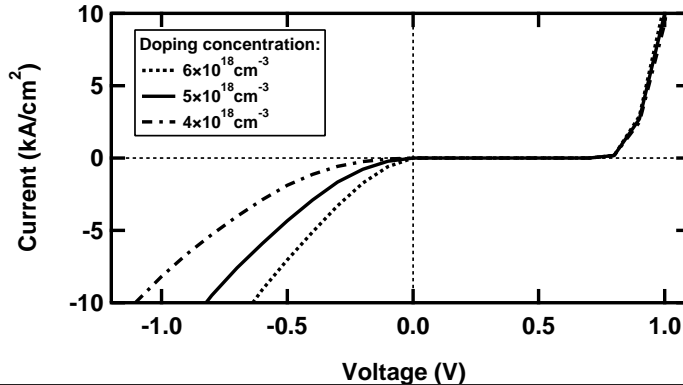
With a band-gap energy higher than the photon energy ($E_G = 0.8$ eV), and also because the optimized growth parameters were already available, we have used for our tunnel junction the material InGaAsP with $\lambda_{\text{PL}} = 1.35$ μm .

5.1.2 Doping level

Another way to reduce the voltage bias is to increase the degeneracy of the materials, i.e. to increase the doping concentration, which will therefore lower the tunneling voltage threshold and increase the built-in electric field, leading to an increased tunneling probability. Unfortunately, dopants, and especially Zn atoms (used in InGaAsP materials grown by MOCVD as p -dopants), have a limited incorporation, and 5×10^{18} atoms per cm^3 is already very close to the incorporation limit [4]. The high diffusion rate and the low incorporation are major issues that will be discussed more in detail in paragraph 5.1.3.

We can nevertheless already estimate the influence of doping of both n - and p -side of the tunnel junction on the electrical characteristics. Figure 5.4 compares the $J(V)$ calculated for $\lambda_{\text{PL}} = 1.35$ μm InGaAsP with doping concentration of $N_A = N_D = 4 \times 10^{18}$, 5×10^{18} and 6×10^{18} cm^{-3} .

Figure 5.4 Comparison of the calculated $J(V)$ characteristics for $\lambda_{\text{PL}} = 1.35$ - μm InGaAsP with doping concentration $N_A = N_D = 4 \times 10^{18}$, 5×10^{18} and 6×10^{18} cm^{-3} .



The voltage bias necessary to reach $10 \text{ kA} \cdot \text{cm}^{-2}$ decreases from 1.10, to 0.82 and to 0.64 V for 4×10^{18} , 5×10^{18} and 6×10^{18} cm^{-3} respectively. The conduc-

tivity of the tunnel junction increases as we increase the doping concentration. We will therefore increase as much as possible the doping level in our structures.

These results also prove that the doping concentration drastically influences the electrical characteristics, and that a small deviation or uncertainty on this factor can lead to dramatically changed performances.

5.1.2.1 Additional losses while increasing the doping concentration

Increasing the doping concentration means also increasing the free carrier absorption. Since the tunnel junction will eventually be placed in the middle of the optical mode, the additional absorption is an important factor to be considered and will be included in the simulation. Once again, a trade-off needs to be found in order to favor the tunneling process without degrading the overall modal gain in the cavity.

The free-carrier losses are increased by the doping concentration in two separate ways:

- The main intrinsic loss mechanism in InGaAsP/InP-lasers is inter-valence band absorption (IVBA) [5–7]. The absorbed photon delivers its energy to a hole which makes an inter-subband transition within the valence band of the semi-conductor.
- Since the material is not perfect, there also exists an extrinsic loss mechanism. The defects (e.g. vacancies), and the dopant atoms provide additional energy levels allowed inside the semiconductor band-gap. They furthermore increase the scattering of the photons leading to light coupling into vanishing optical modes.

It is very difficult to obtain a satisfactory theoretical quantitative description of the free carrier losses. We will therefore use the experimentally reported quasi-linearity of the absorption coefficient with the carrier concentration [7] and use an empirical cross-section parameters for calculating the bulk local absorption coefficient:

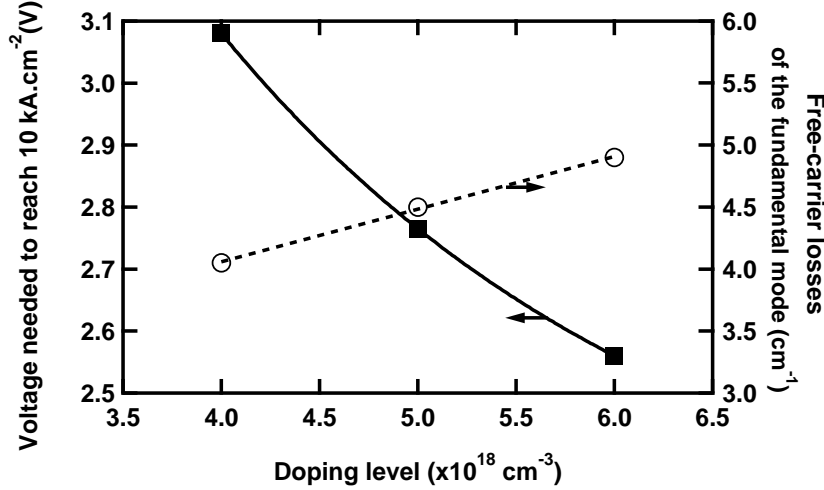
$$\alpha_{fc}(z) = \alpha_n n(z) + \alpha_p p(z)$$

☞ α_n (resp. α_p) is the free carrier cross-section and is taken to be $3 \times 10^{-18} \text{ cm}^2$ (resp. $20 \times 10^{-18} \text{ cm}^2$) [7, 8]

In order to evaluate the influence of a doping concentration increase on the optical losses in the cavity, we performed the simulation of a single-transverse-mode two-active-junction laser structure with one QW per active junction. We compare on figure 5.5 the voltage needed for the laser structure to reach a bias current of 10 kA.cm^{-2} , as well as the modal free-carrier losses of the laser at this bias current, as a function of the doping level of the tunnel junction. The doping level is increased from $4 \times 10^{18} \text{ cm}^{-3}$ to $6 \times 10^{18} \text{ cm}^{-3}$.

5.1 Tunnel junctions

Figure 5.5 Evolution of the voltage needed to supply 10 kA.cm^{-2} to a two-active-regions bipolar cascade laser structure, and of the free-carrier modal losses as a function of the doping level of the tunnel junction.



While decreasing the doping concentration of the tunnel junction from $6 \times 10^{18} \text{ cm}^{-3}$ to $4 \times 10^{18} \text{ cm}^{-3}$, the free-carrier losses undergone by the fundamental mode decreases almost linearly from 5 cm^{-1} to 4 cm^{-1} , which is already rather significant. But the voltage needed to reach 10 kA.cm^{-2} meanwhile have increased faster than linearly from 2.56 V to 3.1 V . This important voltage increase triggers a higher Joule heating energy dissipation which increases losses and non-radiative recombinations [9]. This thermal effect is not taken into account in our simulation.

5.1.2.2 The trade-off given by the technological limit

On the one hand, a high doping concentration increases free-carrier losses, but on the other hand, it decreases the necessary voltage drop and therefore reduces the additional recombinations due to the heating of the device.

Since the free carrier loss increase is linear, whereas the voltage increase is faster-than-linear with the doping concentration, we decide to increase the doping concentration as much as it is technologically possible and deal with additional losses provided that we limit the voltage drop at the tunnel junctions.

5.1.3 Zn diffusion

Zinc is the *p*-type dopant atom generally used in MOCVD for the fabrication of InGaAsP/InP devices (transistors, or lasers). Its main assets are the following [10–12]:

- Strong electrical activity, attributed to a shallow acceptor level [12]
- low toxicity (as compared to cadmium for instance)
- low memory effect [10, 13]
- Low diffusion for concentrations below $10^{18} \text{ atoms.cm}^{-3}$.

5. Design of a single-transverse-mode bipolar cascade laser

However, as we have seen in the previous paragraph, a very high doping concentration (2 to 5×10^{18} atoms.cm⁻³) is a key requirement for obtaining a low-resistivity tunnel junction. At this high doping level, the diffusion coefficient of Zn can be very high. This diffusion of particles may be severe enough to degrade or shift the tunnel junction interface, thus altering the electrical characteristics. Impurities diffusing through the active junctions might also degrade the optical characteristics [14].

In addition, in order to limit the additional losses due to the overlap of the optical mode with highly-doped regions, we want the tunnel junction to be as small as possible. The high diffusion coefficient will impose a minimum junction thickness to achieve a given doping concentration.

In this section, we propose to identify the highest doping concentration obtainable by in-situ MOCVD zinc-doping, and the minimum width of the tunnel junction to ensure a good doping, and a low diffusion. We will first describe briefly the physical phenomena involved in the diffusion process. Afterwards we will discuss the influence of the growth parameters on the resulting Zn distribution. Then we will turn to the influence of the grown structure; and then we will discuss the influence of the post-growth treatments. Eventually, we will be able to estimate the length of diffusion that we can expect in our set of materials, and the maximum reachable level of doping.

5.1.3.1 General description of the zinc diffusion in III-V semiconductors

This paragraph is dedicated to the description of the physical phenomena involved in the diffusion process.

The Fick laws A very general diffusion mechanism is usually described by the first Fick law:

$$\vec{J} = -D\vec{\nabla}C \quad (5.3)$$

This law seems quite natural and indicates that the particle flow \vec{J} is proportional to the gradient of concentration C of the diffusing particles.

The coefficient of proportionality D is called the diffusion coefficient and is expressed in m².s⁻¹. It can either be constant or a varying function of the impurity concentration.

Let us now consider the volume element of a semiconductor depicted on figure 5.6. A flow of particles diffuse through this volume element. During a time period δt , the number of particles that have been fixed inside the volume is written:

$$N_{\text{particules}} = (J_{\text{in}} - J_{\text{out}})A\delta t = \delta JA\delta t$$

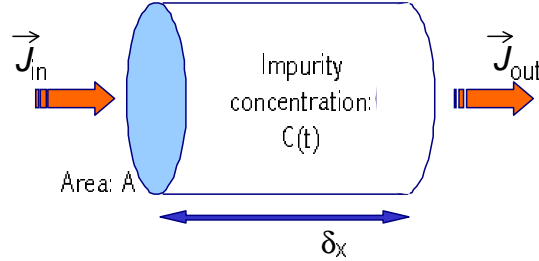
☞ A is the surface of one face of the cylindrical volume element.

The concentration therefore increases by a quantity:

$$\delta C = \frac{\delta J\delta t}{\delta x} \quad (5.4)$$

5.1 Tunnel junctions

Figure 5.6 Schematic representation of a volume element through which a flow of particles diffuses

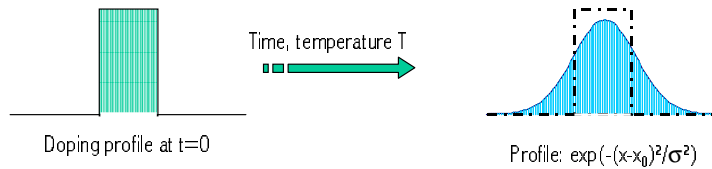


Considering only one diffusion dimension, and combining equation 5.3 and equation 5.4, we obtain the following relation, known as the second Fick law:

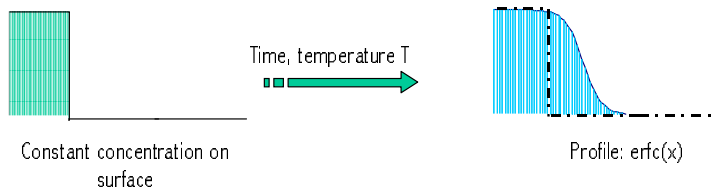
$$\frac{\partial C}{\partial t} = \frac{\partial}{\partial x} \left(D \frac{\partial C}{\partial x} \right) \quad (5.5)$$

Practically speaking, it is possible to find an analytical solution to equation 5.5 only for very few problems; for instance, when the initial conditions represent a finite dose of diffusing atoms, the resulting concentration profile is gaussian (c.f. figure 5.7-(a)). In the case of constant surface concentration, the resulting concentration profile is an error function (c.f. figure 5.7-(b)).

Figure 5.7 Diffusion profile obtained from equation 5.5 for different initial conditions.



(a) A finite dose initial condition leads to a gaussian profile



(b) A constant concentration on surface leads to an error function profile

Furthermore, in the case of constant diffusion coefficient, the second Fick law (equation 5.5) implies the proportionality between the length of diffusion and the square root of the time of diffusion:

$$\delta x \propto \sqrt{\delta t}$$

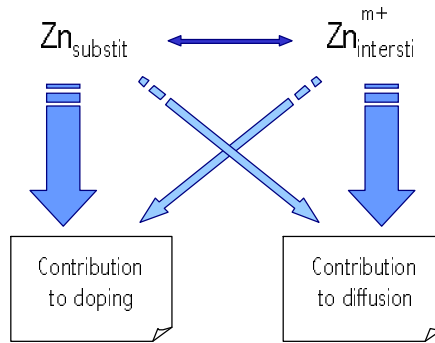
5. Design of a single-transverse-mode bipolar cascade laser

As we will see in the following sections, the diffusion coefficient of zinc atoms in InGaAsP is a varying function of the zinc concentration. This relationship does not directly apply but can sometimes be considered as a good approximation.

Substitutional-interstitial mechanism To account for strange experimental profiles of zinc diffusion, Frank & Turnbull proposed in 1956 that the zinc atoms in the semiconductor may be situated in two different localization in the crystal lattice: one is substitutional, the other one is interstitial [15]. In the first case, the zinc atom replaces a group III atom (indium or gallium) and is fixed to the crystalline lattice with stronger interactions than in the second case, where the atom occupies a tetrahedral site between the lattice atoms. This site has been identified by Chan [16] and Yu [17] with the help of X-ray diffraction measurements.

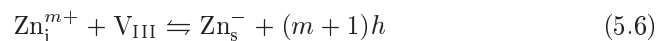
In substitutional sites, zinc atoms behave like acceptor dopants while they develop a covalence link with the other atoms of the lattice. In interstitial sites, the zinc element is a cation Zn^{m+} , where $m \times e$ is the electric charge of the cation and may vary from one theory to another [18–21]. In interstitial site, zinc does not participate to doping (it is even found sometimes that it has a tendency to give electrons to the lattice and therefore slightly compensate for the doping of zinc atoms in substitutional sites [19]). In addition, the interstitial zinc ions have weaker links to the lattice and therefore contribute largely to diffusion processes.

Figure 5.8 Contribution to effective p -type doping and to diffusion of substitutional and interstitial zinc elements.



We will see in the following discussion that the diffusion coefficient will be all the greater since the incorporation of zinc atoms in substitutional sites is low.

The process of transformation of a zinc atom in a substitutional site into an interstitial Zn cation is described by the following chemical reaction:



⇔ V_{III} is a group III atom vacancy in the lattice

⇔ h is a hole

5.1 Tunnel junctions

Assuming that this reaction reaches steady-state more rapidly than any diffusion process, the law of mass action writes:

$$Kp^{m+1}[Zn_s] = [Zn_i][V_{III}]$$

- ☞ p is the effective doping concentration
- ☞ $[]$ indicates that we consider the molar concentration
- ☞ K is a factor of proportionality

On first approximation, only the interstitial zinc ions contribute to diffusion. The second Fick law reads:

$$\frac{\partial[Zn_s]}{\partial t} + \frac{\partial[Zn_i]}{\partial t} = \frac{\partial}{\partial x} \left(D_i \frac{\partial[Zn_i]}{\partial t} \right)$$

- ☞ The diffusion coefficient associated to the interstitial zinc cations D_i is assumed constant.

Since $[Zn_s] \gg [Zn_i]$, we derive:

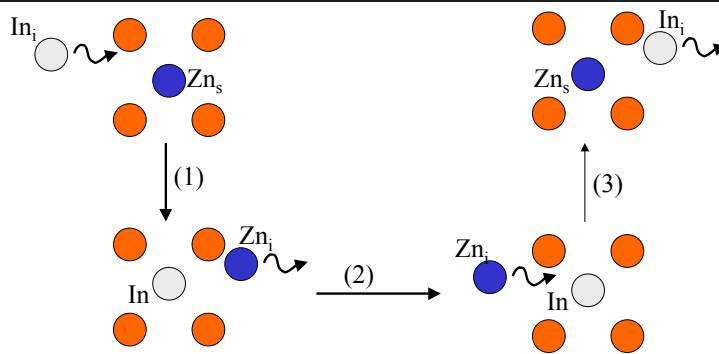
$$\frac{\partial[Zn_s]}{\partial t} = \frac{\partial}{\partial x} \left(\frac{K D_i (m+2)}{[V_{III}]} [Zn_s]^{m+1} \frac{\partial[Zn_s]}{\partial t} \right) \quad (5.7)$$

This equation can be read as a second Fick law with a diffusion coefficient proportional to $[Zn_s]^{m+1}$. If we take $m = 1$, and since $[Zn_s] \gg [Zn_i]$, the diffusion coefficient is proportional to the square of the total zinc concentration. These assumptions actually predict quite well the main part of the available experimental data in our type of materials all showing a very abrupt impurity profile [15, 20, 22].

The kick-out process Even if the diffusion coefficient of atoms in substitutional sites is negligible compared to the one of cations in interstitial sites, we need to report that the substitutional zinc may also diffuse inside the lattice. The chemical equation 5.6 should actually be seen as an equilibrium between the two states of zinc atoms.

Figure 5.9 shows a diffusion mechanism proposed by Otsuka in 1996.

Figure 5.9 Schematical description of the kick-out phenomenon occurring in Zn-doped III-V materials.



Substitutional zinc becomes mobile via interstitial states. Some group III interstitial atoms take the site of a substitutional zinc atom (1). Then the zinc atoms diffuses through the semiconductor in an interstitial state (2), until it settles in another group III atom site (3) or finds a group III vacancy immobile or diffusing in the opposite direction.

This phenomenon is worth mentioning since it is quite specific of heavy zinc atoms. It is sometimes used on purpose for fabricating distributed-Bragg-reflector lasers. The diffused Zn atoms intermix the QWs and the barriers materials in order to prevent the fundamental absorption of QWs in one given region of the device. Heavily-doped layers will be very close to QWs regions in our structures. Therefore we must be aware of the risk of intermixing that might lead to a degradation of characteristics of the active regions [23].

Diffusion and incorporation limit The incorporation limit is the maximum concentration of zinc incorporated in a substitutional site. This value depends greatly on the experimental conditions, and have currently been found around 2×10^{18} to 4×10^{19} atoms.cm⁻³ (at 800 K, depending on the considered material) in our set of materials grown by MOCVD [10, 11, 20, 24, 25].

Below this incorporation limit, the experimental diffusion data indicate a variation of the diffusion coefficient with $[\text{Zn}]^2$, very much in accordance with the substitutional-interstitial process described previously. Above the incorporation limit, zinc atoms are not anymore incorporated in substitutional sites. The additional zinc atoms are incorporated in interstitial sites, the condition of derivation of equation 5.7 do no longer apply, the incorporation into an active site decreases and the diffusion dramatically increases [10, 11, 20, 26].

5.1.3.2 Influence of the epitaxial growth parameters

In-situ doping is generally preferred to post-growth diffusion doping because the epitaxial surface provides in-situ an infinite source of group III element vacancy. It is usually observed a higher incorporation into substitutional sites, and a lower diffusion coefficient [13, 27].

As we saw previously, the zinc is quite well incorporated in substitutional sites until its incorporation limit. Afterwards, all the additional atoms are incorporated in interstitial sites and contribute largely to diffusion (and not to doping). The trade-off of the precise good quantity of zinc atoms available for incorporation is very accurate and the epitaxy parameters are numerous. Growing a good quality Zn-doped layer nearby the solubility limit therefore requires a good control of the parameters and a priceless experience.

We will discuss in this paragraph on the influence of the growth parameters on the Zn diffusion process.

Flow of zinc precursor The trade-off obtained in terms of zinc precursor flow depends largely upon the other parameters (some of them are listed below). In the literature, optimal values vary over two orders of magnitude [11, 21, 24].

Flow of group III and group V elements In a very general way, since the zinc atoms are active when incorporated in a group III vacancy, reducing the group III element flow and increasing the group V element flow increases the doping level [13, 27].

5.1 Tunnel junctions

Overall pressure inside the reactor It has been experimentally proved that the solubility of zinc in III-V semiconductors decreases while the overall pressure of the reactor is increased [13].

Growth temperature The growth temperature T plays a crucial role in doping profiles. In addition, numerous growth parameters are very dependent upon the temperature (for instance vapor pressure). The best growth temperature cannot be guessed from literature and once again, the experience of the epitaxy engineers is our best asset.

First concerning the incorporation level, it is well known that the zinc solubility in III-V semiconductors increases with temperature [13, 28]. Nevertheless, if the temperature is too high, zinc atoms are too much evaporated on the surface and the trade-off zinc atoms quantity available for incorporation cannot be reached [27, 29].

Secondly, the diffusion coefficient is proportional to a term borrowed to the Boltzmann statistics [19]:

$$D \propto \exp\left(-\frac{E_a}{kT}\right) \quad (5.8)$$

☞ k is the Boltzmann constant

☞ The activation energy E_a can be related to the energy needed for moving one diffusing particle from one stable site in the crystal to the next. The values found in the literature are around $E_a = 1.4 - 2.0$ eV [19].

For a low diffusion of the already grown layers, it is preferable to lower the temperature. Nonetheless, the temperature should not be too low neither. If the growth temperature is too low, the PH_3 pyrolyse will be less complete, thus decreasing the group V element proportion in the reactor. In addition, if the temperature is too low, very few zinc atoms will evaporate from the surface. If the zinc precursor flow is not adjusted in consequence, the total zinc atoms quantity available might exceed the trade-off value and many zinc elements will be incorporated in interstitial sites, leading to an increased diffusion [27].

The growth temperature is therefore a parameter of utmost importance and should be optimized carefully [30].

Growth interruption Many groups report (and especially for the growth of the $n++$ -doped base layer in heterojunction bipolar transistors) an improvement of the Zn profile while imposing a growth interruption under Zn-free environment just before the Zn-highly-doped layer [13, 31]. The growth interruption allows for equilibrium to be reached in the previously grown layers [32].

Conclusion The discussion above explains how some different parameters interact. The main conclusion that we can extract from this discussion is that the trade-off is extremely difficult to encounter, especially because of the numerous parameters to be considered. As a consequence, every epitaxy group works towards the optimization of their process, but the recipe cannot be easily transmitted from one group to another. Thanks to many years of experience, we managed at Thales Research & Technology to obtain a set of abrupt-profiled, highly-Zn-doped InGaAsP/InP materials. Our growth temperature is 650 °C for a reactor pressure of 200 mbars, the metalorganic zinc precursor is DEZn,

the group III precursors are TMGa and TMIIn, and the group V precursors are AsH₃ and PH₃.

5.1.3.3 Influence of the grown structure

Surprisingly as it may appear on first thought, there are some serious arguments claiming that the diffusion behavior will depend on the order of growth of the different materials. In particular, a *p*-over-*n* and a *n*-over-*p* junctions will exhibit different diffusion profiles. This paragraph presents the asymmetry in the growth that can lead to this different profiles.

Memory effect The precursor gas used for zinc doping is di-ethyl zinc (DEZn) or di-methyl zinc (DMZn). Its life-time inside the reactor is quite long and some zinc atoms are still present (and available for incorporation) after the *p*-type layer is grown. This phenomenon is called “segregation” and only alters the layers following the *p*-type layer. According to the literature, this effect is small for zinc in our type of material [10, 13].

Better Zn incorporation in *n*-type layers It has been reported that the incorporation of Zn (and more generally of acceptors) in InP was enhanced in *n*-type layers [24, 33, 34]. The phenomenon is attributed to the formation of a complex-donor-acceptor-pair.

Role of the growth temperature Since the diffusion coefficient is higher at high temperature, the Zn-doped layer should be as close as possible to the device surface. A longer exposition to high temperature increases the impurities migration [26, 34].

Built-in electric field When growing a *pn*-junction, a built-in electric field arises, oriented from the *n*-type layer to the *p*-type layer. Interstitial Zn ions are positively charged. They therefore will have a tendency to drift towards the *p*-side. In the case of a *p*-layer grown on a *n*-layer, interstitial zinc drift to the surface and have a high probability to evaporate, whereas in the case of a *n*-over-*p*-junction, interstitial zinc will drift towards deeper layers.

Conclusion Most of these remarks suggest to preferably grow a *p*-over-*n*-junction. Nevertheless, since we will work with *n*-type substrates, our tunnel junction will be grown *n*-over-*p*.

5.1.3.4 Influence of the post-growth treatment

This paragraph describes the influence on the Zn diffusion in our grown structure of the treatment that the structure undergoes after growth.

Thermal annealing It has been reported that a short period thermal annealing at a high temperature (for instance 5 to 10 minutes at 440 °C) activate the impurities and increases the electrically active doping concentration [4, 13, 27].

5.1 Tunnel junctions

This phenomenon is currently attributed either to the evaporation of hydrogen which deactivates substitutional zinc atoms [13], or to the evaporation of interstitial zinc themselves [4, 26].

This thermal annealing should also be optimized because a temperature increase favors diffusion.

Post-growth cooling Accordingly to what was previously explained, and also because the interstitial zinc solubility decreases while the temperature decreases, interstitial zinc atoms have a good opportunity to evaporate during the cooling of the grown wafer (from 650 °C to room-temperature).

Nevertheless, it has been reported that more zinc atoms are incorporated into a substitutional site when the cooling is rapid [17]. This study was realized under intentional diffusion conditions (doping by diffusion).

Two steps epitaxy growth For the fabrication of distributed feedback (DFB) lasers, the Bragg grating is usually buried inside the structure, and the epitaxy is usually performed in two steps. During the first step, the active region(s) is(are) grown. At the end of the first step, a grating is printed on the surface, using a holographic pattern. The wafer is then placed again in the MOCVD reactor to end its growth process. During the second step, the structure grown in the first step undergoes the growth conditions (and particularly the high temperature: 650 °C). Zn diffusion might take place, possibly leading to a degradation of the electro-optical characteristics of the laser structure.

This problem is not relevant in the case of the growth of Fabry-Perot lasers, grown in a single epitaxy step. For DFB lasers, one possible solution consists in fabricating the Bragg grating before growing the active region(s). The active region(s) is(are) then grown during the second epitaxial step.

5.1.3.5 Estimation of the material diffusion characteristics

Very few systematic studies have been done on the diffusion coefficients and the incorporation limit of zinc in $\text{In}_{1-x}\text{Ga}_x\text{As}_y\text{P}_{1-y}$. These characteristics are nevertheless available for the four binary alloys. Table 5.1 displays the diffusion coefficients of zinc in InP, GaP, InAs and GaAs.

	InP	InAs	GaP	GaAs
Diffusion coefficient ($\text{cm}^2.\text{s}^{-1}$)	7×10^{-8}	3×10^{-9}	10^{-9}	6×10^{-10}
Maximum incorporation (cm^{-3})	2×10^{18}	8×10^{18}	8×10^{18}	4×10^{19}

Table 5.1: Binary alloy diffusion coefficients and maximum incorporation of Zn atoms.

☞ The diffusion coefficient have been found for an impurity concentration of 10^{19} cm^{-3} , at 1000 °C for GaAs and GaP, 800 °C for InP, and 700 °C for InAs [35]. The values are compatible with the one found in [15] for InP, GaAs, GaP, and InAs.

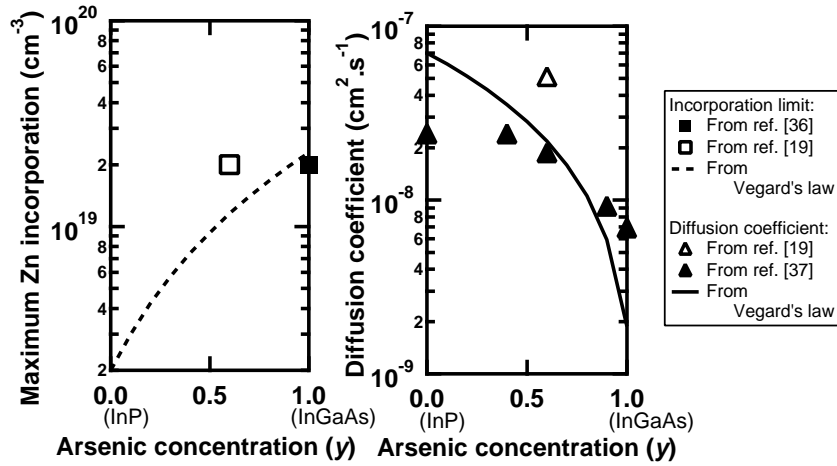
5. Design of a single-transverse-mode bipolar cascade laser

☞ The maximum incorporation values represent the maximum doping concentration obtained in MOCVD for InP [10–13, 20, 24, 27], and for GaAs [4, 19, 22]. Since very few incorporation values have been found in GaP and InAs grown by MOCVD, we have applied a proportionality coefficient between the maximum incorporation of InP and InAs (resp. GaAs and GaP) found in [35].

Use of the Vegard law When no experimental data is available for alloys characteristic, we usually use the Vegard law. As a function of the composition x and y , we can give an estimation of the diffusion coefficient and the incorporation limit of zinc in $\text{In}_{1-x}\text{Ga}_x\text{As}_y\text{P}_{1-y}$ lattice-matched to InP, as a function of y .

Figure 5.10 displays the evolution of the estimated diffusion coefficient and incorporation limit as a function of the arsenic concentration.

Figure 5.10 Diffusion coefficient and incorporation limit of zinc in $\text{In}_{1-x}\text{Ga}_x\text{As}_y\text{P}_{1-y}$ estimated from the Vegard law. Additional experimental data are from [19, 36, 37].



We see from figure 5.10, that as the alloy gets closer to $\text{In}_{0.53}\text{Ga}_{0.47}\text{As}$, the diffusion coefficient decreases but remains close to the value in InP. The incorporation limit increases while the material is getting closer to $\text{In}_{0.53}\text{Ga}_{0.47}\text{As}$, and the values are close to the values found for GaAs.

The additional data for incorporation values for $\text{In}_{0.53}\text{Ga}_{0.47}\text{As}$ and $\text{In}_{1-x}\text{Ga}_x\text{As}_y\text{P}_{1-y}$ are found in [19, 36] (MOCVD, 650 °C). The diffusion values for $\text{In}_{1-x}\text{Ga}_x\text{As}_y\text{P}_{1-y}$ are obtained from [19, 37]; they all have been corrected with the temperature dependence factor of equation 5.8 with $E_a = 1.6$ eV, in order to describe diffusion at $T = 900$ °C. It should also be mentioned that Van Gulp's structures [19] are grown with Liquid-Phase-Epitaxy and not MOCVD.

The estimation of the diffusion coefficient, and of the incorporation limits with the Vegard law are in relatively good agreement with published data. Applying this Vegard law to our tunnel junction material (InGaAsP , $\lambda = 1.35$ μm) gives a coefficient diffusion of 1.8×10^{-8} cm².s⁻¹ (at 10^{19} cm⁻³, $T = 1000$ °C),

5.1 Tunnel junctions

and a MOCVD incorporation limit of $1.3 \times 10^{19} \text{ cm}^{-3}$. It seems therefore to be possible to achieve a tunnel junction Zn-doped to $5 \times 10^{18} \text{ cm}^{-3}$.

Diffusion length due to thermal annealing Following the conclusions of the literature review, we apply to our structure a thermal annealing, in order to activate the dopants. In addition, a thermal annealing at the same temperature is also necessary in the process of fabrication of the platinumium *p*-type contact. These two annealing processes can be performed in one single in order to reduce post-growth thermal treatment. However, we do not want this post-epitaxy-growth heating to trouble the Zn distribution near the tunnel junction. Knowing the temperature (440 °C) and the time (60 s) of the thermal annealing, we can try to calculate the diffusion length of the zinc atoms. If the diffusion length is in the order of magnitude of the total width of the tunnel junction, then the characteristics will probably be degraded.

As we know quite well the diffusion characteristics of Zn in InP and GaAs, we can calculate the diffusion length expected in InP and GaAs for the same thermal annealing. The diffusion length in $\text{In}_{1-x}\text{Ga}_x\text{As}_y\text{P}_{1-y}$ alloy should then lie between the two. We can also try to estimate it with the diffusion coefficient found by applying the Vegard law:

$$\begin{aligned} \delta x_{\text{GaAs}} < \delta x_{\text{In}_{1-x}\text{Ga}_x\text{As}_y\text{P}_{1-y}} \simeq \delta x_{\text{Vegard}} < \delta x_{\text{InP}} \\ 0.1 \text{ \AA} < d x_{\text{In}_{1-x}\text{Ga}_x\text{As}_y\text{P}_{1-y}} \simeq 0.7 \text{ nm} < 8.9 \text{ nm} \end{aligned}$$

Considering that we can accept a few percents of diffusion for our tunnel junction in order not to lose in the thermal annealing the high-doping concentration incorporated by MOCVD which would degrade the electrical characteristics, we have decided to grow a tunnel junction consisting of a 25-nm wide *p++*-type, and a 25-nm wide *n++*-type layer.

5.1.4 Experimental achievements

5.1.4.1 Description of the test-structure

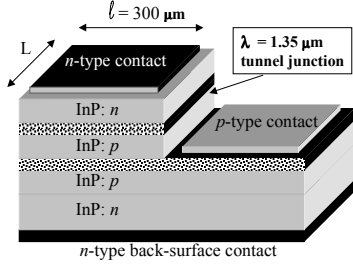
The previous paragraphs describe the trades-off that have been found for designing a low-resistivity tunnel junction. Following the previous conclusions, we have grown a tunnel-test-structure intended to be as similar as possible to the tunnel junction eventually implemented in our bipolar cascade laser. The material constituting the tunnel junction is InGaAsP $\lambda_{\text{PL}} = 1.35 \mu\text{m}$. The intended dopant concentration is the same for *n*-side (Si atoms) and *p*-side (Zn atoms) and equals $5 \times 10^{18} \text{ cm}^{-3}$, which is close to the incorporation limit of Zn atoms in InGaAsP. The layers constituting the tunnel junction are 25 nm-wide and are surrounded by InP layers. In order to reproduce as accurately as possible the growth conditions of the tunnel junction incorporated in the future bipolar cascade laser, we have grown the heavily-doped *n*-type layer on top of the heavily-doped *p*-type layer. We have also used the same *n*-type InP substrate. It was consequently necessary to grow an InP-based *pn*-junction before the heavily-doped tunnel junction under study.

On figure 5.11-(a) is displayed the succession of the semiconductor layers constituting the tunnel-test-structure.

5. Design of a single-transverse-mode bipolar cascade laser

Figure 5.11 Description of the test-structure.

Layer	width	doping (cm^{-3})
InP	$0.5 \mu\text{m}$	$n: 10^{18}$
$\lambda_{\text{PL}} = 1.35 \mu\text{m}$	25 nm	$n: 5 \times 10^{18}$
$\lambda_{\text{PL}} = 1.35 \mu\text{m}$	25 nm	$p: 5 \times 10^{18}$
InP	$0.1 \mu\text{m}$	$p: 10^{18}$
$\lambda_{\text{PL}} = 1.35 \mu\text{m}$	$0.5 \mu\text{m}$	$p: 5 \times 10^{18}$
InP	$0.1 \mu\text{m}$	$p: 10^{18}$
InP	$0.5 \mu\text{m}$	$n: 10^{18}$



(a) Succession of semiconductor layers

(b) Schematic of the technological process (the dotted pattern represents InGaAsP $\lambda_{\text{PL}} = 1.35 \mu\text{m}$ material)

A schematical representation of the technological process of the etched test-structure is shown on figure 5.11-(b). In order to obtain an accurate measurement of the tunnel junction characteristics, we have delimited a $\ell = 300 \mu\text{m}$ -large ridge and etched entirely the tunnel junction by stopping the wet etching on an InGaAsP ($\lambda_{\text{PL}} = 1.35 \mu\text{m}$) stop-layer grown here on purpose. We have then deposited a n -type contact (Au) on top of the ridge, and a p -type contact (Pt-Au) very similar to the one that will be deposited on the BCL. The back-surface n -type contact is also similar to other technological processes (Au-Mo-Au). The p -type contact is annealed (60 seconds, $440 \text{ }^\circ\text{C}$) to melt the platinum with the semiconductor layers. The wafer is then cleaved into test-device bars of different length L , varying from $300 \mu\text{m}$ to $900 \mu\text{m}$.

5.1.4.2 Current-voltage characteristics

In order to check beforehand the low-resistivity of the contact resistance, we have performed 4-probe Transmission Line Method (TLM) measurements for the n -type and for the p -type top contacts. The principle of the 4-probe measurement and of the TLM method are described in detail in annex C. These sets of measurements give a good estimation of the contact resistances. The contact resistances are estimated to be of $8.9 \times 10^{-5} \Omega \cdot \text{cm}^2$ for the n -type contact and $1.7 \times 10^{-4} \Omega \cdot \text{cm}^2$ for the p -type contact.

Then we consider the tunnel-test-structure as a three-terminal device. Point A is the top n -type contact, point B is the p -type contact and point C is the back-surface n -type contact, as it is schematically shown on figure 5.12.

According to the voltage law of additivity, the $V(I)$ characteristic of the tunnel junction writes:

$$\begin{cases} V_{\text{AC}}(I) = R_n I + V_{\text{tunnel}}(I) + V_{\text{diode}}^{\text{InP}}(I) + R_{\text{contact}}^{\text{back}} I \\ V_{\text{BC}}(I) = R_p I + V_{\text{diode}}^{\text{InP}}(I) + R_{\text{contact}}^{\text{back}} I \end{cases}$$

$$\Rightarrow V_{\text{tunnel}}(I) = V_{\text{AC}}(I) - R_n I - V_{\text{BC}}(I) + R_p I \quad (5.9)$$

5.1 Tunnel junctions

- ⇒ $R_{n,p}$ is the n, p -type contact resistance.
- ⇒ V is the voltage drop, while I is the current flowing through the device.

Figure 5.12 Schematic of the three terminal device used for indirect measurement of the tunnel junction characteristics.

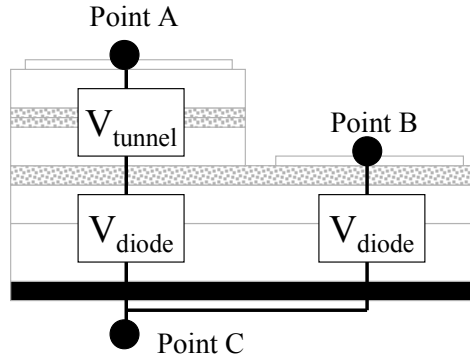
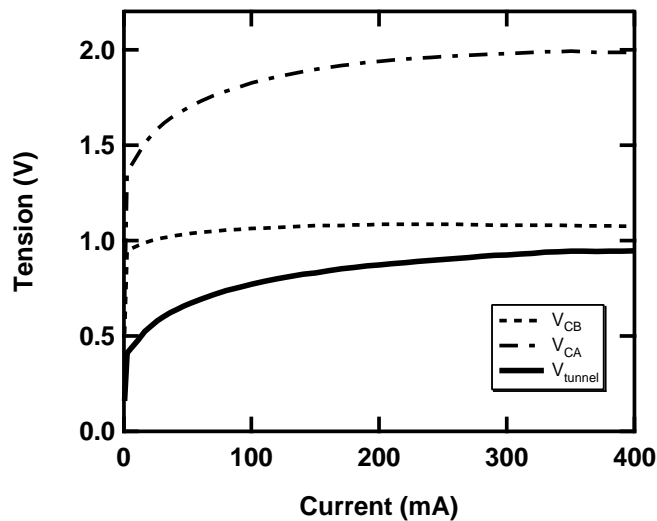


Figure 5.13 presents the measured V_{AC} and V_{BC} as well as the calculated V_{tunnel} as a function of the current flowing through the junction. We are here only interested in the backward current through the tunnel junction (forward through the InP diode). These measurements are performed for a $300\ \mu\text{m}$ device and have been achieved using the 4-terminal technique to increase the measurement accuracy.

Figure 5.13 Indirect voltage-current characteristic measurement of the tunnel junction for a $300\text{-}\mu\text{m}$ -long tunnel-test-device.



The tunnel junction exhibits a differential resistance below $1\ \Omega$ after $150\ \text{mA}$. The voltage threshold for activating the tunnel current is in the order of $0.7\ \text{V}$

5. Design of a single-transverse-mode bipolar cascade laser

which is higher than the few mV predicted by the simulation (see figure 5.4). In addition, another important feature needs to be related here: measurements have not been done over a few hundreds of mA because the device could not support more. The point of destruction typically lies between 200 and 500 mA DC, and did not vary much with the device length.

For a given voltage bias, there can exist several current pathways. Due to existing defaults on the cleaved facets, it is of major interest to estimate the proportion of current flowing through the volume device and running along the facets. For each voltage bias applied on the tunnel junction, we calculate the current I flowing through the tunnel junction as a function of the device length. The current writes:

$$I = I_{\text{facets}} + I_{\text{vol}} \quad (5.10)$$

$$= V \left(\frac{2\ell}{R_{\text{facets}}} + \frac{2L}{R_{\text{ridge}}} + \frac{\ell \times L}{R_{\text{vol}}} \right) \quad (5.11)$$

$$= \frac{2 \times V \times \ell}{R_{\text{facets}}} + L \times \left(\frac{\ell \times V}{R_{\text{vol}}} + \frac{2 \times V}{R_{\text{ridge}}} \right) \quad (5.12)$$

☞ I_{facets} is the surface current running along the facets and assumed to be proportional to $2 \times \ell$

☞ I_{vol} is the volume current assumed to be proportional to $L \times \ell$

☞ R_{facets} is the surface facets resistance expressed in $\Omega \cdot \text{m}$

☞ R_{ridge} is the surface ridge-side resistance expressed in $\Omega \cdot \text{m}$

☞ R_{vol} is the volume resistance expressed in $\Omega \cdot \text{m}^2$

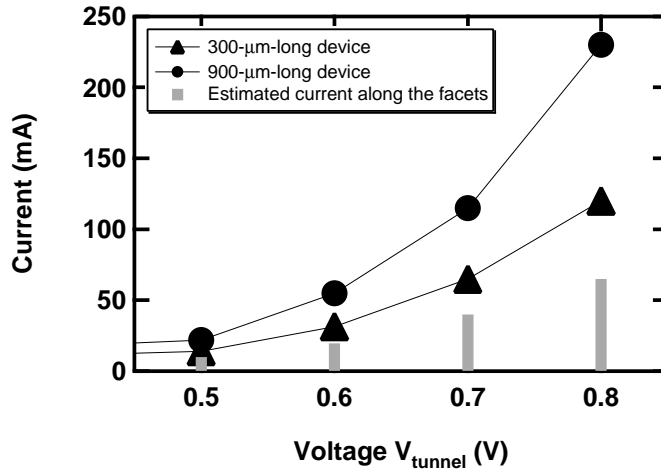
In our model, the surface facet current remains constant while increasing the length of the device. While measuring the device resistance as a function of the device length, the ridge-side surface current can not be discriminated from the volume current. We will therefore consider that there is no ridge-side current flowing through the device. The linear interpolation enables to estimate at a given voltage bias V_{tunnel} the amount of surface current. A 900- μm -long device gives us a second point for a linear regression. We display on figure 5.14 the current flowing through the device (surface and volume) for a 300- μm -long and for a 900- μm -long device, as well as the estimated surface current along the cleaved facets.

Although its proportion tends to decrease with increasing V_{tunnel} , the surface current still represents 28% of the current flowing through the 900- μm device (and almost 50% for the 300- μm device) at 0.8 V applied on the tunnel junction. This important facet current leakage is one of the hypothesis that could explain the damages caused to the devices for current exceeding 500 mA, quite independently of the length of the device.

It should be noted here that this problem is well known and several techniques exist to limit its effect [38–40]. Nevertheless, we did not have the technical opportunity to carry out such passivation processes on our devices.

5.1 Tunnel junctions

Figure 5.14 Estimation of the surface current running along the facets as a function of the applied voltage.

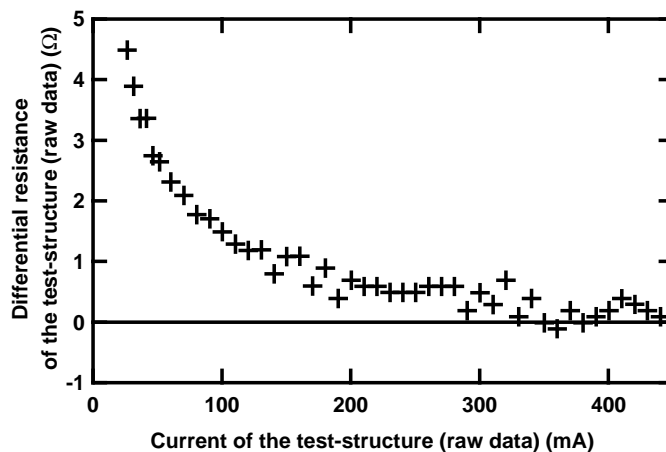


5.1.4.3 Estimation of the tunnel junction resistance while implemented in a real laser

Because of this important surface current pathway, it is rather difficult to estimate the behaviour, and in particular the differential resistance that would exhibit a tunnel junction incorporated in a laser device.

We therefore present on figure 5.15 the raw data (directly from the experiment) of the differential resistance exhibited by the 300- μm -long device as a function of the current (surface and volume) flowing through.

Figure 5.15 Differential resistance measured for the tunnel junction of the test-structure (raw data).



Since the measured differential resistance reduces rapidly to very small values (less than 1 Ω), the accuracy on the resistance measurements, and thus on the

resistance estimation for the laser device is very low. The average resistance between 300 mA and 450 mA gives the value of 0.21Ω (corresponding to an estimation of 42Ω for the tunnel junction incorporated in a laser structure). But the estimated resistance values suffer from a very high variability. The accuracy of the estimation could be enhanced by measuring the resistance of a smaller device, which was not experimentally possible in our configuration. In addition, we are experimentally limited to a current corresponding to 2.5 mA for the $3 \mu\text{m} \times 300 \mu\text{m}$ device because of tunnel-test-structure degradation over 500 mA.

Within all these very strong uncertainties, we finally obtain an estimation of the differential resistance of approximately 42Ω at 2.5 mA for the $3 \mu\text{m} \times 300 \mu\text{m}$ device. Even if still decreasing while increasing the applied current, this value is very high compared to the calculated current-voltage characteristics presented earlier in this chapter (see figure 5.4 on page 141).

5.1.4.4 SIMS measurements of the tunnel junction directly on the laser structures

The doping level and the doping distribution are the main uncertainties concerning the experimental devices. We have seen in previous sections that a small discrepancy in the doping level could lead to dramatically altered characteristics. We have performed SIMS measurements on the tunnel-test-structure and also on a real BCL.

Different primary ions have been used to measure the concentration profile of the studied elements. Cesium cations for measuring the Si profile and the majoritary elements, and O_2^+ for measuring the Zn profile. The calibration as well as the spatial resolution are always serious issues in all SIMS measurements. The rate of etching and the rate of extraction of elements are both dependent on the semiconductor lattice. The calibration for Zn has been done here with a specifically grown structure. The calibration structure is composed of InGaAsP, $\lambda_{\text{PL}} = 1.35 \mu\text{m}$, Zn-doped to $5 \times 10^{18} \text{ cm}^{-3}$. This value has previously been measured by polaron. For the other elements, the rate of etching and extraction are already available.

Figure 5.16 displays a zoom of the tunnel junction composition in the tunnel-test-structure. Figure 5.17 displays a zoom of the tunnel junction composition incorporated in a real BCL (device B2, described in more details in section 5.2.2 on page 165). The concentration of Zn and Si are shown in atoms.cm^{-3} , which means that they have been calibrated before hand.

The SIMS measurement on the test-tunnel-structure proves that it is possible to achieve $5 \times 10^{18} \text{ atoms.cm}^{-3}$ of Zn concentration in deep layers of InGaAsP $\lambda_{\text{PL}} = 1.35 \mu\text{m}$. Nevertheless, it is not possible to completely evaluate the doping concentration in the tunnel junction. The measured profile is quite steep, proving that there is little diffusion, but the value does not reach the intended value, which can be explained though by the low experimental resolution.

5.1 Tunnel junctions

Figure 5.16 SIMS measurement performed on the tunnel-test-structure.

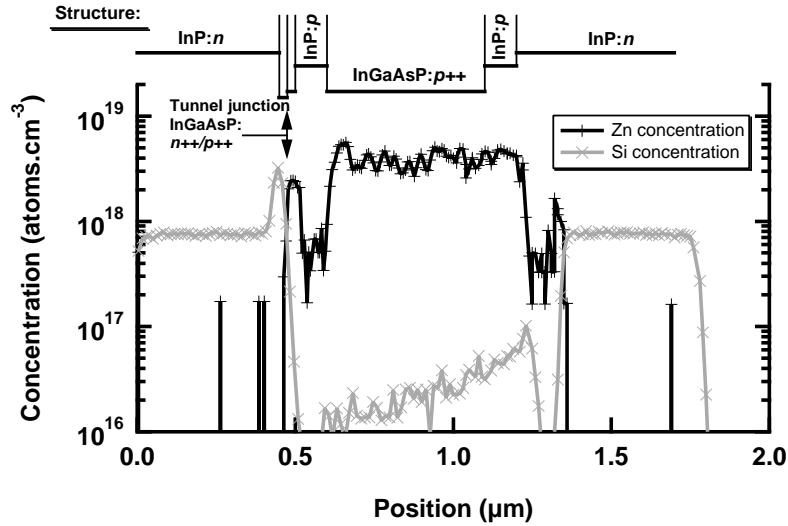
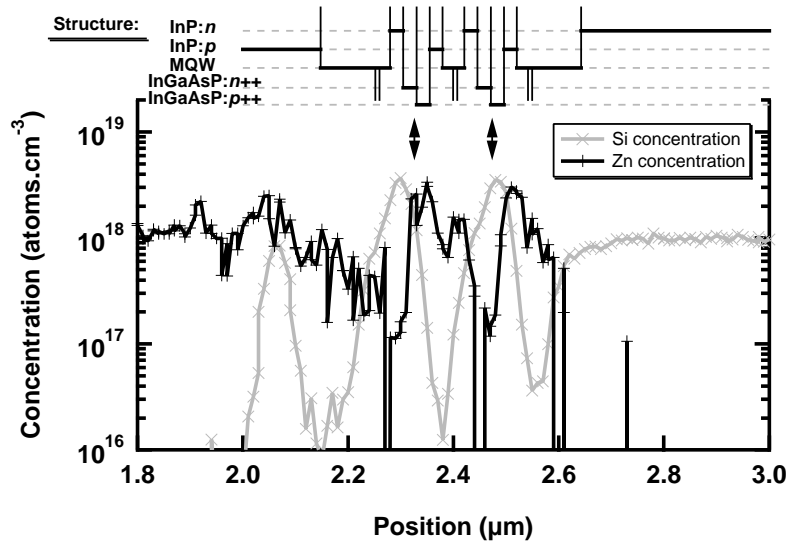


Figure 5.17 Zoom of the SIMS measurement of the tunnel junction incorporated in structure B2 (described in section 5.2.2).



There is no big difference between the dopant distribution of the tunnel-test-structure and the tunnel junction implemented in the BCL. The dopant profile is in both cases very sharp, with little residual diffusion, even for Zn atoms. In addition, the measured doping levels are very close to the intended levels, and are even higher for the tunnel junction implemented in the laser structure.

In brief, no definitive conclusion can be drawn because of the poor resolution of SIMS measurements (10 nm at best) and the uncertainty in the calibration. The main feature to be observed is the incorporation in Si-doped layer of Zn atoms that have diffused from the Zn-doped layers. Even if the phenomenon is

very limited, the device characteristics are, according to the model simulations, very sensitive to small doping level difference or to a bad sharpness of the interfaces.

5.2 Bipolar cascade lasers

In the preceding section, we met a trade-off both for the choice of the material (InGaAsP, $\lambda_{\text{PL}} = 1.35 \mu\text{m}$, doped to $5 \times 10^{18} \text{ cm}^{-3}$), and for the choice of the width of the tunnel junction layers (25 nm each).

Taking these optimizations for granted, we now describe the design of the rest of the structure, beginning with an issue that carries some interest only for bipolar cascade lasers: the width of the large band-gap current confinement layers.

5.2.1 Optimization of the electrical confinement barriers

5.2.1.1 Introduction

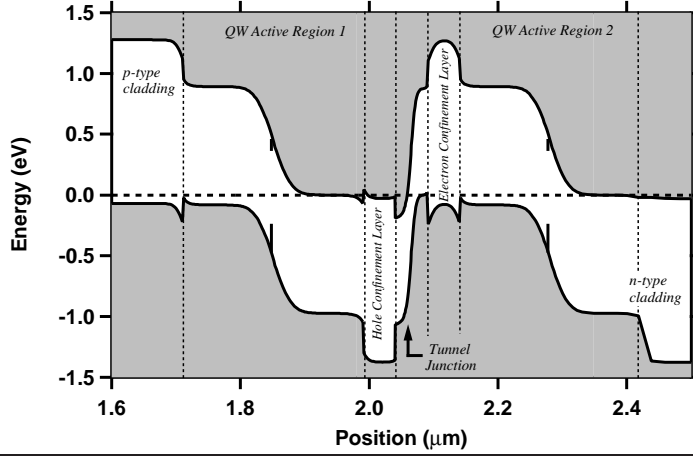
A bipolar cascade laser consists in several stages of active regions monolithically stacked; each one should include at least one quantum well, and electrical confinement layers. In the InGaAsP/InP material system used for 1.55- μm -emission wavelength, these confinement layers usually consist in InP, which has a larger gap than InGaAsP, and a lower refractive index. In order to improve the wave confinement (and the overlap of the optical mode with QWs), these InP layers have to be reduced to minimum width. However, if the layer is too narrow, carriers cannot be efficiently confined, resulting in important leakage over-barrier and poor laser characteristics. A compromise has to be found, and cannot be easily guessed from commonly used tools.

5.2.1.2 Presentation of the designed structures

We have used the self-consistent model described in chapter 4 to design and compare five single-mode structures. Each cavity includes two active regions separated by one Esaki tunnel junctions. The active regions consist of InGaAsP ($\lambda_{\text{PL}} = 1.2 \mu\text{m}$) barriers and one InGaAsP ($\lambda_{\text{PL}} = 1.7 \mu\text{m}$) 7.4-nm-wide QW, for a 1.55- μm emission. As discussed previously, the tunnel junctions are made of one n -type, and one p -type 25-nm-wide, highly doped ($5 \times 10^{18} \text{ cm}^{-3}$) InGaAsP ($\lambda_{\text{PL}} = 1.35 \mu\text{m}$) layers. The tunnel junctions are surrounded by n -doped ($1 \times 10^{18} \text{ cm}^{-3}$) and p -doped ($7 \times 10^{17} \text{ cm}^{-3}$) InP current confinement layers that prevent electrons (on the p^{++} -side) and holes (on the n^{++} -side) from leaking over and being transported to the next active region by the high electric field of the Esaki junction. Figure 5.18 presents one of these structures at thermodynamic equilibrium (unique Fermi-level). We point out the QWs and the InP current confinement layers, which are the object under study in this section.

5.2 Bipolar cascade lasers

Figure 5.18 Two-active region bipolar cascade structure with 50-nm barrier width at thermodynamic equilibrium. The dashed line is the Fermi-level.



In an effort to decorrelate the effect of the change in current confinement barrier width from other effects, the total width of the optical waveguide is kept constant and equal to 420 nm. Therefore, as we increase the width of the confinement layers, the width of InGaAsP ($\lambda_{PL} = 1.2 \mu\text{m}$) layers decreases. We have also kept the QW in the middle of the barrier layers. The structures have InP confinement layers varying in width from 10 nm to 70 nm.

We then performed the simulation of the complex $(pn)-(n^{++}p^{++})-(pn)$ single-mode structures with our fully consistent transport model described in detail in chapter 4. We remind here that the model is compatible with band-to-band tunneling, with multi-quantum-well structures and relies on Fermi-Dirac statistics.

Optical losses mainly arise from the overlap of the single-optical mode with highly-doped tunnel-junction layers and confinement layers. Free carrier losses are estimated with a linear model:

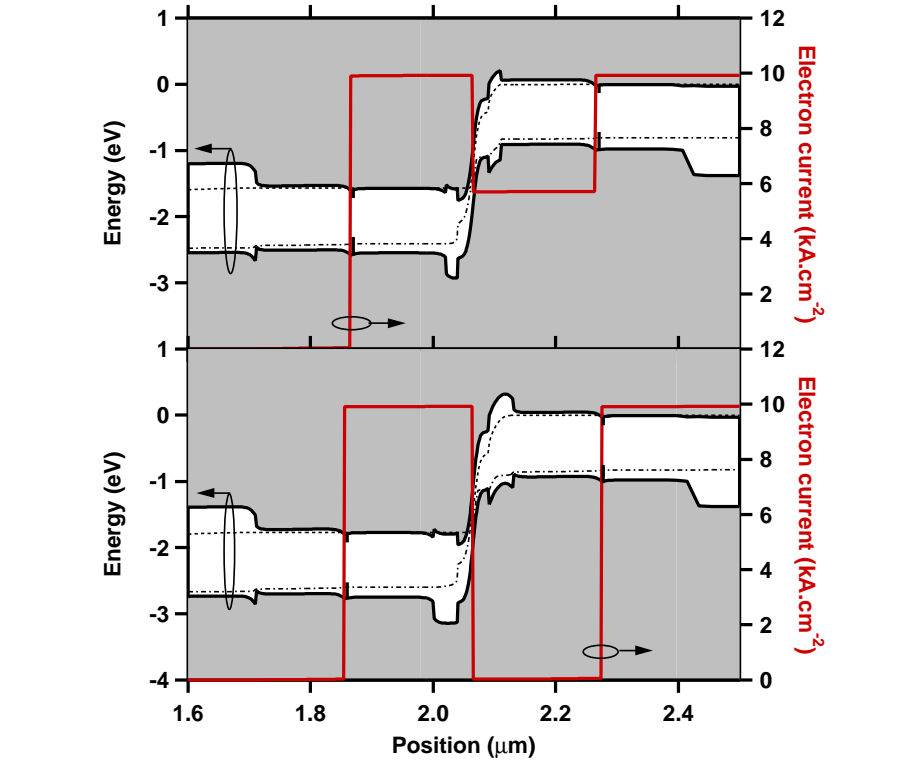
$$\alpha_{fc}(z) = \alpha_n n(z) + \alpha_p p(z)$$

where α_n (resp. α_p) is the free carrier cross section and is taken to be $3 \times 10^{-18} \text{ cm}^{-2}$ (resp. $20 \times 10^{-18} \text{ cm}^{-2}$), as already described in section 5.1. No additional scattering losses are introduced in the calculation.

5.2.1.3 Results of the simulation

Figure 5.19 shows the band diagram obtained for the 20-nm structure, and for the 40-nm structure at $J_{\text{ref}} = 10 \text{ kA.cm}^{-2}$ current density.

Figure 5.19 Bipolar cascade laser structure with 20-nm and 40-nm barrier width at 10 kA.cm^{-2} bias current. On the right axis is shown the electron current. The dashed lines are the quasi-Fermi-level.



Both exhibit the staircase like shape characteristic of BCL which was intuitively described in the literature [41, 42]. A publication relating this work calculates this band diagram under current bias for the first time [43]. We have chosen to compare the band diagram for the same current, therefore the voltage bias differs slightly.

The most noticeable feature is the representation along the structure of the current carried by the electrons which is drawn on the right axis. The total current flow is the same in both devices, is conserved along the structure and equals 10 kA.cm^{-2} . The total current is simply the sum of the current carried by electrons and the current carried by holes. Therefore the electron current going back to zero implies that all the current is carried by holes (as in the case of the p -type region of the left-most active region of figure 5.19) whereas an electron current of 10 kA.cm^{-2} indicates that the current is entirely carried by electrons. For both structures, an increase in the electron current (occurring in the QWs) means that carriers recombine, whereas a drop in the electron current (occurring in the TJs) means that carriers are generated.

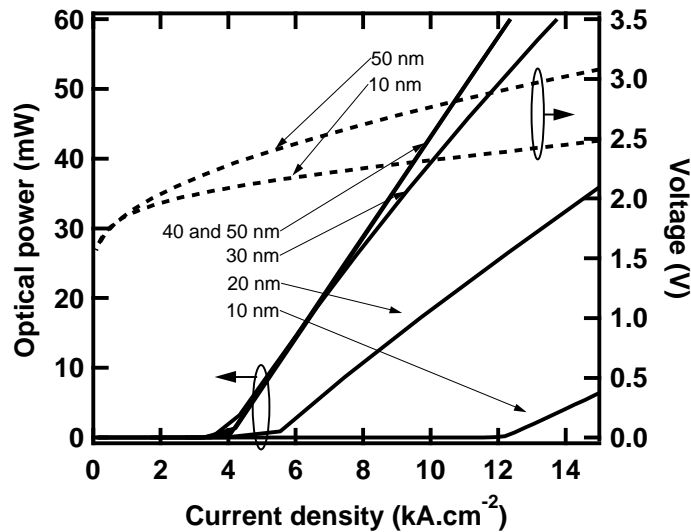
For the 20-nm structure, in the p -type material of the second pn gain junction, 43% of the total current is still carried by electrons, proving that a non-negligible flow of electrons leaks over the 20-nm InP barriers. On the other hand, in all p -type materials of the 40-nm structure, the current is almost entirely ($> 99\%$) carried by holes. All the electron current recombines in the

5.2 Bipolar cascade lasers

right-most QW region (cf. figure 5.19), it is then regenerated in the Esaki TJ which acts as an electron-hole pair source, and is fully available for another recombination in the second active layer. A 40-nm InP barrier almost completely prevents electron current leakage in these structures for 10 kA.cm^{-2} .

Figure 5.20 displays the optical power predicted by the simulation for each device.

Figure 5.20 Power-versus-current and voltage-versus-current characteristics of bipolar cascade laser structures with current confinement width varying from 10 nm to 50 nm.

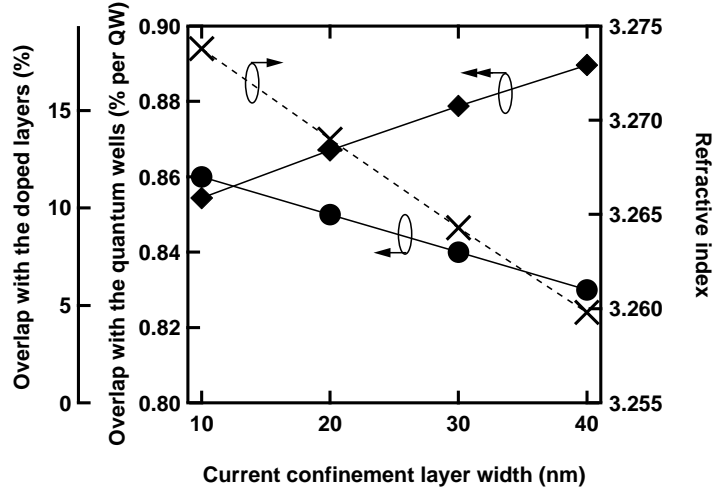


For increasing InP barrier width, the current leakage is reduced and the external efficiency increases. After 40 nm, the barrier is wide enough to completely prevent leakage, and an additional increase does not modify the characteristics below 10 kA.cm^{-2} . The 50-nm characteristic reaches 121% external efficiency (corresponding to 0.49 W/A per facet) in our simulation, proving that the simulation takes into account carrier recycling.

The dashed lines are the $V(J)$ characteristics calculated for the 10-nm and for the 50-nm devices. The threshold voltage is relatively high (of the order of 3 V), and is also characteristic of BCL (see [41, 42, 44] and of course the experimental section 5.2.2 of this chapter for experimental data).

There are however several arguments in favor of reducing as much as possible the use of InP layers. Firstly, InP doped to 10^{18} (n - or p -type) introduce additional free-carrier losses in the structure. Secondly, the carrier blocking layers, in our set of materials, have a lower refractive index than the currently used optical guiding material. Inserting InP blocking layers will lead to decreasing the effective refractive index of the fundamental mode. These two drawbacks are taken into account in the simulation: figure 5.21 displays the evolution of the overlap of the optical mode with the QWs, of the optical mode with the doped layers (tunnel junction and InP carrier stopper layers), as well as the effective refractive index of the vertical structure at a current bias of 10 kA.cm^{-2} .

Figure 5.21 Evolution of the overlap of the optical mode with QWs, of the overlap of the optical mode with the doped layers and of the modal effective refractive index, as a function of the width of the current confinement layers, as calculated by the simulation.



Increasing the barrier width leads to a decrease of the effective refractive index. The resulting effect is a decrease in the vertical optical confinement which implies a lower overlap with the active regions. In addition, the total width of doped layers increases. Therefore the overlap of the optical mode increases slightly while increasing the width of the InP layers. The effect is not very strong however, because the optical confinement is lower and thus less optical power also lies on the highly-doped tunnel junction layers. The free-carrier losses typically lie around 5 to 6 cm^{-1} .

5.2.1.4 Discussion on the results

For these particular structures, a confinement layer of 40 nm ensures less than 1% carrier leakage while minimizing the doped layers overlap. Investigating other types of structures (several QWs per active regions, more than two active regions), we found out that this optimal width can vary from one structure design to another, depending mainly on the resistivity of the current pathways provided to the electrons by the overall structure (either through the tunneling process, or over the barrier).

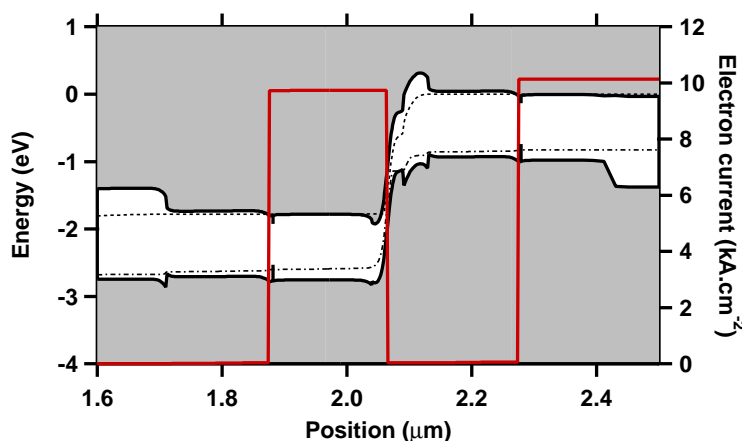
The non-linearity in the 30-nm structure on figure 5.20 is attributed to band filling, which results in more electrons available for leaking over at a high bias current. 30-nm and 50-nm structures are very similar below 8 kA.cm^{-2} (the difference might be explained by the free-carrier absorption and the difference in the QWs overlap). Above 10 kA.cm^{-2} , the 50-nm structure stays linear, whereas some current begins leaking over for the 30-nm structure.

The asymmetry in leakage occurring in the 20-nm structure comes from the difference of electron and hole density of state effective masses. Holes are far less mobile than electrons (their effective mass is one order of magnitude higher than that of electrons), and the 20-nm barrier is already sufficient to stop holes from leaking over (see also [45]). For this reason, we have designed one more

5.2 Bipolar cascade lasers

structure with only electron confining barriers and no hole confining barriers. Figure 5.22 shows the band diagram at $J_{\text{ref}} = 10 \text{ kA.cm}^{-2}$ of a structure with 40 nm electron-stopper barrier, and no hole-stopper barrier. The leakage is as low as the one found for the same structure with a hole-stopper barrier ($< 1\%$), but the effective index (3.269) and the overlap with doped layers (12.85%) have values comparable with the 20 nm structure.

Figure 5.22 Band diagram of a bipolar cascade laser structure without any hole confinement layer. The electron confinement layer is sufficient for obtaining less than 2 % leakage.



5.2.2 Experimental achievements

5.2.2.1 Description of the grown structures

We have grown two sets of bipolar cascade structures. The first set (set A) is composed of 2 active regions, four QWs per active region, and was grown in one single step (no epitaxy regrowth, and no buried Bragg grating). The second set (set B) is composed of three active regions with two QWs per active regions, and includes a Bragg grating for longitudinal mode selection, which therefore has necessitated an epitaxial regrowth.

The following tables display the succession of epitaxial layers of structures A1, A2, B1, and B2. “Q” stands for “Quaternary alloy”, followed by the band-gap energy expressed in wavelength: e.g. “Q1.2” stands for InGaAsP $\lambda_{\text{PL}} = 1.2 \mu\text{m}$

5. Design of a single-transverse-mode bipolar cascade laser

Structure A1		
Layer	Width	Doping (cm^{-3})
Contact layers	0.5 μm	p: $> 10^{18}$
InP	1.5 μm	p: 10^{18}
Q1.2	10 nm	p: 10^{18}
InP	60 nm	p: 7×10^{17}
Q1.2	110 nm	p: 3×10^{17}
4 QWs / Q1.2 barriers	74 Å / 60 Å	-
Q1.2	30 nm	n: 3×10^{17}
InP (Hole stopper)	35 nm	n: 10^{18}
Q1.35 (tunnel junction)	25 nm	n: 5×10^{18}
Q1.35 (tunnel junction)	25 nm	p: 5×10^{18}
InP (Electron stopper)	35 nm	p: 7×10^{17}
Q1.2	30 nm	p: 3×10^{17}
2 QWs / Q1.2 barriers	74 Å / 60 Å	-
Q1.2	110 nm	n: 3×10^{17}
InP (substrate)	100 μm	n: 10^{18}

Structure A2		
Layer	Width	Doping (cm^{-3})
Contact layers	0.5 μm	p: $> 10^{18}$
InP	1.5 μm	p: 10^{18}
Q1.2	10 nm	p: 10^{18}
InP	70 nm	p: 7×10^{17}
Q1.2	110 nm	p: 3×10^{17}
4 QWs / Q1.2 barriers	74 Å / 60 Å	-
Q1.2	30 nm	n: 3×10^{17}
Q1.35 (tunnel junction)	25 nm	n: 5×10^{18}
Q1.35 (tunnel junction)	25 nm	p: 5×10^{18}
InP (Electron stopper)	35 nm	p: 7×10^{17}
Q1.2	30 nm	p: 3×10^{17}
2 QWs / Q1.2 barriers	74 Å / 60 Å	-
Q1.2	110 nm	n: 3×10^{17}
InP (substrate)	100 μm	n: 10^{18}

5.2 Bipolar cascade lasers

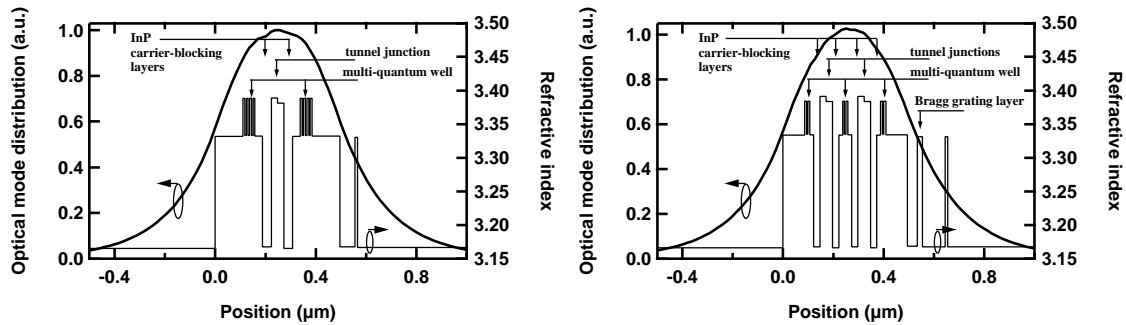
Structure B1		
Layer	Width	Doping (cm^{-3})
Contact layers	0.5 μm	p: $> 10^{18}$
InP	1.5 μm	p: 10^{18}
Bragg grating layer	110 nm	p: 10^{18}
InP	40 nm	p: 10^{18}
Q1.2	60 nm	-
2 QWs / Q1.2 barriers	74 Å / 115 Å	-
Q1.2	30 nm	-
Q1.35 (tunnel junction)	25 nm	n: 5×10^{18}
Q1.35 (tunnel junction)	25 nm	p: 5×10^{18}
Q1.2	40 nm	-
2 QWs / Q1.2 barriers	74 Å / 115 Å	-
Q1.2	40 nm	-
Q1.35 (tunnel junction)	25 nm	n: 5×10^{18}
Q1.35 (tunnel junction)	25 nm	p: 5×10^{18}
Q1.2	30 nm	-
2 QWs / Q1.2 barriers	74 Å / 115 Å	-
Q1.2	60 nm	-
InP (substrate)	100 μm	n: 10^{18}

Structure B2		
Layer	Width	Doping (cm^{-3})
Contact layers	0.5 μm	p: $> 10^{18}$
InP	1.5 μm	p: 10^{18}
Bragg grating layer	110 nm	p: 10^{18}
InP	40 nm	p: 10^{18}
Q1.2	86 nm	p: 3×10^{17}
2 QWs / Q1.2 barriers	74 Å / 60 Å	-
Q1.2	15 nm	n: 3×10^{17}
InP (hole-stopper)	25 nm	n: 10^{18}
Q1.35 (tunnel junction)	25 nm	n: 5×10^{18}
Q1.35 (tunnel junction)	25 nm	p: 5×10^{18}
InP (electron-stopper)	25 nm	p: 10^{18}
Q1.2	15 nm	p: 3×10^{17}
2 QWs / Q1.2 barriers	74 Å / 60 Å	-
Q1.2	15 nm	n: 3×10^{17}
InP (hole-stopper)	25 nm	n: 10^{18}
Q1.35 (tunnel junction)	25 nm	n: 5×10^{18}
Q1.35 (tunnel junction)	25 nm	p: 5×10^{18}
InP (electron-stopper)	25 nm	p: 10^{18}
Q1.2	15 nm	p: 3×10^{17}
2 QWs / Q1.2 barriers	74 Å / 60 Å	-
Q1.2	86 nm	n: 3×10^{17}
InP (substrate)	100 μm	n: 10^{18}

5. Design of a single-transverse-mode bipolar cascade laser

The structures were designed to allow only the fundamental transverse-mode emission (see figures 5.23-(a) and -(b) for the optical mode distribution). Furthermore, two structures belonging to the same set display very similar optical mode properties. For a reason still not completely clear at the moment, structure B2 was emitting only spontaneous light, and it has not been possible to trigger the stimulated emission process leading to laser emission.

Figure 5.23 Optical mode calculation inside the two structure sets. Structures belonging to the same set exhibit very similar optical mode behavior.



(a) Modal distribution of structure A1, belonging to set A

(b) Modal distribution of structure B2, belonging to set B

In the following discussion, we will present a list of relevant thematical characterization that will enable us to understand somewhat the behavior of the different structures. The technological process (including the width and the depth of the ridge) may vary with the structures and with the type of characterization. There are mainly two types of technological process: a shallow ridge and a deep ridge process.

The shallow ridge is usually processed into a “narrow” waveguide ($< 10 \mu\text{m}$). We chemically etch the $1.5\text{-}\mu\text{m}$ -InP layer on top of the active regions. The optical guiding is obtained by evanescent coupling of the optical mode with the passive ridge structure.

The deep ridge cannot be processed on ridges narrower than $10 \mu\text{m}$ (usually between $20 \mu\text{m}$ and $100 \mu\text{m}$). In this case the whole active layers are etched, including all the multi-quantum well layers and the tunnel junction layers. The wet etching is stopped in the substrate.

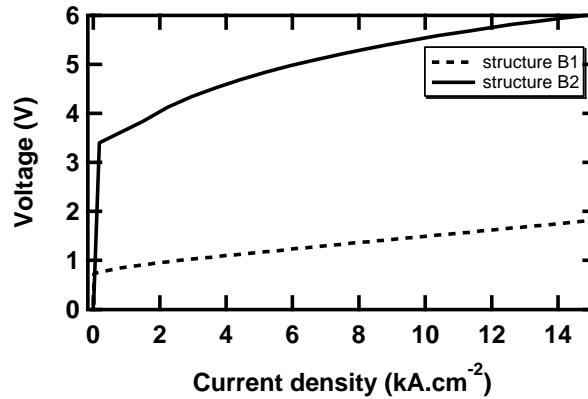
For each characterization, we will indicate the type of technological process that has been used.

5.2.2.2 Influence of the current blocking layers on the V(I) characteristics

Structure B2 is very similar to structure B1. The main difference is the additional very thin (25 nm) InP layers surrounding the tunnel junctions of structure B2. Figure 5.24 displays the comparison between the V(I) characteristic of structures B1 and B2. The measurements have been carried out for $900 \mu\text{m}$ -long $\times 3 \mu\text{m}$ -large ridge devices in both cases.

5.2 Bipolar cascade lasers

Figure 5.24 Comparison of the current-voltage characteristic of structure B1 and B2.

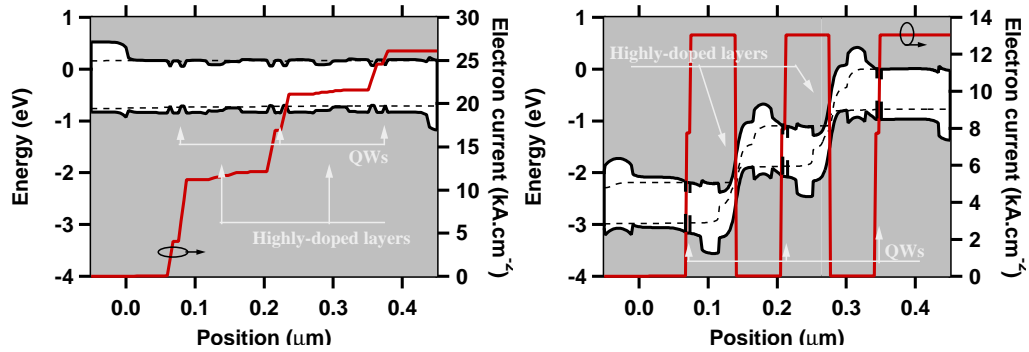


The $V(I)$ characteristic of structure B1 exhibits a voltage threshold of approximately 1 V. The series differential resistance at 5 kA.cm^{-2} is close to 2.4Ω . Meanwhile, the $V(I)$ characteristic of structure B2 exhibits a much higher voltage threshold of almost 3 V. The series resistance at 5 kA.cm^{-2} for B2 is also higher, in the order of 6.6Ω . Despite the highly-doped tunnel junctions, the voltage-current characteristic of structure B1 is very similar to single-active-junction lasers. On the contrary, structure B2 needs a voltage drop three times higher to allow the current going through, in agreement with what was previously calculated in section 5.2.1 for BCL. In order to understand the behaviour of structure B1, we have used a simulation software, Harold, developed by the university of Madrid for modeling MQW lasers [46]. This model does not account for band-to-band tunneling. The result is displayed on figure 5.25 and is compared to the result of the simulation of structure B2 with our model compatible with band-to-band tunneling.

In good agreement with what was described in section 5.2.1, since no large-band-gap material prevents carriers from leaking over the tunnel junctions in structure B1, the current is spread among all the active regions, and the laser behaves very similarly (electrically speaking) to a single-active-region laser, with no carrier recycling. The $V(I)$ characteristic is only slightly perturbed by the highly-doped layers inside the InGaAsP barriers. For structure B2 however, the current pathway is forbidden and the current flows through the tunnel junction, descending the active-regions staircase. More voltage is then necessary to allow the current through the device.

5. Design of a single-transverse-mode bipolar cascade laser

Figure 5.25 Comparison of the calculated band diagram of structure B1 and B2. The band diagram of structure B1 was obtained with a model that does not take into account band-to-band tunneling, the band diagram of structure B2 was obtained with our model compatible with tunnel junction. On the right axis is represented the electron current.



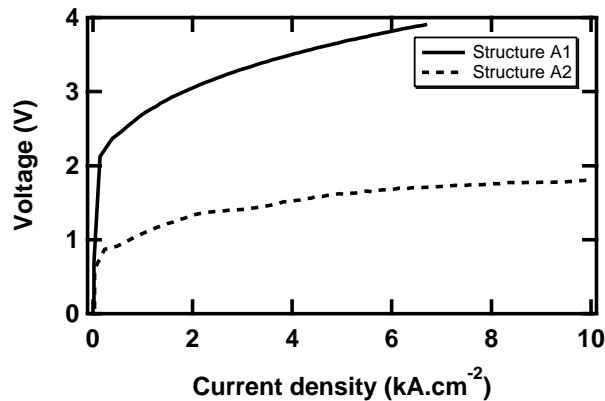
(a) Structure B1, simulated with the model Harold [46].

(b) Structure B2, simulated with the model described in chapter 4.

In section 5.2.1, we noticed that the carrier leakage was asymmetric. Preventing electron leakage was found to be sufficient to ensure a good carrier recycling. In order to experimentally check this assertion, structure A2 has an epitaxial scheme similar to structure A1 but the hole-stopper InP barrier has been suppressed.

Figure 5.26 displays the comparison of the $V(I)$ characteristic of structure A1 and A2. Both characteristics are obtained for $3 \mu\text{m}$ -wide \times $300 \mu\text{m}$ -long devices.

Figure 5.26 Comparison of the current-voltage characteristic of structure A1 and A2.



In opposition with what was calculated with our self-consistent model, structure A2 experiences over-barrier leakage (probably hole leakage) and exhibits

5.2 Bipolar cascade lasers

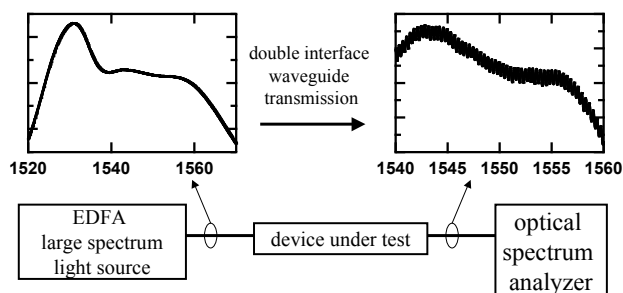
$V(I)$ characteristics very similar to single-active-region lasers. This experimental difference with theory can be attributed to a tunnel resistivity higher than expected.

5.2.2.3 Influence of the highly-doped tunnel junctions on the intrinsic losses

A widespread method for measuring laser intrinsic losses is to make a linear approximation of the evolution of $\frac{1}{\eta_d}$ as a function of the length of the cavity. This method is described in details in appendix C and can only be used above threshold. As a consequence, it was not possible to use it for structure B2, since structure B2 does not exhibit a laser effect (only spontaneous light is emitted, for a currently not completely clear reason).

In order to investigate the influence of the presence of highly-doped layers in the middle of an active region, we have built-up a transmission-based loss measurement set up depicted on figure 5.27. With this set-up it is possible to evaluate the intrinsic losses of the non-lasing structure B2.

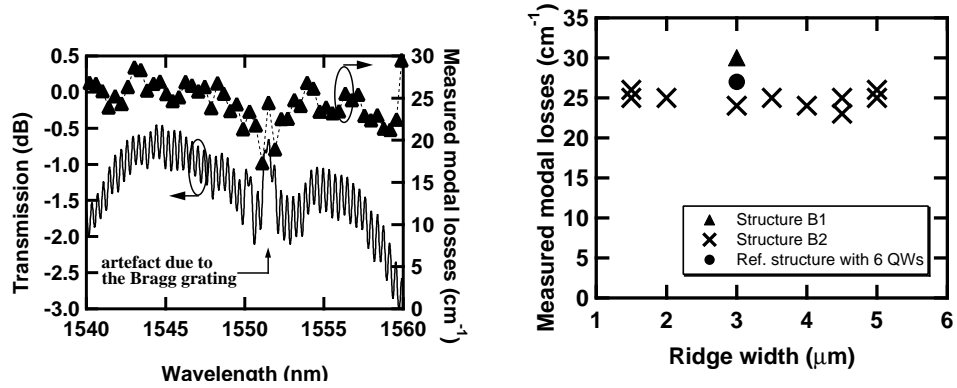
Figure 5.27 Measurement set-up for the determination of the transmission loss, in particular in structure B2.



A wide spectrum light source (spontaneous emission from an erbium-doped fiber amplifier EDFA) is injected in one side of the device under study. An optical spectrum analyzer collects and analyzes the light transmitted through the device waveguide. An analytical method, similar to the one proposed by Hakki and Paoli [47] enables then to obtain the absolute value of the modal spectral transmission loss, by the comparison between minima and maxima of the Fabry-Perot interference fringes. This method is described in details in appendix C.

Figure 5.28-(a) displays an example of the measurements performed with this set-up for structure B2. Meanwhile, figure 5.28-(b) shows the comparison of the intrinsic loss measured for structure B1 and B2 with a reference structure including one single-active region and 6 QWs. In opposition with structures B1 and B2, the reference structure does not include highly-doped layers in the middle of the optical waveguide. Structure B2 was technologically processed into shallow ridge structures with varying ridge width from $1.5 \mu\text{m}$ to $5 \mu\text{m}$. All the measurements are performed on unbiased devices.

Figure 5.28 Measurements of modal losses for comparing structures including highly-doped layers and a reference structure with no highly-doped layers.



(a) Example of measured modal losses for structure B2, on a $3 \mu\text{m} \times 900 \mu\text{m}$ device.

(b) Comparison of measured losses for $\lambda = 1.35 \mu\text{m}$, between structures B1, B2 and a reference structure

All the loss measurements, for structures B1, B2 and for the reference structure approximately fall into the same range. Most of the measurements performed on structure B2 demonstrated even smaller losses than the reference 6 QWs-structure. The highly-doped tunnel junction and carrier-stopper layers do not seem to increase dramatically the intrinsic losses of the waveguides.

As a conclusion, we can say that the heavily-doped layers do not dramatically increase the intrinsic modal losses.

5.2.2.4 Estimation of the facet surface current for BCL

We have seen in section 5.1 while characterizing the tunnel junction, that the facet current was playing a very important role in the total current flowing through the device.

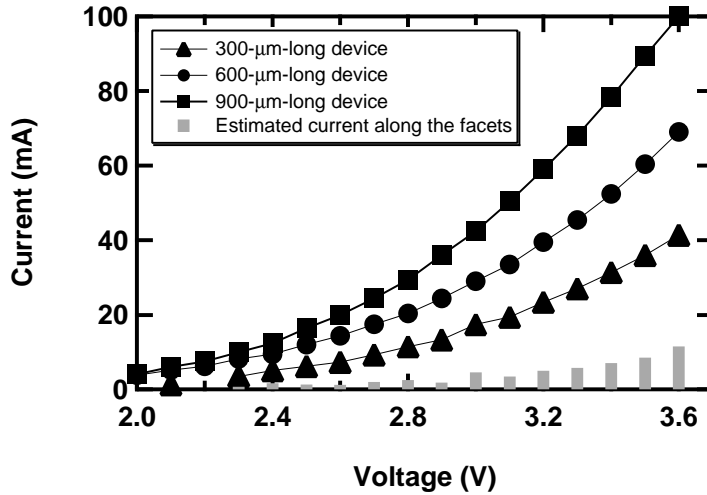
In order to estimate the facet current for the lasers including a tunnel junction, we compare, for a given voltage bias applied on the whole device, the current flowing through structure A1, processed into $3\text{-}\mu\text{m}$ -wide ridge waveguides and clived into dices of length varying from $300 \mu\text{m}$ to $900 \mu\text{m}$.

As we did for the tunnel-test-structure, we calculate the regression line of the current as a function of the device length and consider that the intersection of this regression line with the vertical-current axis gives a good estimation of the facet current.

The results are presented in figure 5.29. The measurements have been done for DC voltage bias.

5.2 Bipolar cascade lasers

Figure 5.29 Estimation of the surface current running along the facets for structure A1 as a function of the applied voltage.



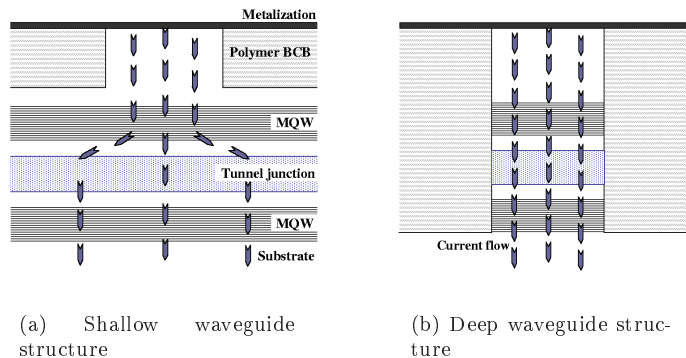
In opposition with what was estimated for the tunnel-test-structure, the estimated facet current is reasonably limited and does not exceed 10% for the 900- μm -long device over the range 0-3.6 V. This “good surprise” is not clearly explained and could be due to the slight differences in the structure fabrication process.

We can nonetheless conclude that despite the high volume resistivity, the facet current is limited in structure A1.

5.2.2.5 Influence of the current spreading

While characterizing the tunnel-test-structure, we noticed the high resistivity of the tunnel junction. This high resistivity is likely to trigger some current spreading in the direction parallel to the interfaces as schematically presented in figure 5.30-(a).

Figure 5.30 Technologically etched structures for investigation on current spreading phenomena.



5. Design of a single-transverse-mode bipolar cascade laser

This current spreading, enhanced by the 10^{18} -doped layers surrounding the tunnel junction has been reported several times in the literature concerning bipolar cascade lasers. For vertical cavity BCLs (BCVCSELs), it is necessary to confine the current by etching a mesa [21, 48–50] and subsequently making an oxide aperture in layers between the active junctions such as in [21, 49, 50]. Knödl *et al.* studied specifically the influence of current spreading (and thus of the adjunction of additional oxide apertures inside the cavity to prevent it) on the BCVCSEL characteristics [51, 52]. They found that “current confinement is a critical issue for the design of high performance BCVCSELs” [52]. Decreasing the spacers between active regions is presented as a possible solution. The same team also intended to use this high current spreading to induce a profitable bistability behavior [53, 54]. Still in the VCSEL domain, tunnel junction-induced current spreading is used to homogenize the current flow before it reaches the active layers [55]. For edge-emitting BCLs, in the devices described in the literature, the etched mesa includes the active regions so that no current spreading is possible [8, 56, 57].

In order to estimate the influence of the current spreading, we technologically processed structure A1 into a $20\text{-}\mu\text{m}$ deep ridge structure, and into a $3\text{-}\mu\text{m}$ shallow ridge structure. A $20\text{-}\mu\text{m}$ -wide (resp. $3\text{-}\mu\text{m}$ -wide) photolithographic mask leads to a $18\text{-}\mu\text{m}$ -wide (resp. $2.5\text{-}\mu\text{m}$ -wide) ridge structure. This difference is taken into account in every calculation, including the modal distribution calculation. We can then compare the threshold current obtained for the deep ridge structure (no current spreading is possible) and the shallow ridge structure where some current spreading occurs. By assuming that the current density is the same at threshold J_{th} for the two structures (i.e. assuming that the optical internal losses are the same for the two ridge structures), we can write, for devices of same length L :

$$\begin{aligned} J_{\text{th}} &= \frac{I_{\text{th}(20)} - I_{\text{facets}(20)}}{w_{20} \cdot L} = \frac{I_{\text{th}(3)} - I_{\text{facets}(3)}}{w_3 \cdot L} \\ w_3 &= w_{20} \cdot \frac{I_{\text{th}(3)} - I_{\text{facets}(3)}}{I_{\text{th}(20)} - I_{\text{facets}(20)}} \end{aligned} \quad (5.13)$$

⇔ $I_{\text{th}(w)}$ is the measured current threshold for a $w\text{-}\mu\text{m}$ -wide structure.

⇔ $I_{\text{facets}(w)}$ is the estimated current flowing through the facets at threshold for the $w\text{-}\mu\text{m}$ -wide structure.

The calculation of the surface facet current of the $3\text{-}\mu\text{m}$ -wide structure has already been described in details previously, and was evaluated to be equal or lower than 10% for the $900\text{-}\mu\text{m}$ structure. For the derivation of the effective current spreading width, we have taken a surface current of 15% for the $3\text{-}\mu\text{m} \times 600\text{-}\mu\text{m}$ structure, and 10% for the $3\text{-}\mu\text{m} \times 900\text{-}\mu\text{m}$ structure. The same measurement is carried out for the $20\text{-}\mu\text{m}$ structure for which we find a facet surface current of 6% for the $20\text{-}\mu\text{m} \times 600\text{-}\mu\text{m}$ structure and 5% for the $20\text{-}\mu\text{m} \times 900\text{-}\mu\text{m}$ structure.

We compute equation 5.13 for a device length of $600\text{ }\mu\text{m}$ and $900\text{ }\mu\text{m}$, and present the results in the following table. The current threshold measurements are performed under pulsed conditions (200 ns every 200 μs) at $20\text{ }^\circ\text{C}$.

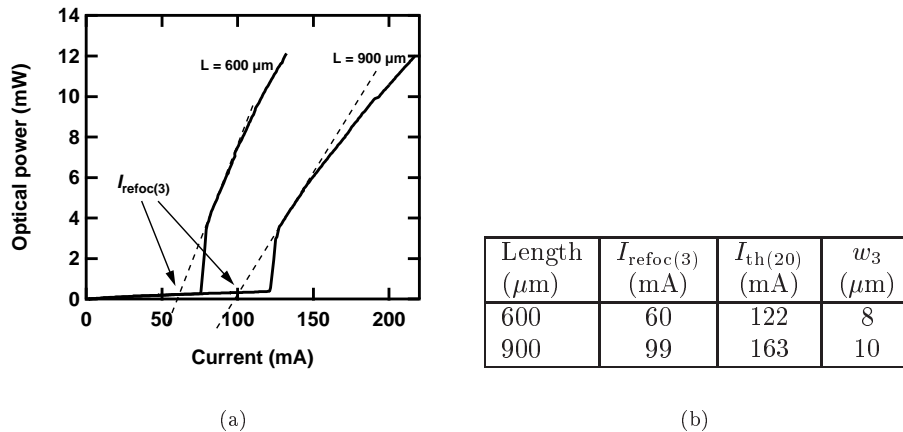
5.2 Bipolar cascade lasers

Device length	$I_{th(3)}$	$I_{th(20)}$	Calculated w_3
600 μm	76 mA	122 mA	10 μm
900 μm	122 mA	163 mA	13 μm

The current spreading at threshold is rather important in our 3- μm -wide structures and lies around 10-13 μm .

Nevertheless, as can be seen on figure 5.31-(a), the optical-power-versus-current characteristic of lasers A1 (processed into 3- μm shallow ridge structure) exhibits a slope accident at threshold. This feature may be explained by a saturable absorption process in the second active region which benefits, because of current spreading, from a lower carrier injection density [50, 53, 54]. However, because the threshold is smooth and continuous, we mainly attribute this behavior to a refocalization of the current at threshold. In order to confirm this assumption, we calculate the effective current spreading width using as a current threshold, $I_{\text{refoc}(3)}$ calculated as the intersection of the horizontal-current axis with the tangent of the power-versus-current characteristic above threshold. Figure 5.31-(a) displays the graphical estimation of the “effective” current threshold after current refocalization, whereas the table inserted in figure 5.31-(b) presents the calculated current spreading width values.

Figure 5.31 Calculation of the current refocalization at threshold.



The reduction of the estimated current spreading width reinforces the assumption of the current refocalization at threshold. In addition, a width of 8-10 μm was evaluated, that has to be compared to similar measurements for standard laser structures.

In any case, even if the current is spread somewhat below the 3- μm ridge, the optical mode is very likely to remain well confined below the real refractive index waveguide.

5.2.2.6 Demonstration of the carrier recycling effect

In order to prove the carrier recycling effect occurring in structure A1, we need a reference structure demonstrating the same optical mode behavior, an epitax-

ial structure as close as possible to structure A1, having undergone the same technological steps and exhibiting a single-active-region lasing behavior.

These conditions are actually fulfilled by structure A2. Structure A1 and A2 have been designed to demonstrate almost exactly the same optical mode behavior (refractive index, overlap with QWs, overlap with highly-doped layers...). The epitaxial structures are similar except for one single n -doped InP hole confinement layer missing in structure A2. This lack of hole blocking layers enables leakage over the carrier confinement barriers and the voltage-versus-current characteristic of structure A2 proves that no carrier recycling is observed in this structure. The lasing behavior is similar to a single-active-region laser.

We compare on figure 5.32 and 5.33 the optical-power-versus-current characteristics for structure A1 and A2 obtained under pulsed operation (200 ns every 200 μ s) at 20 °C. Figure 5.32-(a) displays the measurement obtained from structure A2 which will constitute our reference single-active-region structure. Figure 5.32-(a) display the measurement from structure A1. Both structures were processed into 20- μ m-wide deep ridge waveguides of varying length.

In order to compare the internal (intrinsic) electron-to-photon (quantum) conversion efficiency, we have used the standard method of determination of the internal efficiency described in appendix C. We display on figure 5.32-(b) and 5.33-(b) the external efficiency measured from the power-versus-current characteristics as a function of the device length. The intersection of the regression line with the vertical-efficiency axis displays the internal efficiency.

In order to ensure that our results did not suffer from non-uniform injection (and thus optical gain) distribution over the device even in pulsed operation, we have checked that the evolution of the current threshold was linear over the whole range of cavity length. In addition, due to the high variability of the measured data, we did not take into account the data concerning the 200 μ m-long A2 devices in the calculation of the regression line. The measured internal efficiency is 68% for structure A2 and goes up to 126% for structure A1. This over-100% internal efficiency is specific of BCLs and constitute an evidence of the achievement of a carrier-recycling process.

The slope of the regression line gives the internal losses of the optical mode. It appears that the calculated internal losses are a lot higher (43 cm^{-1}) for structure A1 than for structure A2 (16 cm^{-1}). This additional loss cannot be attributed to device heating since the pulsed conditions impose athermal conditions. In addition, since the optical mode distribution are supposedly very similar and since the epitaxial structure only differs from one very thin (35 nm) n -doped layer, this very high difference is attributed to a different carrier distribution in the “hot” cavity as compared to the “cold” cavity. The terms “hot” and “cold” do not refer to any thermal heating but mean that the structure is voltage biased or not.

Another aspect of the characteristic is not fully understood for now. The current threshold of structure A1 was expected to be almost twice smaller than the current threshold of structure A2 according to the analytical calculations performed in chapter 3. Instead of that it is actually more than twice higher! This high current threshold is obviously a consequence of the high intrinsic losses as measured from the regression line.

Please note also that it is not obvious whether structure A2 behaves like a 4 QWs or a 8 QWs laser since we do not know the proportion of electrons and holes that leak over the carrier blocking layers. Nevertheless, we have seen

5.2 Bipolar cascade lasers

in chapter 3, that a single-quantum-well and a double-quantum-well structure behave quite similarly in terms of power-versus-current characteristic, in a first order approximation.

Figure 5.32 Comparison of the optical power-versus-current characteristics of “reference” structure A2 (20- μm -wide) for device length varying from 200- μm to 1200- μm .

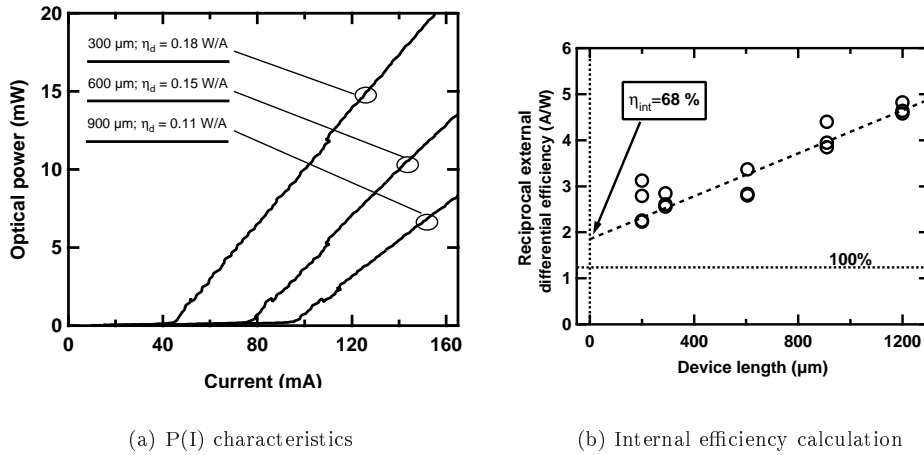
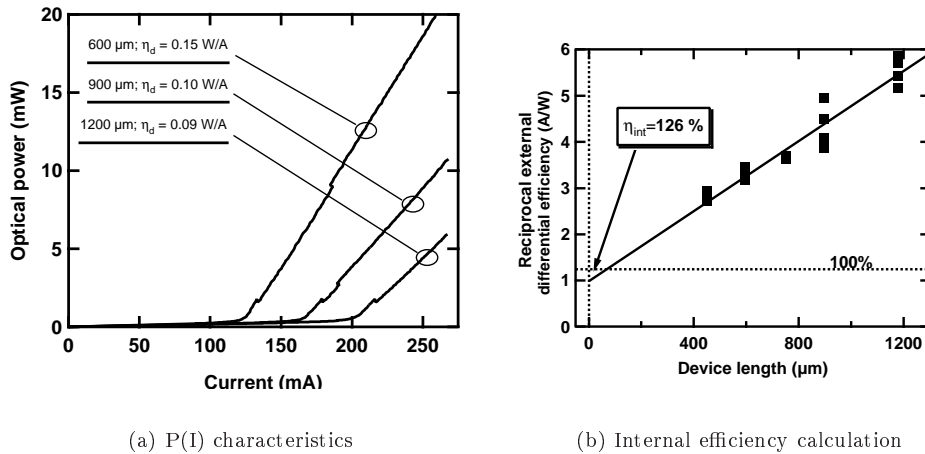


Figure 5.33 Comparison of the optical power-versus-current characteristics of structure A1 (20- μm -wide) for device length varying from 450- μm to 1200- μm .

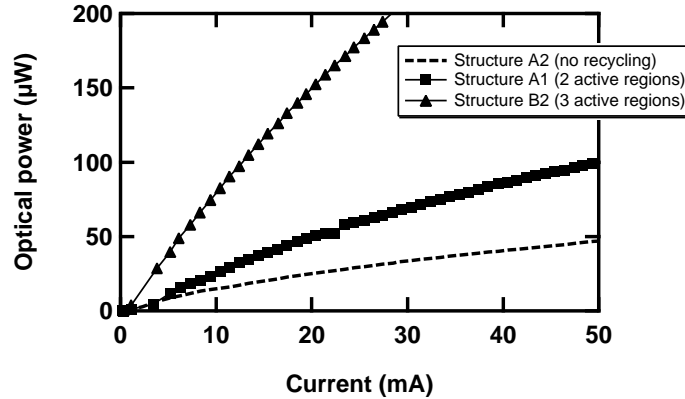


5.2.2.7 Influence of the number of active regions

Structure B2 does not demonstrate a lasing behavior, even in pulsed operation. It was therefore not possible to investigate on the scalability of the external efficiency enhancement by cascading more than two active regions.

We nevertheless display on figure 5.34 the spontaneous emission (under DC current bias) of devices of similar geometry ($3\text{-}\mu\text{m}$ -wide shallow ridge \times $900\text{-}\mu\text{m}$ -long) below threshold.

Figure 5.34 Comparison of spontaneous emission of structures including one, two and three active regions.



In good agreement with what is expected from the analytical calculations of chapter 3, the spontaneous emission increases almost linearly with the number of cascaded active regions. The comparison cannot be achieved completely since the optical mode distribution is not the same for the structures of set A and for structure B2.

5.2.2.8 Explanation of the non-lasing behavior of structure B2

There are several differences in the process of fabrication of structure A1 and B2. We list the major differences here:

1. Structure B2 includes 2 tunnel junctions and structure A1 only one. Tunnel junctions have been proved to suffer from high resistivity. This resistivity might lead to current spreading and device heating that may dramatically alter the device characteristics.
2. The active regions of structure B2 consist of 2 QWs instead of 4 for structure A1. The whole structure B2 therefore only has 6 QWs to compensate for the modal losses that are increased by the doped regions, even if we have observed that this increase was not dramatic. In addition, in order to reach the same gain, the carrier density is higher if the number of wells is lower (as seen from the analytical calculations of chapter 3). This higher carrier density in the QWs and in the barriers might lead to an increased current leakage over the carrier confinement layers.
3. Structure B2, in opposition with structure A1, includes a Bragg grating layer that obviously increases losses and inhibits lasing if the modal gain spectrum does not match the Bragg reflectivity spectrum.
4. Structure A1 was grown in a single epitaxial step. Structure B2 underwent an epitaxial regrowth after the technological treatment to print the Bragg

5.2 Bipolar cascade lasers

grating. The regrowth heats the wafer and might perturb (via diffusion processes) the dopant distribution in the device.

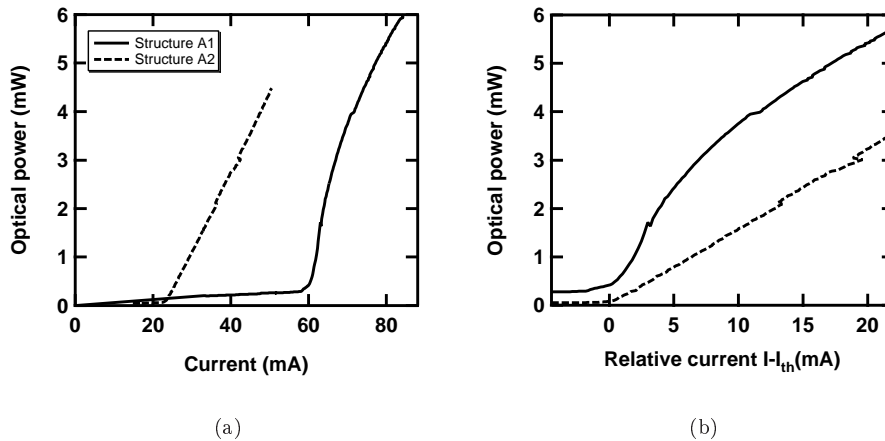
Each one of these differences in the fabrication process can explain (almost by itself) the dramatical power-versus-current characteristic difference observed. The real reason for this difference certainly lies in the conjunction of all the differences in the fabrication process.

5.2.2.9 Demonstration of a single-transverse-mode bipolar cascade laser

The single-vertical-mode emission is forced by the epitaxial structure. But completely etching the active region implies several transverse optical modes (in the direction parallel to the layers) to oscillate in the laser cavity. As already explained in the General Introduction, our approach intends to fabricate a single-transverse-mode bipolar cascade laser. In order to do so, we have processed structure A1 (and structure A2 as a comparative reference) into 3- μm -shallow ridge structures.

We compare on figure 5.35-(a) the optical power-versus-current characteristic of structure A1 and A2 in pulsed conditions (200 ns every 200 μs) at 20 °C for 3- μm -wide \times 300- μm -long devices. In order to facilitate the comparison, figure 5.35-(b) provides the same characteristic as a function of the current relatively to the threshold current.

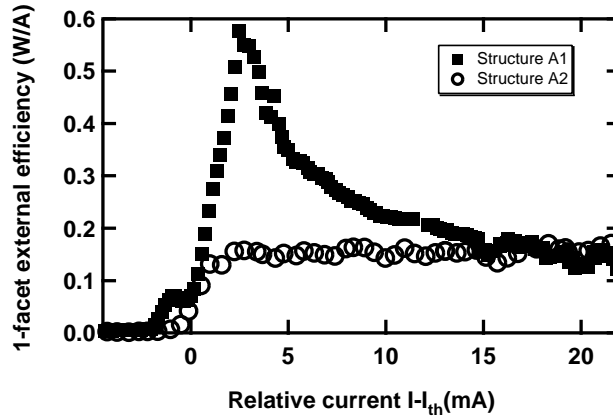
Figure 5.35 Comparison of the optical power-versus-current characteristics of structure A1 and structure A2 (3- μm -wide \times 300- μm -long).



It is obvious from figure 5.35 that the differential external conversion efficiency above the current threshold is higher for structure A1 than for structure A2. To put the emphasis on this feature, we display on figure 5.36 the calculated slope of the optical power-versus-current characteristics for structures A1 and A2 as a function of the relative current ($I - I_{th}$). Each marker corresponds to one measurement. The efficiency is calculated as the slope of the regression

line approximating 5 consecutive measurement points of the raw experimental characteristic.

Figure 5.36 Comparison of the external efficiency out of one facet of structures A1 and A2 ($3\text{-}\mu\text{m}$ -wide \times $300\text{-}\mu\text{m}$ -long) as a function of the relative current $I - I_{th}$.



As expected from an athermal optical power-versus-current characteristic, structure A2 exhibits a very constant efficiency of approximately 0.15 W/A above threshold. This value is in good agreement (although a little lower) than values obtained for single-active-regions 8 QWs lasers of the same geometrical dimension ($3\text{-}\mu\text{m}$ -wide \times $300\text{-}\mu\text{m}$ -long).

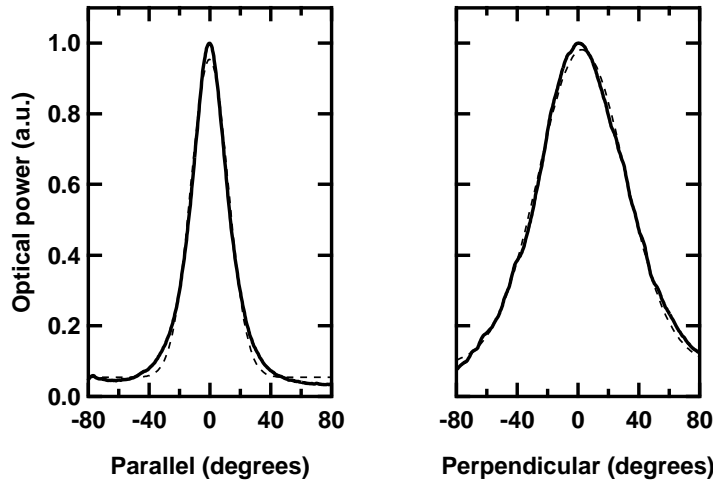
The external efficiency of structure A1 is very different. Over a very large current range (more than 10 mA), the external efficiency largely exceeds the efficiency of the “reference” structure A2. It should be underlined here that the threshold transition is smooth and continuous, and can be achieved regularly by steps of 0.2 mA . Figure 5.36 is an evidence of external efficiency enhancement by cascading several (here two) active regions.

In order to study the optical mode behavior of the $3\text{-}\mu\text{m}$ A1 structure, we measured the angular distribution of the emitted light (far-field measurement). Because of the low optical power emitted within pulsed conditions, we have synchronized the detection system to the drive current. Figure 5.37 displays the angular distribution of the light in the directions parallel and perpendicular to the epitaxial layers.

The far field distribution has a nearly-Gaussian shape in both directions proving that the laser oscillates on the fundamental mode. The best Gaussian fit is also plotted on figure 5.37. The $\frac{1}{e}$ half-width of the mode is 17.3° and 40.5° in the directions parallel and perpendicular respectively. Whereas the parallel-direction far field is very compatible with measurements performed on other more common laser devices, the perpendicular direction large deviation is subsequent to a very thick optical index-guiding region ($>0.5\text{ }\mu\text{m}$) which implies a more important light confinement in this direction.

5.2 Bipolar cascade lasers

Figure 5.37 Synchronized-detection far-field distribution measurement in the direction parallel and perpendicular to the epitaxial layers. The dashed line indicates in each case the best Gaussian fit.



The power-versus-current characteristic of structure A1 suffers from non-linearities. In pulsed operation, these non-linearities cannot be explained by a thermal heating. It is currently attributed to an increasing current leakage over the carrier-blocking layers while the overall current is increased. This non-linear phenomenon was actually predicted by our model (see figure 5.20 on page 163), the characteristic corresponding to 30 nm InP barriers), except that it occurs at a lower current density than expected. This explanation is only an assumption since it does not explain why the non-linearities do not occur for deeply-etched structures.

Whatever the reason why this electrical non-linearity appears, it constitutes a real drawback that should be prevented for use in radio-frequency systems. Above this leakage regime, the external efficiency of structure A1 tends to equal the efficiency of structure A2.

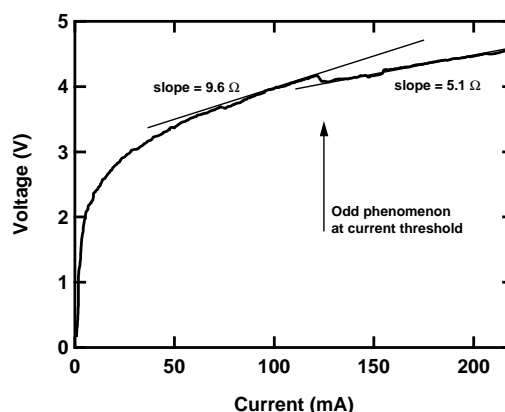
If an increase (by a factor of 2) of the external efficiency can be explained by the carrier recycling process as expected from the analytical calculations performed in chapter 3, it cannot explain simply the very high external efficiency observed soon above threshold (0.6 W/A, corresponding to a quantum external efficiency out of the 2 facets of 150 %). We have already discussed this feature, that is even more noticeable for longer structures ($\geq 600 \mu\text{m}$), and explained it by either saturable absorption or a refocalization of the current when the current pathway recycling electrons (recombination in every active region and recycling through the tunnel junction) is enhanced by stimulated emission. This assumption has been reinforced by current spreading width estimation below and above threshold but still needs to be thoroughly confirmed and understood.

In the 3- μm -wide structures, and more especially for rather long devices ($\geq 600 \mu\text{m}$), the threshold current is corresponding to a very odd phenomenon on the voltage-versus-current characteristic. At threshold current, the laser abruptly changes of voltage-versus-current “regime”. At this point, a negative resistance is actually observed, and the slope of the characteristic (differential

5. Design of a single-transverse-mode bipolar cascade laser

resistance) is lower than below threshold. This phenomenon is directly related to the abrupt laser threshold can either stem from saturable absorption or a re-focalization of the current. An illustration of this very reproducible phenomenon is given on figure 5.38 for a 600 μm laser structure.

Figure 5.38 Voltage-versus-current characteristic of structure A1 processed into a 3- μm -wide \times 900- μm -long shallow ridge.



Even if all the observed phenomena are not fully understood at this time, we have achieved a 3- μm shallow ridge bipolar cascade structure lasing with an increased external efficiency. The geometry and the refractive index distribution allows only the fundamental single-transverse-mode to oscillate in the cavity. It is, to our knowledge, the first demonstration of a edge-emitting single-transverse-mode bipolar cascade laser.

5.3 Conclusion

We have described the complete design of a single-transverse-mode bipolar cascade laser.

We first give our attention to the design of the tunnel junction: we found that InGaAsP $\lambda_{\text{PL}} = 1.35 \mu\text{m}$ has the double advantage of being transparent to 1.55 μm QWs emission, as well as providing a low diffusion coefficient (in the order of $1.8 \times 10^{-8} \text{ cm}^2 \cdot \text{s}^{-1}$ at 10^{19} cm^{-3} , $T = 1000 \text{ }^\circ\text{C}$) and a high incorporation limit for our highly diffusive doping element: Zn. Furthermore, thanks to its relatively low band-gap energy and effective mass this material is a good candidate for low resistivity backward-tunnel junction.

We experimentally implemented a InGaAsP $\lambda_{\text{PL}} = 1.35 \mu\text{m}$ -based tunnel-junction in a tunnel-test-structure. We observe a neat diode-like shape for forward-bias, as well as for backward-bias. The backward resistance of the tunnel-test-device fell to very small values ($< 1\Omega$) and was therefore hard to determine precisely. In addition, we have observed a relatively high facet surfacic current that can reach 50% for a 300 μm -wide \times 300 μm -long device at a bias voltage of 0.8 V. This high facet current might be a consequence of a high volumic resistivity and might be responsible for early device degradation.

Then we turned to the design bipolar cascade lasers. The width of the carrier

5.3 Conclusion

confinement layers appears to be of major interest to be optimized: if the layers are too wide, the overlap of the optical mode with the QWs, as well as the modal effective index decrease. If the layers are too narrow, electron leakage over the barrier appears and degrades the laser characteristics.

We experimentally implemented laser structures optimized with the help of the model described in chapter 4 into two sets of bipolar cascade lasers. The first set includes 2 active regions, and the second set includes 3 active regions.

We found that both electron- and hole-blocking layers are necessary to sustain the carrier recycling process. In addition, we carried out loss measurements on the passive “cold cavity” waveguides to estimate the influence of the doped layers on the modal losses. This influence was found to be very small, but surprisingly, the influence of the current pathway (probably because of different carrier distributions) appeared to be of high influence on the optical mode losses.

We subsequently obtained a two-active-region bipolar cascade laser exhibiting 126% internal electron-to-photon conversion efficiency. We also achieved a sensible increase of the external efficiency for more than 10 mA above threshold with a 3- μm -wide shallow ridge structure that is very likely to exhibit a single-transverse-mode behavior.

For a reason still not completely elucidated, the 3-active-region structure emits a large amount of spontaneous emission but it has not been possible to trigger the stimulated emission process. Eventually, we studied the influence of the spreading of the current on the laser characteristics.

Bibliography

- [1] T.P. Brody. Nature of the Valley Current in Tunnel Diodes. *Journal of Applied Physics*, 33(1):100–111, Jan. 1962.
- [2] H. C. Jr Casey et al. Concentration-dependence of the absorption coefficient for *n*-type and *p*-type GaAs between 1.3 and 1.6 eV. *Journal of Applied Physics*, 46(1):250–257, Jan. 1975.
- [3] H. C. Jr Casey et al. Concentration-dependent absorption and spontaneous emission of heavily-doped GaAs. *Journal of Applied Physics*, 47(2):631–643, Feb. 1976.
- [4] G.J. van Gurp et al. Interstitial and substitutional Zn in InP and InGaAsP. *Journal of Applied Physics*, 65(2):553–560, Jan. 1989.
- [5] Arnaud Fily. *Modèle pour diodes laser de puissance*. PhD thesis, Université Paris X, Paris, France, Dec. 1998.
- [6] A. Haug. Free-carrier absorption in semiconductor lasers. *Semiconductor Science and Technology*, 7:373–378, 1992.
- [7] H. C. Jr. Casey and P. L. Carter. Variation of intervalence band absorption with hole concentration in *p*-type InP. *Applied Physics Letters*, 44(1):82, Jan. 1984.
- [8] S. Adachi. Band structure of InGaAsP, Optical Properties of InGaAsP: Discussion, Optical Functions of InGaAsP: Tables. *INSPEC, Properties of InP and related compounds*, pages 387–428, 1991.
- [9] J. Piprek et al. What Limits the Maximum Output Power of Long-Wavelength AlGaInAs/InP Laser Diodes? *Journal of Quantum Electronics*, 38(9):1253–1259, Sep. 2002.
- [10] E.F. Schubert et al. Phenomenology of Zn diffusion and incorporation in InP grown by organometallic vapor-phase epitaxy OMVPE. *Applied Physics Letters*, 67(5):700–702, Jul. 1995.
- [11] S.N.G. Chu et al. Substitutional, interstitial, and neutral zinc incorporation into InP grown by atmospheric pressure metalorganic vapor phase epitaxy. *Journal of Applied Physics*, 80(6):3221–3227, Sep. 1996.
- [12] A.W. Nelson and L.D. Westbrook. A study of *p*-type dopants for InP grown by adduct MOVPE. *Journal of Crystal Growth*, 68:102–110, 1984.

BIBLIOGRAPHY

- [13] Gaëlle Rondeau. *Photorécepteurs pin-HEMT sur InP : croissance par MOVPE et technologie d'intégration monolithique*. PhD thesis, Université de Nantes, Ecole Doctorale des Sciences et Technologies de l'Information et des Matériaux, Nantes, France, May 2001.
- [14] V. Swaminathan et al. Effect of Zn on the electro-optical characteristics of metalorganic chemical vapour deposition grown 1.3 μm InGaAsP/InP lasers. *Electronics Letters*, 32(7):661–662, Mar. 1996.
- [15] Brian Tuck. *Atomic Diffusion in III-V Semiconductors*. Adam Hilger, Bristol, Great Britain, 1988.
- [16] L.Y. Chan et al. Lattice location of diffused Zn atoms in GaAs and InP single crystals. *Journal of Applied Physics*, 65(5):2998–3006, Mar. 1991.
- [17] Kin Man Yu et al. Effect of rapid quenching on the impurity site location in Zn-diffused InP. *Journal of Applied Physics*, 74(1):86–90, Jul. 1993.
- [18] H.B. Serreze et al. Zn diffusion in InP: Effect of substrate dopant concentration. *Applied Physics Letters*, 49(4):210–211, Jul. 1986.
- [19] G.J. van Gorp et al. Zinc diffusion in InGaAsP. *Journal of Applied Physics*, 64(7):3468–3471, 1988.
- [20] N. Otsuka et al. Control of double diffusion front unintentionally penetrated from a Zn doped InP layer during metalorganic vapor phase epitaxy. *Journal of Applied Physics*, 84(8):4239–4247, Oct. 1998.
- [21] S.N.G. Chu et al. Concentration-dependent Zn diffusion in InP during metalorganic vapor phase epitaxy. *Journal of Applied Physics*, 78(5):3001–3007, Sep. 1995.
- [22] U. Gösele and F. Morehead. Diffusion of zinc in gallium arsenide: A new model. *Journal of Applied Physics*, 52(7):4617–4619, Jul. 1981.
- [23] E.H. Sargent, T. Makino, et al. Experimental Study of LCI Lasers Fabricated by Single MOCVD Overgrowth Followed by Selective Dopant Diffusion. *IEEE Photonics Technology Letters*, 10(11):1536–1538, Nov. 1998.
- [24] C. Blaauw and L. Hobbs. Donor-acceptor pair formation in InP doped simultaneously with Si and Zn during metalorganic vapor deposition. *Applied Physics Letters*, 59(6):674–676, Aug. 1991.
- [25] Youngboo Moon. Low temperature photoluminescence characteristics of Zn-doped InP grown by metalorganic chemical vapor deposition. *Journal of Applied Physics*, 83(4):2261–2265, Feb. 1998.
- [26] Nobuyuki Otsuka. Stability of Zn doping profile in modulation-doped multiple quantum well structure. *Journal of Applied Physics*, 80(3):1405–1413, Aug. 1996.
- [27] M. Glade et al. Diffusion of Zn acceptors during MOVPE of InP. *Journal of Crystal Growth*, 108:449–454, 1991.

-
- [28] H. C. Jr. Casey, B.I. Miller, and E. Pinkas. Variation of minority-carrier diffusion length with carrier concentration in GaAs liquid-phase epitaxial layers. *Journal of Applied Physics*, 44(3):1281, 1991.
- [29] M. Razeghi and J.P. Duchemin. Growth and characterization of InP using metalorganic chemical vapor deposition at reduced pressure. *Journal of Crystal Growth*, 64:76–82, 1983.
- [30] Takashi Kobayashi et al. Growth temperature dependence of Zn diffusion in InP/InGaAs heterojunction bipolar transistor structures grown by metalorganic chemical vapor deposition. *Journal of Crystal Growth*, 146:533–537, 1995.
- [31] Takashi Kobayashi and Kenji Kurishima. Suppression of abnormal Zn diffusion in InP/InGaAs heterojunction bipolar transistor structures. *Applied Physics Letters*, 62(3):284–285, Jan. 1993.
- [32] D.G. Deppe. Thermodynamic explanation to the enhanced diffusion of base dopant in AlGaAs-GaAs *npn* bipolar transistors. *Applied Physics Letters*, 56(4):370–372, Jan. 1990.
- [33] Brian Tuck. Diffusion of acceptors in *n*-type and semi-insulating InP. *Journal of Crystal Growth*, 208:123–129, 2000.
- [34] C. Blaauw et al. Secondary ion mass spectrometry and electrical characterization of Zn diffusion in *n*-type InP. *Journal of Applied Physics*, 66(2):605–610, Jul. 1989.
- [35] H. C. Jr Casey. *Atomic diffusion in semiconductors*. D. Shawn, Plenum Press, London, England, 1973. Diffusion in the III-V compound semiconductors.
- [36] A. Eisenbach et al. MOVPE growth for an integrated InGaAs/InP PIN-HBT receiver using Zn-doped *p*⁺-InGaAs layers. *Journal of Crystal Growth*, 170:451–455, 1997.
- [37] A.V. Kamanin, I.A. Mokina, N.M. Schmidt, L.A. Busygina, and T.A. Yurre. Polymer diffusants in III-V semiconductor compounds technology. In *Proceedings of the 8th International Conference on InP and Related Materials*, volume TuP-D14, Schwäbisch Gmünd, Germany, Apr. 1996.
- [38] F. Capasso et al. A Proposed Hydrogenation/Nitridization Passivation Mechanism for GaAs and Other III-V Semiconductor Devices, Including InGaAs Long Wavelength Photodetectors. *Journal Electrochem. Soc.*, pages 821–824, April 1982.
- [39] R.T. Huang et al. Improvement in Dark Current Characteristics and Long-Term Stability of Mesa InGaAs/InP *p*-*i*-*n* Photodiodes with Two-Step SiNx Surface Passivation. *Photonics Technology Letters*, 3(10):934–936, Oct. 1991.
- [40] H.S. Kim et al. Dark current reduction in APD with BCB passivation. *Electronics Letters*, 37(7):455–457, Mar. 2001.

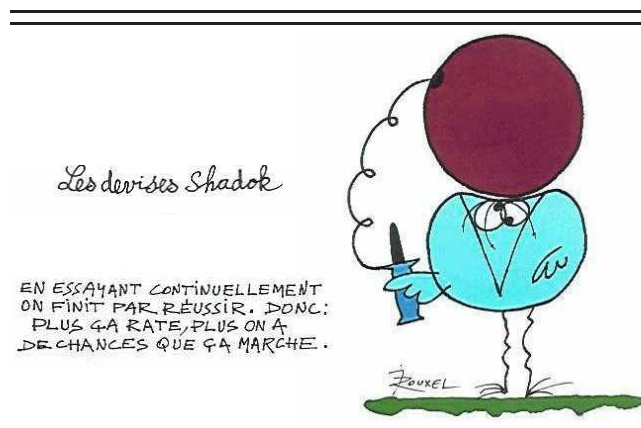
BIBLIOGRAPHY

- [41] J. Ch. Garcia et al. Epitaxially stacked lasers with Esaki junctions: a bipolar cascade laser. *Applied Physics Letters*, 26(71):3752–3754, Dec. 1997.
- [42] J. K. Kim et al. Near-room-temperature continuous-wave operation of multi-active-region 1.55 μm vertical-cavity lasers with high differential efficiency. *Applied Physics Letters*, 77(20):3137–3139, Nov. 2000.
- [43] Frédéric Dross, Frédéric van Dijk, and Borge Vinter. Optimization of Large Band-Gap Barriers for Reducing Leakage in Bipolar Cascade Lasers. *Journal of Quantum Electronics*, 40(8):1003–1007, Aug 2004.
- [44] C. Hanke et al. High-power AlInGaAs/GaAs double and triple microstack lasers at 808 nm. In *Annual Meeting Laser and Electro-Optics Society LEOS'99*, pages 80–81, San Francisco, USA, Nov. 1999.
- [45] Frédéric Dross, Frédéric van Dijk, and Borge Vinter. Improved Bipolar Cascade Lasers Characteristics by Optimization of InP Electron Stopper Layers. In *Proceedings of the 8th International Conference on InP and Related Materials*, Kagoshima, Japan, 2004.
- [46] Universidad Politécnica de Madrid. HAROLD version 3.0. User manual, Spain, 1998.
- [47] B.W. Hakki and T.L. Paoli. CW degradation at 300K of GaAs double-heterostructure junction lasers. II. Electronic gain. *Journal of Applied Physics*, 44(9):4113, 1973.
- [48] J. K. Kim et al. Room-temperature, electrically-pumped multiple-active-region VCSELs with high differential efficiency at 1.55 μm . *Electronics Letters*, 35(13):1084–1085, Jun. 1999.
- [49] T. Knödl et al. Multi-diode cascade VCSEL with 130 % differential quantum efficiency at CW room temperature operation. *Electronics Letters*, 37(1):31–33, Jan. 2001.
- [50] T. Knödl et al. Multistage bipolar cascade vertical-cavity surface-emitting lasers: Theory and experiment. *IEEE Journal on Selected Topics in Quantum Electronics*, 9(5):1406–1414, Sept. 2003.
- [51] T. Knödl et al. Improvement of a Diode Cascade VCSEL Performance. In *Proceedings Conference on Lasers and Electro-Optics Europe CLEO'00*, number CThK7, Nice, France, Sep. 2000.
- [52] T. Knödl et al. Influence of design variations on bipolar cascade VCSEL performance. In *14th Annual Meeting of the IEEE LEOS*, pages 463–464, Nov. 2001.
- [53] T. Knödl et al. Current-spreading-induced bistability in bipolar cascade vertical-cavity surface-emitting lasers. *Applied Physics Letters*, 81(4):583–585, Jul. 2002.
- [54] T. Knödl et al. Bistability in bipolar cascade VCSELs. *Electronics Letters*, 38(8):370–371, Apr. 2002.

- [55] P. Kner et al. A Long-Wavelength MEMS Tunable VCSEL Incorporating a Tunnel Junction. *IEEE Photonic Technology Letters*, 15(9):1183–1185, Sept. 2003.
- [56] J. K. Kim et al. Epitaxially-stacked multiple-active-region 1.55 μm lasers for increased efficiency. In *IEEE Conference on Lasers and Electro-Optics, CLEO '99*, page 139, Baltimore, MD, USA, May 1999.
- [57] J. K. Kim et al. Epitaxially-stacked multiple-active-region 1.55 μm lasers for increased differential efficiency. *Applied Physics Letters*, 74(22):3251–3253, 1999.

Chapter 6

General conclusion and perspectives



6.1 Conclusions

6.1.1 Thesis overlook

This thesis was dedicated to the improvement of the RF gain of directly modulated opto-RF links. We argue that the series connection of laser structures is a powerful concept. The current is recycled from one laser structure to the following, thus increasing the overall electron-to-photon conversion efficiency. The conversion efficiency is not limited anymore and can reach values over 100%. If the device is directly modulated, the RF gain of the link is proportional to the square of the electro-optical conversion efficiency. A series connected composed laser source enables, for the same input RF power, a larger amplitude of the modulated light, and thus a higher amplitude of the current modulation on the photodiode, as compared to a single-laser source.

To implement this principle, the first approach, building a source of several discrete lasers, carries some limitations: the combining of several light beams suffers from either losses, noise increase, or bandwidth shortcomings; the discrete architecture is in any case rapidly limited in terms of frequency bandwidth, due to interconnections between lasers.

Next, a more refined approach stemming from this original concept consists in the integration of several lasers into a single module, then into a single epitaxial structure. The monolithic integrated-multiple-active-region laser is called bipolar cascade laser. The active junctions are electrically connected via highly doped backward tunnel junctions. Furthermore, in an effort to prevent a difficult laser beam combining, we propose all the active regions to be placed into a single-optical-transverse-mode structure.

6.1.2 Work achievements

The principle of bipolar cascade lasers has been described in the General Introduction. We also gave a detailed overview of the past and current research on the subject. It appears that this kind of device has been mainly developed for two applications: high-power lasers, and high-efficiency lasers for analog optical communications. For the latter, the specifications require that the device ensures a single-transverse-mode emission. Up to now, no single-transverse-mode bipolar cascade laser has been proposed. This study was thus framed in perspective of such demand toward research.

Chapter 2 elaborated further the rationale of the study. We compared different electrical architectures and concluded that the series connection architecture is better suited than parallel connection for improving the RF link gain. We then experimentally achieved a 12-dB RF link gain enhancement using four discrete commercially available butterfly-packaged lasers. We also studied the noise behavior and proved theoretically, as well as experimentally, that combining several laser beams can average and thus eventually lower (3-dB noise reduction while using 2 discrete lasers) the intensity noise. Taking into account the problem of possible electrical correlation, the parallel connection presented beforehand an advantage for this application; but no influence of the electrical connection was experimentally found. Besides, an in-depth study of the RIN improvement using a standard coupler was carried out. We elucidated the heterodyne origin of some observed additional noise and managed to prevent it by injecting the light beams with crossed polarization [1]. The compared combined source (for parallel or series connection) however suffers from important bandwidth limitations.

Chapter 3 went down to a “component level” point of view to study the influence of the integration of the concept within the monolithic component. We evaluated theoretically the possible improvements we can expect from an integrated device, using a rate equation formalism, with high-level parameters. In order to discriminate the role of increasing the number of QWs, and increasing the number of active regions, a bipolar cascade laser with two active regions and one QW per active region was compared to a single-QW laser, and to a double-QW laser. It was shown that cascading several junctions increases the differential efficiency of a laser, and imposes in principle no additional fundamental bandwidth limitation. The differential efficiency was expected to scale linearly with N , the number of active regions, the current threshold was ex-

6.1 Conclusions

pected to decrease by a factor of $\frac{1}{N}$. Meanwhile, the carrier-photon relaxation processes are not altered by the concept and the frequency response should remain unchanged. Furthermore, the influence on the intensity noise was investigated. Since the photon noise dominates the relative intensity noise, we found that no improvement can be expected for single-transverse-mode lasers unless the maximum optical power is increased. These results are in opposition to what can be observed for discrete laser combining.

After having predicted the expected behavior of single-transverse-mode bipolar cascade lasers, we reported in chapter 4 on the development of a self-consistent electronic transport model for designing bipolar cascade lasers. The device and the microscopic phenomenon it encompasses was studied from an “electronic level” point of view. We described in detail the transport model, and the severe modifications carried out. We implemented other physical phenomena (such as band-to-band tunneling effect), and had the numerical implementation evolve for modeling 1.55 μm bipolar cascade lasers. With these new features, the model caters for the use of InGaAsP materials lattice-matched to InP, the possibility to input a multi-QW structure, as well as the calculation of the quantum mechanical transport of carriers through the tunnel junction. The self-consistent calculation of the tunnel current was described with great details. Besides, we presented for the first time the calculated band diagram of a bipolar cascade laser [2].

Eventually, the model described in chapter 4 was used in chapter 5 for proposing the design of a BCL. The emphasis was first set on the design of the tunnel junction. The bandgap energy of the material used should be as low as possible to improve the tunnel conductivity. A low-bandgap material has also the asset of providing a low effective mass in our set of materials, which even reduces the tunnel junction resistivity. But on the other hand, the chosen material should not exhibit fundamental absorption at 1.55 μm . The trade-off was obtained for InGaAsP $\lambda_{\text{PL}} = 1,35 \mu\text{m}$. Another trade-off between lowering the tunnel resistivity and increasing the free carrier losses had to be found for optimizing the doping level. For this parameter, as well as for the tunnel junction width, the high-diffusivity of Zn atoms used as *p*-type dopants in the semiconductor lattice drove the decision to a doping level as close as possible to the incorporation limit (at least $5 \times 10^{18} \text{ cm}^{-3}$) and a tunnel junction width of 25 nm, more than one order of magnitude wider than the expected Zn diffusion length during post-epitaxy treatments. An experimental implementation of the tunnel junction in a tunnel-test-structure was also carried out. The characterization revealed that the volume resistivity and the voltage bias necessary to reach a certain amount of current were higher than predicted by the model, leading to an important facet surface current and an early degradation. We attributed this discrepancy to an extreme sensitivity of the characteristics to the dopant concentration and interface sharpness.

The same tunnel junction was then incorporated into a single-transverse-mode structure. Using again the transport model described in chapter 4, some parameters had to be optimized specifically for BCL. It was the case of the confinement current layers. Blocking electrons for leaking over to the following active regions, the confinement layers had to be wide enough. But a too large doped confinement layer have a negative impact on the optical properties, in terms of losses, but also in terms of effective refractive index. The confinement layer width was quite easily optimized with the developed model, but the

ultimate result depends on the design of the rest of the structure (number of QWs...). The hole-locking layer was furthermore expected to have only a small impact on the device characteristics. As for the tunnel junction, the result of the optimization of a bipolar cascade laser was experimentally implemented into the fabrication of two sets of bipolar cascade lasers. The first set included two active layers whereas the second included three active layers. We have successively studied the influence of the confinement layers, of the presence of highly-doped layers inside the optical mode, of the number of active regions and of the current spreading on the opto-electronic characteristics of the devices. We found that the highly-doped layers do not increase dramatically the optical losses of the “cold cavity”. The carrier blocking layers on the contrary influence drastically the electrical behavior and the current pathway (over barrier leakage or pathway recycling the carrier). It was also observed that this change in the current pathway carries a huge influence on the “hot cavity” modal losses, even within athermal pulsed conditions. We suspected the current spreading due to the high volume resistivity of the tunnel junction to trigger power-versus-current non-linearities. This needs to be eradicated for a proper use in system.

Last but not least, an internal efficiency of 126% was reported with a 2-active region BCL and an external efficiency enhancement was observed on a 3- μm -wide shallow ridge BCL structure very likely to exhibit a single-transverse-mode emission. This work constitute the first realization of a edge-emitting single-transverse-mode bipolar cascade laser.

6.2 Perspectives

This work constitute the first step towards the realization of reliable bipolar cascade lasers implemented in systems. We have described the rationale of such effort in this domain, we have developed the optimization tools for tunnel junctions as well as BCL design. Eventually, we experimentally demonstrated a single-transverse-mode bipolar cascade laser emission.

6.2.1 Improvement of the discrete architectures

Because high laser source external efficiency is a key requirement in mid-term opto-RF systems, the perspectives of the work presented in this thesis includes some investigation on discrete combining architectures.

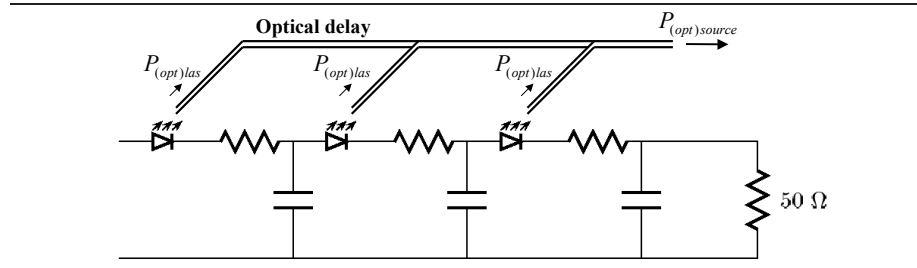
In order to use the discrete architecture in systems, we need to circumvent the bandwidth shortcomings. One possible solution is to integrate as much as possible the different individual lasers in the same package.

Another solution uses the recipe already implemented in distributed photodetectors for combining light beams: the research effort could be placed toward the realization of a traveling-wave cascade diode emitter. Along a line of propagation, we place several laser diodes in series. One optical fiber collect the light from one laser diode, the length of which are designed to compensate for the RF phase shift accumulated during the transmission of the signal to the different lasers. The architecture can be made monolithically, and requires in this case a technological research effort; or it can be an hybrid realization (individual diodes placed along a RF transmission line) and a packaging study is necessary. These light beams can then be combined using any type of ar-

6.2 Perspectives

chitecture described in section 2.2, including the traveling-wave photodetector array.

Figure 6.1 Scheme of principle of proposed traveling-wave cascade laser emitter.



6.2.2 Improvement of the integrated monolithic BCL

For the integrated version of BCL, despite the good results we identified several path of improvement to obtain the system requirements in terms of robustness, reliability and optical mode behavior.

In order to investigate the reasons for the poor robustness and the high rate of degradation of the structures (even during operation in pulsed conditions), the electronic simulation model developed during this work could include the electric field breakdown conditions in the materials.

In addition the devices demonstrate a laser behavior only in pulsed operation. In continuous wave bias conditions, thermal heating prevents the optical gain to exceed the modal losses. In order to understand the laser reliability issues, the developed simulation model could be improved to take self-heating into account.

Besides, the fabricated BCL exhibits a single-transverse-mode behavior but the longitudinal modes are not filtered. We have seen that including a Bragg grating implies some additional treatment and additional optical losses in the cavity that constitute an obstacle to consider for the fabrication of a DFB-BCL.

Last but not least, the shallow waveguide structure used to obtain the single-transverse-mode emission suffers from a high current spreading that degrade the laser characteristics. We identified two different ways to bar the spreading of the current. The first one is banning the current to flow outside of the optical mode region and can be achieved by ion implantation isolation or chemical etching of the tunnel junction followed by an epitaxial regrowth, following the work performed on VCSELs devices [3–5]. A 2-D transport modeling (with commercially available software e.g. ATLAS) of the complex device would also improve the comprehension of the current spreading phenomena. The second proposed field of investigation is decreasing the resistivity of the tunnel junction itself. We believe that this part is the most important future investigation domain and is directly in continuity with the work presented in this thesis. The most straightforward investigation can deal with different types of doping elements, since we have seen that we were limited by the low incorporation and the high diffusivity of Zn atoms in the InGaAsP lattices. We either think about beryllium-doped materials (using Gas Source Molecular Beam Epitaxy to grow the structure), or carbon-doped materials. The latter implies to change the constitutive materials

6. General conclusion and perspectives

and to suppress phosphorus elements in our alloys (for instance InGaAlAs/InP system). Besides, the structure of the tunnel junction can also be a subject of future investigation. For instance, it has been reported good characteristics of super-lattice-based tunnel junctions [6]. The huge domain of band-gap engineering is wide open to enable the improvements and the optimizations of tunnel junctions with materials compatible with $\lambda = 1.55 \mu\text{m}$ emission.

Bibliography

- [1] C. Thibon, F. Dross, Marceaux A., and Vodjdani N. Discussion on RIN improvement using a standard 3-dB coupler. Submitted for Publication, 2004.
- [2] Frédéric Dross, Frédéric van Dijk, and Borge Vinter. Optimization of Large Band-Gap Barriers for Reducing Leakage in Bipolar Cascade Lasers. *Journal of Quantum Electronics*, 40(8):1003–1007, 2004.
- [3] M. Ortsiefer et al. Submilliamp long-wavelength InP-based vertical-cavity surface-emitting laser with stable linear polarisation. *Electronic Letters*, 36(13):1124–1126, 2000.
- [4] V. Jayaraman, M. Mehta, A. W. Jackson, S. Wu, Y. Okuno, J. Piprek, and J. E. Bowers. High-Power 1320-nm Wafer-Bonded VCSELs With Tunnel Junctions. *Photonic Technology Letters*, 15(11):1495–1497, 2003.
- [5] N. Nishiyama, C. Caneau, G. Guryanov, X.S. Liu, M. Hu, and C.E. Zah. High efficiency long wavelength VCSEL on InP grown by MOCVD. *Electronic Letters*, 39(5):437–439, 2003.
- [6] T.C. Lu, H.M. Shieh, and S.C. Wang. Real index-guided InGaAlP red lasers with buried tunnel junctions. *Applied Physics Letters*, 80(11):1882–1884, Mar. 2002.

Appendix A

Notations and parameters used in chapter 3

Item	Description	Find in page	Order of magnitude	Units	Reference
Universal constants					
e	Electronic charge	69	1.6×10^{-19}	C	univ.
c	Speed of light in vacuum	72	3×10^8	m.s^{-1}	univ.
$h\nu$	Planck constant \times light frequency, for $\lambda = 1.55 \mu\text{m}$	73	0.8	eV	calc.
Experimentally varying parameters					
I	Injected current	69	1-200	mA	-
N_{XQW}	Carrier population	69	$0\text{-}10^8$	-	calc.
P_{XQW}	Photon population	71	$1\text{-}10^6$	-	-
S_{XQW}	Output power	76	0-40	mW	calc.
$N_{\text{th(XQW)}}$	Carrier population at threshold (given in density)	78	10^{19}	cm^{-3}	calc.
$I_{\text{th(XQW)}}$	Threshold current	78	10-30	mA	calc.
Experimental specific parameters					
L	Cavity length	73	500	μm	hyp.
R_i	Power reflectivity at mirror i	73	0.27	%	hyp.
V_{active}	Volume of the active region	70	2×10^{-11}	cm^{-3}	hyp.
Material parameters					
η_i	Injection efficiency	69	1	%	hyp.
A	SRH recombination coefficient	70	10^8	s^{-1}	[1, 2]
B_{density}	Bimolecular recombination coefficient (in density)	70	1×10^{-10}	$\text{cm}^3.\text{s}^{-1}$	[1, 3-5]
C_{density}	Auger recombination coefficient (in density)	70	5×10^{-28}	$\text{cm}^6.\text{s}^{-1}$	[1, 2, 6-9]
N_0	Carrier population at transparency (given in density)	71	1.2×10^{18}	cm^{-3}	fit + [8]
<i>See on the next page</i>					

A. Notations and parameters used in chapter 3

Item	Description	Find in page	Order of magnitude	Units	Reference
β	Proportion of spontaneous emission coupled to the dominant mode	72	2.5×10^{-2}	-	fit
G_0	Differential gain	76	5000	s^{-1}	fit+[8]
τ_{parasit}	Parasitic frequency cut	84	35	ps	hyp.
R_S	Series resistance	84	5	Ω	meas.
C_{parasit}	Parasitic capacitance	84	7	pF	hyp. + [8]
τ_{tunnel}	Tunnel delay	86	50	ps	hyp.
R_{tunnel}	Tunnel resistance	86	5	Ω	hyp.
Component parameters					
τ_P	Photon cavity lifetime	72	2	ps	fit.
v_g	Group velocity	72	9.4×10^7	$m.s^{-1}$	hyp.
n_{eff}	Effective dominant mode index	72	3.2	-	hyp.
τ_{RT}	Round-trip time	73	1.1×10^{-11}	s	hyp.
α_i	Internal loss coefficient	73	38	cm^{-1}	fit.
α_m	Mirror loss coefficient	73	14	cm^{-1}	hyp.
η_0	Output conversion coefficient	74	8.5×10^{-9}	W	calc.
τ_E	Carrier lifetime	77	1.6×10^{-9}	s	fit+[4]
τ'_E	Dynamic carrier lifetime	82	1.8×10^{-10}	s	fit.
ω_R	Resonant frequency	83	2-10	GHz	calc.
τ_R	Damping factor	83	3×10^{-10}	s	calc.
η_d	External efficiency	84	0.11	W/A	calc.
W_X	Noise spectral density	88	10^{-19}	$W^2.Hz^{-1}$	calc.
$RIN(\omega)$	Relative intensity noise	89	-140	$dB.Hz^{-1}$	calc.
Other parameters or notations					
δX	Fluctuating variable X	82	-	-	-
ω	RF frequency of modulation	82	0-25	GHz	-
Δf	Whole bandwidth of interest	88	-	-	-
δf	Detection spectral resolution	88	-	-	-
$F_{Y_{XQW}}$	Langevin noise source	82	-	-	-
Δ	Transfer function matrix determinant	83	10^{18}	Hz^2	calc.
$H(\omega)$	Transfer function	84	1	-	calc.
W_{shot}	Shot noise spectral density	88	10^{-21}	$W^2.Hz^{-1}$	calc.
$\langle F_{YZ_{XQW}} \rangle$	Langevin noise force	90	-	-	-
D_{XY}	Langevin diffusion coefficient	91	10^{17}	s^{-1}	calc.

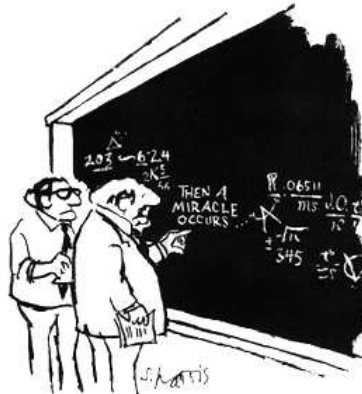
- ☞ “univ.” points out that the parameter is a universal constant,
- ☞ “calc.” means that the parameter is internally calculated,
- ☞ “hyp.” means that the parameter value is taken as an hypothesis, or can be derived easily from parameters taken as hypothesis,
- ☞ “fit” means that the parameter has been fit to match experimental results,
- ☞ “meas.” means that the parameter has been directly experimentally measured.

Bibliography

- [1] CrossLight Software Inc. *PICS3D User's manual*, 2000.
- [2] Ioffe Physico-Technical Institute. Physical Properties of Semiconductors. <http://www.ioffe.rssi.ru/SVA/NSM/Semicond/index.html>.
- [3] E. Rosencher and B. Vinter. *Optoelectronics*. Cambridge University Press, Cambridge, 2002.
- [4] D. McDonald and R.F. O'Dowd. Comparison of Two- and Three-Level Rate Equations in the Modeling of Quantum-Well Lasers. *IEEE Journal of Quantum Electronics*, 31(11):1927–1934, Nov. 1995.
- [5] E. Zielinsky et al. Excitonic transitions and exciton damping processes in InGaAs/InP. *Journal of Applied Physics*, 59(6):2196–2203, Mar. 1986.
- [6] G.P. Agrawal and N.K. Dutta. *Long-Wavelength Semiconductor Lasers*. Van Nostrand Reinhold, 1986.
- [7] Olivier Gilard. *Contribution à la modélisation de diodes laser à puits quantiques contraintes pour Télécommunications optiques*. PhD thesis, Université Paul Sabatier, Toulouse, France, Jan. 1999.
- [8] G. Rossi et al. SPICE Simulation for Analysis and Design of Fast 1.55 μm MQW Laser Diodes. *Journal of Lightwave Technology*, 16(109):1509–1516, Aug. 1998.
- [9] J. Piprek, P. Abraham, and J.E. Bowers. Efficient Analysis of Quantum Well Lasers using PICS3D. In *Integrated Photonics Research Conference*, Santa Barbara, Jul. 1999.

Appendix B

Calculation steps for obtaining the expression of the tunneling current



"I think you should be more explicit here in step two."

Courtesy of S. Harris

In this appendix, we display the calculation steps derived in order to obtain the expression of the tunneling current of equation 4.35. We wanted these Calculation steps as rigorous as possible and therefore the derivation and the notations are sometimes a little bit heavy.

B.1 Calculation step A.

The Bloch-Floquet functions are solution of the undisturbed Schrödinger equation:

$$H_0\varphi_{n,\mathbf{k}}(\mathbf{r}) = \left\{ \frac{\hat{\mathbf{p}}^2}{2m} + V(\mathbf{r}) \right\} \varphi_{n,\mathbf{k}}(\mathbf{r}) = E_n(\mathbf{k})\varphi_{n,\mathbf{k}}(\mathbf{r})$$

We insert $\psi(\mathbf{r}) = \sum_n \psi_n(\mathbf{r})$ from equation 4.13 into equation 4.10:

$$\begin{aligned} \sum_n \int [H_0 - eFx]a_n(\mathbf{k})\varphi_{n,\mathbf{k}}(\mathbf{r})d\mathbf{k} &= \sum_n \int E_n(\mathbf{k})\varphi_{n,\mathbf{k}}(\mathbf{r})d\mathbf{k} \\ \sum_n \left[\int E_n(\mathbf{k})a_n(\mathbf{k})\varphi_{n,\mathbf{k}}(\mathbf{r})d\mathbf{k} - eF \int xa_n(\mathbf{k})\varphi_{n,\mathbf{k}}(\mathbf{r})d\mathbf{k} \right] \\ &= \sum_n \int E_n(\mathbf{k})\varphi_{n,\mathbf{k}}(\mathbf{r})d\mathbf{k} \end{aligned}$$

We now project these expressions on a particular function basis $\varphi_{n',\mathbf{k}'}(\mathbf{r})$:

$$\begin{aligned} \sum_n \left[\int_{\mathbf{k}} E_n(\mathbf{k})a_n(\mathbf{k}) \int_{\mathbf{r}} \varphi_{n',\mathbf{k}'}^*(\mathbf{r})\varphi_{n,\mathbf{k}}(\mathbf{r})d\mathbf{k}d\mathbf{r} - eF \int_{\mathbf{r}} \int_{\mathbf{k}} \varphi_{n',\mathbf{k}'}^*(\mathbf{r})xa_n(\mathbf{k})\varphi_{n,\mathbf{k}}(\mathbf{r})d\mathbf{k}d\mathbf{r} \right] \\ = \sum_n \int_{\mathbf{k}} E_n(\mathbf{k}) \int_{\mathbf{r}} \varphi_{n',\mathbf{k}'}^*(\mathbf{r})\varphi_{n,\mathbf{k}}(\mathbf{r})d\mathbf{k}d\mathbf{r} \end{aligned}$$

Then using $\int_{\mathbf{r}} \varphi_{n',\mathbf{k}'}^*(\mathbf{r})\varphi_{n,\mathbf{k}}(\mathbf{r})d\mathbf{r} = \frac{(2\pi)^3}{V_{\text{cell}}} \Delta_{n,n'}\delta(\mathbf{k} - \mathbf{k}')$ (c.f. Calculation step B.), we get:

$$\begin{aligned} \frac{(2\pi)^3}{V_{\text{cell}}} (E_{n'}(\mathbf{k}') - E) a_{n'}(\mathbf{k}') - eF \sum_n \int_{\mathbf{r}} \int_{\mathbf{k}} \varphi_{n',\mathbf{k}'}^*(\mathbf{r})xa_n(\mathbf{k})\varphi_{n,\mathbf{k}}(\mathbf{r})d\mathbf{k}d\mathbf{r} &= 0 \\ \frac{(2\pi)^3}{V_{\text{cell}}} (E_{n'}(\mathbf{k}') - E) a_{n'}(\mathbf{k}') - eFS(n', \mathbf{k}') &= 0 \end{aligned}$$

According to Calculation step D. $S(n', \mathbf{k}')$ is evaluated to be equal to:

$$S(n', \mathbf{k}') = \frac{(2\pi)^3}{V_{\text{cell}}} \left[i \frac{\partial}{\partial k_x} (a_{n'}(\mathbf{k}')) + \sum_n a_n(\mathbf{k}') X_{nn'}(\mathbf{k}') \right]$$

We finally get equation 4.14:

$$\left\{ E_{n'}(\mathbf{k}') - ieF \frac{\partial}{\partial k_x} - E \right\} a_{n'}(\mathbf{k}') - \sum_n eF X_{nn'}(\mathbf{k}') a_n(\mathbf{k}') = 0 \quad (\text{B.2})$$

B.2 Calculation step B.

Using equation 4.12, we find:

$$\int_{\mathbf{r}} \varphi_{n',\mathbf{k}'}^*(\mathbf{r})\varphi_{n,\mathbf{k}}(\mathbf{r})d\mathbf{r} = \frac{1}{V} \int_{\mathbf{r}} e^{i(\mathbf{k}'-\mathbf{k})\cdot\mathbf{r}} u_{n',\mathbf{k}'}^*(\mathbf{r})u_{n,\mathbf{k}}(\mathbf{r})d\mathbf{r}$$

B.3 Calculation step C.

We consider here that the exponential term under the integral (envelope function) varies a lot more slowly than the periodic functions. Over a unit cell, it is almost constant. We then write $\mathbf{r} = \mathbf{r}_i + \mathbf{r}'$, where \mathbf{r}_i locates the considered cell and \mathbf{r}' indicates the position inside the unit cell. The resulting integral is therefore independent of the considered cell.

We find:

$$\int_{\mathbf{r}} \varphi_{n',\mathbf{k}'}^*(\mathbf{r}) \varphi_{n,\mathbf{k}}(\mathbf{r}) d\mathbf{r} = \frac{1}{V} \sum_{\mathbf{r}_i} e^{i(\mathbf{k}' - \mathbf{k}) \cdot \mathbf{r}_i} \int_{\text{cell}} u_{n',\mathbf{k}'}^*(\mathbf{r}') u_{n,\mathbf{k}}(\mathbf{r}') d\mathbf{r}'$$

According to Calculation step C., we have $\sum_{\mathbf{r}_i} e^{i(\mathbf{k}' - \mathbf{k}) \cdot \mathbf{r}_i} = \frac{(2\pi)^3}{V_{\text{cell}}} N_{\text{cell}} \delta(\mathbf{k}' - \mathbf{k})$. In addition, by definition of the Bloch-Floquet periodic functions normalized over the unit cell, we have

$$\int_{V_{\text{cell}}} u_{n',\mathbf{k}'}^*(\mathbf{r}) u_{n,\mathbf{k}}(\mathbf{r}) d\mathbf{r} = V_{\text{cell}} \Delta_{n,n'}$$

We eventually get:

$$\begin{aligned} \int_{\mathbf{r}} \varphi_{n',\mathbf{k}'}^*(\mathbf{r}) \varphi_{n,\mathbf{k}}(\mathbf{r}) d\mathbf{r} &= \frac{(2\pi)^3}{V_{\text{cell}}} \Delta_{n,n'} \delta(\mathbf{k}' - \mathbf{k}) N_{\text{cells}} \frac{V_{\text{cell}}}{V} \\ &= \frac{(2\pi)^3}{V_{\text{cell}}} \Delta_{n,n'} \delta(\mathbf{k}' - \mathbf{k}) \end{aligned}$$

☞ N_{cells} is the number of cells in the crystal lattice in the volume V

B.3 Calculation step C.

The lattice crystal is not infinite (even if it was, we would have assumed it not to be, to avoid definition problems). This convention leads to a pseudo-quantification of the \mathbf{k} -vectors, as explained in [1, 2]. We can change the integral into a discrete summation with the equivalence:

$$\sum_{\mathbf{k} \in BZ} f_{\mathbf{k}} \equiv \int f(\mathbf{k}) \rho(\mathbf{k}) d\mathbf{k} \quad (\text{B.3})$$

☞ $\rho(\mathbf{k})$ is the density of states in the reciprocal lattice.

☞ For an homogeneous density of states, it usually writes $\rho(\mathbf{k}) = \frac{V}{(2\pi)^3}$, without taking the spin of the electron into account.

Furthermore, we have:

$$\sum_{\mathbf{r}_i} e^{i\mathbf{k} \cdot \mathbf{r}_i} = \begin{cases} 0 & \text{if } \mathbf{k} \neq 0 \\ N_{\text{cells}} & \text{if } \mathbf{k} = 0 \end{cases} \quad (\text{B.4})$$

Therefore we can write:

$$\sum_{\mathbf{r}_i} e^{i\mathbf{k} \cdot \mathbf{r}_i} = \Delta_{\mathbf{k},0} N_{\text{cells}}$$

B. Calculation steps for obtaining the expression of the tunneling current

Now, if we use the equivalence between the discrete sum and the integration over \mathbf{k} , we find:

$$\begin{aligned}
 \int_{-\infty}^{+\infty} \sum_{\mathbf{r}_i} e^{i\mathbf{k}\cdot\mathbf{r}_i} d\mathbf{k} &= \frac{(2\pi)^3}{V_{\text{cell}}} \sum_{\mathbf{k}} \sum_{\mathbf{r}_i} e^{i\mathbf{k}\cdot\mathbf{r}_i} \\
 &= \frac{(2\pi)^3}{V_{\text{cell}}} N_{\text{cells}} \sum_{\mathbf{k}} \Delta_{\mathbf{k},0} \\
 &= \frac{(2\pi)^3}{V_{\text{cell}}} N_{\text{cells}} \tag{B.5}
 \end{aligned}$$

The two equations B.4 and B.5 are exactly the definition of the Dirac function. We therefore have the expression:

$$\sum_{\mathbf{r}_i} e^{i\mathbf{k}\cdot\mathbf{r}_i} = \frac{(2\pi)^3}{V_{\text{cell}}} N_{\text{cells}} \delta(\mathbf{k})$$

B.4 Calculation step D.

We need here to calculate:

$$S(n', \mathbf{k}') = \sum_n \int_{\mathbf{r}} \int_{\mathbf{k}} \varphi_{n', \mathbf{k}'}^*(\mathbf{r}) x a_n(\mathbf{k}) \varphi_{n, \mathbf{k}}(\mathbf{r}) d\mathbf{k} d\mathbf{r}$$

Using $\varphi_{n, \mathbf{k}}(\mathbf{r}) = \frac{e^{i\mathbf{k}\cdot\mathbf{r}}}{\sqrt{V}} u_{n, \mathbf{k}}(\mathbf{r})$ (cf. equation 4.12), let's first notice that:

$$\begin{aligned}
 \frac{\partial}{\partial k_x} (a_n(\mathbf{k}) \varphi_{n, \mathbf{k}}(\mathbf{r})) &= \frac{\partial}{\partial k_x} (a_n(\mathbf{k})) \varphi_{n, \mathbf{k}}(\mathbf{r}) \\
 &\quad + i x a_n(\mathbf{k}) \varphi_{n, \mathbf{k}}(\mathbf{r}) \\
 &\quad + a_n(\mathbf{k}) \frac{1}{\sqrt{V}} e^{i\mathbf{k}\cdot\mathbf{r}} \frac{\partial}{\partial k_x} (u_{n, \mathbf{k}}(\mathbf{r}))
 \end{aligned}$$

Inserting B.6 into the expression of $S(n', \mathbf{k}')$, we find:

$$\begin{aligned}
 S(n', \mathbf{k}') &= \sum_n \int_{\mathbf{r}} \int_{\mathbf{k}} \varphi_{n', \mathbf{k}'}^*(\mathbf{r}) x a_n(\mathbf{k}) \varphi_{n, \mathbf{k}}(\mathbf{r}) d\mathbf{k} d\mathbf{r} \\
 &= \frac{1}{i} \sum_n \int_{\mathbf{r}} \int_{\mathbf{k}_{\perp}} \varphi_{n', \mathbf{k}'}^*(\mathbf{r}) \left\{ \int_{k_x} \frac{\partial}{\partial k_x} (a_n(\mathbf{k}) \varphi_{n, \mathbf{k}}(\mathbf{r})) dk_x \right\} d\mathbf{k}_{\perp} d\mathbf{r} \\
 &\quad - \frac{1}{i} \sum_n \int_{\mathbf{k}} \frac{\partial}{\partial k_x} (a_n(\mathbf{k})) \left\{ \int_{\mathbf{r}} \varphi_{n', \mathbf{k}'}^*(\mathbf{r}) \varphi_{n, \mathbf{k}}(\mathbf{r}) d\mathbf{r} \right\} d\mathbf{k} \\
 &\quad - \frac{1}{i} \sum_n \int_{\mathbf{k}} a_n(\mathbf{k}) \frac{1}{V} \left\{ \int_{\mathbf{r}} e^{i(\mathbf{k}-\mathbf{k}')\cdot\mathbf{r}} u_{n', \mathbf{k}'}^*(\mathbf{r}) \frac{\partial}{\partial k_x} (u_{n, \mathbf{k}}(\mathbf{r})) d\mathbf{r} \right\} d\mathbf{k} \\
 &= 0 \\
 &\quad + i \frac{(2\pi)^3}{V_{\text{cell}}} \sum_n \int_{\mathbf{k}} \frac{\partial}{\partial k_x} (a_n(\mathbf{k})) \Delta_{n, n'} \delta(\mathbf{k} - \mathbf{k}') d\mathbf{k} \\
 &\quad + \frac{(2\pi)^3}{V_{\text{cell}}} \sum_n \int_{\mathbf{k}} a_n(\mathbf{k}) \delta(\mathbf{k} - \mathbf{k}') \left\{ \frac{i}{V_{\text{cell}}} \int_{\text{cell}} u_{n', \mathbf{k}'}^*(\mathbf{r}) \frac{\partial}{\partial k_x} (u_{n, \mathbf{k}}(\mathbf{r})) d\mathbf{r} \right\} d\mathbf{k}
 \end{aligned}$$

B.5 Calculation step E.

The first term equals to 0 because the indefinite integral over k_x is a periodic function of k_x . The second term is transformed according to Calculation step B. ; as for the third term, we assume, as we did for Calculation step B. that the envelope function varies slowly. The integral can be divided into a sum of integrals over the unit cell which are independent of the considered unit cell. By definition, we set $X_{nn'}(\mathbf{k}) = \frac{i}{V_{\text{cell}}} \int_{\text{cell}} u_{n',\mathbf{k}}^*(\mathbf{r}) \frac{\partial}{\partial k_x} (u_{n,\mathbf{k}}(\mathbf{r})) d\mathbf{r}$, we finally have:

$$S(n', \mathbf{k}') = \frac{(2\pi)^3}{V_{\text{cell}}} \left[i \frac{\partial}{\partial k'_x} (a_{n'}(\mathbf{k}')) + \sum_n a_n(\mathbf{k}') X_{nn'}(\mathbf{k}') \right]$$

B.5 Calculation step E.

We can check the normalization of the wave functions over the crystal by calculating according to equation 4.13:

$$\begin{aligned} \int \psi_n^*(\mathbf{r}) \psi_n(\mathbf{r}) d\mathbf{r} &= \frac{V_{\text{cell}}}{(2\pi)^3} \int_{\mathbf{r}} \int_{\mathbf{k}} \int_{\mathbf{k}'} a_n^*(\mathbf{k}') a_n(\mathbf{k}) \varphi_{n,\mathbf{k}}^*(\mathbf{r}) \varphi_{n,\mathbf{k}'}(\mathbf{r}) d\mathbf{k} d\mathbf{k}' d\mathbf{r} \\ &= \frac{V_{\text{cell}}}{(2\pi)^3} \int_{\mathbf{k}} \int_{\mathbf{k}'} a_n^*(\mathbf{k}) a_n(\mathbf{k}') \left\{ \int_{\mathbf{r}} \varphi_{n,\mathbf{k}}^*(\mathbf{r}) \varphi_{n,\mathbf{k}'}(\mathbf{r}) d\mathbf{r} \right\} d\mathbf{k} d\mathbf{k}' \\ &= 1 \end{aligned}$$

We take the convention of normalizing the periodic part of the Bloch-Floquet functions in the unit cell:

$$\int_{V_{\text{cell}}} u_{n,\mathbf{k}}^*(\mathbf{r}) u_{n,\mathbf{k}}(\mathbf{r}) d\mathbf{r} = V_{\text{cell}}$$

which is equivalent to saying that (cf. Calculation step B.):

$$\int_{\mathbf{r}} \varphi_{n,\mathbf{k}}^*(\mathbf{r}) \varphi_{n,\mathbf{k}'}(\mathbf{r}) d\mathbf{r} = \frac{(2\pi)^3}{V_{\text{cell}}} \delta(\mathbf{k} - \mathbf{k}')$$

Therefore, using the solution for $a_n(\mathbf{k})$ found in equation 4.15 on page 120, we find:

$$\int \psi_n^*(\mathbf{r}) \psi_n(\mathbf{r}) d\mathbf{r} = \int_{\mathbf{k}} |a_n(\mathbf{k})|^2 d\mathbf{k} \quad (\text{B.6})$$

$$= |a_n(0)|^2 \int_{\mathbf{k}_{\perp}} |a_n(\mathbf{k}_{\perp})|^2 d\mathbf{k}_{\perp} \int_{k_x} |b_n(k_x)|^2 dk_x \quad (\text{B.7})$$

$$= 1 \quad (\text{B.8})$$

⇨ $b_n(k_x)$ are the exponential part of the $a_n(\mathbf{k})$, as described by equation 4.15

In order to obtain the normalization B.8, we need to have:

$$|a_n(\mathbf{k}_{\perp})|^2 = \delta(\mathbf{k}_{\perp} - \mathbf{k}_{\perp 0})$$

⇨ Equation 4.14 can be solved for any value $\mathbf{k}_{\perp 0}$ of \mathbf{k}_{\perp} , which is conserved when applying an electric field along x .

B. Calculation steps for obtaining the expression of the tunneling current

Thereafter, using the equivalence between sum and integral of Calculation step C. equation B.3, we get:

$$\int_{k_x} dk_x = \frac{2\pi}{L_x} \sum_{k_x} 1 = N_{\text{cells}} \frac{2\pi}{L_x} = \frac{2\pi}{\ell_x} = \kappa_x$$

⇨ κ_x is the length of the BZ in the x -direction

The normalization of equation B.8 is obtained with:

$$a_n(0) = a(0) = \frac{1}{\kappa_x}$$

B.6 Calculation step F.

We need here to calculate the matrix element for two different bands n and n' , that gives an estimation of the coupling strength (or the overlap of the wave functions) between two different bands:

$$\begin{aligned} M_{nn'} &= \langle \psi_n(\mathbf{r}) | -eFx | \psi_{n'}(\mathbf{r}) \rangle \\ &= -eF \int_{\mathbf{r}} \psi_n^*(\mathbf{r}) x \psi_{n'}(\mathbf{r}) d\mathbf{r} \\ &= -eF \frac{V_{\text{cell}}}{(2\pi)^3} \int_{\mathbf{r}} \int_{\mathbf{k}} \int_{\mathbf{k}'} a_n^*(\mathbf{k}) \varphi_{n,\mathbf{k}}^*(\mathbf{r}) x a_{n'}(\mathbf{k}') \varphi_{n',\mathbf{k}'}(\mathbf{r}) d\mathbf{r} d\mathbf{k} d\mathbf{k}' \end{aligned} \quad (\text{B.9})$$

Exactly like we did for Calculation step D., we notice that:

$$\begin{aligned} \frac{\partial}{\partial k_x} (a_n(\mathbf{k}) \varphi_{n,\mathbf{k}}(\mathbf{r})) &= \frac{\partial}{\partial k_x} (a_n(\mathbf{k})) \varphi_{n,\mathbf{k}}(\mathbf{r}) \\ &\quad + i x a_n(\mathbf{k}) \varphi_{n,\mathbf{k}}(\mathbf{r}) \\ &\quad + a_n(\mathbf{k}) \frac{1}{\sqrt{V}} e^{i\mathbf{k}\cdot\mathbf{r}} \frac{\partial}{\partial k_x} (u_{n,\mathbf{k}}(\mathbf{r})) \end{aligned}$$

We then transform equation B.9 into:

$$\begin{aligned} M_{nn'} &= -\frac{eF}{i} \frac{V_{\text{cell}}}{(2\pi)^3} \int_{\mathbf{r}} \int_{\mathbf{k}} a_n^*(\mathbf{k}) \varphi_{n,\mathbf{k}}^*(\mathbf{r}) \int_{\mathbf{k}'_{\perp}} \left\{ \int_{k'_x} \frac{\partial}{\partial k'_x} (a_{n'}(\mathbf{k}') \varphi_{n',\mathbf{k}'}(\mathbf{r})) dk'_x \right\} d\mathbf{k}'_{\perp} d\mathbf{k} d\mathbf{r} \\ &\quad + \frac{eF}{i} \frac{V_{\text{cell}}}{(2\pi)^3} \int_{\mathbf{k}} \int_{\mathbf{k}'} a_n^*(\mathbf{k}) \frac{\partial}{\partial k'_x} (a_{n'}(\mathbf{k}')) \left\{ \int_{\mathbf{r} \in V} \varphi_{n,\mathbf{k}}^*(\mathbf{r}) \varphi_{n',\mathbf{k}'}(\mathbf{r}) d\mathbf{r} \right\} d\mathbf{k}' d\mathbf{k} \\ &\quad + \frac{eF}{iV} \frac{V_{\text{cell}}}{(2\pi)^3} \int_{\mathbf{k}} \int_{\mathbf{k}'} a_n^*(\mathbf{k}) a_{n'}(\mathbf{k}') \left\{ \int_{\mathbf{r} \in V} e^{i(\mathbf{k}'-\mathbf{k})\cdot\mathbf{r}} u_{n,\mathbf{k}}^*(\mathbf{r}) \frac{\partial}{\partial k'_x} (u_{n',\mathbf{k}'}(\mathbf{r})) d\mathbf{r} \right\} d\mathbf{k}' d\mathbf{k} \end{aligned}$$

As previously, the first term equals to 0 because the indefinite integral over k'_x is a periodic function of k'_x . The second term is transformed according to Calculation step B., and is proportional to $\Delta_{n,n'}$. Since we calculate the matrix element between two different band, this second term also equals 0. As for the third term, we assume, as we did for Calculation step B. and D. that the envelope function varies slowly. The integral can be divided into a sum of integrals over the unit cell which are independent of the considered unit cell.

B.7 Calculation step G.

We eventually have:

$$\begin{aligned}
 M_{nn'} &= \frac{eF}{i} \frac{N_{\text{cell}}}{V} \int_{\mathbf{k}} \int_{\mathbf{k}'} a_n^*(\mathbf{k}) a_{n'}(\mathbf{k}') \delta(\mathbf{k}' - \mathbf{k}) \left\{ \int_{\mathbf{r} \in V_{\text{cell}}} u_{n,\mathbf{k}}^*(\mathbf{r}) \frac{\partial}{\partial k'_x} (u_{n',\mathbf{k}'}(\mathbf{r})) d\mathbf{r} \right\} d\mathbf{k}' d\mathbf{k} \\
 &= -eF \int_{\mathbf{k}} a_n^*(\mathbf{k}) a_{n'}(\mathbf{k}) \left\{ \frac{i}{V_{\text{cell}}} \int_{\mathbf{r} \in V_{\text{cell}}} u_{n,\mathbf{k}}^*(\mathbf{r}) \frac{\partial}{\partial k_x} (u_{n',\mathbf{k}}(\mathbf{r})) d\mathbf{r} \right\} d\mathbf{k}
 \end{aligned}$$

With the definition,

$$\begin{aligned}
 X_{nn'}(\mathbf{k}) &= \frac{1}{V_{\text{cell}}} \int_{\text{cell}} u_{n,\mathbf{k}}^*(\mathbf{r}) x u_{n',\mathbf{k}}(\mathbf{r}) d\mathbf{r} \\
 &= \frac{i}{V_{\text{cell}}} \int_{\text{cell}} u_{n,\mathbf{k}}^*(\mathbf{r}) \frac{\partial}{\partial k_x} u_{n',\mathbf{k}}(\mathbf{r}) d\mathbf{r}
 \end{aligned}$$

we eventually find:

$$\begin{aligned}
 M_{nn'} &= -eF \int_{\mathbf{k}} X_{nn'}(\mathbf{k}) a_n^*(\mathbf{k}) a_{n'}(\mathbf{k}) d\mathbf{k} \\
 &= -\frac{eF}{\kappa_x} \int_{k_x} X_{nn'}(\mathbf{k}) \exp \left\{ \frac{i}{eF} \int_0^{k_x} (E_{n'}(\mathbf{k}') - E_n(\mathbf{k}')) dk'_x \right\} dk_x
 \end{aligned}$$

B.7 Calculation step G.

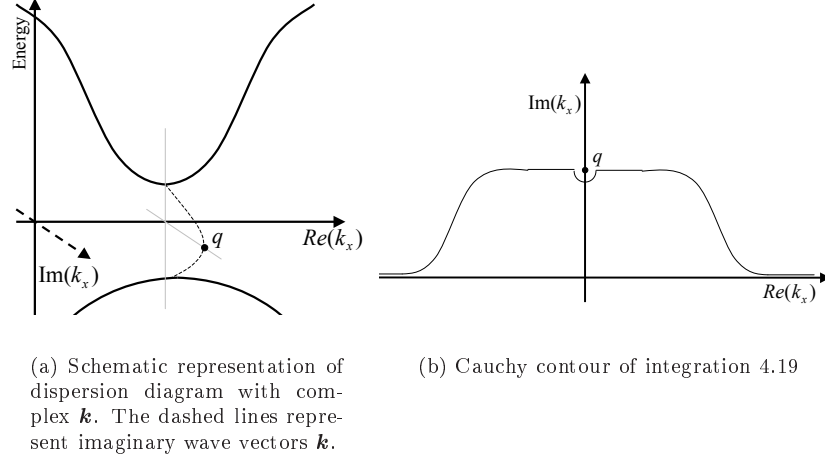
There are two main contributions to the integration of the contour of equation 4.19 that we recall here with the notations used to derive the $\mathbf{k} \cdot \hat{\mathbf{p}}$ -method:

$$\begin{aligned}
 M_{cv} &= -\frac{eF}{\kappa_x} \int X_{cv}(\mathbf{k}) \exp \left\{ \frac{i}{eF} \int_0^{k_x} \eta dk'_x \right\} dk_x \\
 &= -\frac{ieF \hbar E_g^{\frac{3}{2}}}{2m_r^{\frac{1}{2}} \kappa_x} \int \frac{1}{\eta^2} \exp \left\{ \frac{i}{eF} \int_0^{k_x} \eta dk'_x \right\} dk_x \quad (\text{B.10})
 \end{aligned}$$

We also reproduce figure 4.10 in order to facilitate the reading of this calculation step.

B. Calculation steps for obtaining the expression of the tunneling current

Figure B.1 Reproduction of figure 4.10: the maximum tunneling probability occurs near the “pole” q .



The major contribution comes from the integration over the semi-circle around the pole, whereas the contribution of the horizontal integration should not be neglected. We will calculate separately these two contributions and then add them to obtain the result of the whole integration over the contour:

$$M_{cv} \equiv \int \equiv \oint + \int_{\text{hor}}$$

According to the theorem of the Residues, we can write the first contribution as:

$$\oint = \frac{1}{2} \oint = i\pi \Re(q)$$

The residue $\Re(q)$ is defined as the term factor of $\frac{1}{z-q}$ in the development of the integrand in Laurent series, where q is the pole of the integrated function.

The integrand of equation B.10 can be Laurent-series developed as follows:

$$\begin{aligned} \frac{1}{\eta^2} \exp \left\{ \frac{i}{eF} \int_0^{k_x} \eta dk'_x \right\} &= \frac{f(k_x)}{\eta(k_x)^2} = \frac{f(k_x)}{\frac{E_g \hbar^2}{m_r} (k_x - q)(k_x + q)} \\ &\underset{k_x \rightarrow q}{\simeq} \frac{f(q)}{\frac{E_g \hbar^2}{2q m_r}} \frac{1}{k_x - q} + \dots \end{aligned}$$

We find for the semi-circle contribution:

$$\oint = \frac{\pi E_g^{1/2} m_r^{1/2}}{4 \hbar q \kappa_x} eF \exp \left\{ \frac{i}{eF} \int_0^q \eta dk'_x \right\} \quad (\text{B.11})$$

Now, for the contribution of the horizontal integral, we need the principal

B.7 Calculation step G.

part of:

$$\begin{aligned}
\int_{\text{hor}} &= -\frac{ieF\hbar E_g^{\frac{3}{2}}}{2m_r^{\frac{1}{2}}\kappa_x} \int_{\text{horizontal contour}}^{k_x \in} \frac{1}{\eta^2} \exp\left\{\frac{i}{eF} \int_0^{k_x} \eta dk'_x\right\} dk_x \\
&= -\frac{ieF\hbar E_g^{\frac{3}{2}}}{2m_r^{\frac{1}{2}}\kappa_x} \int_{\text{horizontal contour}}^{k_x \in} \frac{1}{\eta^2} \exp\left\{\frac{i}{eF} \left[\int_0^q \eta dk'_x + \int_q^{k_x} \eta dk'_x\right]\right\} dk_x \\
&= -\frac{ieF\hbar E_g^{\frac{3}{2}}}{2m_r^{\frac{1}{2}}\kappa_x} \exp\left\{\frac{i}{eF} \int_0^q \eta dk'_x\right\} \int_{\text{horizontal contour}}^{k_x \in} \frac{1}{\eta^2} \exp\left\{\frac{i}{eF} \int_q^{k_x} \eta dk'_x\right\} dk_x
\end{aligned}$$

We introduce the integration variable $v = k'_x - q$ ($v \in \mathbb{R}$) for the integral inside the integration over k_x . We also introduce the real variable $\sigma = k_x - q$ (σ also $\in \mathbb{R}$). Since the major contribution comes from the vicinity of q for k_x , we can develop $\eta(k'_x)$ in the vicinity of $v = 0$ from equation 4.28, with the result:

$$\eta = \sqrt{2}\hbar\sqrt{\frac{E_g}{m_r}}q^{1/2}v^{1/2} + \dots$$

The horizontal contribution becomes:

$$\begin{aligned}
\int_{\text{hor}} &= -\frac{ieF\hbar E_g^{\frac{3}{2}}}{2m_r^{\frac{1}{2}}\kappa_x} \exp\left\{\frac{i}{eF} \int_0^q \eta dk'_x\right\} \\
&\quad \int_{\text{horizontal contour}}^{k_x \in} \frac{1}{\eta^2} \exp\left\{\frac{i}{eF} \int_{v=0}^{v=\sigma} \sqrt{2}\hbar\sqrt{\frac{E_g}{m_r}}q^{1/2}v^{1/2}dv\right\} dk_x \\
&= -\frac{ieF\hbar E_g^{\frac{3}{2}}}{2m_r^{\frac{1}{2}}\kappa_x} \exp\left\{\frac{i}{eF} \int_0^q \eta dk'_x\right\} \int_{\text{horizontal contour}}^{k_x \in} \frac{1}{\eta^2} \exp\left\{iq^{1/2}\frac{2\sqrt{2}\hbar}{3eF}\sqrt{\frac{E_g}{m_r}}\sigma^{3/2}\right\} dk_x
\end{aligned}$$

We change the integration variable into $\gamma = (k - q)^{3/2} = \sigma^{3/2}$ and find:

$$\int_{\text{hor}} = -i\frac{E_g^{1/2}m_r^{1/2}}{6\kappa_x\hbar q}eF \exp\left\{\frac{i}{eF} \int_0^q \eta dk'_x\right\} \int_{\gamma=-\infty}^{\gamma=+\infty} \frac{1}{\gamma} \exp\left\{iq^{1/2}\frac{2\sqrt{2}\hbar}{3eF}\sqrt{\frac{E_g}{m_r}}\gamma\right\} d\gamma$$

The choice of the square root of q is ambiguous and needs to be treated separately if we want to have convergence. We therefore separate the integral over \mathbb{R} into one integral over $\mathbb{R}+$ and one integral over $\mathbb{R}-$.

For $\gamma > 0$, we need to take $\sqrt{q} = \left(\frac{1+i}{\sqrt{2}}\right)$ to ensure convergence, and we split the integral into two:

$$\begin{aligned}
\int_0^{+\infty} \frac{1}{\gamma} \exp\left\{i\sqrt{q}\frac{2\sqrt{2}\hbar}{3eF}\sqrt{\frac{E_g}{m_r}}\gamma\right\} d\gamma &= \int_0^{+\infty} \frac{1}{\gamma} e^{iC\gamma} e^{-C\gamma} d\gamma \\
&= I_1 + I_2
\end{aligned}$$

$$\Leftrightarrow C = |q|^{1/2} \frac{2\hbar}{3eF} \sqrt{\frac{E_g}{m_r}}$$

$$\Leftrightarrow C \in \mathbb{R}$$

$$\Leftrightarrow C > 0$$

B. Calculation steps for obtaining the expression of the tunneling current

Where we can write [3]:

$$\begin{aligned}
 I_1 &= \lim_{\Gamma \rightarrow +\infty} \int_0^{+\Gamma} \frac{\cos(C\gamma)}{\gamma} e^{-C\gamma} d\gamma \\
 I_2 &= i \int_0^{+\infty} \frac{\sin(C\gamma)}{\gamma} e^{-C\gamma} d\gamma \\
 &= i \frac{\pi}{4}
 \end{aligned}$$

For $\gamma < 0$, we need to take the other square root for q ($\sqrt{q} = \left(\frac{1-i}{\sqrt{2}}\right)$) to ensure convergence, and we obtain similarly:

$$\begin{aligned}
 I_3 &= \lim_{\Gamma \rightarrow +\infty} \int_{-\Gamma}^0 \frac{\cos(C\gamma)}{\gamma} e^{C\gamma} d\gamma \\
 &= -I_1 \\
 I_4 &= i \int_{-\infty}^0 \frac{\sin(C\gamma)}{\gamma} e^{C\gamma} d\gamma \\
 &= I_2
 \end{aligned}$$

We eventually get for the horizontal contribution:

$$\int_{\text{hor}} = \frac{\pi E_g^{1/2} m_r^{1/2}}{12 \kappa_x \hbar q} eF \exp \left\{ \frac{i}{eF} \int_0^q \eta dk'_x \right\} \quad (\text{B.12})$$

Combining equation B.11 and B.12, we get for M_{cv} :

$$\begin{aligned}
 M_{cv} &\equiv \int \equiv \int + \int_{\text{hor}} \\
 M_{cv} &= \frac{\pi E_g^{1/2} m_r^{1/2}}{3 \kappa_x \hbar q} eF \exp \left\{ \frac{i}{eF} \int_0^q \eta dk'_x \right\}
 \end{aligned}$$

I thank you very much for having read all this part!

Bibliography

- [1] E. Rosencher and B. Vinter. *Optoelectronics*. Cambridge University Press, Cambridge, 2002.
- [2] E. Rosencher and B. Vinter. *Optoelectronique*. Dunod, Paris, 2nd edition, 2002.
- [3] Gradshtein and Ryzhik. *Tables of Integrals, Series and Products*. Academic Press, INC, London, UK, 1980.

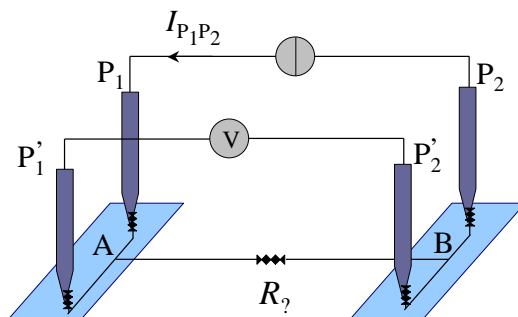
Appendix C

Methods of structure characterization used in chapter 5

C.1 Four-probe measurement technique

The four-probe measurement technique is used for estimating the resistance between two pads A and B. Figure C.1 displays a schematic of the measurement technique.

Figure C.1 Description of the four-probe measurement technique.



The easiest way to measure a resistance is to flow some current between the two pads with the help of two probes P_1 and P_2 , and to measure the resulting voltage. If the same probes are used to inject the current and to measure the voltage, then the voltage measured V_{meas} writes:

$$\begin{aligned} V_{\text{meas}} &= V_{AP_1} + V_{\gamma} + V_{P_2B} \\ &= R_{\gamma} I_{P_1P_2} + (R_{AP_1} + R_{P_2B}) I_{P_1P_2} \end{aligned}$$

☞ V_{γ} and R_{γ} are the voltage and resistance to be determined by the measurement technique.

The measurement is therefore biased by the probe resistances which needs to be determined and can be quite high if the probe is very thin.

To prevent this uncertainty, we use a second set of probes P'_1 and P'_2 to measure the voltage while the current flows through P_1 and P_2 . The measured voltage writes in this configuration:

$$\begin{aligned} V_{\text{meas}} &= V_{AP'_1} + V_{P'_2} + V_{P'_2B} \\ &= R_{P_1P_2} I_{P_1P_2} + (R_{AP'_1} + R_{P'_2B}) I_{P'_1P'_2} \\ &\approx R_{P_1P_2} I_{P_1P_2} \end{aligned}$$

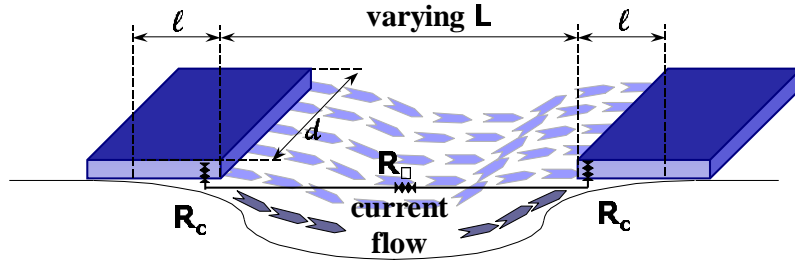
Since $I_{P'_1P'_2}$, the current flowing through the probes P'_1 and P'_2 is negligible, the measurement is more accurate.

C.2 Transmission Line Method

The Transmission Line Method (TLM) technique is used to estimate the contact resistance (R_c expressed in $\Omega \cdot \text{cm}^2$) and the resistance by square (R_{\square} expressed in Ω) of a succession of contact layers. R_{\square} is the surfacic resistance of the material underneath the contact for a square surface. Its value is not dependent on the dimensions of the square.

For measuring the contact and square resistances, we measure the resistance between pads separated by an increasing length L of material, as shown on figure C.2.

Figure C.2 Experimental setup for a TLM measurement.



Due to the huge resistivity difference between the contact material (usually gold) and the material underneath (usually a semiconductor material), it is then assumed that the current penetrates the material underneath only over a small length ℓ beneath the contact, as it is shown on figure C.2. The measured resistance (usually obtained with a four probe measurement) then writes:

$$R_{\text{meas}} = \frac{R_{\square}}{d} \times L + \frac{2R_c}{\ell \times d} \quad (\text{C.1})$$

↪ d is the width of the pads

The measured resistances are experimentally reported on a graph as a function of the length between the pads, and the relation are approximated by a straight regression line:

$$R_{\text{meas}} = c_1 \times L + c_2$$

C.3 Loss transmission measurement

The square resistance is obtained very easily when the regression line crosses the resistance vertical axis:

$$R_{\square} = d \times c_2$$

For obtaining the contact resistance, we need to know the length of the current pathway underneath the contact. Decreasing the length L even below 0, we can assume in first approximation that the resistance will be equal to 0 when $L = -2\ell$. Therefore the current pathway length ℓ can be estimated by the intersection of the regression line with the horizontal axis:

$$\ell = \frac{c_2}{2c_1}$$

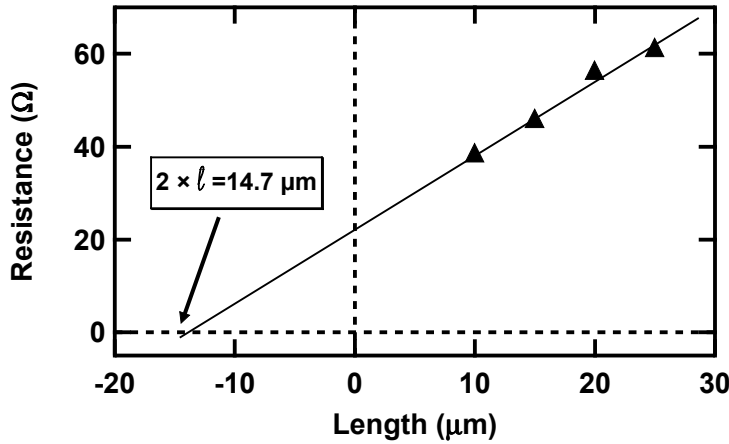
Then we can derive the contact resistance as follows:

$$R_c = \frac{\ell \times d \times c_2}{2} = \frac{d \times c_2^2}{4c_1}$$

In order to obtain a good accuracy in the measurements, the measured resistance should lie in the 10-20 Ω range. The TLM patterns should then be designed accordingly to the expected resistances to measure.

As an illustrative example, we display on figure C.3 the measurement of the p -type contact resistance for the tunnel-test-structure described in more details in section 5.1.4.

Figure C.3 Example of the measurement of the p -type contact resistance using the TLM technique.



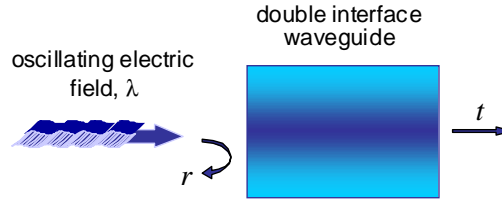
The pad width equals $d = 200 \mu\text{m}$. The measured length of the current pathway is $\ell = 7 \mu\text{m}$ (whereas the pad length is over $60 \mu\text{m}$), the measured square resistance is $R_{\square} = 314 \Omega$, and the measured contact resistance is $R_c = 1.7 \times 10^{-4} \Omega.\text{cm}^2$.

C.3 Loss transmission measurement

The method described here is used to evaluate the losses of a passive waveguide. We have used it in chapter 5 to evaluate the intrinsic losses of structure B2,

which does not exhibit a lasing behaviour. We inject a wide light spectrum into the device under test and collect the light filtered by the device with an optical spectrum analyzer as shown on figure 5.27 on page 171. The analysis of the collected light enables to give an absolute value of the modal waveguide intrinsic losses, with only one device length.

Figure C.4 Schematical representation of the double interface device under study.



We consider an electric field reaching a double interface (constituted by the passive waveguide under test), as depicted on figure C.4. The electric field complex transmittance t coefficient writes:

$$t = \frac{(1 - r^2) \exp(-ik_{\text{wg}}L)}{1 - r^2 \exp(-2ik_{\text{wg}}L)}$$

⇨ $r = \frac{n_{\text{eff}} - i\chi_{\text{eff}} - 1}{n_{\text{eff}} - i\chi_{\text{eff}} + 1}$ is the electric field complex mirror reflectance, with n_{eff} the real part of the modal effective refractive index, and χ_{eff} the imaginary part of the modal effective refractive index, related to the intrinsic loss coefficient.

⇨ L is the length of the waveguide under test.

⇨ $k_{\text{wg}} = \frac{2\pi}{\lambda}(n_{\text{eff}} - i\chi_{\text{eff}})$ is the complex wavevector inside the waveguide, with $\lambda \approx 1.55 \mu\text{m}$ the wavelength of incident light in void.

This expression leads to destructive and constructive interferences while varying λ :

$$\left\{ \begin{array}{l} \text{if } \frac{2\pi}{\lambda}n_{\text{eff}}L = m \times (2\pi), \text{ the transmittance is maximal} \\ \text{if } \frac{2\pi}{\lambda}n_{\text{eff}}L = (2m + \frac{1}{2}) \times 2\pi, \text{ the transmittance is minimal} \end{array} \right.$$

Taking λ_{max} and λ_{min} , two successive incident light wavelength exhibiting a maximum transmittance t_{max} and a minimum transmittance t_{min} , we can write:

$$\left| \frac{t_{\text{max}}}{t_{\text{min}}} \right| = e^{(-\chi_{\text{eff}}L(\frac{2\pi}{\lambda_{\text{max}}} - \frac{2\pi}{\lambda_{\text{min}}}))} \times \frac{1 + r^2 e^{-\frac{4\pi}{\lambda_{\text{min}}}\chi_{\text{eff}}L}}{1 - r^2 e^{-\frac{4\pi}{\lambda_{\text{max}}}\chi_{\text{eff}}L}} \quad (\text{C.2})$$

We inject the first order approximation $\lambda_{\text{max}} \approx \lambda_{\text{min}}$. We then notice that $r^2 = R$ is the power mirror reflectivity and $\frac{4\pi}{\lambda_{\text{min}}}\chi_{\text{eff}} = \alpha_i$ is the modal intrinsic losses in the cavity. Finally, we replace the transmittance coefficients t by the power transmittivity coefficients T with the relation $\left| \frac{t_{\text{max}}}{t_{\text{min}}} \right| = \sqrt{\frac{T_{\text{max}}}{T_{\text{min}}}}$.

C.4 Laser loss measurement

This parameter is experimentally obtained by dividing the power detected at a maximum, and at a minimum. Equation C.2 then derives:

$$\sqrt{\frac{T_{\max}}{T_{\min}}} = \frac{1 + Re^{-\alpha_i L}}{1 - Re^{-\alpha_i L}}$$

$$\alpha_i = \frac{1}{L} \ln R - \frac{1}{L} \ln \left(\frac{\sqrt{\frac{T_{\max}}{T_{\min}}} - 1}{\sqrt{\frac{T_{\max}}{T_{\min}}} + 1} \right)$$

This method is only valid for a single-transverse-mode Fabry-Perot waveguide. Here, we have applied it to DFB structures but we have taken for granted only the results found away from the Bragg grating artefact. Since the method only relies on the measurement of $\frac{T_{\max}}{T_{\min}}$, it is strictly independent of the coupling losses.

As an illustrative example, we calculate the intrinsic loss coefficient of structure B2 at $\lambda = 1.55 \mu\text{m}$. With the help of figure 5.28-(a) on page 172, we find $\frac{T_{\max}}{T_{\min}} = 0.61 \text{ dB}$. The length of the structure is $900 \mu\text{m}$, the power reflectivity coefficient lies around 0.3 ($n_{\text{eff}} \approx 3.4$, $\chi_{\text{eff}} \ll (n_{\text{eff}}, 1)$). The calculation then gives the loss coefficient:

$$\alpha_i = 23.5 \text{ cm}^{-1}$$

C.4 Laser loss measurement

The method presented here is the very usual method for determining both the internal conversion efficiency η_i from electrons to photons and the intrinsic loss α_i of semiconductor lasers. It necessitates to measure the external efficiency of the laser for different cavity lengths.

According to equation 3.14 and equation 3.3, and assuming identical mirror reflectivities, the differential efficiency out of the two facets can write:

$$\eta_{d(2 \text{ facets})} = \eta_i \frac{\alpha_m}{\alpha_i + \alpha_m} \frac{h\nu}{e}$$

- ☞ η_i is the internal conversion efficiency that was assumed to be equal to unity in chapter 3.
- ☞ with $\alpha_m = \frac{1}{L} \ln(\frac{1}{R})$ the distributed mirror loss coefficient.
- ☞ R is the power reflectivity of one mirror, and writes $R = \left| \frac{n_{\text{eff}} - 1}{n_{\text{eff}} + 1} \right|^2$, with n_{eff} the modal effective refractive index of the lasing mode.
- ☞ L is the varying length of the cavity.

We thereafter write the expression of $\eta_{d(2 \text{ facets})}^{-1}$ as a function of the length of the laser cavity:

$$\eta_{d(2 \text{ facets})}^{-1} = \left(\eta_i^{-1} \frac{\alpha_i}{-\ln(R)} \frac{e}{h\nu} \right) \times L + \left(\eta_i^{-1} \frac{e}{h\nu} \right)$$

$$= c_1 \times L + c_2$$

We report on a graph the inverse of the external efficiency as a function of the cavity length and determine the parameters of the regression line. The

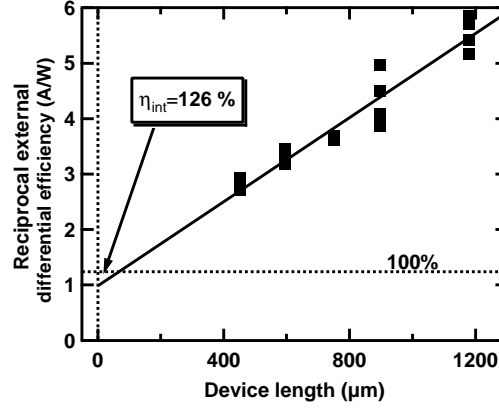
internal efficiency η_i as well as the intrinsic losses are then extracted as follows:

$$\eta_i = \frac{1}{c_2} \frac{e}{h\nu}$$

$$\alpha_i = \frac{c_1}{c_2} \ln\left(\frac{1}{R}\right)$$

As an illustrative example, we display on figure C.5 the determination of the internal efficiency and of the intrinsic losses for structure A1 (processed into a deep 20- μm -wide ridge structure).

Figure C.5 Example of the measurement of internal efficiency and loss parameters performed on structure A1 processed into a deep 20- μm -wide ridge structure.



For an emission at $\lambda = 1.55 \mu\text{m}$, we have $\frac{h\nu}{e} = 0.8 \text{ W/A}$. In addition, since the effective refractive index is close to $n_{\text{eff}} \approx 3.4$, the mirror reflectivity is close to $R \approx 0.3$. The regression line gives the parameters:

$$c_1 = 37.9 \text{ A/(W.cm)}$$

$$c_2 = 0.99 \text{ A/W}$$

Leading to the laser characteristics:

$$\eta_i = 126.4 \%$$

$$\alpha_i = 46.5 \text{ cm}^{-1}$$

Index

- absorption, 71
 - free carrier absorption, 142
 - inter-valence band absorption, 142
 - saturable absorption, 175
- Airy functions, 121
- bandwidth, 9
 - bandwidth improvement, 87
 - bandwidth limitation, 29, 61
 - high-bandwidth applications, 28, 37
- bias-T, 34
- bipolar cascade laser, 9, **12**, 160
 - BCVCSEL, 14, 174
 - experimental, 165
 - high-power BCL, 13
 - microwave optic BCL, 16
 - single-transverse-mode BCL, 31, **137**, 179
 - state-of-the-art, 13
- Bloch
 - Bloch oscillations, 126
 - Bloch theorem, 119
 - Bloch-Floquet functions, 119, 122, 202
- Boltzmann, Ludwig, 105
 - Boltzmann statistics, 111, 149
 - Boltzmann transport equation, 105
- boundary conditions, 120
- Bragg grating, 178, 193
- Brillouin zone, 120, 122
- carrier
 - carrier population, 118
 - carrier population inversion factor, 96
 - carrier recycling effect, 175
- cold cavity, 176
- combining, 24, 25
- compression point, 40
- contact
 - n*- and *p*-type, 154
 - contact resistance, 154, 214
- coplanar RF waveguide, 36
- correlation
 - correlation between noise, 92
 - correlation function, 89
 - cross-correlation, 90
 - inter-correlation, 49, 58
 - self-correlation function, 88, 90
- coupler
 - 3-dB optical coupler, 25
 - 4:4 optical coupler, 46
 - MMI coupler, 30
 - optical Y-coupler, 31
 - RF coupler, 25, 34
- current
 - asymmetric current leakage, 170
 - current confinement layers, 160, 168
 - current leakage, 68, 162, 181
 - current modulation, 83
 - current pathways, 156
 - current spreading, 173, 178
 - current threshold, 72, 78, 79, 81, 176, 181
 - DC component, 33
 - electron and hole current, 115, 162
 - facet surface current, 156, 172
 - recombination current, 113
 - refocalization, 175, 181
 - RF component, 34
 - tunnel current, 127
- data base, 104, 108
- degeneracy, 138
 - degeneracy factors, 131
- density of joint states, 126
- DFB peak, 59

- doping concentration, 129, 141
drift-diffusion model, 105
dynamic behavior, **81**
- effective mass, 108, 124, 129
 effective mass approximation, 121
 effective masses method, 122
 tunnel effective mass, 124, 138
- efficiency
 external differential efficiency, 12, 78, 79, 81, 84, 179
 external differential quantum efficiency, 12, 43
 injection efficiency, 69
 internal differential quantum efficiency, 76, 176, 217
- electric field, 131, 138
 built-in electric field, 118, 150
 internal electric field, 129
- electroluminescence, 81
electron leakage, 69
electron mobility, 109
electronic transport, 104
electronic warfare, 10
- energy band
 band diagram, 104, 118, 139, 161
 band offset, 109
 band-gap energy, 109, 129, 138
 band-tailing, 141
 conduction band, 121, 123
 valence band, 121, 123
- envelop function approximation, 122
epitaxial growth parameters, 148
epitaxial regrowth, 178
erbium-doped fiber amplifier, 171
Esaki, Leo, 116
external modulation, 24
- Fermi
 Fermi Golden Rule, 126
 Fermi-Dirac statistics, 111, 112, 131
 Fermi-level, 160
 quasi-Fermi-level, 116, 131
- Fick laws, 144
four-terminal measurement, 154, **213**
- gain
 optical differential gain, 85
 optical gain factor, 76
 optical linear gain, 85
 optical modal gain, 77
 RF gain, 12, **31**, 32, 44
 RF gain (experimental), 47
- growth temperature, 149
- Hülsmeier, Christian, 8
Hakki and Paoli, 171
Hamiltonian, 119
Hertz, Heinrich Rudolf, 7
hole mobility, 110
Hollmann, Dr. Hans E., 8
hot cavity, 176
- impedance
 characteristic impedance, 36
 contact resistance, 154
 impedance matching, 23
 impedance mismatch, 33
 impedance-matching scheme, 35
 laser series resistance, 43
 no impedance matching, 35, 44
 noisy laser impedance, 50
 parasitic laser complex impedance, 84, 87
 reactive impedance matching, 38
 resistive impedance matching, 37, 45
- implantation isolation, 193
interband interaction, 120
intermediate states, 70
intra-band transition, 70
- Jacobian matrix, 107, 114
Joule heating, 143
- kick-out process, 147
 $\mathbf{k} \cdot \hat{\mathbf{p}}$ -hamiltonian matrix, 123
 $\mathbf{k} \cdot \hat{\mathbf{p}}$ -method, 122, 207
 $\mathbf{k} \cdot \hat{\mathbf{p}}$ -momentum matrix element, 123
- Langevin
 Langevin composed noise source, 94
 Langevin diffusion coefficients, 91, 92, 96
 Langevin method, 92
 Langevin noise forces, 90
 Langevin noise sources, 82, 89, 92, 93

INDEX

- Langevin shot noise method, 96
- laser
 - current threshold, 72
 - directly modulated laser, 31, 83
 - high-frequency laser, 115
 - multi-quantum-well laser, 112
 - multiple cavity cascade lasers, 41
 - parasitic laser complex impedance, 84, 87
 - series resistance, 43
 - split waveguide cascade lasers, 41
 - VCSEL, 174
- loss, 61
 - cold cavity loss, 72
 - extrinsic loss, 142
 - free carrier loss, 161
 - internal scattering loss, 73
 - intrinsic insertion loss, 26, 29, 32
 - intrinsic laser loss measurement, 176, 217
 - intrinsic waveguide loss measurement, 171, 215
 - medium transmission loss, 32
 - mirror loss, 73
 - optical cavity loss, 72
- Luttinger coefficients, 108
- matrix element, 119, 122, 206
- Maxwell, James, 7
 - Maxwell equation solver, 104
- memory effect, 150
- mode group velocity, 72
- multi-core fiber, 27
- Newton method, 106
- noise
 - 1/f noise, 130
 - additional RF noise, 61
 - correlation between noise, 92
 - laser noise spectral density, 88
 - noise figure, 12, 48, 53, 53, 56
 - noisy laser impedance, 50
 - optical heterodyne beating noise, 59
 - optical power fluctuations, 82, 89
 - partition noise, 90, 93
 - phase-to-amplitude conversion, 26
 - RIN, 34, 48, 88, 91, 97
 - RIN (experimental), 57
 - self-induced intensity modulation, 88
 - shot noise, 48, 93, 95
 - shot noise spectral density, 89
 - signal-to-noise ratio, 48, 53, 56
- normalization, 120, 205
- optical
 - band-pass filter, 59
 - mode distribution, 168
 - power modulation, 86
 - spectrum analyzer, 171
- opto-RF link, 9, 11
- overlap factor, 77
- Parseval's theorem, 88
- phased-array antennas, 25
- phonons, 69
- photodiode, 27, 33
 - distributed, 30
- photon, 70
 - photon lifetime, 72
 - photon population, 72
- p-n* junction, 12, 118, 131
- point of view
 - component level, 67
 - electronic level, 103
 - system level, 23
- Poisson, Siméon Denis, 105
 - Poisson equation, 105
- polarization
 - crossed polarization, 60
 - polarization controller, 57, 60
 - polarization maintaining fibers, 60
 - polarization splitter/combiner, 27, 60
 - polarization states, 26
- post-growth treatment, 150
- power
 - optical power, 73
 - RF power, 33, 35
- quantum well
 - cascade quantum well, 74, 75, 80, 86

- double quantum well, 74, 75, 78, 84
- multi-quantum well, 112
- number of wells, 178
- QW injection, 115
- single quantum well, 74, 77, 83
- radar, 7
 - ground radar, 9
- rate equation, 68, 81
- reciprocal lattice, 120
- recombination
 - Auger recombination, 70, 110
 - bimolecular recombination, 69
 - non-radiative recombination, 70, 143
 - radiative recombination, 69
 - recombination current, 113
 - Shockley-Read-Hall recombination, 70
 - spontaneous recombination, 69, 77
- refractive index, 104, 110
- reliability, 193
- resonance frequency, 84, 91
- ridge
 - shallow and deep ridge, 168, 174, 179
 - varying width, 171
- Scharfetter & Gummel scheme, 111
- Schrödinger equation, 119, 123, 202
 - Schrödinger equation solver, 104
- SIMS measurement, 158
- splitting, 25
- spontaneous emission, 72
- squeezing, 68, 93
- statistics, 112
- steady-state, 77
- stimulated emission, 70
- substitutional-interstitial mechanism, 146
- thermal annealing, 150
- thermodynamic equilibrium, 160
- threshold
 - current threshold, 72
 - voltage threshold, 169
- transfer function, 84, 85
- transmission coefficient, 126, 127
- transmission-line method, 154, **214**
- transparency, 71
- transport model, 104
- traveling-wave
 - cascade diode, 192
 - electrodes, 28
- tunnel
 - differential resistance, 155
 - Kane tunneling model, 129
 - tunnel current, 138
 - tunnel effective mass, 124, 138
 - tunnel junction, 44, **116**, 137
 - tunnel-test-structure, 153
 - tunneling matrix element, 125
 - tunneling transit time, 130
 - Zener tunneling, 116
- Vegard law, 108, 109, 152
- voltage threshold, 169
- Wattson-Watt, Robert, 7
- wavefunctions, 120
- wavelength multiplexer, 11, 26, 59
- Wiener-Khinchin relations, 88, 89
- Woodbury formula, 114
- Zener process, 118
- zinc
 - diffusion, **143**
 - diffusion length, 153
 - diffusion rate, 141, 148, 151, 152
 - incorporation limit, 141, 148, 152